Study of Role of Crystal Orientation in Phase Transformation and Deformation of Zr Based Alloys

by

K. V. Mani Krishna
(Roll No. ENGG01200904017)

Bhabha Atomic Research Centre, Mumbai

A thesis submitted to the
Board of Studies in Engineering Sciences
in partial fulfillment of requirements
for the Degree of

DOCTOR OF PHILOSOPHY

of

HOMI BHABHA NATIONAL INSTITUTE

March, 2015

Homi Bhabha National Institute

Recommendations of the Viva Voce Committee

As members of the Viva Voce Committee, we certify that we have read the dissertation prepared by K. V. Mani Krishna, entitled "Study of Role of Crystal Orientation in Phase Transformation and Deformation of Zr Based Alloys " and recommend that it may be accepted as fulfilling the thesis requirement for the award of Degree of Doctor of Philosophy.

Chairman - Prof. V. Kain **Date:**

Guide - Prof. D. Srivastava **Date:**

Co-Guide - Prof. G. K. Dey **Date:**

External Examiner - Prof. Subramanya Sarma **Date:**

Member 1 - Prof. J. B. Singh **Date:**

Member 2 - Prof. A. Awasthi **Date:**

Member 3 - Prof. A. Arya **Date:**

Final approval and acceptance of this thesis is contingent upon the candidate's submission of the final copies of the thesis to HBNI. I/We hereby certify that I/we have read this thesis prepared under my/our direction and recommend that it may be accepted as fulfilling the thesis requirement.

Date :
Place:

Co-Guide Guide

STATEMENT BY AUTHOR

This dissertation has been submitted in partial fulfillment of requirements for an advanced degree at Homi Bhabha National Institute (HBNI) and is deposited in the Library to be made available to borrowers under rules of the HBNI. Brief quotations from this dissertation are allowable without special permission, provided that accurate acknowledgment of source is made. Requests for permission for extended quotation from or reproduction of this manuscript in whole or in part may be granted by the Competent Authority of HBNI when in his or her judgment the proposed use of the material is in the interests of scholarship. In all other instances, however, permission must be obtained from the author.

K V Mani Krishna

DECLARATION

I, hereby declare that the investigation presented in the thesis has been carried out by me. The work is original and has not been submitted earlier as a whole or in part for a degree / diploma at this or any other Institution / University.

K V Mani Krishna

Publications

Published in Peer Reviwed Journals

1. **Publication #1.**

   K. V. Mani Krishna, P. Tripathi, V.D. Hiwarkar, P. Pant, I. Samajdar, D. Srivastava, G.K. Dey, "Automated Reconstruction of Pre-Transformation Microstructures in Zirconium", Scripta materialia , Vol 62, (2010) pp 391-394.

2. **Publication #2.**
   K. V. Mani Krishna, D. Srivastava, G.K. Dey, V. Hiwarkar, I. Samajdar, S. Banerjee,"Role of Grain/Phase Boundary Nature on the Formation of Hydrides in Zr-2.5%Nb Alloy", J. Nucl. Mater. 414 (2011) pp-270-275.

3. **Publication #3.**
   K. V. Mani Krishna, R. Raghavan, D. Srivastava, G. K. Dey, S. K. Sahoo and I. Samjadar, "Study of evolution of dislocation structure with the deformation in Zirconium alloys", Transactions of IIM, 64 (2011) pp 309-313.

4. **Publication #4.**
   K. V. Mani Krishna, D. Srivastava, G. K. Dey, V. Hiwarkar, I. Samajdar, N. Saibaba, Comparative study of methods of the determination of Kearns Parameter in Zirconium, J. Nucl. Mater. 414 (2011) pp- 492-497.

5. **Publication #5.**
   K. V. Mani Krishna and Prita Pant, "Dislocation Dynamics Simulations", Mater. Sci.

Forum, Vol. 736 (2013) pp 13-20.

6. **Publication #6.**
   K. V. Mani Krishna, Sudipto Mandal, Ankur Agrawal, V. Hiwarkar, D. Srivastava, I. Samjadar and G. K. Dey, “Evolution Of Grain Boundary Texture in Zirconium Alloys”, Mater. Sci. Forum, Vols. 702-703 (2012) pp 710-713.

7. **Publication #7. K. V. Mani Krishna**, D. G. Leo Prakash, D. Srivastava, N. Saibaba, J. Quinta da Fonseca, G. K. Dey, M. Preuss, “Influence of Sn on deformation mechanisms during room temperature compression of binary Zr-Sn alloys”, J. ASTM Intnl., in press, 2014

Under Review

1. **Publication #1.**
   K. V. Mani Krishna, S. K. Sahoo, A. Majumdar, D. Srivastavaa, I. Samjadar, G. K. Dey, P. Pant, “Heterogeneous Plastic Deformation in Zirconium: Addressing Temperature and Orientation Dependence Through Discrete Dislocation Dynamics”, Under review, Acta Materialia, 2014

2. **Publication #2.**

   K.V. Mani Krishna, D. G. Leo Prakash, Gabor Timor, D. Srivastava, N. Saibaba, J. Quinta da Fonseca, G. K. Dey, M. Preuss, Under review, Acta Materialia, 2014

3. **Publication #3.**
   K. V. Mani Krishna, D. Srivastava, G.K.Dey, “Role of crystal oreiantion on homogenous nucleation of dislocations in Zr”, under preparation.

International conferences

1. **Conference #1.**
   K. V. Mani Krishna, S. K. Sahoo, A. Majumdar, D. Srivastavaa, I. Samjadar, G. K. Dey, P. Pant, “Dislocation Dynamics simulations investigating deformation heterogeneity in Zirconium”, Oral presentation by Prof. Pant, Society for Engineering Sciences, Annual Technical Meeting, Brown University, Providence, RI, USA, July 28 - 31, 2013.

2. **Conference #2.**
   K. V. Mani Krishna, D. G. Leo Prakash, D. Srivastava, N. Saibaba, J. Quinta da Fonseca, G. K. Dey, M. Preuss, “Influence of Sn on deformation mechanisms during room temperature compression of binary Zr-Sn alloys”, ASTM conference on ‘Zirconium in Nuclear Industry’, Hyderabd, India 2013.

Dedicated to

My family and teachers

Acknowledgments

I would like to take this opportunity to convey my deepest sense of gratitude to my guides Prof. D. Srivastava and Prof. G. K. Dey who initiated me into the area of “Zirconium Alloys”, took time off their busy schedules to encourage me in times of difficulties and showed the right path in times of confusion. Their guidance has always been a crucial component of the present work. They have given me enough freedom and encouragement in trying new things during my research and provided all the support that I needed. I am also thankful to Prof. I. Samajdar and Prof. Prita for their continuous support during various experimental and theoretical works done as part of the thesis. They extended their helping hand and sagely advices at every stage of my work. It has been a pleasure being associated with them. I must make a particular mention of Prof. Michael Presuss, Prof. Leo Prakash and Arnas (University Of Manchester, U.K.) for their contribution with respect to work on neutron diffraction. It was a great experience for me to work with them. I was fortunate to be able to work with several colleagues and derive benefit of their expertise and wisdom in fine tuning my research. Some of the colleagues whom I owe special mention are my lab mates at IIT Bombay (Sahoo, Vijay, Ajay and Jain) and my colleagues at BARC (Dr. Tewari, Visu, Suman and Sanjay) and collaborators from NFC (Shri. S.K. Jha and Vaibhaw).

On personal front, I must thank all my mentors (Annayyagaru, Radhanarasinga Rao sir and Subbarao Uncle) for making me come to this stage. If not for their timely (particularity during my B. Tech days) help I wound not have been in this stage at all. My deepest gratitude to all of them.

Most importantly my special thanks to my wife, Amrutha, who took all the burden of taking care of a hyperactive child and let me concentrate on the research and thesis. My thanks are also to my mother and other family members whose blessings and well wishes ensured I complete this thesis.

Last but not least, I wish to thanks all those people who have developed the open source technologies because of which people like me benefited a lot. I am proud to use some of the best open source programmes for this work. These include LaTeX(my favorite programme of all times) , LAMMPS, Mtex, Ovito, ParaView, DXATool and ParaDis. I wish to thank all those people involved in developing these great softwares and salute their spirit.

K V Mani Krishna

Abstract

Metals, which form the significant proportion of the engineering materials, are in general, crystalline. Deformation and phase transformation are two principal modes of microstructural control/evolution in these materials. The crystalline nature of these materials makes '*how these crystals are oriented*' influence the material behavior in the deformation and/or phase transformations. The role of the crystal orientation is even more dominant in case of materials with low symmetry such as Zirconium, a *hcp* metal. A thorough understanding of the role of orientation in these phenomena can go a long way in optimization of the fabrication processes of the Zr based components used in the nuclear reactors. Present thesis is aimed at furthering the understanding of the phenomena of deformation and phase transformation in these alloys, using a combination of experimental and modeling techniques with a focus on the role played by the local crystal orientation.

For studying the $\beta \rightarrow \alpha$ phase transformation (one of the most prominent phase transformation in Zr alloys), an algorithm for automated reconstruction of parent microstructure, from the microtexture data of product phase, was developed. It uses the microtexture (local crystal orientation) information of the product phase to reconstruct the high temperature phase orientation information and thus its microstructure. It involves identifying triplets of neighboring product grains with a common parent variant and linking such neighboring triplets with a generalized misorientation criterion. The algorithm was successfully applied for quantifying the variant selection during $\beta \rightarrow \alpha$ transformation. The role of variant selection in determining the grain boundary nature of the transformed product was demonstrated.

Another phase transformation of interest in case of Zr is the formation of hydride phase ($\alpha \rightarrow \delta$). Hydride formation in a dual phase microstructure of Zr was studied. Hydrides were found to have preferentially formed along the α/β interfaces. Microtexture measurements showed that the orientation relationship between α and δ-hydride phase was $\{0001\}_\alpha \parallel \{111\}_\delta$ and $\langle 2\bar{1}\bar{1}0\rangle_\alpha \parallel \langle 110\rangle_\beta$. It was shown that the hydrides have higher preference to form along

such α/β interfaces which have one of the low index planes of the β phase constituting the interface.

Another mode of microstructural modification *i.e.*, deformation, was studied in terms of role of local orientation on the deformation heterogeneity, role of alloying elements and initial orientation distribution (texture) and microstructure on different modes of deformation (slip and twinning). Orientation and temperature dependent heterogeneous deformation in Zr was investigated for plane strain loading. Extensive degree of strain partitioning was observed between grains of different orientations, particularly in room temperature deformation. Deformation at higher temperatures, however, had shown significant reduction in deformation heterogeneity. Discrete dislocation dynamics simulations, incorporating temperature dependent threshold criterion for the activation of various slip systems, has successfully explained these observations. These simulations have brought out a novel phenomenon whereby dormant slip systems *i.e.*, slip systems on which the applied stress is below critical resolved shear stress, are activated due to interactions with active primary dislocations. It is proposed that this mechanism can play an important role in reducing orientation dependent deformation heterogeneity in *hcp* materials at high temperatures.

Role of Sn and orientation on the deformation mechanisms of Zr was investigated using *in-situ* neutron diffraction and complementary electron microscopy techniques. Binary Zr-Sn alloys having fully recrystallized microstructure and typical rolling texture were subjected to *in-situ* loading and diffraction experiments. Critical stress for the twin nucleation and the extent of twinning were found to be strongly influenced by the Sn content and loading direction (or orientation). Critical plastic strain for the nucleation of twining, however, was observed to be weakly dependent on the Sn content. Results indicate significant plastic slip activity to be a necessary condition for the onset of twinning. Further, the probability of twinning was shown to be a strong function of the initial orientation.

Using Molecular dynamics simulations, dependence of homogeneous nucleation of dislocations on the crystal orientation had been studied. The asymmetry in the critical stress for nucleation of dislocations in tension Vs compression had been brought out. Using a detailed analysis of the defect structures, it had been shown that nucleation of defects on prismatic planes is much more favorable than on the basal or pyramidal planes in case of Zr.

SYNOPSIS

Introduction

Metals, which form the significant proportion of the engineering materials, are in general crystalline in nature. Their wide spread applicability in the engineering applications stems form many reasons. The two most important of those include (a) good mechanical properties and (b) ease of fabrication into the required shape and size [1]. Both these aspects are a result of excellent control one can exercise on the microstructural parameters using a combination of '*deformation*' and '*phase transformations*'. The fact that the underlying phases are crystalline in nature makes '*how these crystals are oriented*' influence the material behavior in the deformation and/or phase transformations. The role of the crystal orientation is even more dominant in case of materials with low symmetry such as Zirconium, a *hcp* metal. Zr is one of the most crucial structural material in nuclear reactor core. Its applicability is essentially due to a rare combination of good mechanical properties coupled with compatibility to reactor environment and low neutron absorption cross section for thermal neutrons [2, 3]. Zr is the material of choice for a range of critical nuclear core components such as clad tubes, pressure tubes *etc*. The integrity and service performance of these components determine the overall safety and efficiency of reactor. It has long been established that the crystal orientation of the constituent phases (crystallographic texture) in these Zr based components play a significant role in determining the service performance. There are continuous ongoing efforts to further improve and optimize the properties of these Zr based components to achieve higher burn up life of nuclear fuel elements at improved reliability. Such efforts naturally call for stringent control of as fabricated microstructure and texture of Zr components. This necessitates a more deeper understanding of the microstructural and textural modifications brought about by '*deformation*' and '*phase transformations*.

The as fabricated microstructre and texture of a Zr based components is, in general, a cumulative result of changes that take place in a series of Thermo Mechanical Processing (TMP)s that a typical Zr based component goes through during its fabrication [4]. Typically the TMPs used for the fabrication of the Zr based structural components involve, deformation and/or phase transformation during individual stages of the processing. For instance, β-quenching operation is one inevitable operation in any of the fabrication flow sheets so also the hot extrusion. While the former involves a phase transformation, later, is essentially driven by deformation and to some extent by the phase transformation characteristics (depending on the temperature of extrusion and composition of the alloy). On the other hand, cold pilgering and drawing (used in the manufacture of clad tubes and pressure tubes) are essentially deformation processes. Thus the understanding and tailoring of the final microstructure developed after the fabrication, necessarily depends on our ability to understand these individual processes/phenomena of deformation and phase transformation. In addition to optimizing the fabrication processing, understanding of the fundamental mechanisms of phase transformation and deformation are crucial for enhancing service life and mitigating the in service degradation mechanisms. For instance, hydride formation is an important phase transformation ($\alpha \rightarrow \delta$) that some times limit the life of the components [5]. In all these phenomenon/processes the behavior of the material is expected to be highly influenced by the local crystal orientation.

In this context, the present thesis had been conceptualized to study the role of local crystal orientation on phase transformation and deformation in Zr based alloys. Specific issues pertaining to these processes were identified for the study, based on the scientific challenge and their industrial relevance. The objectives of the present study include

1. Variant selection during the $\beta \rightarrow \alpha$ transformation has the effect of influencing the resulting texture distribution and thus it is beneficial to be able to identify and quantify the the same in this transformation. It was aimed to develop an algorithm to reconstruct the pre-transformed phase microstructure using the orientation information of the parent phase microstructure to achieve this objective.

2. Study the Formation of deleterious hydride phase through $\alpha \rightarrow \delta$ phase transformation with a focus on role of relative orientations of α and β phases in relation to the hydride phase.

3. Understand the role of local crystal orientation on deformation of behavior in Zr alloys with respect to following important issues.

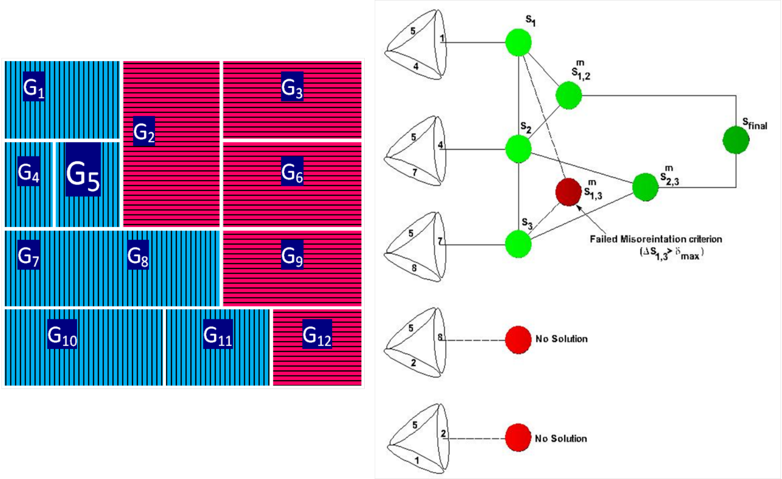

Figure 1: (a) Schematic showing the product α grains. Grains belonging to common parent β are marked with the same color. Subscripts (G_i) are the product grain IDs. (b) Algorithm. The triplets formed by G_5 are $[5,1,2]$, $[5,2,8]$, $[5,8,7]$, $[5,7,4]$ and $[5,4,1]$. Triplets either have a common parent variant, *i.e.* a 'potential' solution for the parent β, or 'no solution'. Next step is to link the 'potential' solutions through a generalized misorientation criterion.

- The orientation sensitive deformation heterogeneity in Zr alloys as a function of temperature.
- Investigating the role of alloy composition and starting texture (orientation) on the twinning behavior in Zr to answer the fundamental question of basic criteria governing the nucleation of deformation twins in *hcp* systems.
- To understand the orientation dependence of the phenomenon of dislocation nucleation in Zr.

$\beta \rightarrow \alpha$ Phase Transformation

This is perhaps the most common phase transformation through which literally every Zr based component goes through its fabrication cycle and hence was made part of the present thesis. An automated method for the reconstruction of the high temperature β phase, based on the measured microtexture data of the product phase (α) was developed. The algorithm is based on a novel misorientation based weightage factor for arriving at optimized solution for the parent grain. Fig. 1 illustrates the schematic of the algorithm adopted and Fig. 2 demonstrates the application of the algorithm for the reconstruction of parent phase in different modes of $\beta \rightarrow \alpha$, including diffusional and martensitic phase transformations in Zr.

Using the algorithm, it had also been demonstrated that exact identification and hence quantification of the variant selection during the $\beta \rightarrow \alpha$ phase transformation is possible. Using this aspect of the algorithm variants could be identified and their number frequency could

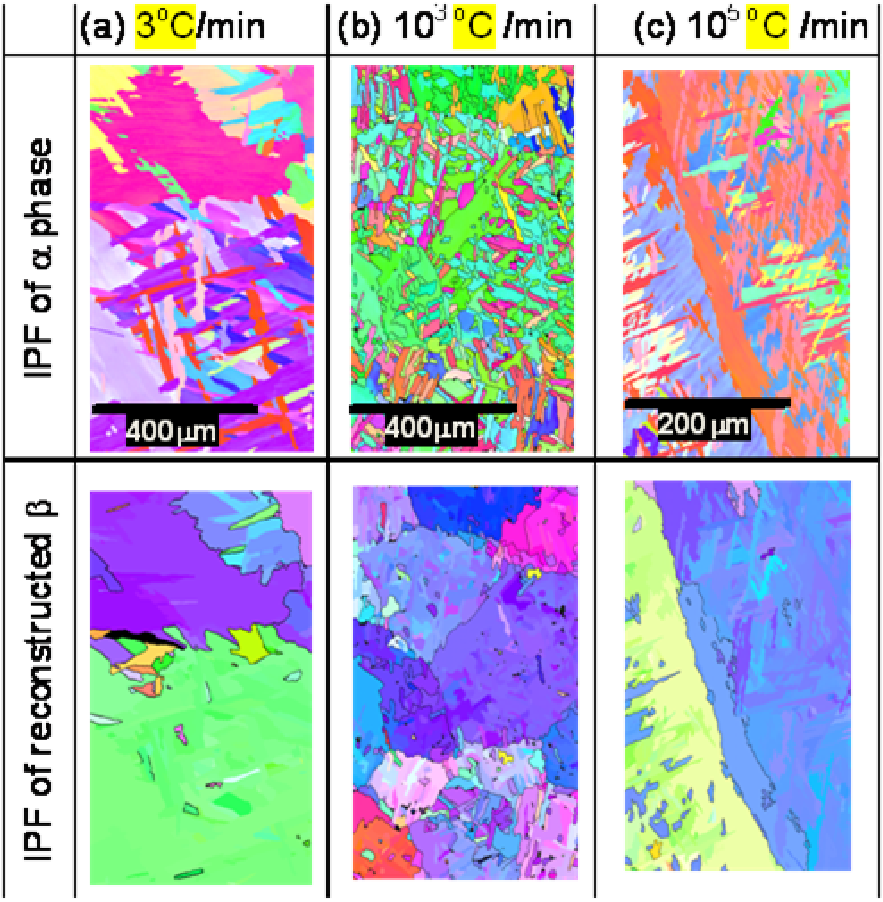

Figure 2: Post-transformation α-Zr IPFs and corresponding reconstructed β-Zr IPFs. α-Zr structures were obtained by using three different cooling rates : 3, 10^3 and 10^5 °C min^{-1}.

be estimated to bring out the degree of variant selection, see Fig. 3. The consequence of such variant selection was demonstrated by the presence of characteristic misorientation angle distribution in the transformed microstructure.

Hydride Formation ($\alpha \rightarrow \delta$ Transformation)

Due to its deleterious effects on the properties of the Zr alloys, this transformation had been studied extensively in the past using Transmission Electron Microscope (TEM). However, present study focused on the role of local orientations and interfaces on the formation of hydrides using Electron Back Scatter Diffraction (EBSD). For this purpose Zr-2.5%Nb alloy, which is the pressure tube material for the CANDU type of nuclear reactors, was chosen as the material. The objective being to asses the role of the presence of β phase on the $\alpha \rightarrow \delta$ transformation.

The study had conclusively shown that α/β interfaces are the most favorable sites for the formation of the hydrides in this system (Fig. 4). The study had provided the quantitative

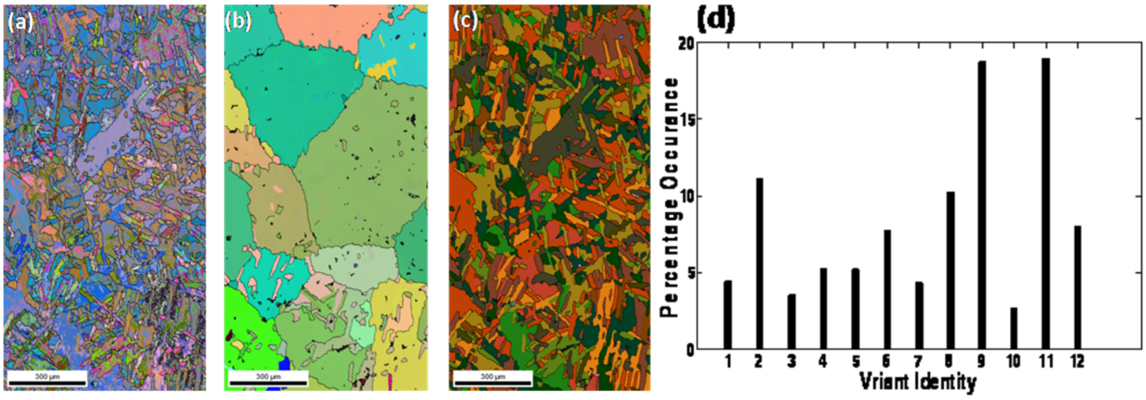

Figure 3: (a) EBSD microstructure of beta quenched microstructure of Zircaloy-4 (b) The reconstructed map of parent phase (β) (c) Microstructure of product phase with each product grain colored according to its variant identity (d) Frequency distribution of product variants.

measure of strain partitioning during the formation of hydrides at the α/β interfaces. It was confirmed that the actual strain in the hydrides was rather small when they formed along the suitable α/β interfaces. It was observed that hydride precipitation depends on the level of hydrogen partitioning at the hydrogenation temperature and availability of suitable β interfaces which are conducive for epitaxial growth of hydride phase in to the adjoining α phase. By analyzing several tens of hydrides, following orientation relationship had been established between the α, β and δ phases.

$$\begin{array}{ccc} (0001)_\alpha \parallel & (011)_\beta \parallel & (111)_\delta \\ [2\bar{1}\bar{1}0]_\alpha \parallel & [100]_\beta \parallel & [110]_\delta . \end{array}$$

Deformation Heterogeneity in Zr: Role of Orientation and Temperature

Probably ‘heterogeneity in plastic deformation’ is one of the most well accepted but least understood phenomenon in case of crystalline materials in general and more so in case of lower symmetry materials like *hcp* Zr. In the present thesis, the heterogeneity in deformation had been studied with respect to two important variable *viz*, local crystal orientation and temperature. For this purpose single phase Zr based alloy (Zircaloy-2) was subjected to plane-strain compression at different temperatures and was analyzed by detailed EBSD for identifying orientation sensitive deformation behavior. In order to rationalize the experimental observations, a Dislocation Dynamics (DD) simulation approach had been adopted.

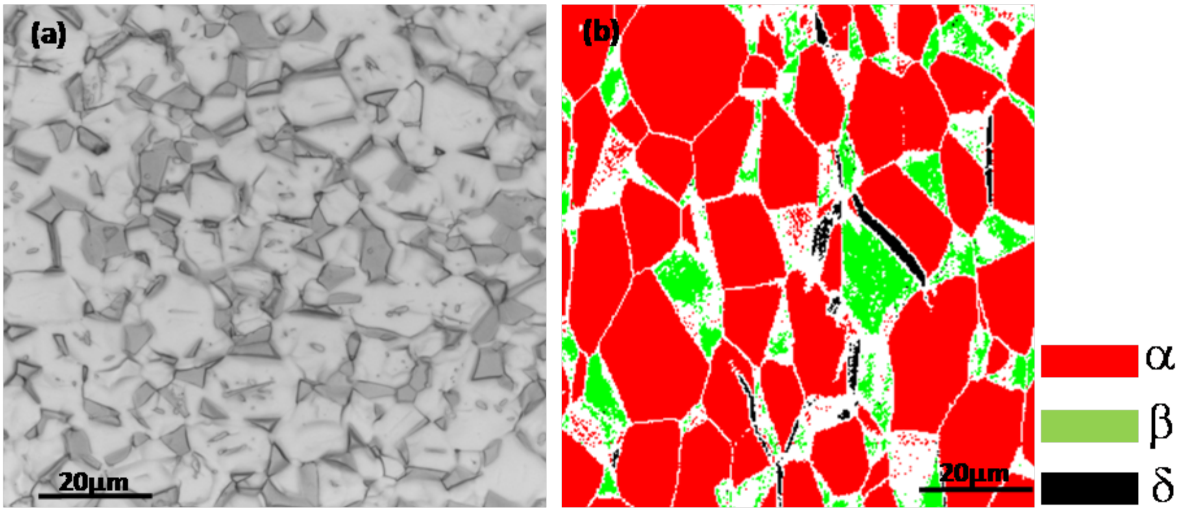

Figure 4: (a) Optical and (b) EBSD micrographs showing the distribution of the hydrides in Zr-2.5%Nb alloy charged with 300 ppm (by weight) of hydrogen.

Experimental observations highlighted the orientation and temperature sensitive plastic deformation in *hcp* zirconium. The starting microstructure had nearly equiaxed grains of $> 3\mu m$ size. Deformed microstructures contained below $3\mu m$ fragmented grains, and also larger grains, generically termed as non-fragmented, see Fig. 5. The latter was predominantly 'basal oriented' for all working temperatures. Temperature dependent plastic deformation, in terms of grain size/shape refinement and in-grain misorientaion developments, showed a remarkable difference between room temperature and warm (200 ° and $400°C$) rolling. Warm rolled microstructures contained significantly higher signatures of the plastic strain.

DD simulations of room temperature Plane Strain Compression (PSC) successfully captured the deformation response of basal and prismatic orientations. Both dislocation density and plastic strain were significantly lower for basal orientations relative to prismatic orientation. However, simulations for the elevated $(400°C)$ temperature deformations showed higher strain accumulation in basal orientation (in comparison to corresponding room temperature deformation of basal) through increased pyramidal slip activity. DD simulations also brought out a novel effect of dislocation-dislocation interactions. Dormant slip systems, slip systems where the applied stress was below Critical Resolved Shear Stress (CRSS), were activated due to interactions with active primary dislocations, see Fig. 6. This mechanism was shown to activate dormant dislocations in basal orientations, thus contributing to reduction in deformation heterogeneity during warm rolling.

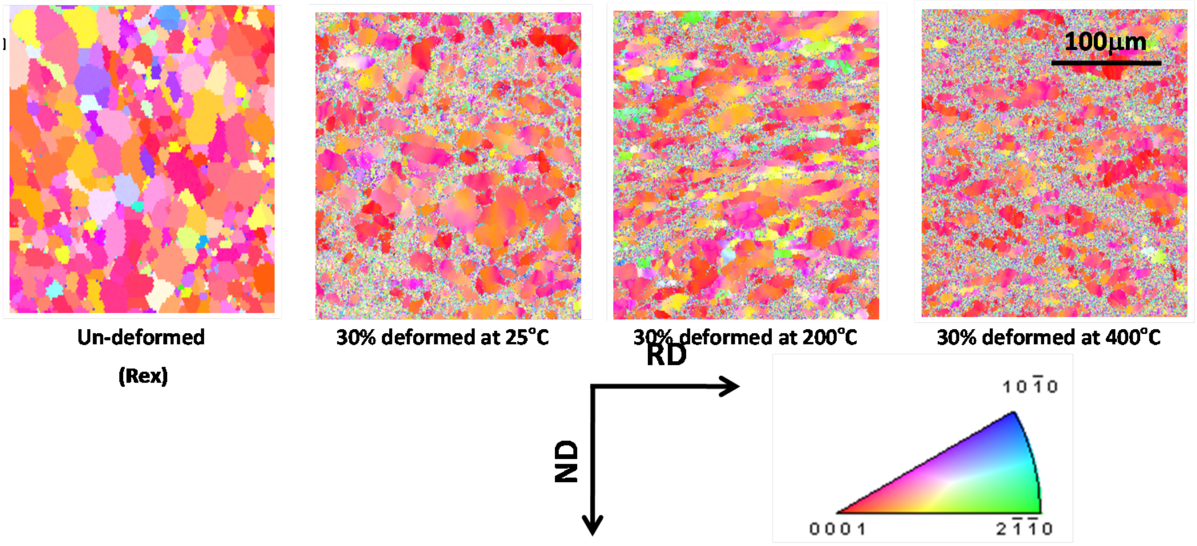

Figure 5: IPF maps of Zircaloy 2 at different working temperatures, demosntrating that some grains/orientations retained (*esp.* red colored grains representing basal orientated grains) their shape and size even after considerable deformation.

Role of orientation in Deformation Twinning

Studies on deformation mechanisms in *hcp* materials are far from complete with out dealing with the twinning. One of the fundamental questions that remained elusive for understanding was : Is twin nucleation strain controlled or stress controlled? Present thesis tried to provide an answer to this long standing question by performing a series of controlled *in-situ* deformation experiments under neutron diffraction apparatus to look for signatures of twinning and corresponding stress and strain state of the samples. For this purpose Zr-Sn binary alloys with systematic variation in their Sn content were used in different crystallographic texture conditions for the deformation studies. In addition, detailed postmortem analysis by EBSD and TEM was carried out to gain insights into the data provided by the neutron diffraction experiments.

The role of Sn on the deformation mechanisms (twinning in particular) was seen to be deformation direction dependent, in other words texture dependent. It was observed that deformation along Rolling Direction (RD) was characterized by huge influence of Sn on the extent of twinning while the deformation along Transverse Direction (TD) was found to be least sensitive to amount of Sn of the alloy for the extent of twinning. In general (for both RD and TD deformations) it was observed that the critical stress required for the twining increased with the Sn content while the critical macroscopic strain for the onset of twinning was rather insensitive to the amount of Sn of the alloy, see Fig. 7. Using the combined evidence of EBSD, TEM (see

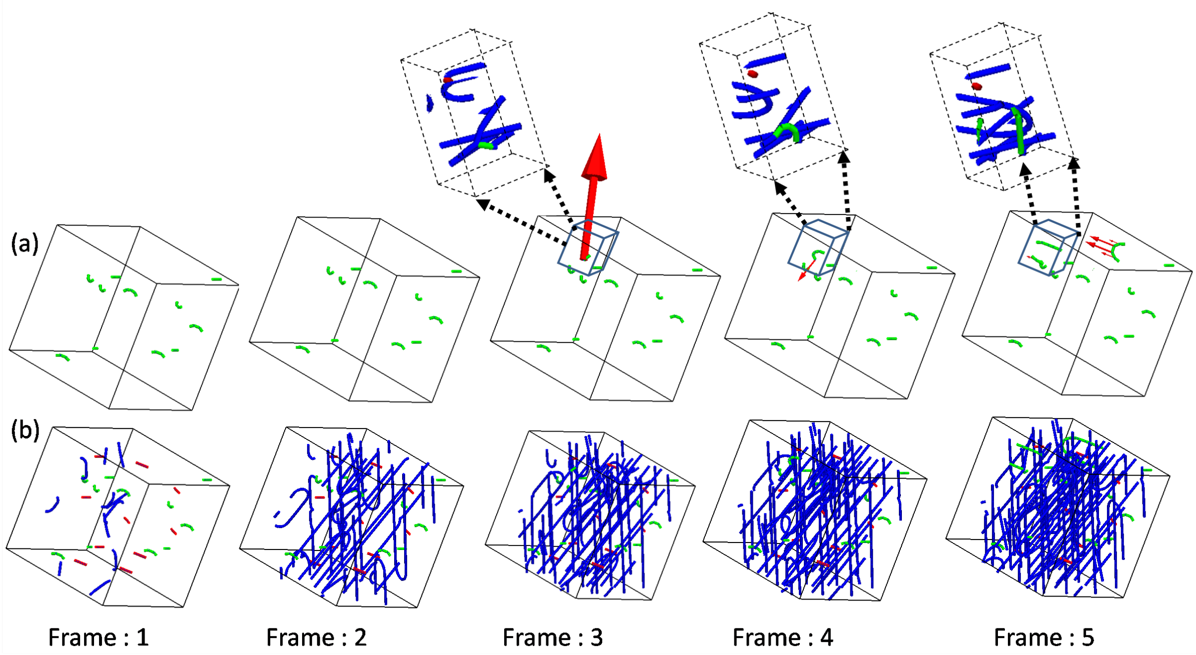

Figure 6: (a) Depiction of nodal forces along burgers vectors of prismatic dislocations in case of simulation of basal orientation at 700 K at various time steps. The red color arrows indicate the direction and magnitude of the resolved nodal force along local burgers vector. For the purpose of clarity, forces on prismatic dislocations only are shown. It can be observed that, the resolved nodal forces in the initial state are negligibly small rendering red arrows on them invisible (a reflection of orientation effect). However, as the pyramidal dislocations evolve, significant forces (due to interaction) are observed on certain prismatic dislocation. Once a critical force is generated frame (3), a prismatic source is observed to have got activated and starts to evolve. (b) Evolution of the overall dislocation structure at above time steps. For the sake of clarity, a zoomed in version of (a) from a different viewing angle, are shown (of the boxed region) of the region in which an inactive prismatic dislocation has been activated by the interacting pyramidal dislocations.

Fig. 8) and neutron diffraction it was inferred that there needs to be some critical plastic strain for the initiation of twinning. The data suggested that once the critical plastic strain required for the onset of twining is achieved, the extent of the twining is chiefly governed by the crystal orientation (texture effect) followed by intragranular strain state.

Homogenous Nucleation of Dislocations : Role of Crystal Orientation

The thesis had extended the study on the role of orientation to atomic scale by exploring the variation brought in by the crystallographic orientation on the critical stress required for the nucleation of the dislocations: the fundamental defects responsible for the deformation behavior. Simulations have indicated significant asymmetry in the stress required for the nucleation

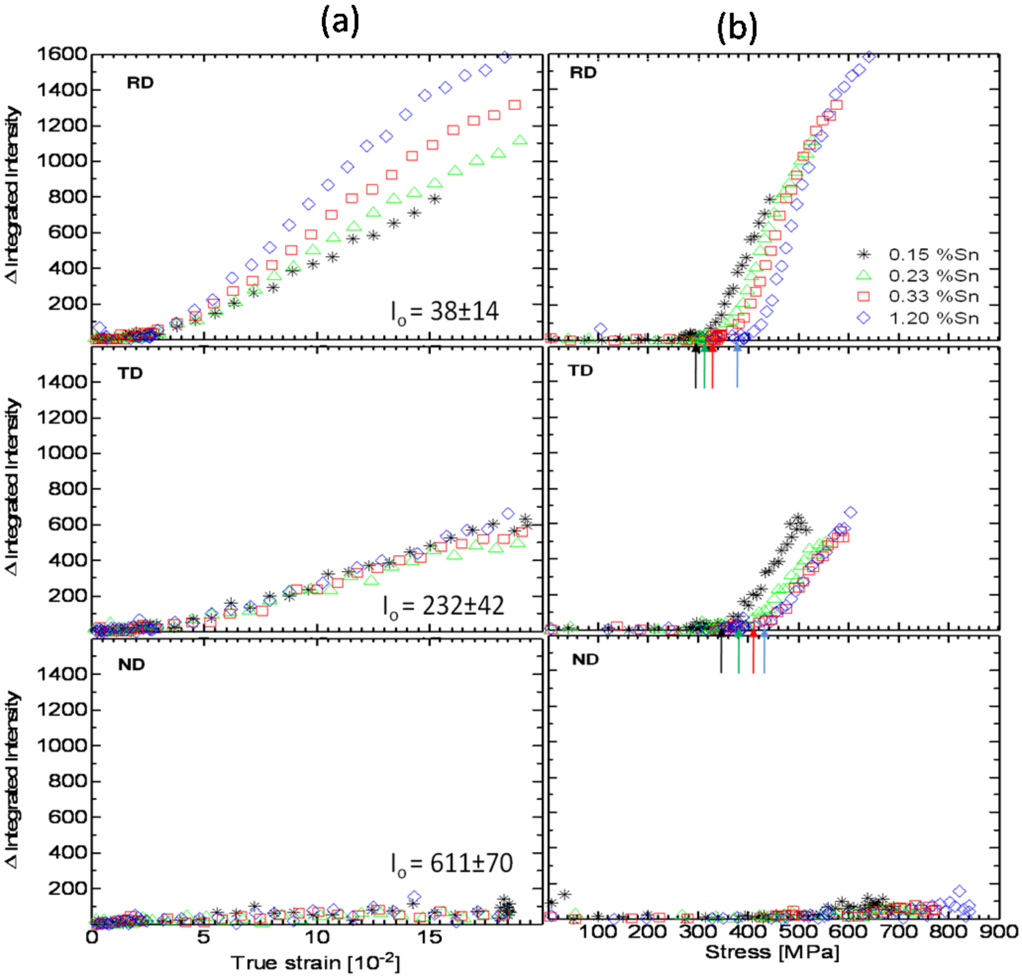

Figure 7: Change in integrated intensity of 0002 reflection for all four alloys as a function of applied (a) strain and (b) stress, recorded during *in-situ* neutron diffraction/deformation experiments. I_o values included in the plots represent the mean initial intensify of the unloaded (initial state) samples.

of dislocations in the tension and compression. Simulations have predicted nucleation of $<a>$ type dislocations on the prismatic planes to be more favorable than the competing $<a>$ type dislocations on basal planes, see Fig. 9. Under certain crystallographic orientations, formation of $<c>$ type dislocations had also been noticed. Present simulations, however, did not show the formation of $<c+a>$ dislocations. Thus the experimental observation of these dislocations could be due to the interaction of the existing $<a>$ and $<c+a>$ type dislocations or conditions other than those imposed in the present simulations are responsible for their formation.

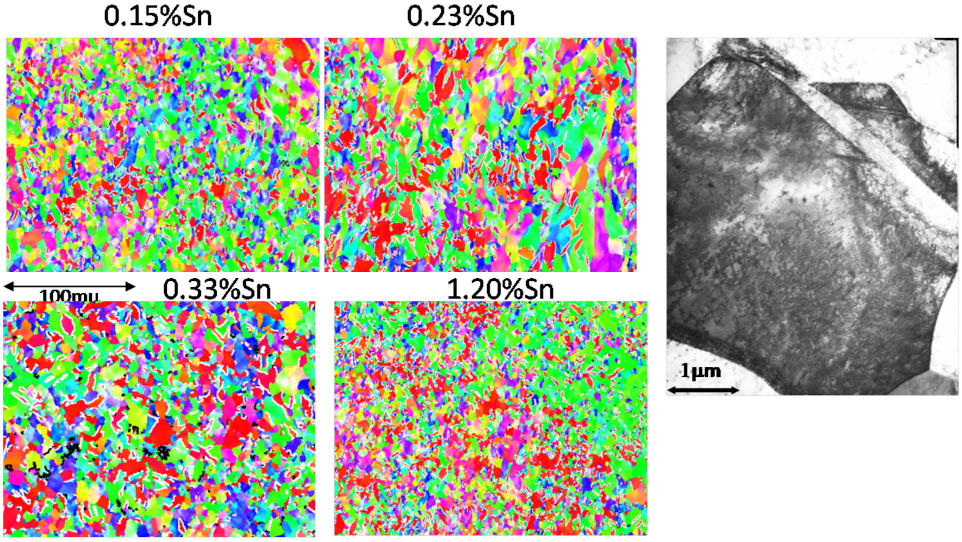

Figure 8: (a)EBSD images of the RD deformed samples with different Sn contents, showing that as the Sn content increases so does the twinning for a given amount of deformation. (twin boundaries are marked in white color) (b)TEM bright field image of twin showing high dislocation density in the parent grain from which twin got nucleated.

Thesis Organization

The thesis has number of chapters. The chapter "Literature Review" presents the overview of zirconium based alloys, their historical development and applications. The chapter then delves into review of existing knowledge on various phase transformations (relevant to present thesis) and deformation mechanisms for these materials. Although focus is on Zr alloys the descriptions shall be applicable to any *hcp* materials and thus has wider academic application range. The chapter then deals with the deformation mechanisms, and various modeling and simulation techniques being used for the understanding of the phenomenon deformation. The next chapter "Experimental" presents an overview of various experimental methods followed in the present thesis with special emphasis on some of the advanced characterization techniques used for the present work.

Chapter 4 presents the results of the studies on $\beta \rightarrow \alpha$ transformation. It starts with a description of a new algorithm developed as part of the present work, for the automated reconstruction of the parent phase microstructure from the micro texture data of the product phase. The application of the algorithm and its efficacy in handling various modes of $\beta \rightarrow \alpha$ transformation has been shown in the subsequent parts of the chapter. The identification and quantification of the variant selection during the $\beta \rightarrow \alpha$ transformation has been demonstrated. In continuation of important phase transformations in Zr alloys, the next chapter, chapter 5,

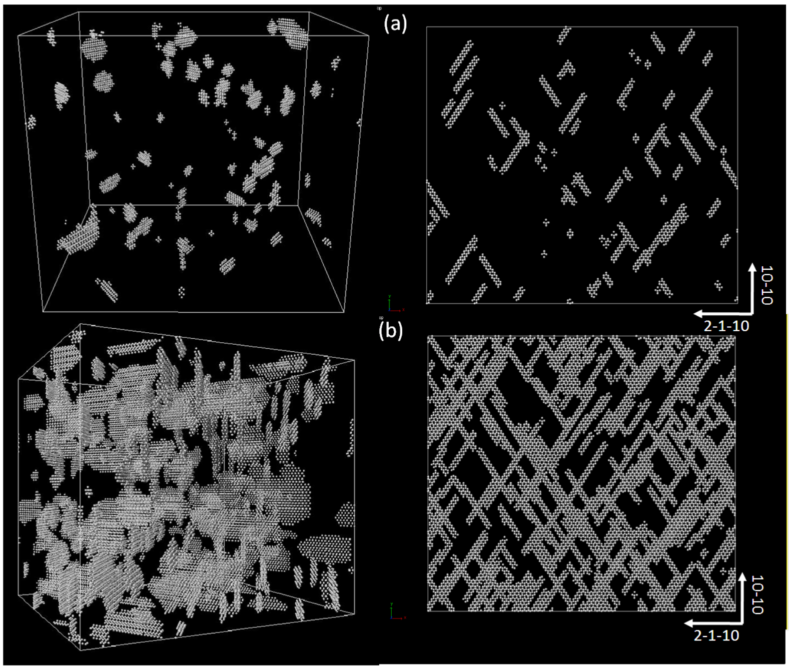

Figure 9: Dislocation nucleation as captured by the MD simulation of tensile deformation along $[01\bar{1}0]$ direction of the Zr crystal. (a) Snap shot at the beginning of the nucleation event (corresponding to the peak stress of in a given simulation (a). (b) Snap shot at at an advanced stage of simulation, corresponding to larger strains, showing growing dislocation loops. For the purpose of visualization all the '*good atoms*' *i.e.*, those atoms which have their neighborhood corresponding the *hcp* configuration, are omitted from the image. Two views (isotropic and XY projection) of the same snap shots are presented side by side for gaining insights into the crystallographic aspects of the planes of the dislocation loops. It can be seen that all of them lie on the prismatic planes, $< 10\bar{1}0 >$ for this case.

focuses on yet another interesting and phase transformation, *i.e.*, $\alpha \rightarrow \delta$ phase transformation in the presence of β phase of Zr. The role of the β phase and its interfaces on the formation of hydride phase has been brought out.

Orientation sensitive deformation behavior, which is one of the most important aspects of the deformation of *hcp* materials like Zr, has been dealt with in the chapter 6. The results of a detailed experimental investigations are presented in this chapter along with the discrete dislocation dynamics simulations to explain the experimental observations. Chapter 7 presents the results of the *in-situ* neutron diffraction and deformation studies that are aimed at bringing out the role of Sn on the deformation mechanisms in Zr. The chapter brings into light some novel observations of role of Sn on the twinning behavior in Zr. Lastly, molecular dynamics simulations of the homogeneous nucleation of dislocations in Zr are described in the chapter 8. It has been shown that there is considerable asymmetry in the stress required for the nucleation of dislocations in the compression and tension.

Bibliography

[1] B. Verlinden, J. Driver, I. Samajdar, and R. R. Doherty, *Thermo Mechanical Processing of Metallic Materials*. Elsevier Ltd, 1st editio ed., 2007.

[2] B. Cox, "Some thoughts on the mechanisms of in-reactor corrosion of zirconium alloys," *J. Nucl. Mater.*, vol. 336, pp. 331–368, Feb. 2005.

[3] E. Tenckhoff, "Review of Deformation Mechanisms, Texture, and Mechanical Anisotropy in Zirconium and Zirconium Base Alloys," *J. ASTM Int.*, vol. 2, no. 4, p. 12945, 2005.

[4] K. L. Murty and I. Charit, "Texture development and anisotropic deformation of zircaloys," *Prog. Nucl. Energy*, vol. 48, pp. 325–359, May 2006.

[5] S. Banerjee and P. Mukhopadhyay, *Phase Transformations - Examples from Titanium and Zirconium Alloys*, vol. 12 of *Pergamon Materials Series*. Pergamon, 2007.

Contents

List of Figures

List of Tables

CHAPTER 1

Introduction

1.1. Introduction

Metals, which form the significant proportion of the engineering materials, are in general crystalline in nature. Their wide spread applicability in the engineering applications stems from many reasons. The two most important of those include (a) good mechanical properties and (b) ease of fabrication into the required shape and size [1]. Both these aspects are a result of excellent control one can exercise on the microstructural parameters using a combination of '*deformation*' and '*phase transformations*'. The fact that the underlying phases are crystalline in nature makes '*how these crystals are oriented*' influence the material behavior in the deformation and/or phase transformations. The role of the crystal orientation is even more dominant in case of materials with low symmetry such as Zirconium, a *hcp* metal. Zr is one of the most crucial structural material in nuclear reactor core. Its applicability is essentially due to a rare combination of good mechanical properties coupled with compatibility to reactor environment and low neutron absorption cross section for thermal neutrons [2, 3]. Zr is the material of choice for a range of critical nuclear core components such as clad tubes and pressure tubes. The fact that these Zr based alloys are used for the critical applications in the core of nuclear reactors, puts severe demand on their reliable service performance. Zr-2.5%Nb pressure tubes, for instance, are designed to operate under a relatively aggressive environment of nuclear reactor in which there is a constant interplay of mechanical, thermal and irradiation induced damage mechanisms, for periods extending up to 30 years [4–6]. Zircaloy based fuel clads on the other hand, have to sustain severe pellet clad interactions and ensure fuel bundle integrity for avoiding the leakage of radioactivity into the coolant [2]. It is obvious that such a performance requirement mandate stringent requirement on the properties of these components. The integrity and service performance of these components naturally determine the overall safety and efficiency of reactor. It has long been established that the crystal orientation of the constituent phases (crystallographic texture) in these Zr based components play a significant role in determining the service performance [7, 8].

The as fabricated microstructure and texture of a Zr based components is, in general, a cumulative result of changes that take place in a series of Thermo Mechanical Processing (TMP)s that a typical Zr based component goes through during its fabrication [9]. Typically the TMPs used for the fabrication of the Zr based structural components involve, deformation and/or phase transformation during individual stages of the processing. For instance, β-quenching operation is one inevitable operation in any of the fabrication flow sheets so also the hot extrusion. While the former involves a phase transformation, later, is essentially driven by deformation and to some extent by the phase transformation characteristics (depending on the temperature of extrusion and composition of the alloy). On the other hand, cold pilgering and drawing (used in the manufacture of clad tubes and pressure tubes) are essentially deformation processes. Thus, the understanding and tailoring of the final microstructure developed after the fabrication, necessarily depends on our ability to understand these individual processes/phenomena of deformation and phase transformation. In addition to optimizing the fabrication processing, understanding of the fundamental mechanisms of phase transformation and deformation are crucial for enhancing service life and mitigating the in service degradation mechanisms. For instance, hydride formation is an important phase transformation ($\alpha \rightarrow \delta$) that some times limit the life of the components [10]. In all these phenomenon/processes the behavior of the material is expected to be highly influenced by the local crystal orientation.

In this context, the present thesis had been conceptualized to study the role of local crystal orientation on phase transformation and deformation in Zr based alloys. Specific issues pertaining to these processes were identified for the study, based on the scientific challenge and their industrial relevance. The objectives of the present study include

1. Variant selection during the $\beta \rightarrow \alpha$ transformation has the effect of influencing the resulting texture distribution and thus it is beneficial to be able to identify and quantify the the same in this transformation. It was aimed to develop an algorithm to reconstruct the pre transformed phase microstructure using the orientation information of the parent phase microstructure to achieve this objective.

2. Study the formation of deleterious hydride phase through $\alpha \rightarrow \delta$ phase transformation with a focus on role of relative orientations of α and β phases in relation to the hydride

(δ) phase.

3. Understand the role of local crystal orientation on deformation of behavior in Zr alloys with respect to following important issues.
    - The orientation sensitive deformation heterogeneity in Zr alloys as a function of temperature.
    - Investigating the role of alloy composition and starting texture (orientation) on the twinning behavior in Zr to answer the fundamental question of basic criteria governing the evolution of deformation twins in *hcp* systems.
    - To understand the orientation dependence of the phenomenon of dislocation nucleation in Zr.

1.2. Thesis Overview

Fig. 1.1 depicts the brief outline of the work carried out under the present thesis. Chapter 2 presents the overview of zirconium based alloys, their historical development and applications. The chapter then delves into review of existing knowledge on various phase transformations (relevant to present thesis) and deformation mechanisms for these materials. Although focus is on Zr alloys the descriptions shall be applicable to any *hcp* materials and thus has wider academic application range. The chapter then deals with the deformation mechanisms, and various modeling and simulation techniques being used for the understanding of the phenomenon of deformation. The next chapter (chapter 3), presents an overview of various experimental methods followed in the present thesis with special emphasis on some of the advanced characterization techniques used for the present work.

Chapter 4 presents the results of the studies on $\beta \rightarrow \alpha$ transformation. It starts with a description of a new algorithm developed as part of the present work, for the automated reconstruction of the parent phase microstructure from the micro texture data of the product phase. The application of the algorithm and its efficacy in handling various modes of $\beta \rightarrow \alpha$ transformation has been shown in the subsequent parts of the chapter. The identification and quantification of the variant selection during the $\beta \rightarrow \alpha$ transformation has been demonstrated. In continuation of important phase transformations in Zr alloys, Chapter 5 focuses on yet another interesting and phase transformation, *i.e.*, $\alpha \rightarrow \delta$ phase transformation in the presence of β phase of Zr.

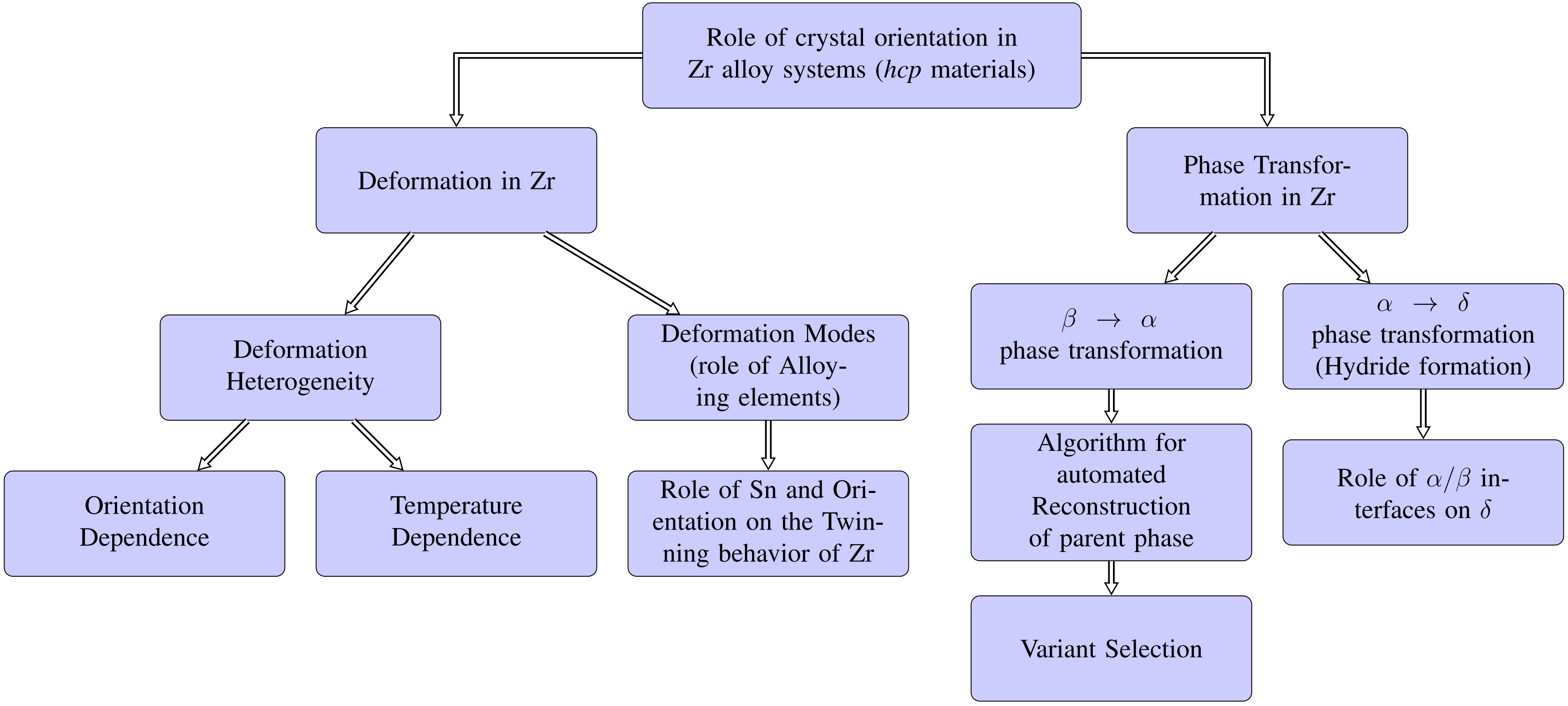

Figure 1.1: Layout of the thesis.

The role of the β phase and its interfaces on the formation of hydride phase has been brought out.

Orientation sensitive deformation behavior, which is one of the most important aspects of the deformation of *hcp* materials like Zr, has been dealt with in the chapter 6. The results of a detailed experimental investigations are presented in this chapter along with the discrete dislocation dynamics simulations to explain the experimental observations. A novel mechanism of dislocation activation by active secondary slip systems, that is very specific to *hcp* materials, has been brought through the dislocation dynamics simulations. Chapter 7 presents the results of the *in-situ* neutron diffraction and deformation studies that are aimed at bringing out the role of Sn on the deformation mechanisms in Zr. The chapter brings into light some novel observations of role of Sn on the twinning behavior in Zr. Lastly, molecular dynamics simulations of the homogeneous nucleation of dislocations in Zr are described in the chapter 8. It has been shown that there is considerable asymmetry in the stress required for the nucleation of dislocations in the compression and tension.

Chapter 9 presents the summary of the main observations/findings of the present thesis followed by the future direction of the work that need to be carried out to gain further insights. Finally Appendix-I gives the details of the new automated reconstruction algorithm developed as part of the present work. A complete worked example with actual orientation data of the product phase is presented to illustrate working of the algorithm.

CHAPTER 2

Literature Review

2.1. History of Zr Based Alloys

Zirconium alloys are extensively used in various types of fission reactors (both light and heavy water types) for different applications. These include clad tubes for the fuel elements, grids, channels in Boiling Water Reactor (BWR)s as well as pressure and calandria tubes in PHWRs [9]. The development of zirconium alloys is essentially due to the nuclear industry, where these alloys have been regarded as the proven structural material. The actual application of zirconium based alloys for nuclear applications started after the realization that the removing the naturally associated Hf from the Zr greatly reduces the neutron absorption cross section of the Zr. This had prompted Admiral Rickover to put zirconium to use in their Naval Nuclear Propulsion program for water cooled reactor for submarine Nautilus [9, 11]. From then onwards there were several developments in the zirconium based alloys resulting in a series of alloys suited for various reactor conditions and applications. Fig. 2.1 schematically describes the historical evolution of the Zr based alloys.

2.2. Properties and Applications of Zr Based Alloys

Table 2.1 illustrates various Zr alloys and their applications (along with the properties that are crucial for that application). It is very clear that Zr based alloy form the most integral part of several nuclear reactor materials.

2.3. Thermo Mechanical Processing of Zr Alloys

Various structural components (*e.g.*, clad tubes, pressure tubes *etc.*) listed in table 2.1 are typically fabricated through a complex series of TMPs. Fig. 2.2 illustrates two such typical flow sheets for the fabrication of the clad tube and pressure tube as practiced by NFC, Hyderabad,

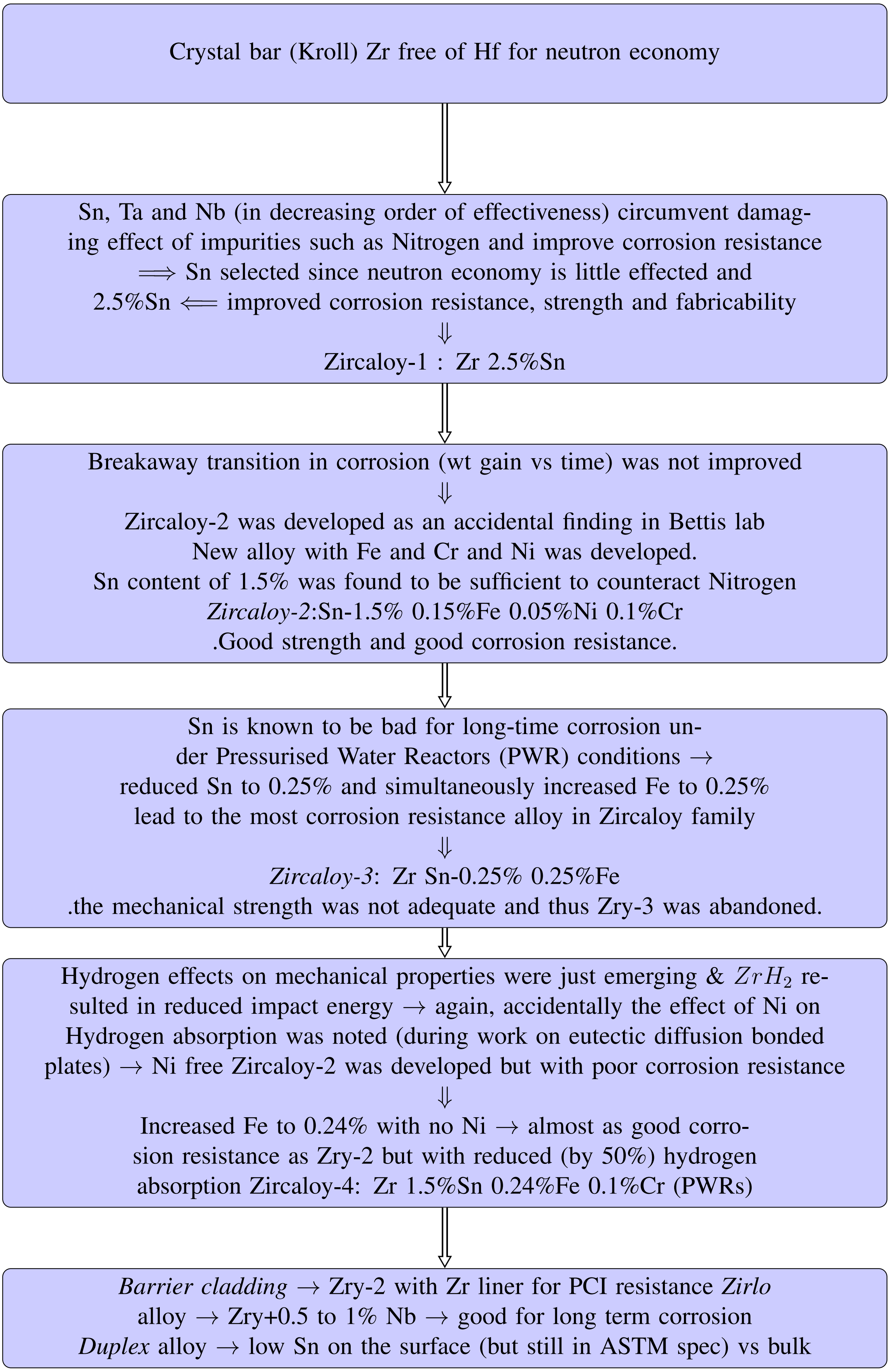

Crystal bar (Kroll) Zr free of Hf for neutron economy

Sn, Ta and Nb (in decreasing order of effectiveness) circumvent damaging effect of impurities such as Nitrogen and improve corrosion resistance
⟹ Sn selected since neutron economy is little effected and
2.5%Sn ⟸ improved corrosion resistance, strength and fabricability
⇓
Zircaloy-1 : Zr 2.5%Sn

Breakaway transition in corrosion (wt gain vs time) was not improved
⇓
Zircaloy-2 was developed as an accidental finding in Bettis lab
New alloy with Fe and Cr and Ni was developed.
Sn content of 1.5% was found to be sufficient to counteract Nitrogen
Zircaloy-2:Sn-1.5% 0.15%Fe 0.05%Ni 0.1%Cr
.Good strength and good corrosion resistance.

Sn is known to be bad for long-time corrosion under Pressurised Water Reactors (PWR) conditions →
reduced Sn to 0.25% and simultaneously increased Fe to 0.25%
lead to the most corrosion resistance alloy in Zircaloy family
⇓
Zircaloy-3: Zr Sn-0.25% 0.25%Fe
.the mechanical strength was not adequate and thus Zry-3 was abandoned.

Hydrogen effects on mechanical properties were just emerging & ZrH_2 resulted in reduced impact energy → again, accidentally the effect of Ni on Hydrogen absorption was noted (during work on eutectic diffusion bonded plates) → Ni free Zircaloy-2 was developed but with poor corrosion resistance
⇓
Increased Fe to 0.24% with no Ni → almost as good corrosion resistance as Zry-2 but with reduced (by 50%) hydrogen absorption Zircaloy-4: Zr 1.5%Sn 0.24%Fe 0.1%Cr (PWRs)

Barrier cladding → Zry-2 with Zr liner for PCI resistance *Zirlo* alloy → Zry+0.5 to 1% Nb → good for long term corrosion
Duplex alloy → low Sn on the surface (but still in ASTM spec) vs bulk

Figure 2.1: Flow chart illustrating the historical development of Zr based alloys, adapted from [9]

Table 2.1: Usage of Zr based components in various nuclear reactors.

Reactor	Component	Alloy used	Properties Required
PHWR	Fuel clad tube	Zircaloy-4	Good ductility, Predominantly radial texture of basal poles (for mitigating hydride embitterment)
	Pressure tube	Zr-2.5%Nb	Good strength, Fracture toughness, low hydrogen pick up rate, Texture having circumferential basal poles
	Calandria tubes	Zircaloy-4	Good ductility
BWR	Clad tube	Zircaloy-2	Good ductility, good nodular corrosion resistance
PWR	Clad tube	Zirlo	Good ductility, good nodular corrosion

India. Typically such complex fabrication process flow sheets are necessitated by the stringent dimensional control of the final products and also to achieve the required microstructural and textural distribution in the final components. The later undergo considerable modifications during the processing and the process variable such as deformation temperature, extent of deformation, annealing time and temperature *etc.*, are chosen to achieve the desired final properties. Figs. 2.3 and 2.4 illustrates the extent of microstructrual and textural modifications experienced by the Zircaly-4 clad tube during the fabrication. Following is the summary of microstructural and textural changes during the fabrication steps [12]

- Textural developments during fabrications steps were mainly in terms of changes in the intensity of orientation fibers, *viz*, $<10\bar{1}0>$and (0001) fibers. In general, deformation (both hot extrusion, as well as pilgering) strengthen $<10\bar{1}0>$, while annealing enhances (0001).

- The processing steps also modify microstructure in the following sequence : Widmanstatten structure (β quenched) → bimodal grain size/shape (Hot Extruded) → relative grain growth (1st Annealing) → heterogeneous deformation (1st Pilgered) → fully recrystallized (2nd Annealed) → heterogeneous deformation (2nd Pilgered) → partially recrystallized (3rd Annealed) → heterogeneous deformation (3rd Pilgered) → partially recrystallized (Final Annealed).

- The pilgering operations involve heterogeneous deformation - majority of the grains getting fragmented, while some specific grains /orientations remaining relatively unaffected. Textural developments were observed to be associated with the latter. During annealing, involving complete or partial recrystallization, larger recrystallized grains had a stronger contribution to the developments of crystallographic texture.

It may be noted that these clad tubes need to have high degree of basal pole alignment towards radial direction of the tube for appropriate hydride embrittlement resistance and accordingly the fabrication flow sheet was designed.

Similarly in case of Zr-2.5%Nb, microstructural and textural evolution during each fabrication stage was characterized by Srivastava *et al.* [13]. They show that the during extrusion in the two-phase field, both the α and β_I phases undergo dynamic recrystallization and the β_{II} phase layers get sandwiched between elongated α - phase (stringers). The elongated α units were essentially made up of a number of nearly equi-axed α-grains. They have demonstrated that the aspect ratio of the phases is related to the imposed extrusion ratio. A typical microstructure in radial-axial section is shown in Figure Fig. 2.5(a) which shows elongated α-grains separated by β-phase. It was observed that the elongated two-phase structure could be retained only if the intermediate annealing temperature was kept below $575°\mathrm{C}$. Annealing at lower temperature, for example, at $500°\mathrm{C}$ for 6 h resulted in recovery of α-stringers as evidenced by the presence of sub-grain boundaries. In addition to these, a high density of unrecovered dislocations was also noticed (Fig. 2.5(c)). The tensile strength of the resultant structure was higher than the as-extruded material. In contrast to this, annealing at higher temperature, *e.g.*, $600°\mathrm{C}$, even for 1 h resulted in complete recrystallization and morphological modifications of both α- and β-phases (Fig. 2.5(d)). The annealed microstructure comprised essentially of nearly equiaxed α-grains, and β_I-phase was noticed primarily at the boundaries and tri-junctions of α-grains. Kiran *et al.* have shown that the majority of the textural changes take place during the hot extrusion of this alloy while subsequent stages of cold pilgering and annealing have minimall role in defining the final texture [14]. They explained the absence of the textural changes during the pilgering as due to the presence of continuous film of β phase in between α lamallae. In summary, these works thus highlight that both textural and microstructural evolution happen during each stage of the fabrication flow sheet and the extent of the such changes are specific to alloy system and conditions employed.

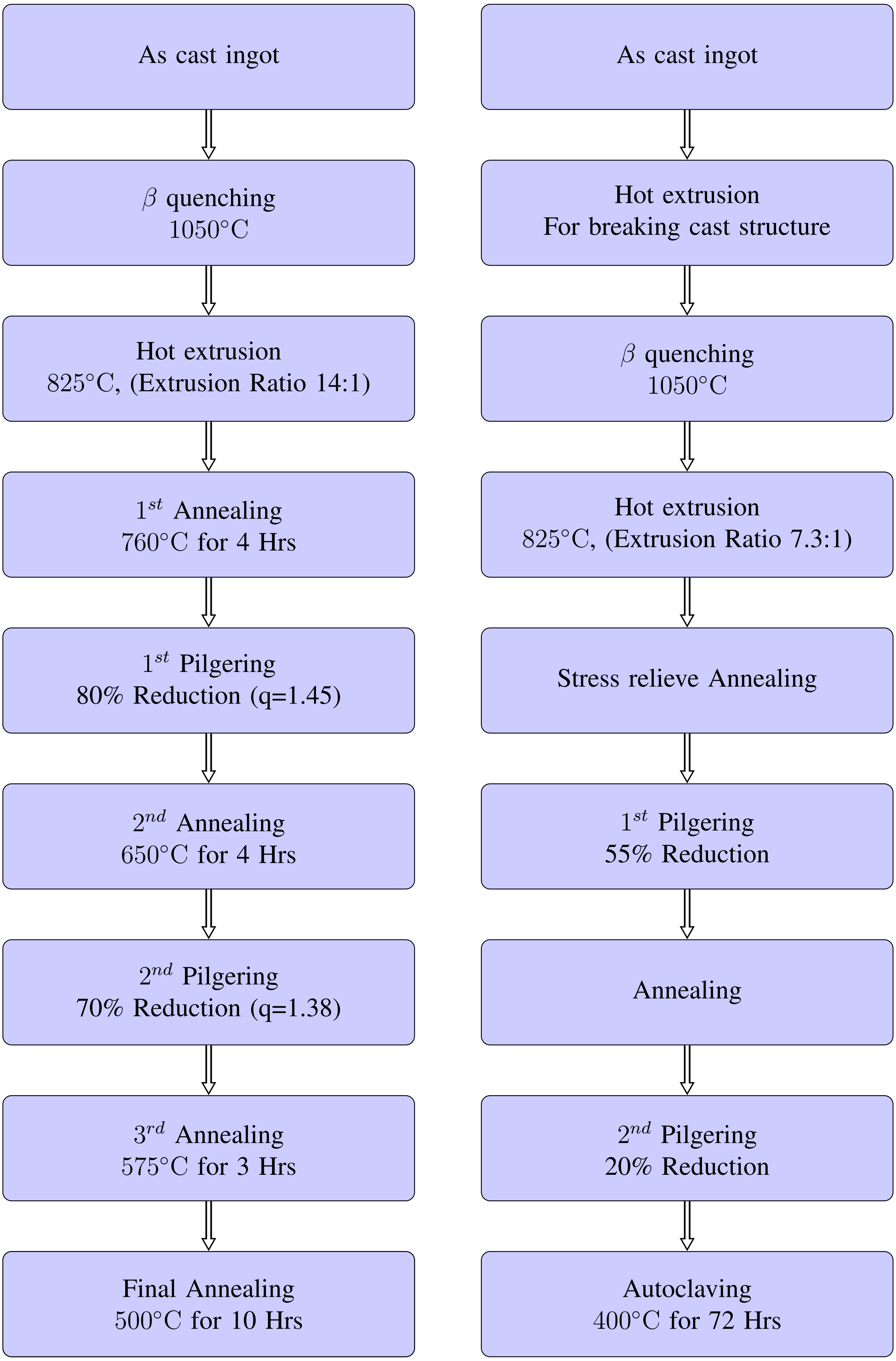

(a) Flow sheet of Zircaloy-4 clad tubes. **(b) Flow sheet of Zr-2.5%Nb pressure tubes.**

Figure 2.2: Important stages of fabrication flows sheets for the production of Zirconium based nuclear structural componetns of Indian PHWR as being practiced by NFC, Hyderabad.

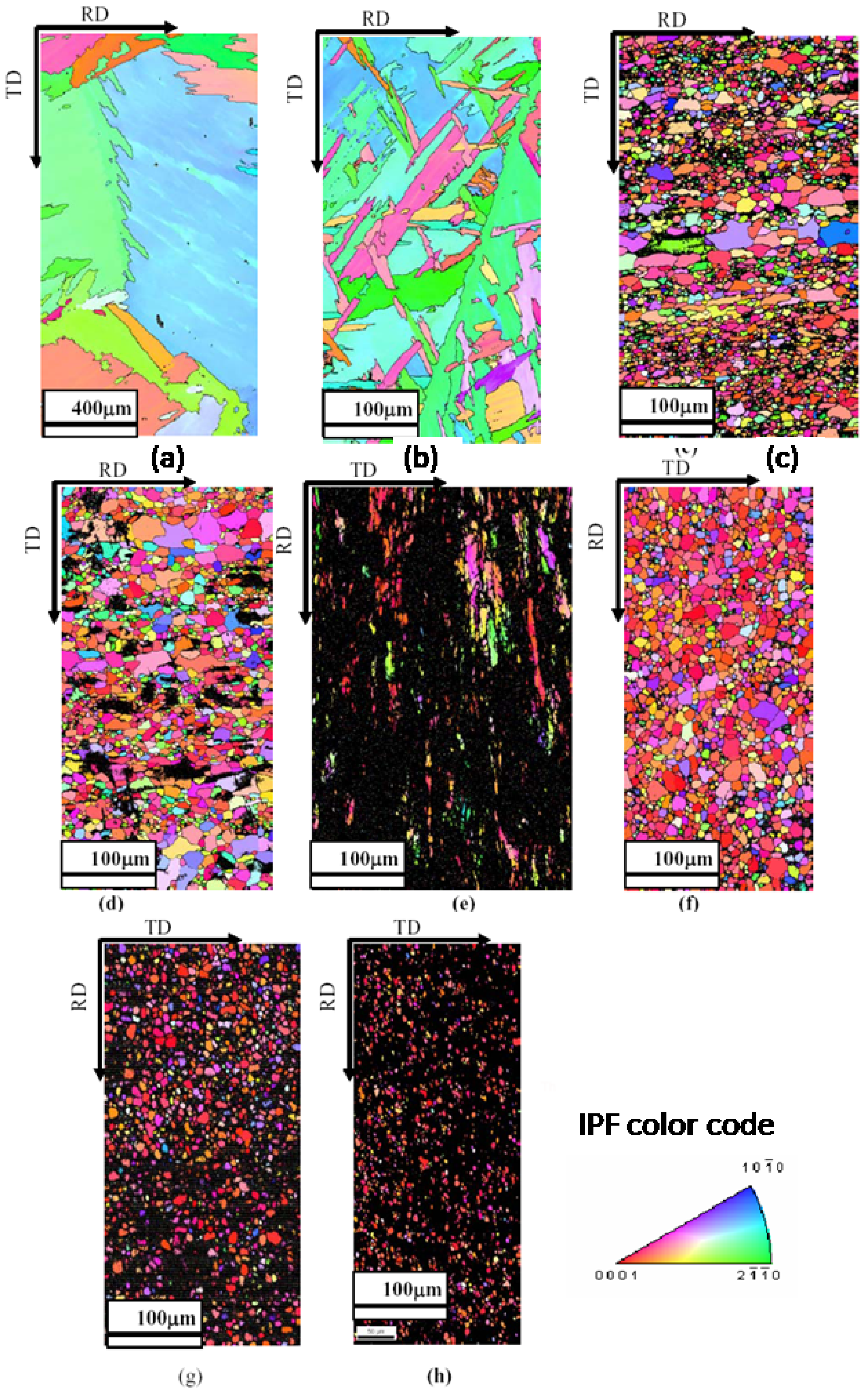

Figure 2.3: EBSD images of (a) As cast (b) β quenched (c) Hot Extruded, (d) 1^{st} Annealed, (e)1^{st} Pilgered (f) 2^{nd} Annealed (g) 3^{rd} Annealed (h) Final Annealed. Images were plotted using IPF - grain boundaries being marked for above 15° misorientation. Measurement points with confidence index (an approximate measure of accuracy of indexing) values below 0.03 are marked as black. RD and TD correspond respectively to axial and circumferential directions of the tube [12].

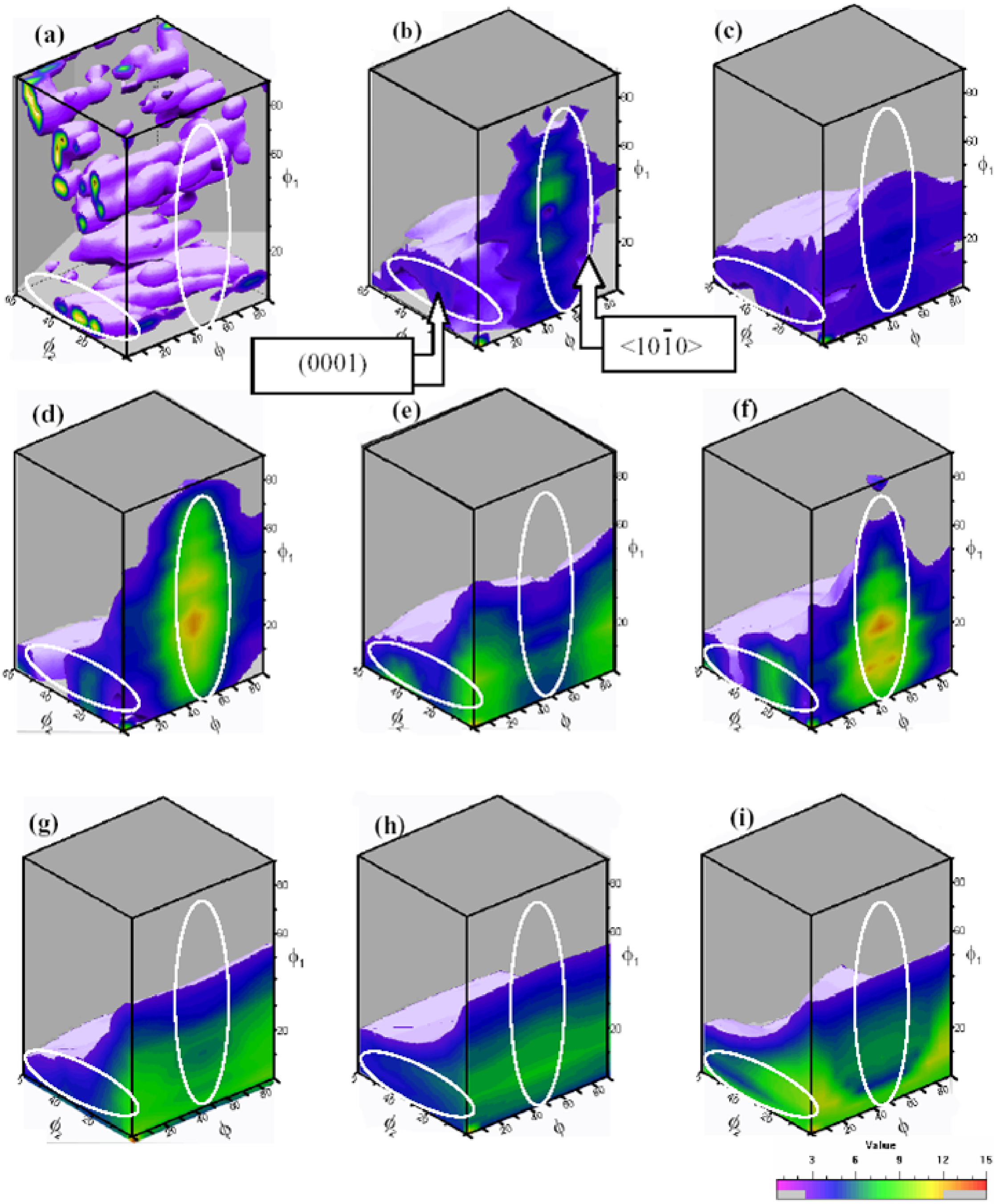

Figure 2.4: 3-dimensional ODF plots for (a)β quenched , (b) Hot Extruded, (c) 1^{st} Annealed, (d) 1^{st} Pilgered, (e)2^{nd} Annealed , (f) 2^{nd} Pilgered, (g) 3^{rd} Annealed, (h) 3^{rd} Pilgered, (i) Final Annealed. ODF Iso-intensity levels of 3 times or more are marked. The two distinct fibers, $<10\bar{1}0>$ and (0001) fibers, are shown on the ODFs [12].

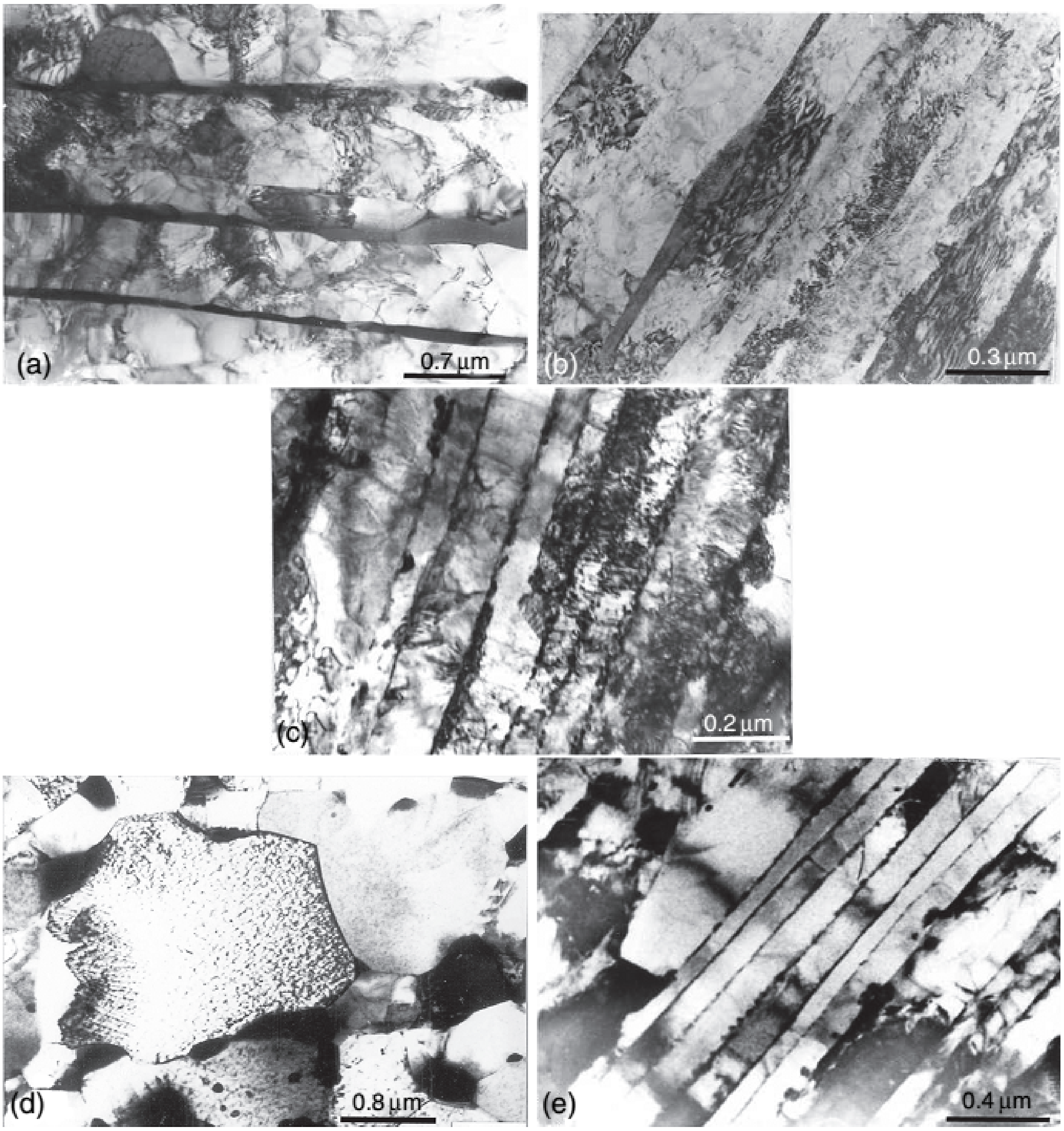

Figure 2.5: TEM of Zr-2.5%Nb alloy: (a) as-extruded microstructure showing elongated morphology of α-phase separated by β-phase stringers. (b) First pilgered microstructure illustrating the very high dislocation density. The dislocations are concentrated primarily at the α/β interface. (c) Incomplete recrystallization of the α-stringers as evidenced by the presence of a substantial number of dislocations after annealing at $500^{\circ}\mathrm{C}$ for 6 h. (d) Coarsening of the α-grains caused by redistribution and agglomeration of β-phase. The β-phase is located at the triple junctions of α-grains after annealing at $600^{\circ}\mathrm{C}$ for 1 h and (e)completely recrystallized α-lamellae obtained after annealing at $550^{\circ}\mathrm{C}$ for 3 h. The lamellar morphology of the two phases is not altered by this annealing treatment [10, 13].

2.4. Phase Transformations in Zr alloys

Zr undergoes allotropic transformation from the high temperature *bcc* phase β to the low temperature *hcp* α phase at 862°C. The addition of alloying elements, called as α or β stabilizers, respectively may either raise or lower the α to β transus [10, 15, 16]. Examples of typical α stabilizers are Al, Sn, O and N. On the other hand, elements like Nb, Cu, Fe, Cr, Ni, Mo and H are classified as β stabilizers. Usually the α stabilizers result in peritectoid reaction and β stabilizers give rise to a eutectoid system [10]. As discussed earlier, the most important Zr based alloys used for nuclear applications are Zircaloys (*i.e.*, Zr-Sn alloys) and Zr-Nb alloy. The binary phase diagrams for these two system are presented in the Fig. 2.6. As can be seen in these two diagrams there is a quite wide variety of solid state phase transformations possible in Zr based systems. In fact the excellent monograph by Banerjee *et al.* [10] shows that the Ti and Zr based systems have far wider range of the solid state phase transformations than any other known metallic system including Fe based. Zr exhibits a whole lot of different phase transformation such as diffusional, displacive, shuffle dominated, mixed mode of transformations, first order and seconder order, continuous, discontinuous, order-disorder transformations [10, 17]. However in relation to the present thesis, two phase transformations, *viz*, $\beta \rightarrow \alpha$ and $\alpha \rightarrow \delta$ shall be described here.

2.5. $\beta \rightarrow \alpha$ Transformation in Zr

This is one phase transformation that is invariably present in the fabrication flow sheet of practically every Zr based structural component used in the nuclear reactors. Depending on the cooling rate from the β phase field, this can happen either by displacive mode (in case of fast quenching) or by diffusional mode when the imposed cooling rate is low. In all cases the transformation is known to follow strict Orientation Relationship (OR), the crystallography of which has been a subject matter of several investigations [10, 18, 19].

2.5.1. Crystallography of $\beta \rightarrow \alpha$ Transformation

The lattices of the parent (β) and the product phases (α) can be related in a number of ways. The correct choice of the lattice correspondence is generally made by selecting one which involves the minimum distortion and rotation of the lattice vectors. One such solution was originally proposed by Burgers, according to which the basal plane of α is derived from an $\{011\}_\beta$ type

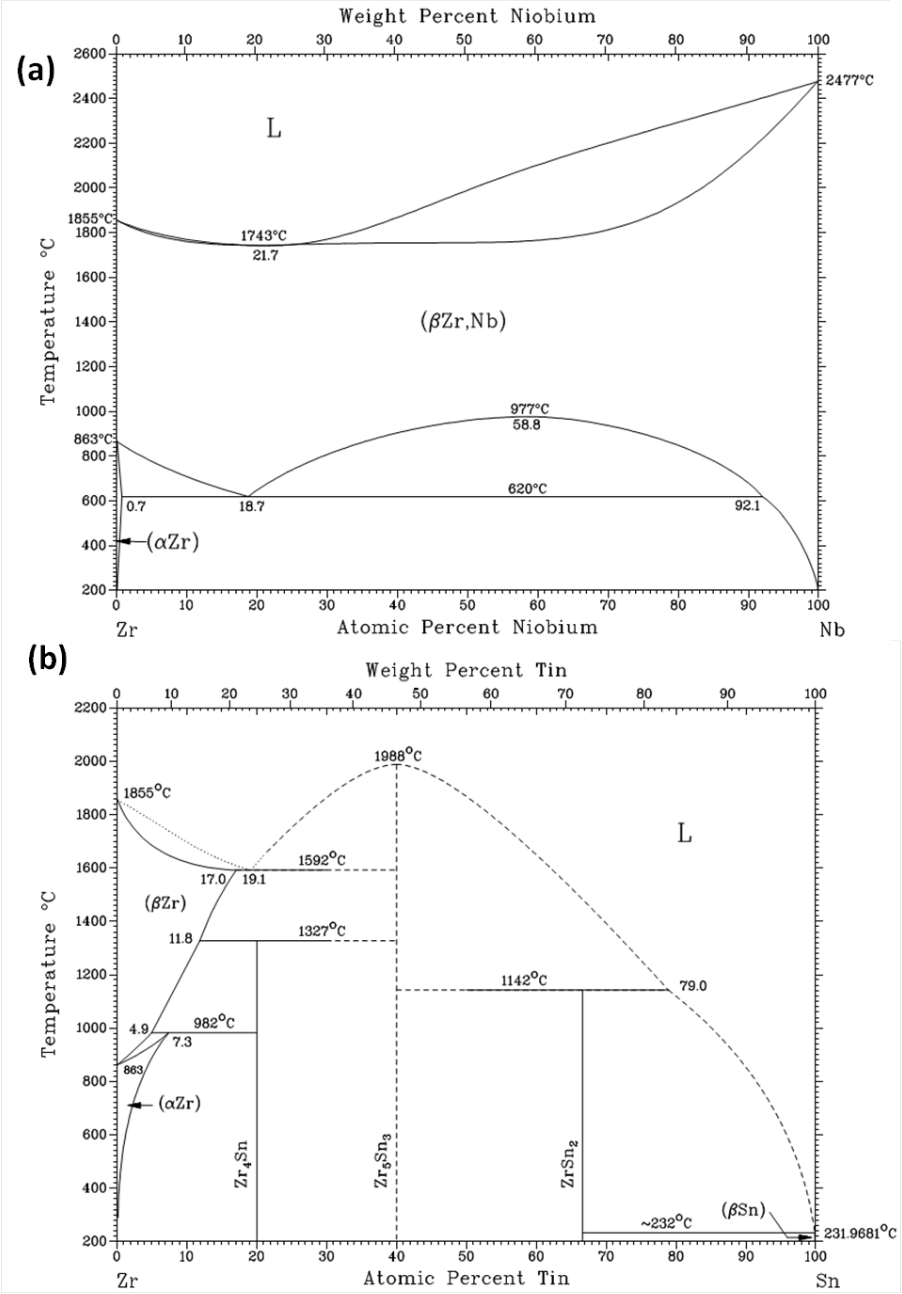

Figure 2.6: Equilibriam diagrams of (a) Zr-Nb and (b) Zr-Sn binary systems [10].

plane and $[01\bar{1}]_\beta$ and $[100]_\beta$ directions transform into $[01\bar{1}0]_\alpha$ and $[2\bar{1}\bar{1}0]_\alpha$ directions, respectively. The close-packed directions $[1\bar{1}1]_\beta$ and $[\bar{1}1\bar{1}]_\beta$ lying on the $\{110\}_\beta$ plane transform to two close-packed $<11\bar{2}0>_\alpha$ directions. The other $<11\bar{2}0>_\alpha$ directions are derived from $<100>_\beta$ directions. This makes there are six possible crystallographically equivalent lattice correspondences between the α and β phases which are shown in the Fig. 2.7.

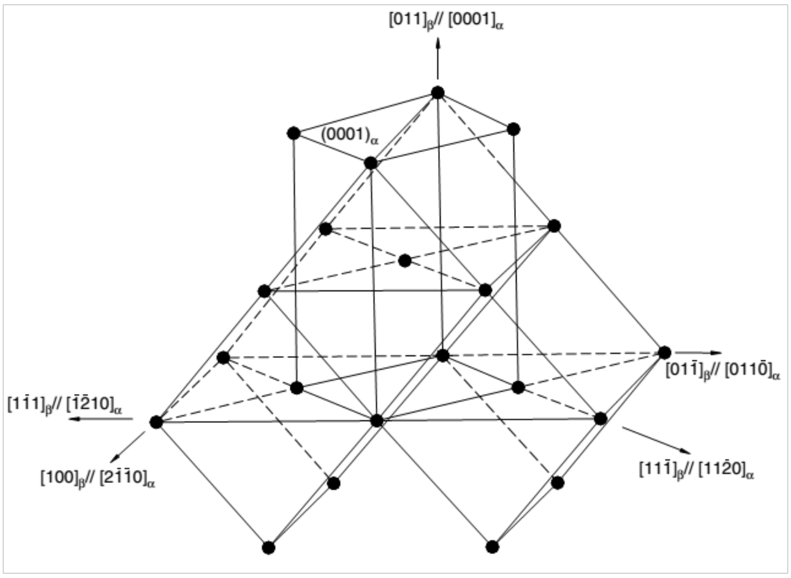

Figure 2.7: The distorted closed-packed hexagonal cell (*hcp*), derived from the parent bcc lattice [10].

The lattice distortion associated with this transformation is given by

$$\mathbf{B} = \begin{bmatrix} \eta_1 & 0 & 0 \\ 0 & \eta_2 & 0 \\ 0 & 0 & \eta_3 \end{bmatrix}. \tag{2.1}$$

where $\eta_1 = \sqrt{\frac{3}{2}}(a_\alpha/a_\beta)$, $\eta_2 = a_\alpha/a_\beta$ and $\eta_3 = 1/2(c_\alpha/a_\beta)$. The above lattice correspondence gives rise to the famous Burger's OR and is described as follows

$$(0001)_\alpha \parallel \{110\}_\beta$$

$$[2\bar{1}\bar{1}0]_\alpha \parallel [111]_\beta.$$

For a given orientation of the α phase, the rotation matrix describing this orientation, $\mathbf{P}^\alpha$, can be transformed to a rotation matrix describing the orientation of the β phase, $\mathbf{B}^\beta$,

$$\mathbf{D}\mathbf{S}_k^\beta \mathbf{B}^\beta = \mathbf{S}_j^\alpha \mathbf{P}^\alpha, \tag{2.2}$$

where, $\mathbf{S}_k^\beta$ and $\mathbf{S}_j^\alpha$ are the symmetry operators (shown in Tables 2.2 and 2.3) for the cubic and hexagonal systems and the matrix $\mathbf{D}$ is a rotation matrix which describes the burgers relationship. If Euler angles notation is employed for the description of D they turn out to be $\phi_1 = 135°$, $\phi = 90°$ and $\phi_2 = 325°$. Further, following commutation relationship between [20, 21] symmetry operators of the cubic and hexagonal phases on the rotation matrix $\mathbf{D}$ is applicable

$$\mathbf{C}_{2z}^{\alpha}\mathbf{D} = \mathbf{D}\mathbf{C}_{2a}^{\beta} \tag{2.3}$$

upon applying the hexagonal symmetry operator $\mathbf{C}_{2z}^{\alpha}$ on both sides of the Eq. 2.2

$$\mathbf{C}_{2z}^{\alpha}\mathbf{D}\mathbf{S}_{k}^{\beta}\mathbf{B}^{\beta} = \mathbf{C}_{2z}^{\alpha}\mathbf{S}_{j}^{\alpha}\mathbf{P}^{\alpha} \tag{2.4}$$

Eq. 2.4 can now be rewritten using the Eq. 2.3,

$$\mathbf{D}\mathbf{C}_{2a}^{\beta}\mathbf{S}_{k}^{\beta}\mathbf{B}^{\beta} = \mathbf{C}_{2z}^{\alpha}\mathbf{S}_{j}^{\alpha}\mathbf{P}^{\alpha} \tag{2.5}$$

since $\mathbf{C}_{2a}^{\beta}$ is a cubic symmetry operator, it turns out that not all 12 variants produced from the above euqation are distinct when referred to cubic system of reference frame but only 6 variants are distinguishable. Thus a single product α grain can have originated from any of the 6 possible parent β orientations. This is the principle used in estimation of the parent phase reconstruction provided one has access to the product phase orientations [21–27].

2.6. Formation of Hydride Phases in Zr Alloys ($\alpha \rightarrow \delta$ Transformation)

The phase transformation resulting in the formation of hydrides from the matrix Zr phase assumes importance because of the deleterious effects of brittle hydride phase on the mechanical properties of the Zr. A thorough understanding of this transformation in terms of crystallography and kinetics is needed for developing improved structural components with better hydride embrittlement resistance [28–34]. Fig. 2.8 shows the phase diagram of the Zr-H binary system. It can be observed that the solubility of the hydrogen in Zr is rather limited at room temperature (less than few ppm) but increases substantially at higher temperatures (70 ppm at 823 K). The excess hydrogen precipitates from the matrix in the form of hydride. There are two equilibrium hydride phases *viz*, δ and ϵ forms of hydrides. Further, there is one meta stable γ hydride that occurs under specific cooling conditions and concentrations of the hydrogen. Table 2.4 shows the crystallographic details of these phases.

Table 2.2: The symmetry operators for the cubic systems

$E^{\beta} = \begin{bmatrix} +1 & 0 & 0 \\ 0 & +1 & 0 \\ 0 & 0 & +1 \end{bmatrix}$	$C^{\beta}_{2x} = \begin{bmatrix} +1 & 0 & 0 \\ 0 & -1 & 0 \\ 0 & 0 & -1 \end{bmatrix}$	$C^{\beta}_{2y} = \begin{bmatrix} -1 & 0 & 0 \\ 0 & +1 & 0 \\ 0 & 0 & +1 \end{bmatrix}$	$C^{\beta}_{2z} = \begin{bmatrix} -1 & 0 & 0 \\ 0 & -1 & 0 \\ 0 & 0 & +1 \end{bmatrix}$
$C^{\beta}_{31+} = \begin{bmatrix} 0 & 0 & +1 \\ +1 & 0 & 0 \\ 0 & +1 & 0 \end{bmatrix}$	$C^{\beta}_{32+} = \begin{bmatrix} 0 & 0 & -1 \\ +1 & 0 & 0 \\ 0 & -1 & 0 \end{bmatrix}$	$C^{\beta}_{33+} = \begin{bmatrix} 0 & 0 & -1 \\ -1 & 0 & 0 \\ 0 & +1 & 0 \end{bmatrix}$	$C^{\beta}_{34+} = \begin{bmatrix} 0 & 0 & +1 \\ -1 & 0 & 0 \\ 0 & -1 & 0 \end{bmatrix}$
$C^{\beta}_{31-} = \begin{bmatrix} 0 & +1 & 0 \\ 0 & 0 & +1 \\ +1 & 0 & 0 \end{bmatrix}$	$C^{\beta}_{32-} = \begin{bmatrix} 0 & +1 & 0 \\ 0 & 0 & -1 \\ -1 & 0 & 0 \end{bmatrix}$	$C^{\beta}_{33-} = \begin{bmatrix} 0 & -1 & 0 \\ 0 & 0 & +1 \\ -1 & 0 & 0 \end{bmatrix}$	$C^{\beta}_{34-} = \begin{bmatrix} 0 & -1 & 0 \\ 0 & 0 & -1 \\ +1 & 0 & 0 \end{bmatrix}$
$C^{\beta}_{4x+} = \begin{bmatrix} +1 & 0 & 0 \\ 0 & 0 & -1 \\ 0 & +1 & 0 \end{bmatrix}$	$C^{\beta}_{4y+} = \begin{bmatrix} 0 & 0 & +1 \\ 0 & +1 & 0 \\ -1 & 0 & 0 \end{bmatrix}$	$C^{\beta}_{4z+} = \begin{bmatrix} 0 & -1 & 0 \\ +1 & 0 & 0 \\ 0 & 0 & +1 \end{bmatrix}$	$C^{\beta}_{4x-} = \begin{bmatrix} +1 & 0 & 0 \\ 0 & 0 & +1 \\ 0 & -1 & 0 \end{bmatrix}$
$C^{\beta}_{4y-} = \begin{bmatrix} 0 & 0 & -1 \\ 0 & +1 & 0 \\ +1 & 0 & 0 \end{bmatrix}$	$C^{\beta}_{4z-} = \begin{bmatrix} 0 & +1 & 0 \\ -1 & 0 & 0 \\ 0 & 0 & +1 \end{bmatrix}$	$C^{\beta}_{2a} = \begin{bmatrix} 0 & +1 & 0 \\ +1 & 0 & 0 \\ 0 & 0 & -1 \end{bmatrix}$	$C^{\beta}_{2b} = \begin{bmatrix} 0 & -1 & 0 \\ -1 & 0 & 0 \\ 0 & 0 & -1 \end{bmatrix}$
$C^{\beta}_{2c} = \begin{bmatrix} 0 & 0 & +1 \\ 0 & -1 & 0 \\ +1 & 0 & 0 \end{bmatrix}$	$C^{\beta}_{2d} = \begin{bmatrix} -1 & 0 & 0 \\ 0 & 0 & +1 \\ 0 & +1 & 0 \end{bmatrix}$	$C^{\beta}_{2e} = \begin{bmatrix} 0 & 0 & -1 \\ 0 & -1 & 0 \\ -1 & 0 & 0 \end{bmatrix}$	$C^{\beta}_{2f} = \begin{bmatrix} -1 & 0 & 0 \\ 0 & 0 & -1 \\ 0 & -1 & 0 \end{bmatrix}$

Table 2.3: The symmetry operators for the hexagonal systems

$E^{\alpha} = \begin{bmatrix} +1 & 0 & 0 \\ 0 & +1 & 0 \\ 0 & 0 & +1 \end{bmatrix}$	$C^{\alpha}_{6z+} = \begin{bmatrix} 1/2 & -\sqrt{3}/2 & 0 \\ \sqrt{3}/2 & 1/2 & 0 \\ 0 & 0 & 1 \end{bmatrix}$	$C^{\alpha}_{3z+} = \begin{bmatrix} -1/2 & -\sqrt{3}/2 & 0 \\ \sqrt{3}/2 & -1/2 & 0 \\ 0 & 0 & 1 \end{bmatrix}$
$C^{\alpha}_{2z} = \begin{bmatrix} -1 & 0 & 0 \\ 0 & -1 & 0 \\ 0 & 0 & -1 \end{bmatrix}$	$C^{\alpha}_{6z-} = \begin{bmatrix} 1/2 & \sqrt{3}/2 & 0 \\ -\sqrt{3}/2 & 1/2 & 0 \\ 0 & 0 & 1 \end{bmatrix}$	$C^{\alpha}_{3z-} = \begin{bmatrix} -1/2 & \sqrt{3}/2 & 0 \\ -\sqrt{3}/2 & -1/2 & 0 \\ 0 & 0 & 1 \end{bmatrix}$
$C^{\alpha}_{21+} = \begin{bmatrix} 1 & 0 & 0 \\ 0 & -1 & 0 \\ 0 & 0 & -1 \end{bmatrix}$	$C^{\alpha}_{22+} = \begin{bmatrix} -1/2 & \sqrt{3}/2 & 0 \\ \sqrt{3}/2 & 1/2 & 0 \\ 0 & 0 & -1 \end{bmatrix}$	$C^{\alpha}_{23+} = \begin{bmatrix} 1/2 & \sqrt{3}/2 & 0 \\ \sqrt{3}/2 & -1/2 & 0 \\ 0 & 0 & -1 \end{bmatrix}$
$C^{\alpha}_{21-} = \begin{bmatrix} -1 & 0 & 0 \\ 0 & +1 & 0 \\ 0 & 0 & -1 \end{bmatrix}$	$C^{\alpha}_{22-} = \begin{bmatrix} 1/2 & -\sqrt{3}/2 & 0 \\ -\sqrt{3}/2 & -1/2 & 0 \\ 0 & 0 & -1 \end{bmatrix}$	$C^{\alpha}_{23-} = \begin{bmatrix} -1/2 & -\sqrt{3}/2 & 0 \\ -\sqrt{3}/2 & 1/2 & 0 \\ 0 & 0 & -1 \end{bmatrix}$

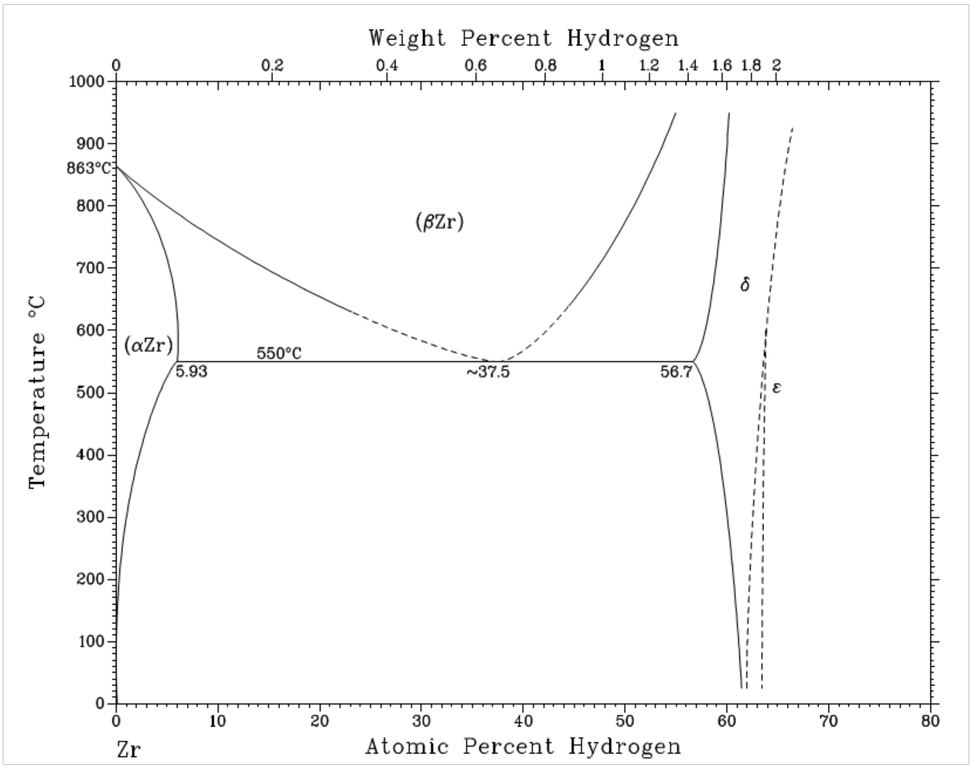

Figure 2.8: Zr-H phase diagram [10].

2.6.1. Hydride Morphology, Distribution and Habit Planes

Not only the amount of hydride but also its morphology, orientation with respect to stress, and its distribution, are all equally important in determining the extent of possible damage to mechanical properties. Hence a considerable work went into knowing the causes and effects of different hydride morphologies and orientations [28, 35, 36].

Different Morphologies of Hydrides

Depending upon hydrogen concentration and thermal treatment, following morphologies are observed: [28]

1. Needles
2. Platelet (its existence can be established from observation of a single hydride on two planes of crystal)
3. Composite platelets (having single platelets grown end to end), Fig.2.9 (a).
4. In Zr 2.5% Nb, composite platelet can be made of smaller platelets orientated at 45° to the principal direction, Fig. 2.9 (b).

Table 2.4: The crystallography of different hydrides in Zr-H system [28].

S. No	Hydride	Crystal Structure,Lattice Parameter (nm)	Location of Hydrogen atoms	Remarks
1	ZrH (γ)	Tetragonal (Primitive) a=0.4596, c=0.4969	Ordered tetrahedral sites in Zr lattice	a, c depend slightly on composition and thermal treatment. It is a meta stable phase
2	$ZrH_{1.5}$ (δ)	FCC c/a=1, a=0.4773	Some of tetrahedral interstices of FCC lattice at $\frac{1}{4}\frac{1}{4}\frac{1}{4}$ and equivalent positions	Equilibrium phase, but forms only under very slow cooling rates
3	ZrH_2 ϵ	Tetragonal c/a<1, a=0.4980, c=0.4445	Interstitial sites of tetragonal symmetry at $\frac{1}{4}\frac{1}{4}\frac{1}{4}$	There is no strain energy when the site is occupied,by hydrogen, as radius of site is 0.043nm and that of hydrogen is 0.004 nm

Factors affecting hydride morphology & Orientation

- Crystallographic factors: It has been generally observed that within grains, a few habit planes are preferred, notably $\{10\bar{1}0\}$ and $\{10\bar{1}7\}$ [10, 28, 29].
- Prior strains: Hydride platelets tend to form parallel to the direction of drawing of the wire
- Thermal treatments affect the distribution and size to great extent.

Effect of cooling rate on Hydride distribution

A good example of hydride size versus cooling rate [30] in Zry-2 is given in Fig.2.10. If the cooling rate is sufficiently low, the preferred sites of nucleation are grain boundaries.

Habit planes for hydride precipitation

One of the chief reasons for the observed strong effect of crystallographic texture on the hydride morphological orientation is existence of strong habit plane in case of hydride precipitation. Several studies have focused on this aspect but came up with several possible habit planes

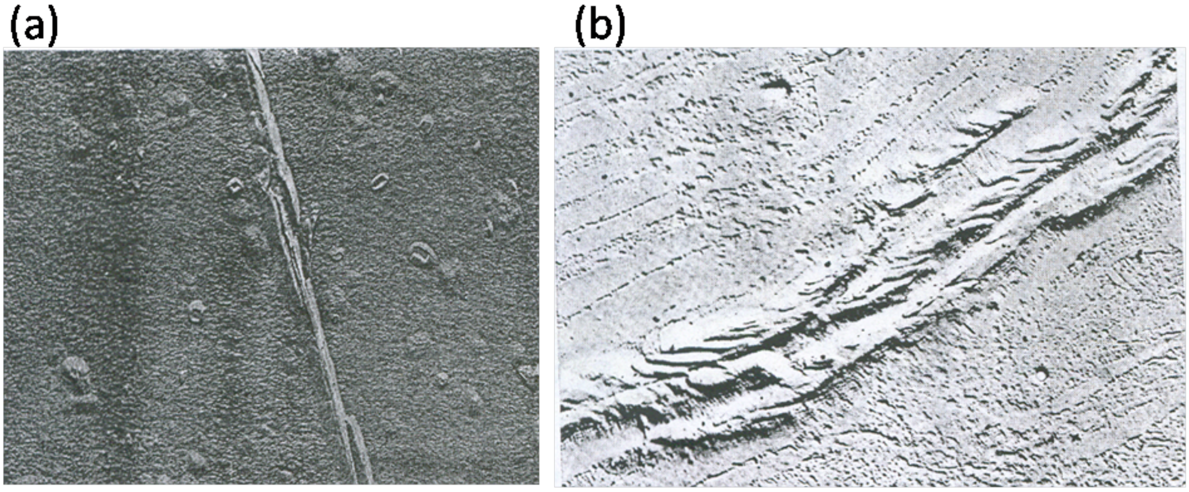

Figure 2.9: Illustration of different morphologies of hydrides in Zirconium alloys. (a) Composite structure of hydride platelet in Zry -4. The colony of platelets and segments are aligned within 12° of the principal hydride direction. (b) Composite structure of a hydride of a platelet in Zr-2.5 wt% Nb alloy. Segments of the platelet appear to be oriented at 45° to principal hydride direction [30].

depending on the conditions used in the study [28]. These studies had reported habit planes which were contradicting each other, but Westlake explained much of the contradictions [37, 38]. It seems likely that the primary habit plane in pure Zr is $10\bar{1}0$ and in Zry-2 and Zry-4 $10\bar{1}7$. Westlake raises an interesting question as to the validity of reported habit planes of various authors. This is due to the possible error in identification of hydride habit plane that arises from the fact that what appears to be trace of a single hydride may in fact be a disjointed stringer of platelets with traces not parallel to the stringer. This is demonstrated in Fig.2.11, which shows hydrided grain at 150 X (2.11(a)). The traces seemed to be attributable to one family of planes of the $10\bar{1}l$ type but definitely not $10\bar{1}7$. They would make an angle of 7.5° with basal plane. Inspection at 1500 X (2.11(b)) reveals, however, that the long traces are disjointed stringers of small platelets on $10\bar{1}7$ planes.

2.7. Deformation Mechanisms in Zr

The deformation systems in hexagonal-close-packed (*hcp*) metals are not as symmetrically distributed as in cubic metals [3]. Furthermore, because the primary slip systems are not as numerous and are not as effective as their cubic counterparts, in addition to being limited to deformations in the $<a>$ direction, twinning competes substantially with slip in plastic deformation and thus can play an essential role, depending on the deformation conditions. In *hcp* metals, the presence of low number of easy slip systems, their asymmetrical distribution, and the strict

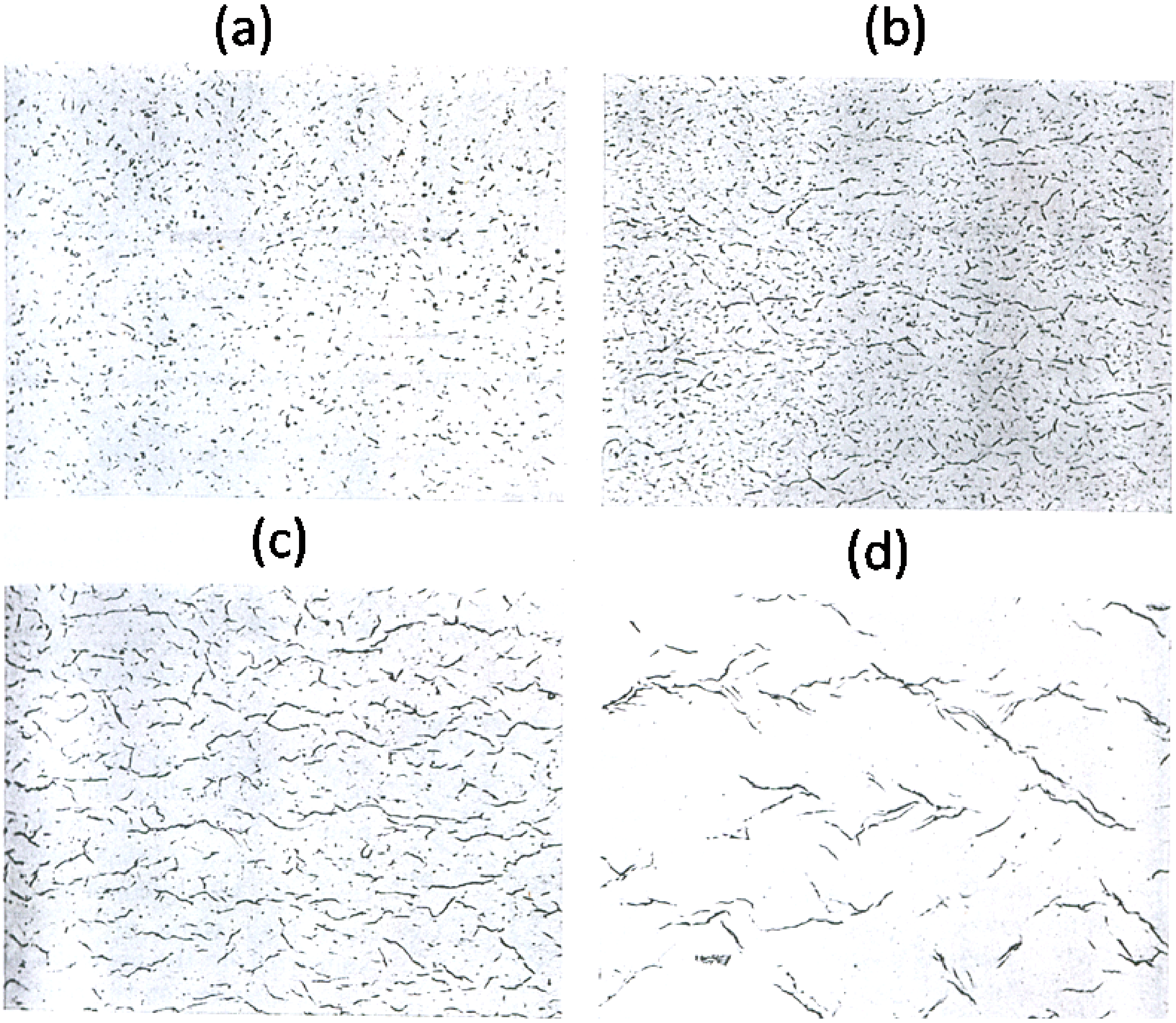

Figure 2.10: Effect of cooling rate on hydride agglomeration in Zry-2. Hydrogen concentration 200 ppm. Specimens cooled from $400°\mathrm{C}$ **(a) Quenched into cold water; (b) Quenched into boiling water; (c) Cooled in still air; (d) Furnace cooled [30].**

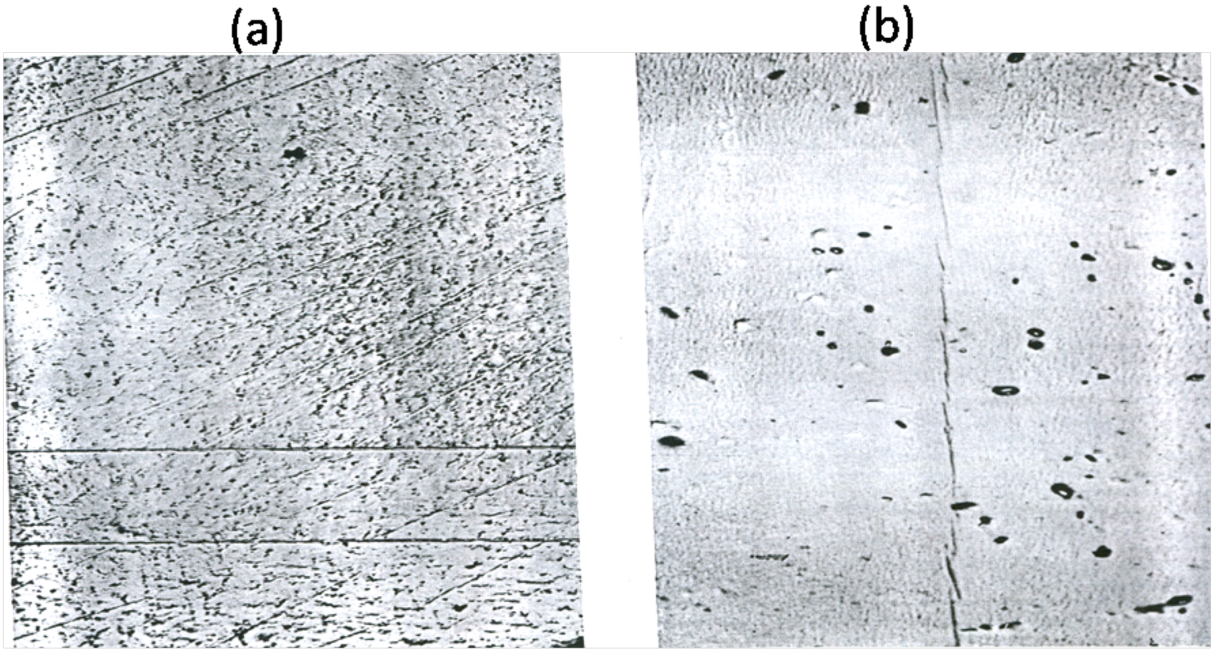

Figure 2.11: (a) Hydride traces of Zry-4 containing 50 ppm Hydrogen, at 150X. (b) Same area as in (a) at 1500X [30].

crystallographic orientation relationships for twinning result in the formation of a strong deformation texture. (If the material is subsequently heat-treated, a pronounced annealing texture also develops). For textured materials, on the other hand, the deformation mechanisms are also responsible for the strong anisotropy of the mechanical properties. The foregoing points represent three aspects that are mutually interdependent.

2.7.1. Slip Systems in Zr

At temperatures below $850°\mathrm{C}$, zirconium and its alloys are dominantly in the α- phase with a *hcp* structure. The usually shown hexagonal cell of Zr consists of three elementary cells, one of which is marked by thicker lines in Fig. 2.12. The elementary cell is defined by the axial sections $<a_1>$, $<a_2>$, and $<c>$. Essential planes are the basal plane and the prism planes of first and second order. Basal and prism planes are perpendicular to each other and have an $<a>$ direction as the common lattice vector. The planes oriented in-between are pyramidal planes of different type and order. Besides other factors, *e.g.*, the stacking fault energy and the dependence of the crystal orientation, the c/a ratio especially has a dominant influence on the deformation systems to be activated. According to the Peierls-Nabarro model, one expects that basal slip will be replaced by prism slip as soon as the c/a ratio becomes $<\sqrt{3}$. Then the inter-planar spacing of the prism planes and their atomic packing density become larger than the corresponding values for the basal plane. This is the reason why the dominant mode of slip in Zr based alloys is slip of dislocations on prismatic planes. In the α-structure of zirconium, slip takes place (at least at room temperature and higher, up to about $500°\mathrm{C}$) usually on the first-order prism planes $\{10\bar{1}0\}$ along the $<a>$ directions $<11\bar{2}0>$ (Fig. 2.13). Slip has also been observed in the same direction on the basal plane, although to a far lower extent [39, 40]. In regions of high stress concentration, such as grain boundaries, $10\bar{1}1$ slip traces occur. A slip system with a component in the $<c>$ direction has been observed only under constraints and at high deformation temperatures. The corresponding slip mode is slip that occurs on first or second-order pyramidal planes $\{10\bar{1}1\}$ or $\{1\bar{2}11\}$ in $<c+a>$ directions $<11\bar{2}3>$.

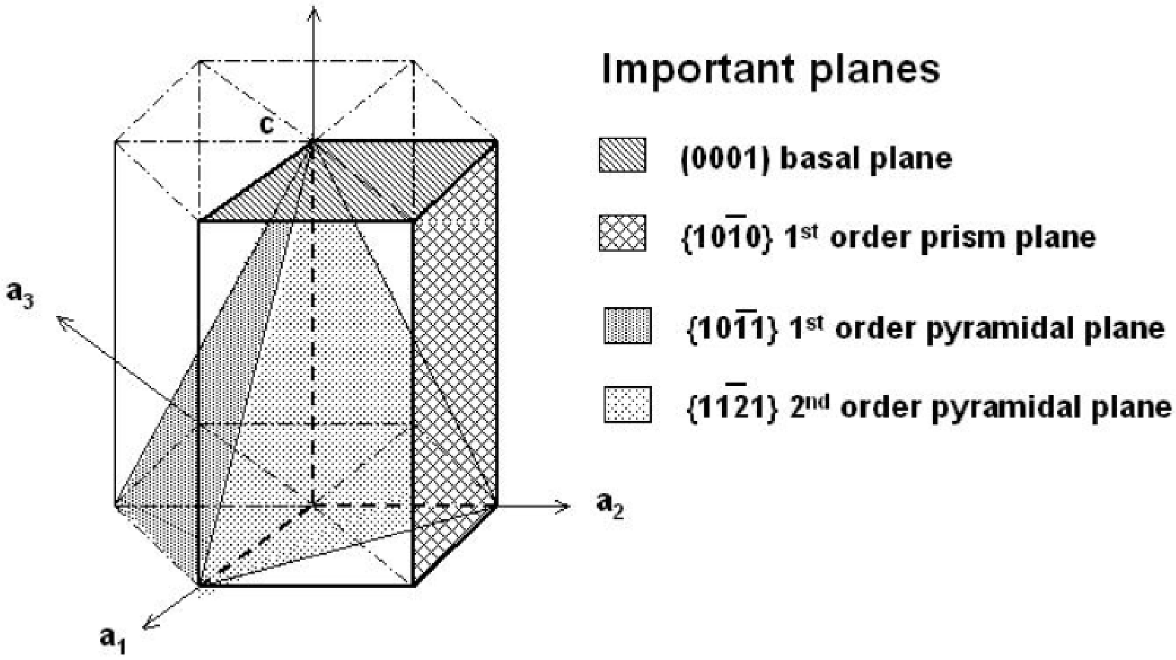

Figure 2.12: Illustration of important crystallographic directions and planes for deformation systems of *hcp* materials.

2.7.2. Twinning Systems in Zr

Because of the limited number of easy slip systems available, Zr undergoes substantial twinning during the plastic deformation. Under tensile stress along the direction of the c axis, $\{10\bar{1}2\}$ $<10\bar{1}1>$ twins are activated and less commonly, $\{11\bar{2}1\}$ $<11\bar{2}6>$ twins. Under compression in a $<c>$ direction $\{11\bar{2}2\}$ $<11\bar{2}3>$ and at elevated temperatures $\{10\bar{1}1\}$ $<10\bar{1}2>$ twinning are observed. Fig. 2.14 shows the commonly observed modes of twins in the deformation of Zr based alloys. Twinning does not allow high rates of deformation. However, it may play an important role in deformation, since lattice regions initially unfavorable for slip are reoriented

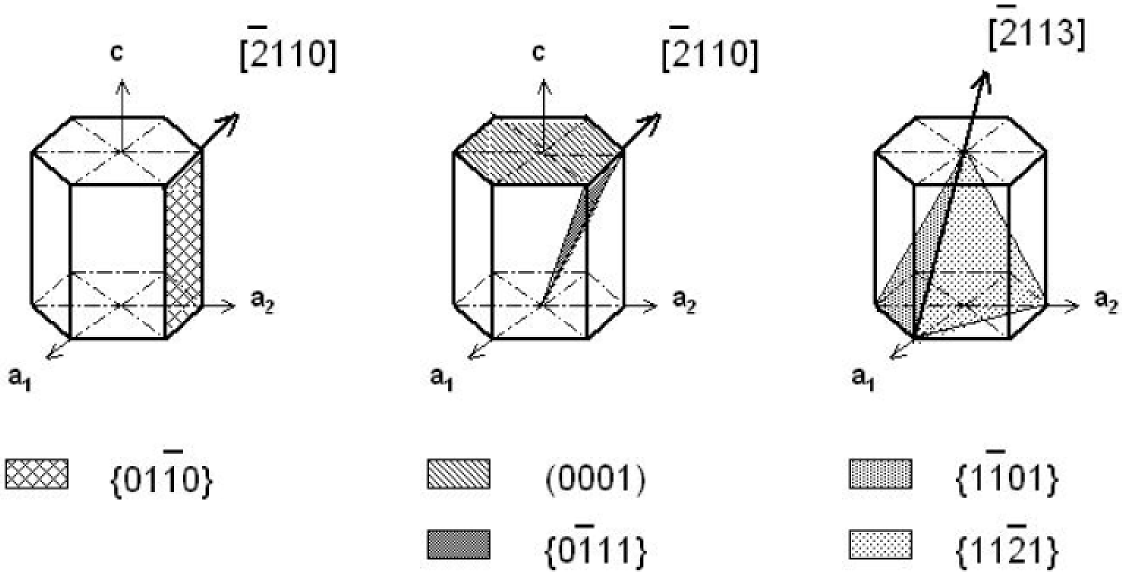

Figure 2.13: Schematic of slip systems in α - Zirconium.

by the lattice rotation, thus potentially becoming more favorably oriented for slip and allowing the possibility of larger strains. Moreover, it should be noted that twinning activates new slip systems even in regions of local stress concentration, such as twin boundaries or by interactions between dislocation and twinning. This possibility has been discussed especially for slip systems with $<c + a>$ Burgers vector.

2.7.3. Microstructural Developments During the Deformation

Unlike high symmetry cubic materials, the substructural developments in hexagonal system can not be easily generalized [3, 16]. These have a different scheme of formation depending on the material, alloying additions and the deformation mode and has to be studied separately for individual alloys. Unfortunately, not many such studies exist in the domain of published literature. Some of them are included here. The dislocation arrangements observed in deformed zirconium depend upon the purity of the metal. In commercial zirconium containing 0.1 wt% of O and N, the dislocation arrangement is of the type to be expected if slip occurs predominantly on $\{10\bar{1}0\}$ planes. In relatively pure crystal bar zirconium containing 0.03 wt% of O and N a tangled arrangement of dislocations is observed together with loops and dislocation dipoles, which are difficult to account for in terms of $\{10\bar{1}0\}$ slip alone. While the slip traces of moving dislocations show that slip occurs on $\{10\bar{1}0\}$ planes, evidence that slip can occur on the basal plane has been found from studies of the dislocations associated with hydride precipitates. This change in dislocation structure is associated with a large increase in the flow stress at equivalent strains. It

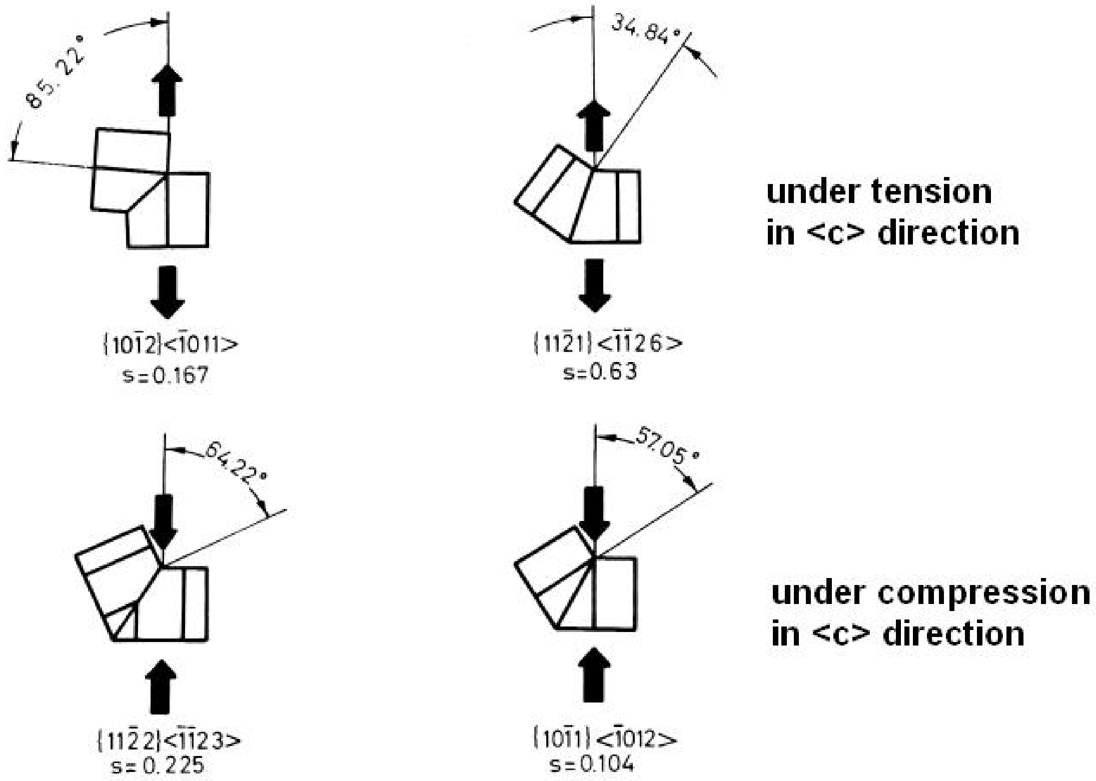

Figure 2.14: Schematic of common deformation twin systems in α - Zirconium.

is proposed that the observations can be explained if the stress for dislocation glide on $\{10\bar{1}0\}$ planes increases and glide on the basal plane becomes more difficult relative to glide on $\{10\bar{1}0\}$ with increasing impurity. The generation of $<c>$ component dislocations in zirconium alloys is a much common phenomenon. $<c>$ component dislocations are generated to maintain compatibility between crystallites which differ greatly in their ability to accommodate the applied strain by $<a>$ slip [41]. They are found in abundance near deformation twins, in particularly oriented, small martensite plates and to a lesser extent, at the grain boundary junctions in large grained material. Pure $<c>$ and $<c+a>$ type dislocations have been identified in deformed Zircaloy-2 and Zircaloy-4. Dislocation segments tend to be long, straight and to lie in either the basal or the pyramidal planes [42]. The typical dislocation substructure in Zircaloy-4 fatigued under in-phase (IP) biaxial loading [41] is composed of parallel dislocation bands formed by $\{10\bar{1}0\}$ prismatic slip. As the equivalent strain range increases, dislocation substructure changes from single slip to multi slip structure accompanied by a tendency to form dislocation tangles and undefined dislocation cells [41]. Typical substructure in Zircaloy-4 fatigued under biaxial loading changes from parallel dislocation walls to well developed dislocation tangles as the phase angle increases [43–46].

2.8. Deformation Modeling

Several different modeling techniques are being used for the simulation and prediction of plastic deformation in metallic materials. Exact mode of model depends on the nature of phenomenon investigated and length scale of investigation. Fig. 2.15 schematically illustrates various length and time scales and corresponding modeling techniques being employed for the modeling of materials deformation [47]. While the first priciple based density functional theory calculations are good tools for the estimation of the defect characteristics like Stacking Fault Energy (SFE), dislocation core structure *etc.* [48], phenomenon like dislocation nucleation, glide, twin nucleation, grain boundary penetration, dislocation nucleation, interaction with precipitates *etc*, are better handled by the MD [49–54]. Similarly, phenomenon with length scales in the range of few microns and time scales of the order of pico to micro seconds such as dislocation interactions, annihilations, junction formations, multiplications *etc*, fall in the domain of discrete dislocation dynamics [55–62]. Continuum based finite element based models on the other hand are best suited for the prediction of phenomena on a much larger length and time scales and are routinely used for the prediction of flow behavior, textural evolutions, mechanical behavior *etc.* These methods now a days are being used in conjunction with crystal plasticity theory to bring out orientation sensitive deformation behavior in the polycrystalline bulk materials [47, 63, 64]. As far as the present thesis is concerned, two modeling techniques (Dislocation Dynamics and Molecular Dynamics) are of relevance and hence are described in more details in the following sections.

2.9. Discrete Dislocation Dynamics

The plastic deformation of the metallic materials is essentially a result of collective behavior of underlying dislocations. Line dislocation dynamics or Discrete Dislocation Dynamics, an emerging computation field, essentially attempts to capture the evolution of the dislocation structure in response to imposed conditions of stress, strain rate *etc.* and helps us to gain insights into fundamental mechanisms that govern the material behavior at meso-scale [60, 65–67]. Over the past few decades, experimental and theoretical developments have firmly established the principal role of dislocation mechanisms in defining material strength. It is now understood

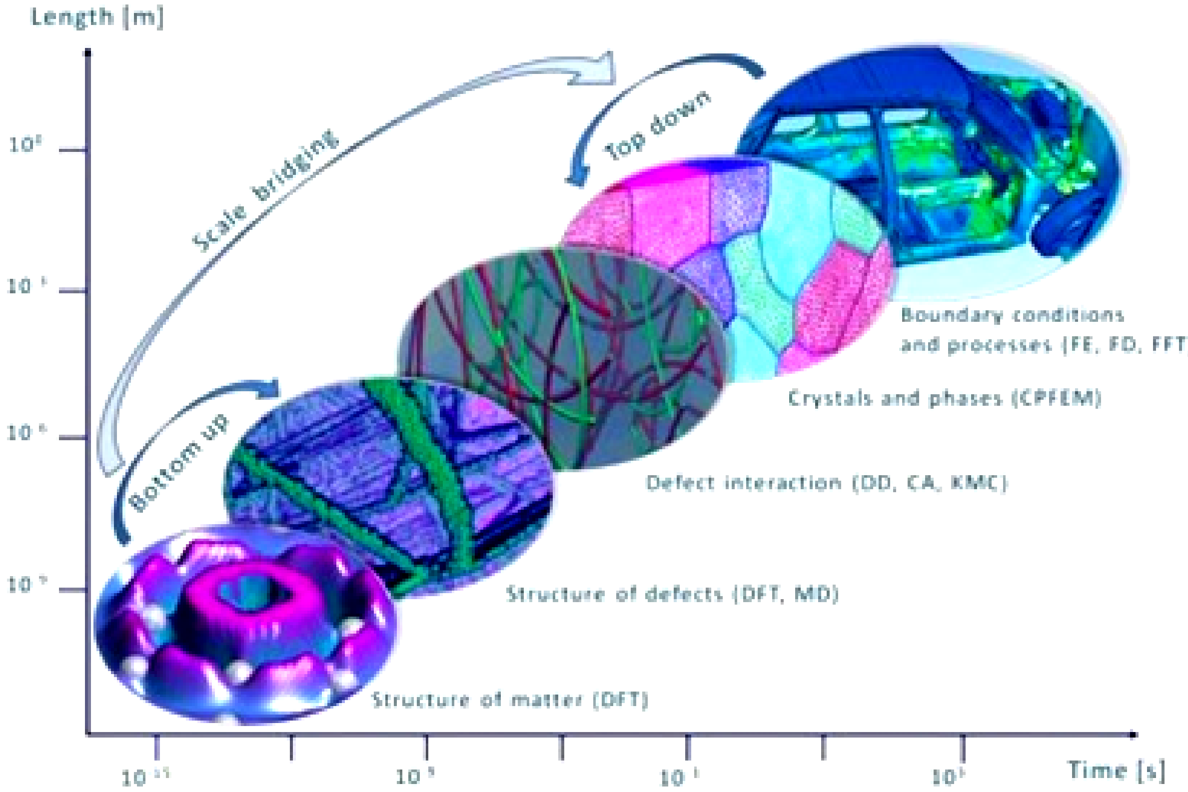

Figure 2.15: Schematic of various modeling techniques and the length and time scales of phenomena studied using them [47].

that macroscopic properties of crystalline materials are derivable, at least in principle, from the behavior of their constituent defects. However, this fundamental understanding has not been translated into a continuum theory of crystal plasticity based on dislocation mechanisms. The major difficulty in developing such a theory is the multiplicity and complexity of the mechanisms of dislocation motion and interactions that make it impossible to develop a quantitative analytical approach. The problem is further complicated by the need to trace the spatio-temporal evolution of a very large number of interacting dislocations over very long periods of time, as required for the calculation of plastic response in a representative volume element. Such practical intractability of the dislocation-based approaches, on one hand, and the developing needs of material engineering at the nano and micro length scales on the other, have created the current situation when equations of crystal plasticity used for continuum modeling are phenomenological and largely disconnected from the physics of the underlying dislocation behavior. Bridging the gap between dislocation physics and continuum crystal plasticity has become possible with the advancement in computational technology with bigger and faster computers. To this end, over the past two decades various Discrete Dislocation Dynamics (DDD) models have been developed.

In these models, dislocation motion and interactions with other defects, particles and surfaces are explicitly considered. However, complications with respect to dislocation multiplications, self-interactions and interactions with other defects, and keeping track of complex mechanisms and reactions have provided a new set of challenges for developing efficient computational algorithms. Essentially these models discretize the dislocations into finite segments connected by nodes and track the temporal and spacial evolution of the dislocation structure by computing the interactions among all the dislocation segments and the external stimuli using a set of physics based mobility rules for the nodal points. In summary, the 3D DD accounts for the following geometric aspects

- Dislocation topology; 3D geometry, Burgers vector and line sense.
- Identification of all possible slip planes for each dislocation.
- Changes in the dislocation topology when part of it cross-slips and or climbs to another plane.
- Multiplication and annihilation of dislocation segments.
- Formation of complex connections and intersections such as junctions, jogs and branching of the dislocation in multiple directions.

2.9.1. Nodal Representation of Dislocation Networks

Fig. 2.16 illustrates a simple nodal representation to describe dislocation networks of arbitrary topology. The dislocation lines are represented by a set of nodes connected to each other by straight segments. Each segment has a non-zero Burgers vector. Given the freedom of choice between two opposite line directions, the usual convention is to define $\mathbf{b}_{ij}$ with respect to the line sense pointing from node i to node j. Likewise, $\mathbf{b}_{ji}$ is the Burgers vector of the same segment but defined with respect to the opposite line sense, *i.e.* from node j to node i. Obviously, $\mathbf{b}_{ij} + \mathbf{b}_{ji} = 0$. Under this convention, the conservation of Burgers vector means that the Burgers vectors of all segments pointing out from the same node must sum up to zero, *i.e.* $\sum_k \mathbf{b}_{ij} = 0$, where the sum is over all nodes k connected to node i. These sum rules provide useful checks for topological self-consistency during line DD simulations. While there is no limit on the maximum number of nodes that can be connected to a given node, each node must be connected to at least two other nodes, because dislocation lines cannot terminate inside the crystal. Also, to avoid redundancy, no two nodes can be connected by more than one segment.

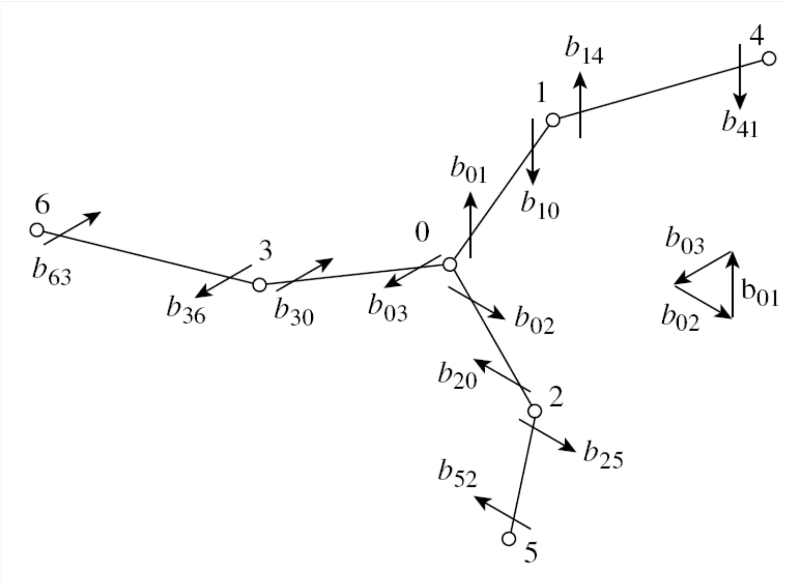

Figure 2.16: Dislocation network is represented by a set of nodes (circles) connected by straight segments. b_{ij} is the Burgers vector of the directed segment connecting node i to node j [67].

2.9.2. Evaluation of Plastic Strains

One of the principal outputs of a typical DD simulation is the plastic strain tensor as a function of time on account of various dislocation interactions in response to applied external stress fields. The motion of each dislocation segment gives rise to plastic distortion, which is related to the macroscopic plastic strain rate tensor $\dot{\epsilon}^p$, and the plastic spin tensor $\mathbf{W}^p$ via the relations

$$\dot{\epsilon}^p = \sum_{s=1}^{N_s} \frac{l_s v_{gs}}{2V} (\mathbf{n}_s \otimes \mathbf{b}_s + \mathbf{b}_s \otimes \mathbf{n}_s) \tag{2.6}$$

$$\mathbf{W}^p = \sum_{s=1}^{N_s} \frac{l_s v_{gs}}{2V} (\mathbf{n}_s \otimes \mathbf{b}_s - \mathbf{b}_s \otimes \mathbf{n}_s), \tag{2.7}$$

where $\mathbf{n}_s$ is a unit normal to the slip plane, v_{gs} is the magnitude of the glide velocity of the segment, V is the volume of the representative volume element and $N_s = N_l \times n_s^{(l)}$ is the total number of segments. The above relations provide the most rigorous connection between the dislocation motion (the fundamental mechanism of plastic deformation in crystalline materials) and the macroscopic plastic strain, with its dependence on strength and applied stress being explicitly embedded in the calculation of the velocity of each dislocation. Nonlocal effects are explicitly included into the calculation through long-range interactions. Another microstructure quantity, the dislocation density tensor α, can also be calculated according to

$$\alpha = \sum \frac{l_s}{V} \mathbf{b}_s \otimes \xi_s \tag{2.8}$$

This quantity provides a direct measure for the net Burgers vector that gives rise to strain gradient relief (bending of crystal).

2.9.3. Evaluation of Energies and Nodal Forces

The most important and time consuming step of any DD simulation is the evaluation of nodal forces which arise due to interaction of dislocations and also due to the externally applied stress fields. For this we introduce the total energy of the dislocation network as a function of the nodal positions and Burgers vectors, *i.e.* $E_{tot}(\{\mathbf{r}_i, \mathbf{b}_{ij}\})$. The force on node i is then defined as negative derivative of the total energy with respect to its position $\mathbf{r}_i$, *i.e.*

$$\mathbf{f}_i = -\frac{\partial E_{tot}(\{\mathbf{r}_i, \mathbf{b}_{ij}\})}{\partial \mathbf{r}_i} \tag{2.9}$$

The total energy of a dislocation can be partitioned into elastic and a core-energy contributions, *i.e.*,

$$E_{tot}(C) = E_{el}(C, r_c) + E_{core}(C, r_c), \tag{2.10}$$

where in, C represent the entire dislocation network, *i.e.*, $C \equiv \{\mathbf{r}_i, \mathbf{b}_{ij}\}$, and r_c is the cut-off distance for the core of the dislocation and serves the purpose of eliminating singularity in the stress field computed using linear elastic theory. Thus the nodal forces can also be expressed as sum of elastic and core components as below

$$\mathbf{f}_i = \mathbf{f}_i^{el} + \mathbf{f}_i^{core} \tag{2.11}$$

Using the non-singular formulation for the stress field of the dislocation, WeiCai[68] *et al.* have come up with following expression for the elastic energy of dislocation

$$\begin{aligned} E_{el}(C, r_c) \;=\; & \tfrac{\mu}{16\pi} \oint_C \oint_C b_i b'_j \partial_k \partial_k R_a \,\mathrm{d}\,x_i \,\mathrm{d}\,x'_i \\ & -\tfrac{\mu}{8\pi} \oint_C \oint_C \epsilon_{ijq}\epsilon_{mnq} b_i b'_j \partial_k \partial_k R_a \,\mathrm{d}\,x_m \,\mathrm{d}\,x'_n \\ & +\tfrac{\mu}{8\pi(1-\nu)} \oint_C \oint_C \epsilon_{ikl}\epsilon_{jmn} b_k b'_m \partial_i \partial_j R_a \,\mathrm{d}\,x_l \,\mathrm{d}\,x'_n, \end{aligned} \tag{2.12}$$

where in $R_a = \sqrt{R^2 + r_c^2}$. Another contribution to the forces on the nodes is from the core of the dislocations. The above formulations are all derived from the theory of linear elasticity, which, unfortunately does not hold near the core of the dislocation. One way to account for this is to derive the energy of the core from alternate means (*e.g.* firs principle based MD) as a function of orientational angles of dislocation segments (θ_{i-j} and ϕ_{i-j})

$$E_{core}(C, r_c) = \sum_{(i-j)} E_c(\theta_{i-j}, \phi_{i-j}; r_c) \parallel \mathbf{r}_i - \mathbf{r}_j \parallel \tag{2.13}$$

where the summation is over all of the connected components of the dislocation segments.

2.9.4. Nodal Mobility Functions

Having computed the nodal forces as per the previous listed formulations, next step is to estimate by how much the nodes move in response to the above forces. Although, in principle, the nodal forces are related linearly to acceleration experienced by the nodes (as per the Newton's laws), in the over damped conditions of the dislocation motion typical of majority of the practical situations, nodal velocity can be taken to be liner related to nodal forces [69].

Further, the mobility is the actual part of the DD simulations, which is material specific. For example, the mobility law should reflect the fact that nodal movement is mostly constrained to be along the specific slip planes, and out of the slip planes motion is rather difficult. In addition, nodal movement along the local line vector (in spite of having significant force component in that direction) is to be ignored because of the basic discretization scheme, making the motion of nodes along the line vector irrelevant.

2.9.5. Time Integration

Taken together, the nodal forces and the mobility model comprise the equations of motion for the nodes:

$$v_i = \frac{\mathrm{d}\,\mathbf{r}_i}{\mathrm{d}\,t} = \mathbf{g}_i(\mathbf{r}_j), \tag{2.14}$$

where function g_i subsumes both the nodal force and the mobility model. This is a first-order ordinary differential equation (ODE), for which the simplest numerical integrator is the so-called Euler forward method:

$$\mathbf{r}_i(t + \Delta t) = \mathbf{r}_i + \mathbf{g}_i(\mathbf{r}_j(t))\Delta t. \tag{2.15}$$

In some cases of unsuitable values of Δt, Euler forward method can encounter stability issues, and can lead to inaccurate results. A better alternative is the *trapezoind*integrator which can be expressed as

$$\mathbf{r}_i(t+\Delta t) = \mathbf{r}_i + \frac{\mathbf{g}_i(\mathbf{r}_j(t) + \mathbf{g}_i(\mathbf{r}_j(t+\Delta t)}{2}\Delta t \tag{2.16}$$

Since the above equation contains unknown term $(\mathbf{g}_i(\mathbf{r}_j(t))$ on either side, its an implicit formulation and is thus computationally cumbersome. The computationally efficient strategy would be to combine the above two methodologies in what is known as predictor-corrector as shown below

$$\mathbf{r}_i^P(t+\Delta t) = \mathbf{r}_i + \mathbf{g}_i(\mathbf{r}_j(t))\Delta t. \tag{2.17}$$

$$\mathbf{r}_i(t+\Delta t) = \mathbf{r}_i + \frac{\mathbf{g}_i(\mathbf{r}_j(t) + \mathbf{g}_i(\mathbf{r}_i^P(t+\Delta t)}{2}\Delta t \tag{2.18}$$

While the Eq. 2.17 serves as predictor, Eq. 2.18 serves as corrector. If the difference between these two is too large, Δt is suitably reduced.

2.9.6. Topological Operations

The next most essential step of the DD simulation is to incorporate the topological changes in the dislocation networks. These include creation and deletion of nodes, formation of junctions, cross slip *etc*.

2.9.7. Typical Fields of Applications of DD

Over the past decade, the discrete dislocation dynamics has been utilized by a number of researchers to investigation many complicated small-scale crystal plasticity phenomena that occur under a wide range of loading and boundary conditions and covering a wide spectrum of strain rates. Some of the major phenomena that have been addressed include:

- The role of dislocation mechanisms in strain hardening [55–57].
- Dislocation pattern formation during monotonic and cyclic loading.
- Dislocation-defect interaction problems, including dislocation-void interaction [58], dislocation-stacking fault/void-clusters interaction in irradiated materials and the role of dislocation mechanisms on the formation of localized shear bands [59].
- Effect of particle size on hardening in metal-matrix composites [60].
- Crack tip plasticity and dislocation-crack interaction [61, 62].

- The role of various dislocation patterns such as geometrically necessary boundaries (GNBs) in hardening phenomena [70].
- Plastic zone and hardening in Nano-indentation tests [71, 72].
- The role of dislocation mechanisms in increased strength in nano-layered structures.
- High Strain Rate Phenomena and shock wave interaction with dislocations.

2.10. Molecular Dynamics

MD simulation is a technique for computing the equilibrium and transport properties of a classical many-body system. This is one of the important simulation techniques that is being used for studying the fundamental properties of dislocations and their role in plasticity of materials. MD simulations are carried out for understanding the properties of assemblies of molecules in terms of their structure and the microscopic interactions between them. We provide a guess at the interactions between molecules, and obtain predictions of bulk properties [67, 73, 74]. Essentially these simulations act as a bridge between theory and experiment.

MD simulation consists of the numerical, step-by-step, solution of the classical equations of motion, which for a simple atomic system may be written as

$$m_i \times \vec{r_i} = f_i \tag{2.19}$$

$$f_i = -\frac{\partial}{\partial r_i} U \tag{2.20}$$

For this, calculations have to be done for the forces f_i acting on the atoms, and these are usually derived from a potential energy $U\left(r^N\right)$, where $r^N = (r_1, r_2, ...r_N)$ represents the complete set of $3N$ atomic coordinates [74].

2.10.1. Molecular Interactions

The part of the potential energy $U_{non-bonded}$ representing non-bonded interactions between atoms is traditionally split into 1-body, 2-body, 3-body . . . terms

$$U_{non\,bounded}(r^N) = \sum_i u\left(r_i\right) + \sum_i \sum_{j>i} v\left(r_i, r_j\right) \tag{2.21}$$

The $u(r)$ term represents an externally applied potential field or the effects of the container walls; it is usually dropped for fully periodic simulations of bulk systems. Also, it is usual to concentrate on the pair potential $v(r_i, r_j) = v(v_ij)$ and neglect three-body (and higher order) interactions.

2.10.2. Methodology of MD

MD simulations are in many respects very similar to real experiments. In real experiment, we prepare a sample, connect this sample to a measuring instrument, and measure the property of interest during a certain time interval. If measurements are subject to statistical noise then longer we average the more accurate is our measurement becomes. In a MD simulation, we follow exactly the same approach. First, we prepare a sample, select a model system consisting of N particles and solve Newton's equation of motion for this system until the properties of the system no longer change with time. After equilibration, we perform actual measurement. In fact, some of the most common mistakes that can be made when performing a computer experiment are very similar to the mistakes that can be made in real experiments. These include, sample being not prepared correctly, measurement being too short, or not measuring what we think to measure.

The simple MD program is constructed as follows:

1. Read in the parameters that specify the condition of the run (*e.g.* initial temperature, number of particle, density, time step).
2. Initialize the system (*i.e.*, we select the initial positions and velocities).
3. Compute the forces on all particles.
4. Integrate Newton's equations of motion. This step and the previous one make up the core of the simulation. They are repeated until one has computed the time evolution of the system for the desired length of time.
5. Compute and print the averages of the measured quantities, and stop.

2.10.3. Initialization

Positions and velocities to all the particles in the system should be assigned to start the simulation. The particle position should be chosen compatible with the structure to simulate.The

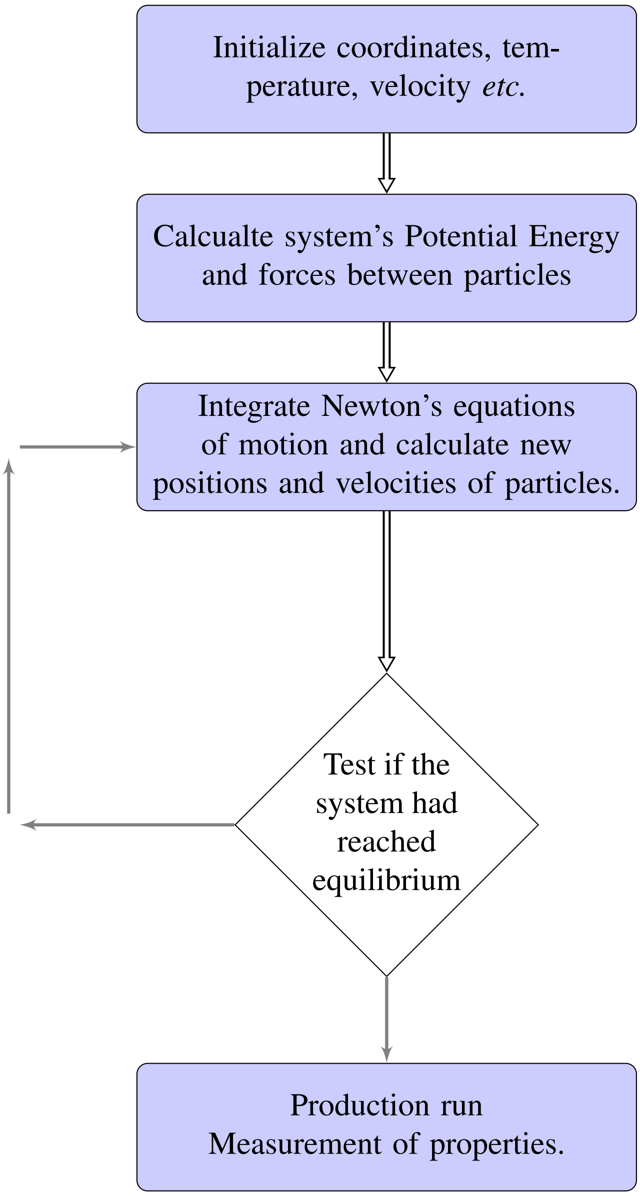

Figure 2.17: Flow chart for MD simulation

velocities are shifted such that the total momentum is zero and the velocities are scaled to adjust the mean kinetic energy to the desired value. In thermal equilibrium, the following relation should hold:

$$\left\langle v_{\alpha}^{2}\right\rangle = \frac{k_B}{m} \tag{2.22}$$

where v_α is the α component of the velocity of a given particle. The instantaneous temperature at time t ($T(t)$) can be defined as

$$k_B T\left(t\right) \equiv \sum_{i=1}^{N} \frac{m v_{\alpha,i}^{2}\left(t\right)}{N_f} \tag{2.23}$$

2.10.4. Force Calculation

The calculation of forces on every particle is the most time consuming part of MD simulation. If we consider a model system with pair wise additive interactions we have to consider the contribution to the force on particle i due to all its neighbors. If we consider only interaction between a particle and the nearest image of another particle, this implies that, for a system of N particles, we must evaluate $N \times \left(N-1\right)/2$ pair distances.This implies that time needed for the evaluation of the forces scales as N^2. There exist different techniques to speed up the evaluation of both short range and long-range forces in such a way that computing time scales as N, rather than N^2 [73].

2.10.5. Integrating the Equations of Motion

After computing all forces between the particles, we integrate Newton's equations of motion. Algorithms have been designed to do this. Verlet algorithm is usually the best.

$$r\left(t+\Delta t\right) + r\left(t-\Delta t\right) = 2r\left(t\right) + \frac{f\left(t\right)}{2m}\Delta t^{2} + O\left(\Delta t^{4}\right) \tag{2.24}$$

$$r\left(t+\Delta t\right) \approx 2r\left(t\right) - r\left(t-\Delta t\right) + \frac{f\left(t\right)}{2m}\Delta t^{2} \tag{2.25}$$

The estimate of the new position contains an error that is of the order Δt^4, where Δt is the time step of our MD scheme.The velocity can be derived from the knowledge of the trajectory, using

$$v\left(t\right)=\frac{r\left(t+\Delta t\right)+r\left(t-\Delta t\right)}{2\Delta t}+O\left(\Delta t^{2}\right) \tag{2.26}$$

It is possible to cast Verlet algorithm in a form that uses positions and velocities computed at equal times. This velocity Verlet algorithm looks like a Taylor series expansion for the coordinates:

$$r\left(t+\Delta t\right)=r\left(t\right)+v\left(t\right)\Delta t+\frac{f\left(t\right)}{2m}\Delta t^{2} \tag{2.27}$$

where the update of the velocities is given by

$$v\left(t+\Delta t\right)=v\left(t\right)+\frac{f\left(t+\Delta t\right)+f\left(t\right)}{2m}\Delta t \tag{2.28}$$

In this algorithm, we can compute the new velocities only after we have computed the new positions and, from these the new forces. Now that we have computed the new positions, we discard the positions at time $(t-\Delta t)$. The current positions become the old positions and the new positions become the current positions. After each time step we compute the current temperature, the current potential energy and the total energy. The total energy should be conserved.

2.10.6. Boundary Conditions

Small sample size means that, unless surface effects are of particular interest, periodic boundary conditions need to be used. Consider 1000 atoms arranged in a $10\times10\times10$ cube. Nearly half the atoms are on the outer faces, and these will have a large effect on the measured properties. Even for 100^3, the surface atoms amount to 6 percent of the total, which is still nontrivial. Surrounding the cube with replicas of itself takes care of this problem. Provided the potential range is not too long, we can adopt the minimum image convention that each atom interacts with the nearest atom or image in the periodic array. In the course of the simulation, if an atom leaves the basic simulation box, attention can be switched to the incoming image. This is shown in Figure

That is, if atoms in the computational cell have positions r_i, the periodic boundary condition also produces mirror images of the atoms at the positions defined as $\overset{\rightarrow image}{r_i} = \overset{\rightarrow}{r_i} + l\mathbf{a} + m\mathbf{b} + n\mathbf{c}$, where **a**, **b**, **c** are vectors that correspond to the edges of the box, l, m, n are any integers from $-\infty$ to $+\infty$. Each particle in the computational cell is interacting not only with

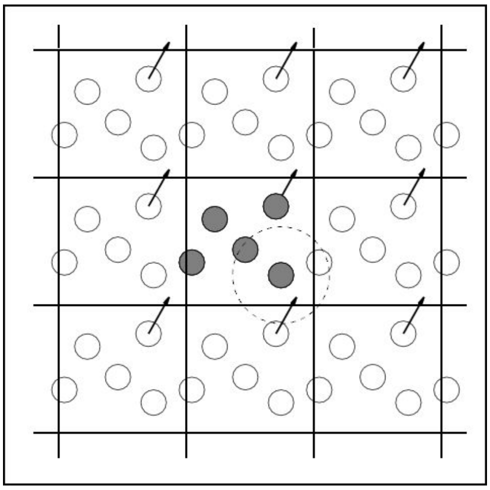

Figure 2.18: Periodic boundary conditions - As a particle moves out of the simulation box, an image particle movesin to replace it.

other particles in the computational box, but also with their images in the adjacent boxes.

The size of the computational cell should be larger than $2R_{cut}$, where R_{cut} is the cutoff distance of the integration potential. In this case any atom i interacts with only one image of any atom j. It does not interact with its own image. This condition is called “minimum image criterion”.

2.10.7. Ensembles

Ensemble is a set of all states, which a system can acquire with keeping some macroscopic parameter constants.

In the micro canonical, or NVE ensemble, the system is isolated from changes in moles (N), volume (V) and energy (E). It corresponds to an adiabatic process with no heat exchange. A micro canonical MD trajectory may be seen as an exchange of potential and kinetic energy, with total energy being conserved.

In the canonical, or NVT ensemble, moles (N), volume (V) and temperature (T) are conserved. It is also sometimes called constant temperature MD (CTMD). In NVT, the energy of endothermic and exothermic processes is exchanged with a thermostat. A variety of thermostat methods is available to add and remove energy from the boundaries of an MD system in a more or less realistic way, approximating the canonical ensemble. Popular techniques to control temperature include velocity rescaling, the Nose-Hoover thermostat, Nose-Hoover chains, the Berendsen thermostat and Langevin dynamics. In the isothermal-isobaric, or NPT ensemble, moles (N), pressure (P) and temperature (T) are conserved. In addition to a thermostat, a barostat is needed. It corresponds most closely to laboratory conditions with a flask open to ambient temperature and pressure.

2.10.8. Limitations of MD

MD like every other computational methods comes with some limitations and restrictions.The major limitations of MD are

- Need for sufficiently realistic interatomic potential functions to start with. Potentials used reflect what we really know fundamentally about the chemical bonding of the system we want to study. MD is very much dependent and quite sensitive to the interatomic potential used.
- Time scale constraints. The major challenge in MD simulations is in the time scale, because most of the processes of interest and experimental observations are at or longer than the time scale of a milli-second.In order to resolve atomic level vibrations MD time step is required to be of the order of one-hundredth of a pico second.Such higher time scales requires robust system requirements which are not always feasible.
- The algorithm is entirely classical entirely based on Newtonian mechanics. As such, it misses relativistic and quantum effects. Below the Debye temperature, quantum effects become important. For quantum dynamical properties outside of thermal equilibrium, or even for evaluating equilibrium time-correlation functions, the treatment based on MD algorithm becomes very complex.

CHAPTER 3

Experimental Methods

3.1. Materials

Essentially Zr based alloys (Zircaloy-2, Zircaloy-4, and Zr-2.5%Nb) were employed in different parts of the present work. The chemical composition, pre treatment, processing *etc.* of the samples have been given in detail in the context where they appear in the thesis. In general, majority of these samples were received from the various stages of the fabrication flow sheets of the Zr components from NFC, Hyderabad. Depending on the requirement these have been subjected to further TMPs such as cold/hot deformation and recrystallization, or grain growth annealing details of which are given in appropriate places of the thesis.

3.2. Hydriding

Gaseous hydrogen charging system with constant volume was used for charging the samples. The system consisted of a quartz tubes to hold the specimen, a uranium trap for oxygen, a vacuum pumping system (turbo molecular pump with a backing rotary pump), a capacitance based manometer and a resistance heated furnace to heat the specimen to desired temperature, see Fig. 3.1 for more details. It is to be noted that entire gas line for hydrogen charging was made up of quartz to ensure minimum contamination from the system. A high purity hydrogen gas from a cylinder was connected to the system after achieving required vacuum (of the order of 1×10^{-7} torr). Unlike electrolytic charging and $LiOH$ autoclaving, this is a contamination free process and ensures uniform hydrogen absorption [34]. Hydriding was carried out at $380°$C. The purpose of choosing this temperature had been to prevent any significant microstructural changes in the sample during the process of hydrogen charging. The apparatus was purged with the hydrogen before starting the heating of sample. This helps removing of any traces of oxygen *etc.* present in the specimen chamber and thus minimizes the chances of unintentional oxidation of the sample. The drop in the pressure of hydrogen (ΔP), was taken as measure of hydrogen absorbed the sample and the process was stopped when predetermined amount of pressure drop was achieved. The actual concentration of hydrogen in the sample (C_H) with a mass (M_s) can be calculated as

$$C_H = \frac{Z(\Delta P)V}{M_s RT}, \tag{3.1}$$

in which V represents volume of the specimen chamber, R universal gas constant, T the absolute temprature at which hydrogen charging was done.

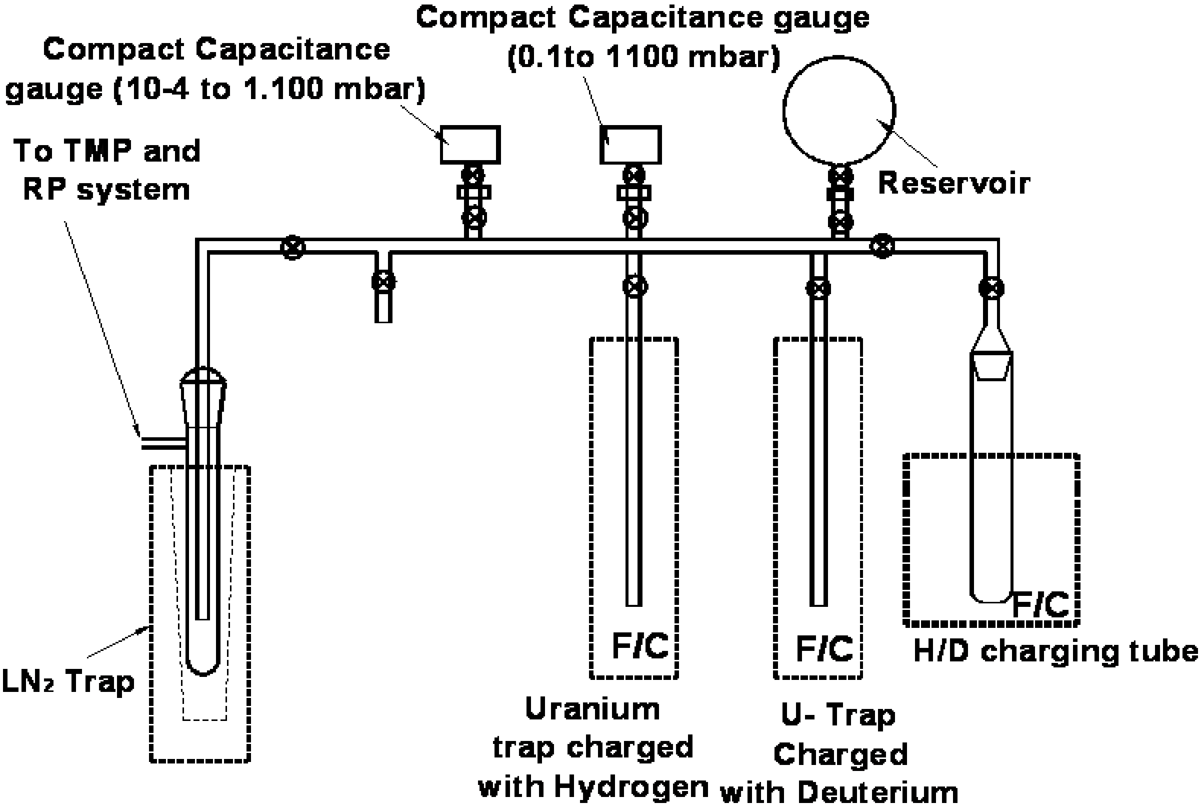

Figure 3.1: Schematic of hydrogen charging setup used in the present study.

3.3. Deformation

The present investigations have used different modes of deformations *viz* rolling, uni-axial compression for the purpose of investigating the orientation sensitive deformation behavior and twin nucleation criteria respectively. Deformation by rolling was performed using a laboratory rolling mill. In case of hot rolling of samples the samples were jacketed using mild steel pipes to prevent oxidation. For the purpose of determining the flow properties, as a precursor to the *in-situ* neutron diffraction and deformation studies (described in subsequent sections) Instron mechanical testing system was employed.

3.4. Microtexture (EBSD)

The samples were prepared by standard metallographic technique followed by electro polishing to remove the superficial deformed layer (to improve the quality of Kikuchi Pattern). Electro Polishing was done at 5°C with an operating voltage of 21 V in an electrolyte of 90% methanol and 10% perchloric acid for about 60 seconds for each sample. The polishing was performed using a commercial electro-polisher LectroPol®. An Scanning Electron Microscope (SEM) based EBSD was used for micro texture study. FEI- Quanta 3D microscope with TSL-OIM system mounted on it was used for EBSD measurements. A tilt of 70° was used for the sample with respect to electron beam axis to capture the Kikuchi Patterns by the CCD camera. A working distance of 10mm was employed for the recording of the EBSD maps. For the analysis of the EBSD data, grain identification was done using a grain tolerance angle of 5°. The remnant plastic strains inside the deformed grains was indirectly correlated with GAM. GAM for each grain is estimated by finding out the misorientation between all of the neighboring pixels of that grain. The average of these all misorientations represents the GAM for that grain. The mean GAM for the selected area of the EBSD map then is estimated by taking either area based average or number based average of individual grains' GAM values. For the purposes of analysis, all the raw measured data sets were subjected to clean up based on the confidence index (CI). Only those data points which exceeded a CI cutoff value of 0.1 were included in the analysis.

3.5. TEM studies

Thin slices of samples were cut and small discs of 3mm were punched. Punched samples were further thinned by jet polishing at $-40°C$, using a solution of 20% perchloric acid and 80% methanol as electrolyte. This made the sample electron transparent. JOEL 2000Fx, FEI-Technai, TEMs were used for TEM studies.

3.6. In-situ Neutron Diffraction and Deformation Studies

A dedicated Time of Flight neutron transmission diffraction instrument, ENGINE-X of ISIS, based on spallation source was employed for the *in-situ* neutron diffraction studies. Table 3.1 gives some of the technical details of the instrument. Simultaneous loading and recording of the diffraction spectra from the sample allowed evaluation of the evolution of intragranular strains as a function of applied load on the samples. The measurement of the strains by this instrument is based on the following principle.

- The spallation source of the instrument produces short pulse of neutrons of various energy levels.
- The generated neutrons are made to impinge onto the sample and undergo diffraction with the crystallographic planes of the sample.
- The diffracted neutrons then arrive at a detector positioned at a distance and scattering angle from the sample. The time at which a neutron is detected by the detector corresponds to the energy (or equivalently velocity) of the neutrons. Thus the arrival time of the neutron (t) is indication of the energy of the neutron which in turn determines its wavelength from which one can arrive at the d-spacing of the diffracting plane using Bragg' law.

$$t = L/v = \lambda(m_n L/h), \tag{3.2}$$

where m_n is the neutron mass (1.67×10^{-27} kg) and h is Plank's constant (6.63×10^{-34} J) and L is the total length of neutron's flight path from the pulse source to detector (typically 10 to 100m). The detector at a fixed scattering angle of 2θ thus counts neutrons as function of time. Diffraction peaks occur when Bragg's conditions is satisfied

$$\lambda = 2d_{hkl}\sin(\theta). \tag{3.3}$$

Hence the relation between the inter-planar spacing d_{hkl} and the peak with position T is

$$d_{hkl} = \frac{th}{2m_n L\sin(\theta)}. \tag{3.4}$$

Eq. 3.4 forms the basis of the measurement of intragranular strains using this technique. The measured values of d_{hkl} of specimen can be compared with the strain free reference values of d^*_{hkl} to arrive at the lattice strains as below.

$$\epsilon_{hkl} = \frac{d_{hkl} - d^*_{hkl}}{d^*_{hkl}}. \tag{3.5}$$

In order to accurately estimate the peak parameters (position, FWHM, Integrated intensity *etc.*) reitveild refinement procedure was followed. The analysis of the diffraction data was performed by 'open genie software', an open source Reitveild refinement software developed by ISIS for the neutron diffraction data analysis [75].

Table 3.1: Technical details of the ISIS- Engine X instrument

Description	Details
Primary flight path	50m
Secondary flight path	1.5m
Choppers	Disc choppers at 6.4m and 9.6m
Detectors	$\pm 90°$ diffraction banks, ZnS scintillators, $3mm$ horizontal resolution. 10×10 pixel transmission detector ($2.5mm$ square pixel pitch)
Detector Coverage	$2q = 76°$ to $104°$
Vertical coverage	$\pm 21°$
Wavelength Range	0.5-6 Å
Incoming collimation - vertical	$0.2 - 20mm$
Incoming collimation - horizontal	$0.2 - 10mm$
Outgoing collimation - horizontal	$0.5,\ 1,\ 2,\ 3$ or $4mm$

3.7. X-ray Florescence Spectroscopy (XRF)

For characterizing the composition of the Zr-Sn binary alloys which were synthesized for the *in-situ* neutron diffraction studies, XRF was used. This technique is a preferred way of compositional analysis due to the fact that elemental identification is done by the wave length of the characteristic X-rays and signal is obtained from a larger area of the sample (typically few square centimeters). These two characteristics make this technique ideal for getting accurate average composition in a relatively short time.

CHAPTER 4

Identification and Quantification of Variant Selection During $\beta\rightarrow\alpha$ Phase Transformation

4.1. Introduction

One of the important stages of fabrication of any Zr based components is beta quenching treatment [3, 12]. This operation is yet another crucial operation that has bearing on the final microstructure and texture of the Zr based components. This treatment is normally applied for ensuring homogeneous composition and randomizing the texture, after breaking of the cast structure of the ingots [76]. The texture randomization requires formation of as many α phase variants as possible from the parent β grains and also as small β grains at the soaking temperature as possible. Thus β quenching process optimization and its tailoring to achieve the desired goals requires knowledge/understanding of the prior β grains size and extent of variant selection during the actual $\beta \rightarrow \alpha$ phase transformation in the quenching operation. This is the reason for such a wide range of studies on this phase transformation in Zr [10].

The subject of phase transformation, in general, and more specifically the topic of variant selection have been areas of active research for past several decades [10]. Phase transformations are expected to obey certain orientation relationships (ORs) [17]. For a variety of reasons, all the variants corresponding to such ORs may not be observed with equal probability [10, 20, 21, 77, 77–80]. This brings us to the topic of variant selection - a topic which can be used effectively to bring out underlying mechanisms of phase transformations [10, 20, 21, 80–82]. The biggest limitation of any research on microstructural developments through phase transformation is in experimental difficulties of viewing both pre and post transformed structures [83]. An appropriate heating-cooling stage can provide an alternative [83]. However, measurements are never instantaneous and are mostly restricted to the surface. Volumetric measurements using synchrotron and neutron are relatively cumbersome and can't be carried out on a routine basis [84]. Another alternative is to preserve or decorate the high temperature structures [77]. Such an alternative is specific to a system and is possible only in specific metallic materials. In this context it is highly useful to have a generalized scheme/methodology by which one can reconstruct the pre-transformed microstructure along with its local orientation information (*i.e.*) microtexture. Such a parent phase reconstruction methods in fact do exist and they exploit the measured local crystal orientation/micro texture of the product phase. Following is the brief review of the existing methods based on which a new algorithm has been developed in the present work.

4.2. Existing Methods of Parent Phase Reconstruction

There have been two different methods: (i) neighbor-to-neighbor [20, 21] and (ii) groupoid [26, 27, 85, 86]. Though the approaches can be used/adopted for any phase transformation, subsequent description is tailored more towards $\beta \rightarrow \alpha$ (bcc $\rightarrow$ hcp) transformations typical of Zirconium (Zr) and Titanium (Ti). The OR for such transformation is Burgers, where $\{0001\}_\alpha \parallel \{110\}_\beta$ and $\langle 110\rangle_\alpha \parallel \langle 111\rangle_\beta$ [20, 21, 87]. As per this OR, a single β grain can transform into twelve crystallographic variants of α, while the inverse transformation of $\alpha \rightarrow \beta$ has six α variants [20, 22]. If one expresses the crystallographic orientation and Burgers transformation in terms of respective rotation matrices, the effect of inverse transformation on the α orientation is mathematically equivalent to multiplication of its orientation matrix by suitable transformation matrix or operator. Since there are six equivalent transformation matrices or operators, each product α grain can have six possible β orientations. Both (i) and (ii) are based on this general principle, though subsequent reconstruction algorithm differs. In (i) clusters of neighboring α grains are identified based on their probability to have a common parent β. The probability is decided firstly by a local (neighbor-to-neighbor) minimization of misorientation of the calculated β variant. Subsequently, the solution is refined by the minimization of global misorientation through iterative Monte-Carlo approach [20]. This was historically the first, and relatively simple conceptually, and was tested with reasonable success in Ti [20, 21]. The approach can, however, lead to erroneous reunification of grains belonging to different parents at higher angular tolerances [26, 27, 85, 86]. Arguably in the diffusional transformations the misorientation developments may not approach such higher tolerances, but this may not be the case for displacive phase transformations. To circumvent this problem, the second or the groupoid approach was proposed [26, 27, 85, 86]. The groupoid structure is formed by the variants and their operators. The method consists of searching a triplet of neighboring product grains, which satisfies groupoid composition with a very low ($\leq 3°$) tolerance angle. Then the triplet is made 'nucleus' and is grown by considering its neighbors obeying certain conditions of coherence. The process is repeated until no new nucleus can be found. This is an iterative process and expected to be 'time consuming'. With such a background, the need for a faster and accurate method of automated reconstruction appears warranted. This was the motivation behind the present work. The computational speed would depend on the appropriate conceptualization - simplification without compromising the actual physics. The new algorithm developed as part of the present thesis is described in the next few paragraphs.

4.3. New Algorithm for Automated Reconstruction of Parent Phase

The first step is to process the EBSD data of the product (e.g. hcp α) phase. Following are the necessary steps:

- Raw data needs to be free from wrongly indexed points. If such points exist, appropriate clean-up(s) needs to be conducted. The orientation data representation is reduced to the minimum Euler space required by the symmetry of the product phase to avoid redundancy in orientation description [20].

- A data set is created from the refined EBSD data, containing unique grain IDs $G_i = 1, 2, 3, ...$ average grain orientation and grain IDs of all neighboring grains. A grain, in a standard EBSD program, is identified from the continuous presence of a boundary exceeding a specified misorientation - which was taken in this work as 5°.

Rest of the proposed algorithm (also shown in Fig. 4.1) can be described in the following steps:

1. Consider a product grain $\boldsymbol{G}_i$ (where $i = 1, 2, 3, ...$) has $\boldsymbol{G}_{i+1}, \boldsymbol{G}_{i+2}, ...\boldsymbol{G}_{i+N}$ as its neighbors - see Fig. 4.1a. Fig. 4.1b shows possible triplets containing $\boldsymbol{G}_i$ and its neighbors with the condition that each grain of the triplet is neighbor to other two. In the limiting case of all the neighbors of the $\boldsymbol{G}_i$ being neighbors to each other, ${}^N\boldsymbol{C}_2$ number of triplets are formed. In general, however, the number of triplets will be much smaller.

2. For grains in a given triplet find all possible parent orientations

$$\boldsymbol{B}_{li}^{\beta} = \boldsymbol{T}_{l}^{\alpha \rightarrow \beta} \boldsymbol{G}_{i}^{\alpha} \tag{4.1}$$

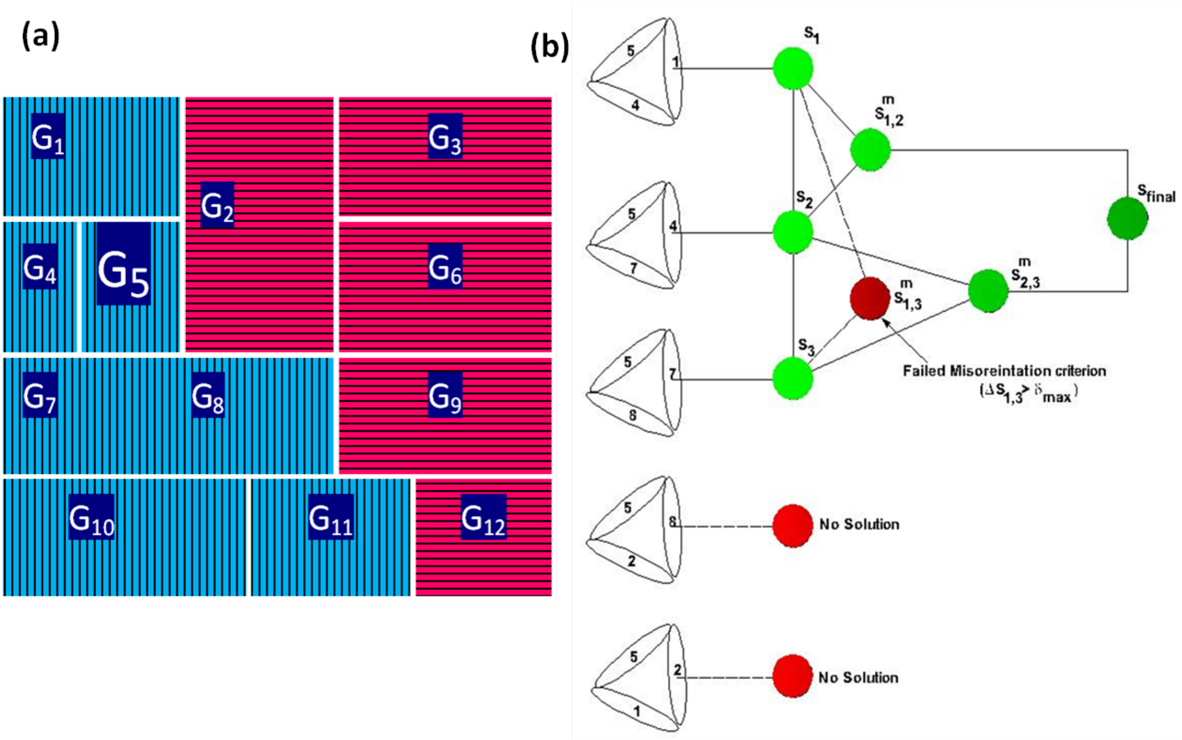

Figure 4.1: (a) Schematic showing the product α grains. Grains belonging to common parent β are marked with the same color. Subscripts (G_i) indicate the product grain IDs. (b) Adopted algorithm. Let $G_i = 5$. Neighbors of G_5 are G_1, G_2, G_4,G_7 & G_8. The triplets formed by G_5 are $[5, 1, 2]$, $[5, 2, 8]$, $[5, 8, 7]$, $[5, 7, 4]$ and $[5, 4, 1]$. Note that all the three grains of these triplets are neighbors to each other. Triplets either have a common parent variant, *i.e.*, a 'potential' solution for the parent β, or 'no solution'. Next step is to link the 'potential' solutions through a generalized misorientation criterion.

where,

$$\boldsymbol{T}_l^{\alpha\rightarrow\beta} = \boldsymbol{D}^{-1}\boldsymbol{S}_{1...6}^{\alpha} \tag{4.2}$$

in which $\boldsymbol{S}_{1...6}^{\alpha} = (E_\alpha, C_{6z+}, C_{3Z+}, C_{21+}, C_{22+}, C_{23+})$ are six of the hexagonal symmetry operators, see Table 2.3, $\boldsymbol{D}$ is the matrix representing Burgers OR for $\alpha \rightarrow \beta$ and $i = 1..3$ are the grain IDs in the selected triplet, $\boldsymbol{B}_{li}$ is the parent orientation for the product orientation of $\boldsymbol{G}_i$.

3. The common solution to all the three grains in a triplet is selected as a potential solution. In case of no such common solution, it is inferred that the grains of the triplet are not from a common parent.

4. These steps are repeated for all triplets of $\boldsymbol{G}_i$, yielding, say n, potential solutions for G_i. In the ideal case, all the potential solutions of $\boldsymbol{G}_i$ should be identical. However, due to transformation strains and measurement uncertainties there could be misorientations among the potential solutions. In order to assign an 'optimum' solution to $\boldsymbol{G}_i$, the computer program finds the mean solution ($S_{k,l}^m$) and mis-orientation($\Delta S_{k,l}$) between each pair of the potential solutions: $\boldsymbol{S}_k$, and $\boldsymbol{S}_l$ where k and l run from 1 to n.

$$\boldsymbol{S}_{k,l}^m = mean(\boldsymbol{S}_k, \boldsymbol{S}_l), \forall\, k \neq l \tag{4.3}$$

$$\Delta S_{k,l} = cos^{-1}\left(\frac{Trace\left(\boldsymbol{S}_k\boldsymbol{S}_l^{-1}\right) - 1}{2}\right), \forall\, k \neq l \tag{4.4}$$

Reject any $S_{k,l}^m$ for which $\Delta S_{k,l}$ is more than user specified maximum misorientation tolerance (δ_{max}) . Final solution (S_{final}) for G_i is the mean of all $S_{k,l}^m$ weighted by $W_{k,l}$ (weightage factor for $S_{k,l}^m$).

$$\boldsymbol{S}_{final} = \sum_{k=1}^{n-1}\sum_{k=l+1}^{n}\left(W_{k,l}\boldsymbol{S}_{k,l}^m\right), \forall\, \boldsymbol{S}_{k,l}^m < \delta_{max} \tag{4.5}$$

in which,

$$W_{k,l} = \frac{(\delta_{max} - \Delta S_{k,l})}{\displaystyle\sum_{k=1}^{n-1}\sum_{k=l+1}^{n}(\delta_{max} - \Delta S_{k,l})} \tag{4.6}$$

As can be seen, the weightage factor ($W_{k,l}$) formulation ensures higher weightage to those potential solutions ($\boldsymbol{S}_k$ and $\boldsymbol{S}_l$) which are closer to each other (with increased probability of being the correct solution). In case of failure to find the solution to any grain in the above step (for example, a grain is embedded inside a larger grain), the solution(s) obtained from its neighboring grains is/are used. Similar weightage factor approach is used to ascertain the parent grain orientation in such case(s).

It is to be noted that in the above formulation, all the orientations are expressed in their rotational matrices notation. However, in general, the EBSD measurements are stored in the form of more popular Euler angle [88] notation. Following is the conversion of Euler angles into corresponding rotational matrix notation.

$$\begin{aligned}
g_{11} &= (+\cos\phi_1\cos\phi_2 - \sin\phi_1\sin\phi_2\cos\phi)\\
g_{12} &= (+\sin\phi_1\cos\phi_2 + \cos\phi_1\sin\phi_2\cos\phi)\\
g_{13} &= (+\sin\phi_2\sin\phi)\\
g_{21} &= (-\cos\phi_1\sin\phi_2 - \sin\phi_1\cos\phi_2\cos\phi)\\
g_{22} &= (-\sin\phi_1\sin\phi_2 + \cos\phi_1\cos\phi_2\cos\phi)\\
g_{23} &= (+\cos\phi_2\sin\phi)\\
g_{31} &= (+\sin\phi_1\sin\phi)\\
g_{32} &= (-\cos\phi_1\sin\phi)\\
g_{33} &= (+\cos\phi)
\end{aligned} \tag{4.7}$$

For automated reconstruction, the algorithm described above was implemented in MATLAB®. The program uses post-transformation EBSD data and appropriate OR along with δ_{max} as inputs. As shown in Fig. 4.2, the program could successfully compute the expected (based on the IQ map) pre-transformation microstructure. A worked example of the algorithm has been presented in Appendix-I in which main parts of the algorithm have been explained in more detail.

4.4. Application of Algorithm for Reconstruction in Case of Zr

The present algorithm was tested for different $\beta \rightarrow \alpha$ transformations in a commercial Zircaloy 4 (1.32 wt% Sn, 0.20 wt% Fe, 0.1 wt% Cr, Hf $<$ 50 ppm, balance Zr). The alloy samples were processed in three different ways in the β phase field: (a) furnace cooling, (b) water quenching,

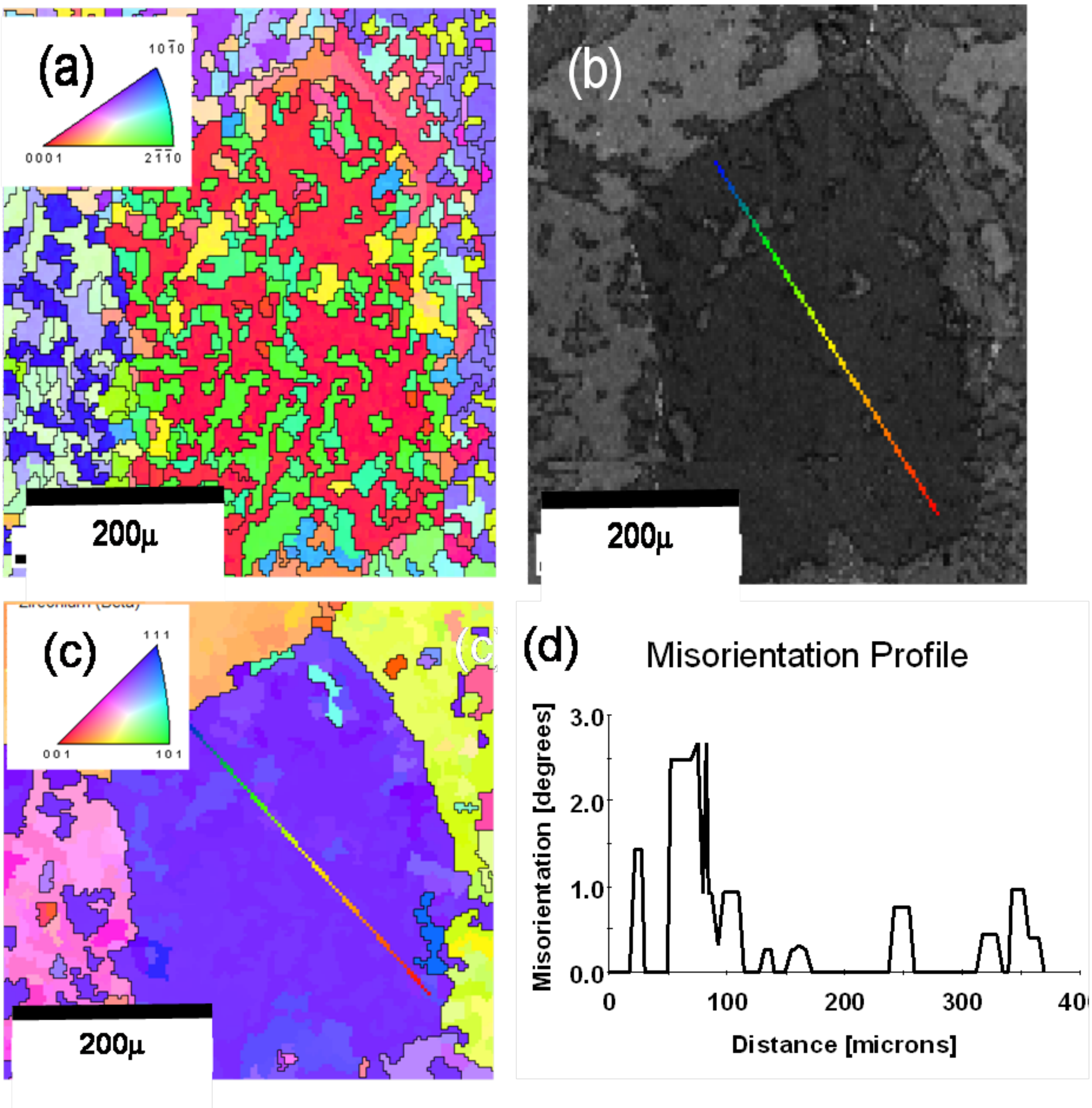

Figure 4.2: (a) IPF representation of α-Zr (post-transformation) microtexture. (b) IQ map of (a). IQ map, in this case, delineated the prior β structure. (c) IPF of α-Zr (pre-transformation) microtexture - reconstructed using an angular tolerance (δ_{max}) of 3°. Notice the similarity between b and c. (d) Misorientation in a single reconstructed β grain - along the line shown in b & c. Relatively minor misorientations indicate the success of the present automated reconstruction.

and (c) solidification from liquid state. The latter was achieved in a water cooled electric arc furnace. Different transformation mechanisms, from reconstructive to displacive [10, 17], and correspondingly different microstructures were obtained, see Fig. 4.3. As shown in Fig. 4.3, in all three cases the algorithm of reconstruction was quite successful. This is confirmed by the correct sequence of β grain sizes (expected from the thermal history of the samples) shown in reconstructed maps. Sample (c) having its β structure inherited directly from liquid shows the largest β grains. Sample (a), having spent considerably higher time in β phase field due to slow cooling, shows comparatively larger β grains than the sample (b). The three cases, however, had clear differences in misorientation developments of the reconstructed β microstructures. This is easily represented by the Kernal Average Misorientation (KAM) values, which is a measure of average local misorientation, relative to immediate neighbors [89]. KAM values increased systematically, in the reconstructed β, with increased cooling rates: 0.32°, 0.51° and 0.81°. A KAM value of 0.4° is observed in fully recrystallized samples, using the same beam and video conditions, and hence can be taken as measurement uncertainty. In other words, the automated reconstruction was not only successful for different $\beta \rightarrow \alpha$ transformations/microstructures in Zr (Fig. 4.3), but also could bring out clear developments in KAM at higher cooling rates. Higher cooling rates and displacive nature of phase transformations may lead to the formation of variants misoriented from their ideal orientations. By solving independently the product grain triplets to ‘optimum’ parent grain orientation(s), the present approach appears to capture possible effects of transformation strains.

4.5. Advantages of the Present Method

Significant improvements in quality, and in scope, of parent structure predictions, over the previous methods, are achieved. These can be summarized as:

- weighing each potential solution by its misorientation effectively neutralizes the deviations caused by transformation strains,
- internal consistency check of the predicted parent solutions by comparing different potential solutions,
- higher tolerance to experimental errors as potential solutions are linked together by the respective weightage factors

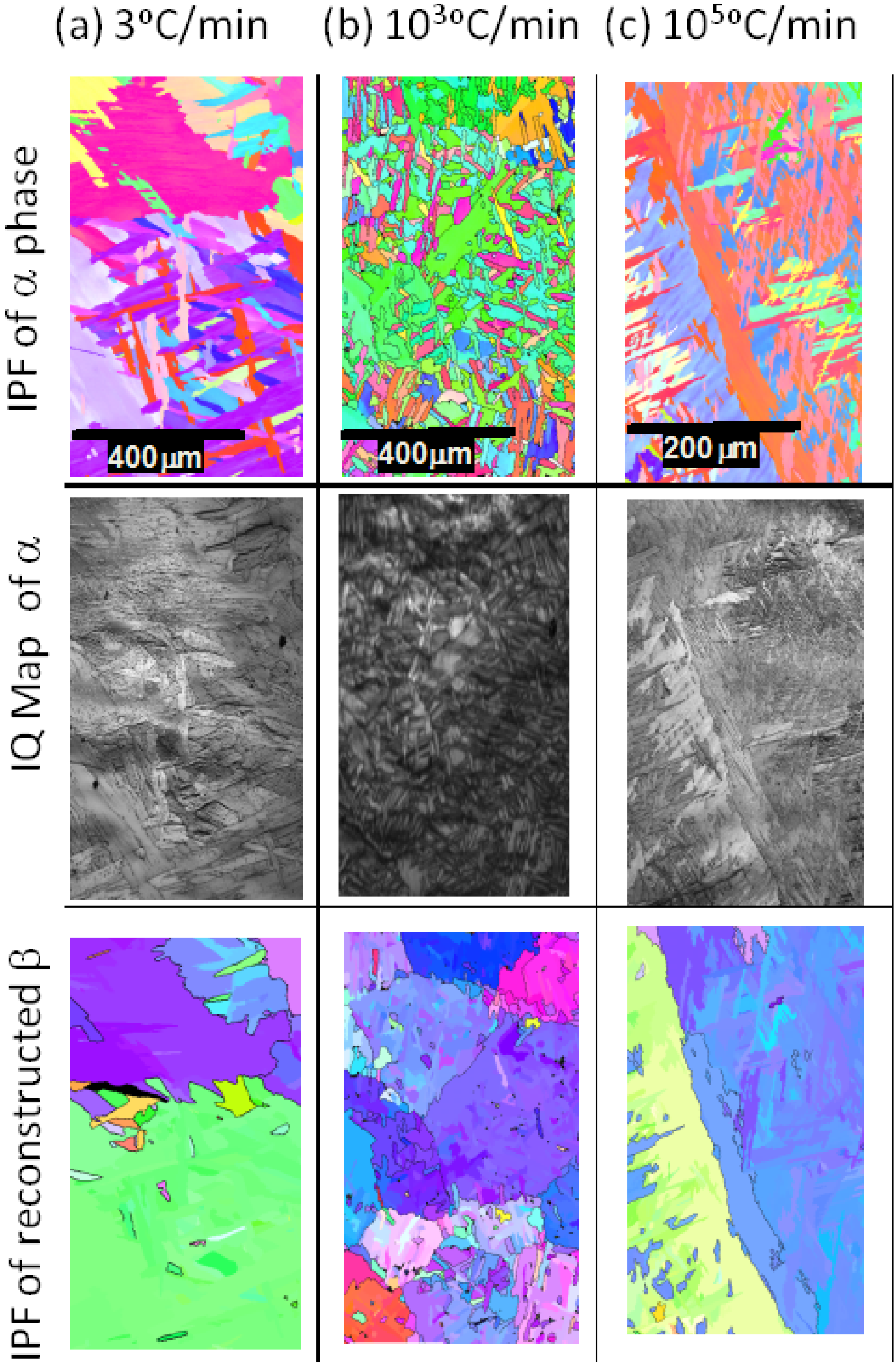

Figure 4.3: Post-transformation α-Zr IPFs, IQ maps and corresponding reconstructed β-Zr IPFs. α-Zr structures were obtained by using three different cooling rates : $3, 10^3$ and 10^5 °C min^{-1}. An angular tolerance or $\delta_{max} = 3°$ was used for the reconstruction.

- less sensitivity to user defined maximum misorientation tolerance (δ_{max}) on the quality of reconstruction as illustrated in Fig 4.4.

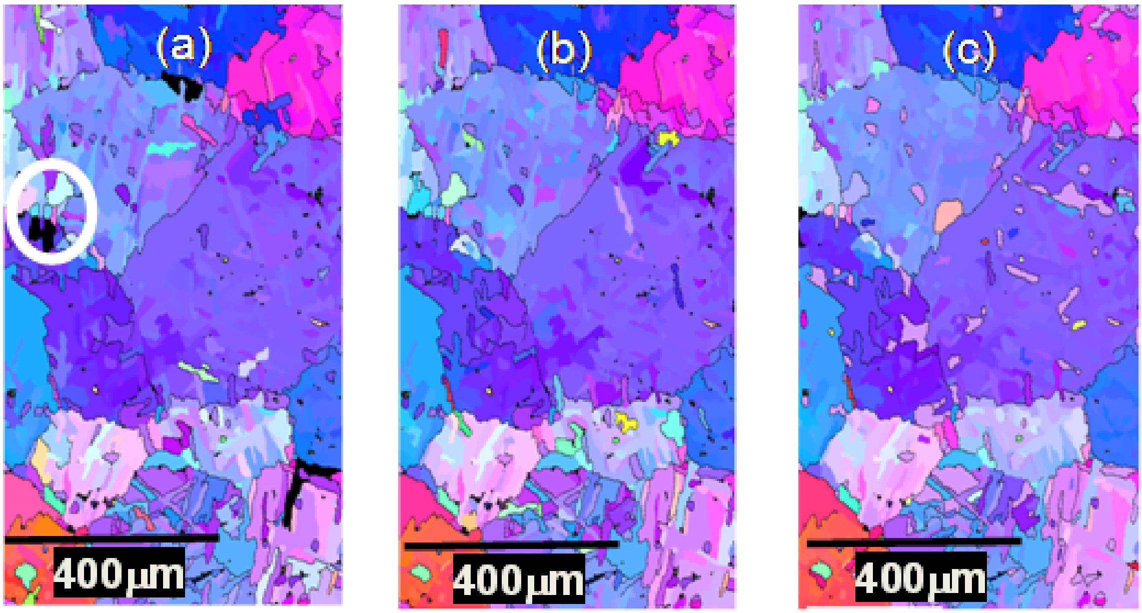

Figure 4.4: Role of the user defined tolerance angle (δ_{max}) on the reconstructed maps. It is evident that tolerance agle effect is rather low. (a), (b) and (c) correspond to δ_{max} of 3°, 5° and 10° respectively. The circled region (a) represents the unsolved portion of the microstructure due to too low value of δ_{max}.

Another main advantage of the present algorithm is its computational efficiency. One needs to evaluate the possible parent variants for each product grain only once. Then the common solution is selected for each triplet. Using 1000 Zr_α grains as input, the present method of reconstruction of the Zr_β microstructure took 10 minutes on a desktop computer having a 3.2 GHz processor and 1 Gb RAM. This is definitely faster than the earlier [20, 26] methods. In the present method both computation time and memory requirement scales linearly with the number of product grains (N). Memory requirement of the computationally efficient [20] neighbor-to-neighbor method scales with N^2. Though memory requirement, with appropriate connectivity tables, can be reduced; still it will be significantly higher than the present algorithm.

The earlier models [20] were based on the identification of the possible parent(s) and then subsequent optimization for the probable solution. In contrast, the present approach solves each product grain to its ‘optimum’ parent orientation pseudo independently of others, see Fig. 4.1. This solution is obtained through ‘grouping’ certain number of neighboring product ($\alpha - Zr$)

grains. Considering triplets is adequate for the $\alpha \rightarrow \beta$ transformation in Zr which involves only 6 variants. For transformations involving more variants, *e.g.* ferrite to austenite transformation in steel, groupings of neighbor product grains might have to be extended beyond 3. Pseudo-independent solutions for parent orientation(s) also brings in clear possibilities of massive parallelization.

The fact, that a solution is obtained by solving multiple neighboring product grains in conjunction, virtually eliminates the possibility of artificial reunification of grains belonging to different parents. The estimated [26] probability of two randomly oriented grains having an accidental misorientation equal to one of the Burgers operators is, approximately, 10% at 5° tolerance. In a triplet this probability is reduced further to 0.1%. This can, arguably, be reduced further by extending the triplets to quadruplets. This was, however, considered unnecessary in the present study. The present method thus combines the merits of the previous algorithms: simplicity of neighbor to neighbor correlation [20] with the accuracy of triplets based solution of the groupoid method [26] with a novel misorientation based criterion to arrive at 'optimum' reconstruction of the pre-transformation microtexture.

4.6. Variant Selection in $\boldsymbol{\beta} \rightarrow \boldsymbol{\alpha}$ Transformation

As explained in the previous section, 12 possible α variants can form from a single β grain while reverse transformation of $\alpha \rightarrow \beta$ involves 6 possible β variants. Once the parent phase orientations were identified, using the just mentioned approach, it is easy to identify the type of α variants produced during the phase transformation from the β field. This can be achieved by following methodology.

- For each of the product grain, G_α apply a rotation by the inverse of its corresponding parent orientation G_β.

$$\boldsymbol{G}_\alpha^{Rotated} = \boldsymbol{G}_\beta^{-1}\boldsymbol{G}_\alpha. \tag{4.8}$$

- Find which of the 12 possible variants of the Burgers operator ($\boldsymbol{T}_{i=1..12}^{\beta\rightarrow\alpha}$) matches with the $\boldsymbol{G}_\alpha^{Rotated}$. This is the identity of the α variant.

Fig. 4.5(c) shows the various variants formed during the transformation (identified by just mentioned methodology) of the β phase during the water quenching from β phase field. Also shown in the figure is the frequency distribution of the variants (4.5(d)). It is clear that the distribution points towards high degree of variant selection during the phase transformation. It may be pointed out that this work brought out the direct evidence of the variant selection (previous studies have shown the indirect evidences of the variant selection by bulk textural measurements of high temperature and room temperature phases and calculating the transformation texture [90, 91]).

The direct consequence of this variant selection is of course on the misorientation distribution profile or grain boundary texture distribution. Fig. 4.6 shows the actual mis orientation profile along with expected misorientation profile for a random distribution of the crystals (Mackenzie distribution for hexagonal system [92, 93]). As can be observed from the figure, there are some specific misorientations (highlighted with circles in the figure) which exist in a proportion far more than what is expected from a corresponding random distribution. Partly this is due to the fact that only few mis orientations are possible among different product variants generated from the product phase. In addition, occurrence of the variant selection introduces further deviation of the misorientation profile from the ideal expected distribution. Some of the possible reasons for the observed variant selection include (a) Local stresses generated due to the influence of the neighboring grains (b) Grain size of the parent phase (c) Distribution and interaction of the dislocations. Understanding which of these mechanisms is the controlling factor in the present case requires further study. In case of martensitic transformation of Ni-Ti and Zr alloys it has been shown that the martensite variants form in a self accommodating morphology [10]. It has been shown that the stress/strain fields of the variants interact with each other and result in a net drop of the elastic energy of the system. In such circumstances, the number of possible variants gets reduced because of requirement of stress accommodation leading to the observed variant selection. Further increase in the variant selection tendency can happen if there are externally imposed stress fields. This can happen in case of samples undergoing simultaneous plastic deformation as well as transformation.

4.7. Conclusions

1. An efficient algorithm for the reconstruction of high temperature β phase from the micro-texture data of the room temperature α phase of Zr had been developed and shown to be working in different modes of $\beta \rightarrow \alpha$ phase transformations.

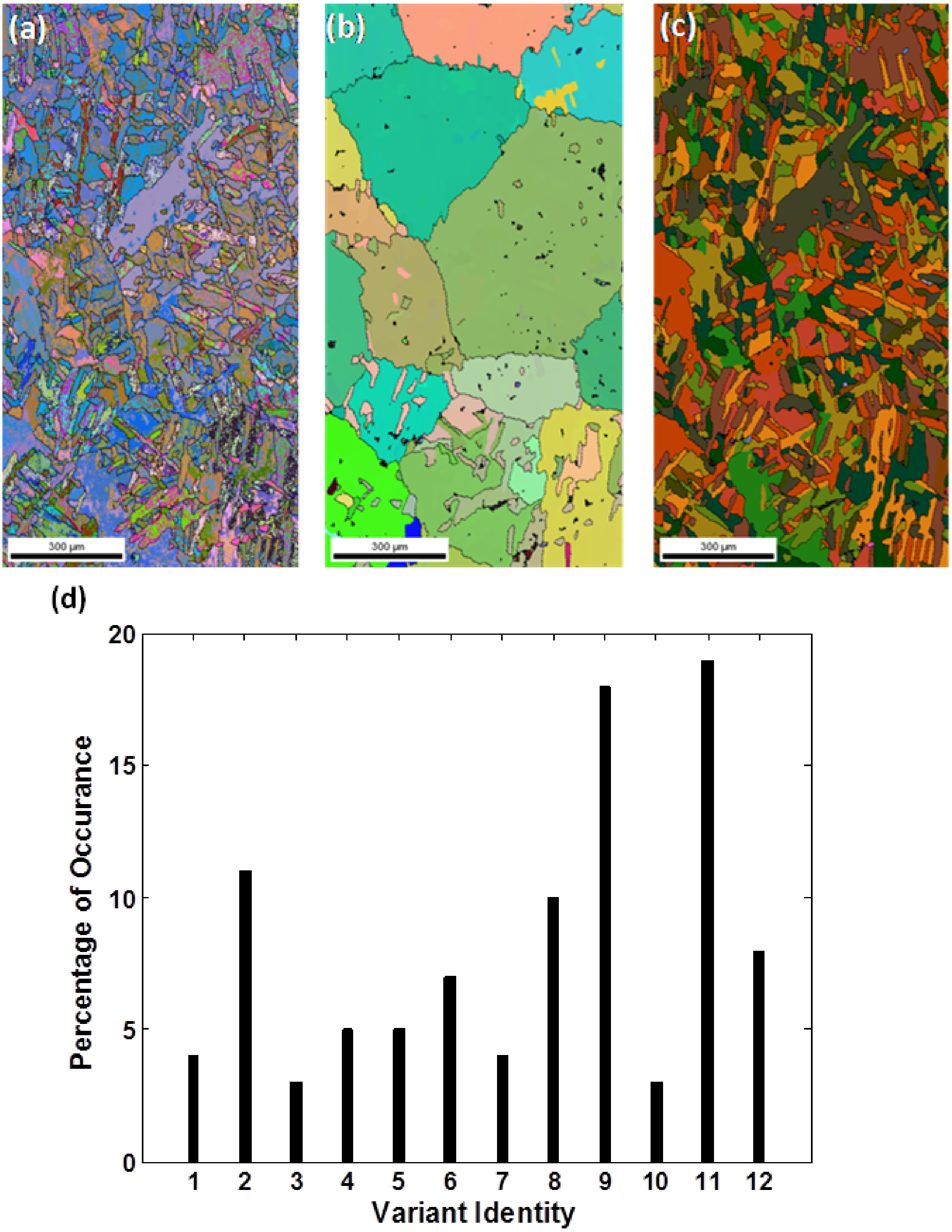

Figure 4.5: (a) EBSD microstructure of beta quenched microstructure of Zircaloy-4 showing α grains. (b) The reconstructed map of parent phase (β) (c) Microstructure of product (α) phase with each product grain colored according to its variant identity (d) Frequency distribution of product variants.

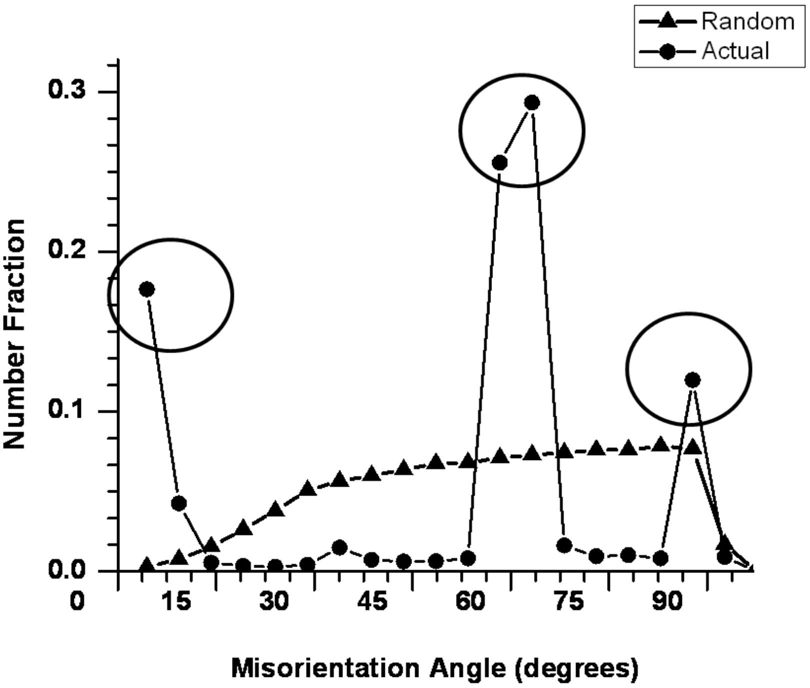

Figure 4.6: Misorientation distribution profile for the Zircaloy -4 sample subjected to β quenching. Also shown is the misorientation distribution for a random textured sample of hexagonal crystal system. The circles mark the specific misorientations which far exceed random distribution values.

2. The algorithm uses a novel weightage factor for arriving at an optimized solution for the parent phase orientation by considering the misorientation among the potential solutions obtained using various triplets of the neighboring product grains.

3. Using the algorithm, it had also been demonstrated that exact identification and hence quantification of the variant selection during the $\beta \rightarrow \alpha$ phase transformation is possible.

CHAPTER 5

Role of Orientation in Hydride Formation ($\alpha \rightarrow \delta$ Transformation) in Dual Phase Zr alloy

5.1. Introduction

Hydride phase formation is of interest both academically and industrially in case of zirconium based alloys. Its academic interest stems from the fact that it is a result of behavior of two widely different elements Zr and H. While former is of high atomic weight, the latter is a highly mobile low atomic weight species. Consequenctly their behavior is expected to be widely differnt during the phase transforamtion [10]. Its industrial importance arises due to the deleterious effects of hydride phase on the mechanical properties of the Zr based structural components used in nuclear reactors [28, 94]. In order to minimize such hydride induced degradation, it is desirable to develop optimized microstructures which can mitigate the problem of damage due to hydride formation to a reasonable extent [33]. Development of 'hydride embrittlement' resistant microstructures, requires an understanding of the effect of microstructural parameters such as phase distribution, morphology *etc.*, on the formation of hydrides. In particular, knowledge of the role of second phase (β) on the precipitation behavior of the brittle hydrides is of much practical and scientific interest. Thorough understanding of the changes in hydride formation mechanism because of the presence of the second phase can help tailor the microstructures for a better 'hydride embrittlement' resistance.

Earlier studies have shown the grain boundaries to be preferential sites for the hydride formation, particularly under conditions of slow cooling relevant to nuclear reactors [29]. However, most of these observations are valid in case of hydride precipitation in the single phase Zr alloys such as Zircaloy-2 and Zircaloy-4 [29, 95–103]. Some limited studies have shown that the α/β interfaces act as preferential sites for the precipitation of the hydrides in case of the two phase Zr alloys such as Zr-2.5%Nb alloy [104–106]. However, such studies largely depended on the TEM and/or optical microscopic examinations for the characterization of the hydrides

Table 5.1: Composition of the alloy used in the present study.

Element	Nb	O	H	N	Zr
Amount by weight	2.5%	1100 ppm	<5 ppm	30 ppm	Balance

and matrix microstructures. It was shown that OR (orientation relationship) derived from optical microscopy is different from what is observed at a higher resolution in TEM [28, 107]. On the other hand, observations from TEM have the limitations of statistical validity. In order to address these issues (of accurate determination of OR with improved statistics) and bring out the role of interfaces on the hydride precipitation, SEM based EBSD technique is employed in the present study for the characterization of the hydrides. Following important issues are being addressed in this present work.

- The role of orientation and interfaces of the α and β phases on the formation and growth of the hydrides,
- The reasons, if any, for the preference of hydrides for specific boundaries/interfaces.

Zr-2.5%Nb alloy (two phase alloy containing hcp-α and bcc-β) has been selected as candidate material to meet the above objectives. A detailed characterization of the hydrided microstructures was carried out using the conventional techniques of optical and TEM along with extensive EBSD.

5.2. Experimental

The composition of the Zr-2.5%Nb alloy used in the present study is shown in table 5.1. The alloy samples were subjected to 58% cold deformation by pilgering, followed by annealing at 700°C for 14 days. The objective was to get equiaxed microstructure of the constituent phases, with beta grains at the tri-junctions of the alpha grains. Such microstructure is expected to have significant amount of special interfaces (interfaces with specific misorientations) whose role on hydride formation is interesting to study. The details of the hydriding scheme can be found in Chapter 3. Samples were charged to nominal hydrogen levels of 200 and 300 ppm (by weight).

5.3. Results

5.3.1. Distribution and Nature of Hydrides

Fig. 5.1 shows the distribution of the hydride phase in the Zr-2.5%Nb alloy sample with 300 ppm of hydrogen. The matrix microstructure essentially consisted of equiaxed grains of α phase with relatively large β grains at the tri-junctions of the α grains. Such a structure was a result of prolonged annealing at 700°C for a period of 14 days following cold deformation. Grain sizes of the α phase were in the range of 5-10μm. β phase grain size ranged from 3 to 7μm. The relative volume fractions of the α and β phases in the samples were 0.83 and 0.17 respectively. The hydrides in these samples were observed to be predominantly located along the interface boundaries of the α and β grains. The size of the hydrides was of the order of 5 to 10μm along the length.

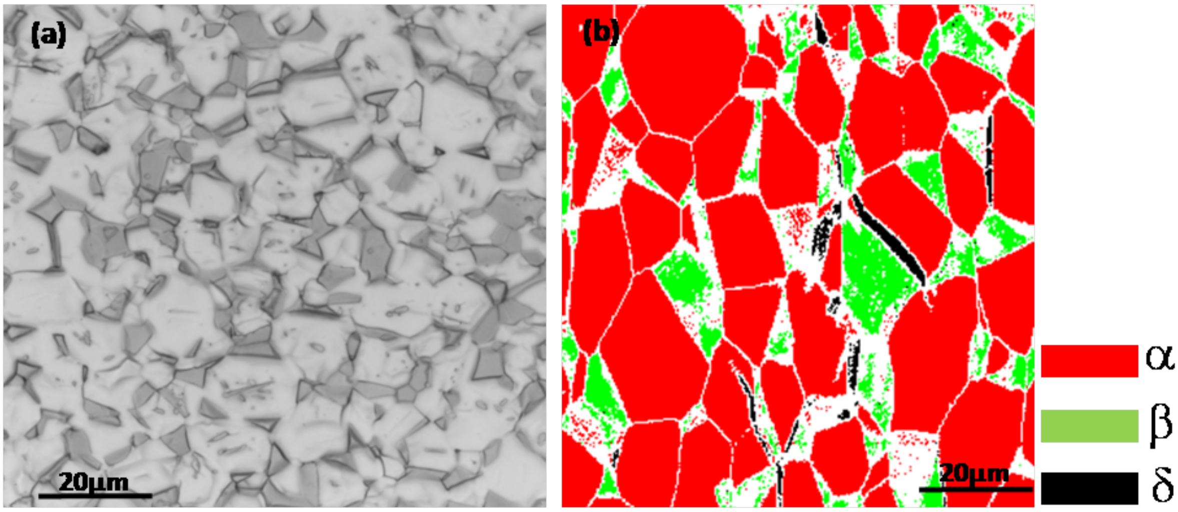

Figure 5.1: (a) Optical and (b) EBSD micrographs showing the distribution of the hydrides in Zr-2.5%Nb alloy charged with 300 ppm (by weight) of hydrogen.

The thickness of the hydrides on the other hand, ranged from 0.5 to 2μm. Some minor fraction of the hydrides were observed to have formed inside the α grains (intra-granular hydrides) and along the α/α grain boundaries as well. Morphology of the interface hydrides was evidently very different from that of the intra-granular hydrides. While the former followed the contours of the α/β interface, latter have formed in sharp and straight needle like fashion along specific crystallographic planes. Though the formation of the hydrides was predominately along the α/β interface, their growth was always into adjacent α grain only. Interestingly, even though there are a considerable number of α/α grain boundaries present in these two phase samples,

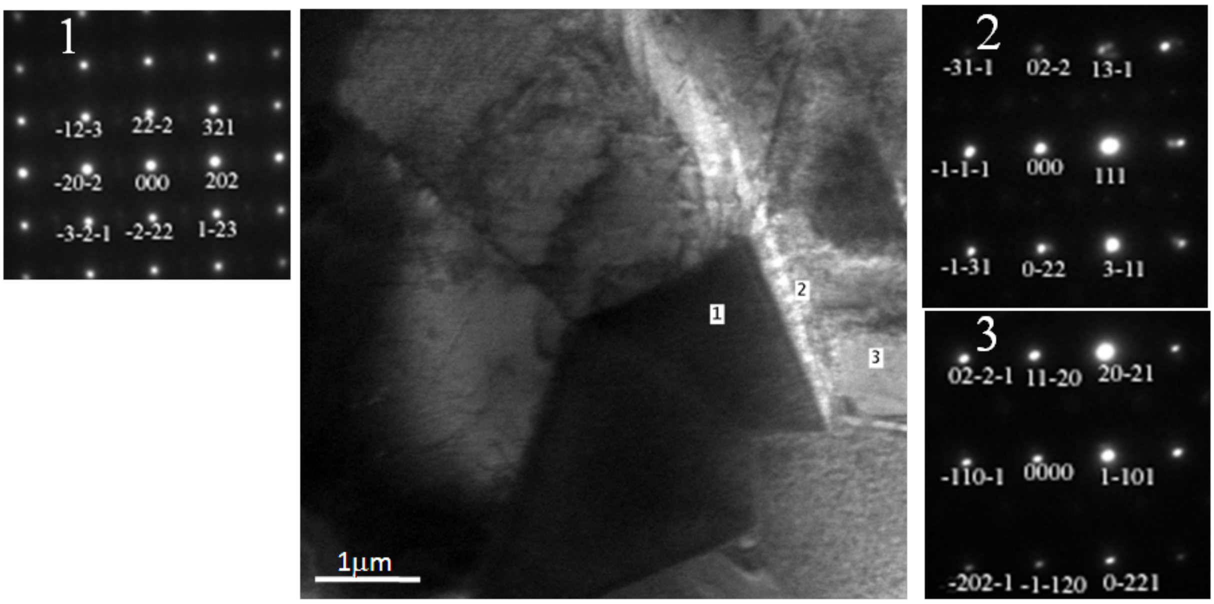

Figure 5.2: TEM micrograph showing the presence of the hydride (marked as 2) along the α/β interface. β and α are marked as 1 and 3 respectively. Diffraction patterns from the different regions (marked with the numbers) are superimposed.

a majority of the hydrides have formed along the α/β interfaces only. No major differences in the crystallographic or morphological features of hydrides in samples with 200 and 300 ppm hydrogen were observed. Hence results from only 300 ppm samples are presented and are valid for samples with 200 ppm hydrogen as well.

EBSD had confirmed that the hydrides formed in these samples were of "δ" type which is an equilibrium hydride phase in the Zr-H system with a composition $ZrH_{1.5}$. Since the δ-hydride is the dominant hydride formed under reactor operation conditions (relatively slow cooling), the observations of the present study bear more practical significance. TEM characterization of the hydrided samples had further confirmed that the α/β interface is the most preferred site for the hydride formation in these samples, see Fig. 5.2. TEM also had shown that, though hydrides had formed along the α/β interface, they had grown into adjoining α grains only. Further, the δ and β interface was more sharper and showed relatively less strain contrast in comparison to the corresponding δ/α interface as can be observed from Fig. 5.2. The diffraction patterns recorded in the TEM also had confirmed the hydrides to be equilibrium δ-hydride. Super imposition of the diffraction patterns from α, β and δ-hydride phases indicated that they are having OR with each other.

5.3.2. Microtexture of the Hydrides

EBSD measurements of the orientations inside the hydride phase have indicated that even the largest hydrides (observed in this study) which were of nearly $10\mu m$ in length were having single orientation with an orientation spread not exceeding 2°. This is in contrast to the previous studies which have reported that most of the large hydrides which are visible under optical microscope were actually stacks of several hydride plates in succession [107, 108]. The nature of the α/δ and β/δ interfaces are shown in terms of the respective misorientation distribution function (MODF) plots in the Fig. 5.3. An MODF plot is a graphical representation of the presence (or lack) of preference of grain/interface boundaries with reference to what is expected from a random distribution of boundaries [88]. The nature of a boundary can suitably be represented by the misorientation of the grains forming the boundary (expressed by angle/axis pair). As can be seen from the Fig. 5.3(a), there is a strong OR between the α-Zr and δ-hydride, as indicated by the maximum intensity value of 21 times to the random distribution. The observed OR corresponds to

$$\{0001\}_\alpha \parallel \{111\}_\delta$$
$$< 2\bar{1}\bar{1}0 >_\alpha \parallel < 110 >_\delta .$$

It may be emphasized that this OR was arrived at by analyzing a number of hydrides in a two phase zirconium alloy using the EBSD information (with higher statistical validity), and is in agreement with the previous studies based on TEM observations [28, 105, 106] and other EBSD based studies of single phase zirconium alloys [100–102]. The OR between the β phase and δ-hydride, on the other hand, is not as strong, see Fig. 5.3(b), maximum MODF intensity being close to 8 times to the random distribution. Analysis of individual interface hydrides had shown the presence of following OR (with considerable scatter of 20°) between the β and δ-hydride.

$$\{011\}_\beta \parallel \{111\}_\delta$$
$$< 100 >_\beta \parallel < 110 >_\delta$$

Since TEM as well as EBSD results have shown conclusively, that the hydride phase was growing only into the adjoining α grains but not into the β phase, existence of the OR between the δ-hydride and β phase is somewhat surprising and shall be discussed in detail in the next section.

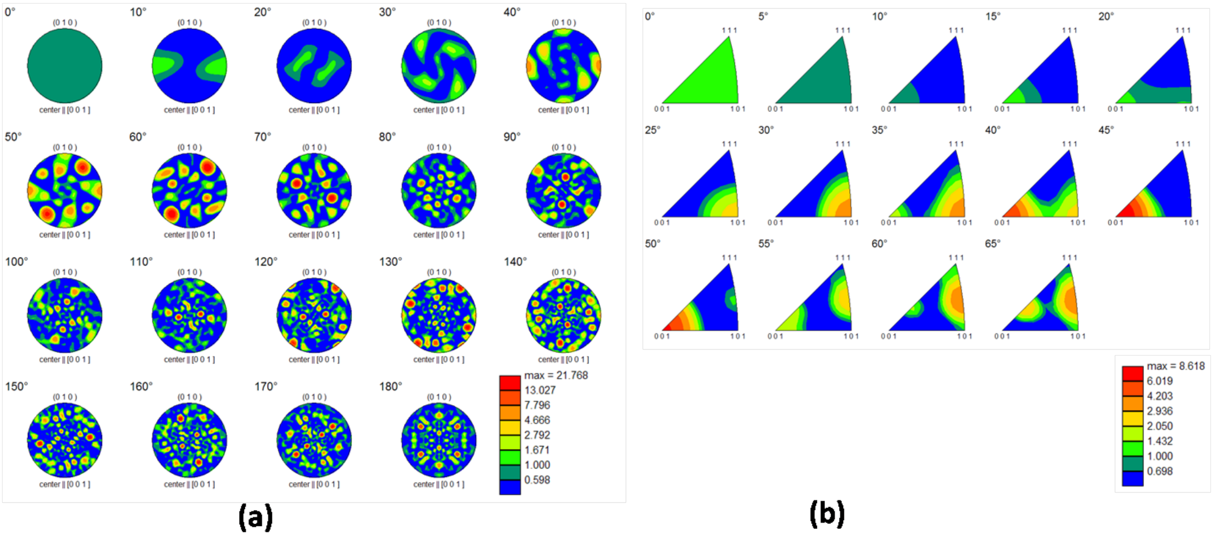

Figure 5.3: (a) Misorienation distribution function plot (MODF) for the α and δ - hydride boundaries.(b) MODF for the β and δ - hydride boundaries.

The three phases *i.e.*, α, β and δ-hydride had clear difference in their in-grain misorieantion profiles. This is clearly shown in Fig. 5.4, which is a plot of grain average misorientation (GAM) distribution in the different phases. GAM is a measure of extent of remnant plastic strain in the grains. Under the measurement conditions of the EBSD used in the present study, 0.3° of error in orientation measurement is to be expected, which can be taken as the cut off for the presence or absence of remnant plastic strain. The plot clearly shows that the GAM distribution of β phase is lowest and is close to machine error, indicating virtually strain free β grains. In contrast δ-hydride shows highest development in GAM suggesting towards accumulation of considerable plastic strain inside it. α phase on the other hand, showed GAM distribution intermediate to the former two phases. Present study, thus, provides a quantitative measure of strain partitioning between the various phases arising out of transformation strain caused by hydride precipitation. The observed strain partitioning could be attributed to selective partitioning of hydride transformation strains to α phase in preference to β phase. Since the formation of the $ZrH_{1.5}$ involves a volume expansion of 17%, considerable plastic strain is expected both in the hydride as well as the α grains into which it was growing. These observations, are in line with the TEM observations which indicated absence of any significant strain at the β/δ interface, Fig. 5.2.

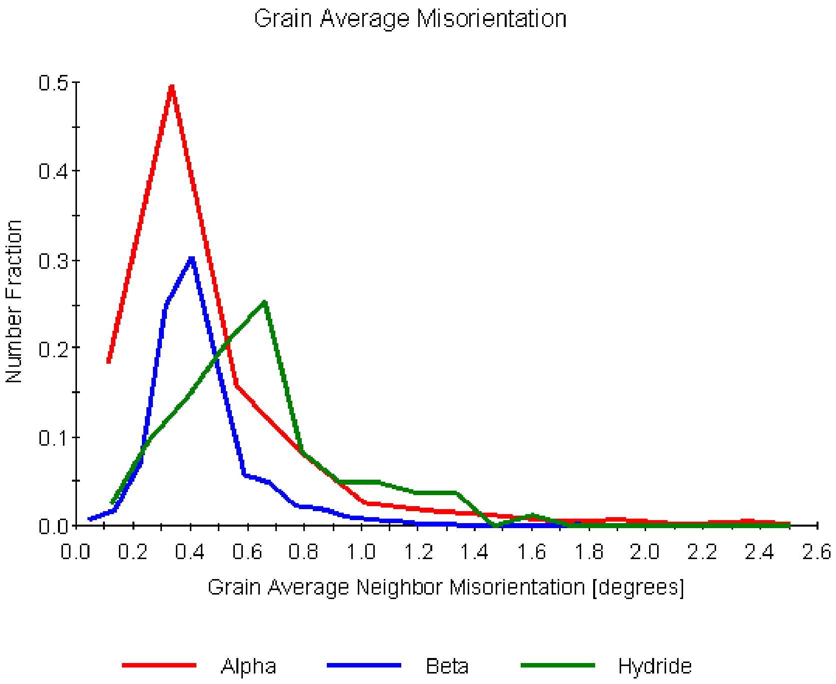

Figure 5.4: Grain average misorientation (GAM) distribution in α, β and δ - hydride phases.

5.3.3. Preference of Hydrides for Specific α/β Interfaces

The results presented so far have unequivocally confirmed the formation of the hydrides preferentially along the α/β interfaces. However, in order to investigate if all of the α/β boundaries (characterized by their misorientation expressed in angle/axis pair) have equal probability of hydride formation, specific boundaries are superimposed on the EBSD-phase map as shown in the Fig. 5.5. The blue lines in the figure indicate *Burger's boundaries*, *i.e.*, those α/β interfaces which have a misorientation corresponding to Burger's OR (45°@$[2\bar{1}\bar{1}0]_\alpha$ or 45°@$[001]_\beta$) within a tolerance of 10°. EBSD analysis of the, grain boundaries showed that the length fraction of such *Burger's boundaries* was 10% of the total boundary length which includes all of the α/β and α/α boundaries. If the hydrides have no specific preference to these *Burger's boundaries*, only 10% of the hydrides are expected along these interfaces. However, as shown in the Fig. 5.5, nearly all of the hydrides are located along the *Burger's boundaries* only, indicating a strong preference of the hydrides to form along the α/β interfaces which follow Burger's OR. It is also interesting to note that not all the interfaces, which are found to be following Burger's OR are having hydrides forming along them. This suggests that apart from misorientation between the α and β some additional factors govern the feasibility of hydride formation.

Boundary trace analysis was performed on the interface hydrides to determine the interface

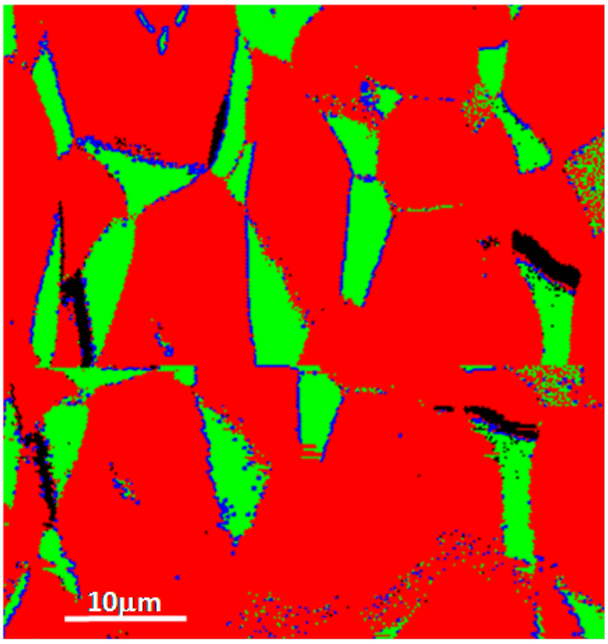

Figure 5.5: Phase map showing the interface hydrides along with the α/β interfaces following the Burgers OR within a tolerance of 10° from the ideal Burgers OR (in blue). The color scheme used for the representation of the phases is identical with that used in Fig. 5.1(b)

plane on which δ-hydride was forming. In doing this analysis it was assumed that the observed interface plane was perpendicular to the plane of measurement, *i.e.*, interface plane normal lied in the plane of the measurement. This assumption was necessitated because of 2-D nature of the EBSD measurement which does not allow knowing the tilt and twist nature of the boundary [88]. Even then, the information gained using such assumption can be useful in differentiating the hydride forming and non forming boundaries to some qualitative extent. The results of the analysis, indicated that the hydrides were growing parallel to one of the low index planes of the β phase. $(100)_\beta, (110)_\beta$ were found to be the most commonly observed β planes onto which δ-hydrides were growing. The interface plane between the α and δ-hydride, on the other hand, was found to be some what arbitrary.

5.4. Discussion

Studies aiming at the understanding of the formation of the hydrides in Zirconium alloys have largely been driven by their immense practical relevance in controlling the damage due to the hydride embrittlement. Most of such previous studies, however, have depended mainly on the optical and/or TEM techniques for the characterization of the hydrides [103–106]. With the advent of modern tool of EBSD, it is possible to revisit some of the previous observations to gain new insights in to the phenomena governing the formation of hydrides [29, 100–102]. In a recent study, extensive use of microtexture data obtained from EBSD, has been shown to give invaluable information on the role played by the special boundaries on the formation of the hydrides in case of single phase recrystallized Zicaloy-2 [29]. Investigation of the role played by the interfaces, if any, in case of two phase alloy systems on the formation of hydrides, naturally is a logical extension of such studies and thus becomes the motivation for the present study.

The main observations of the present study can be summarized as :

- Hydrides in the two phase Zr-2.5%Nb alloy in a completely recrystallized condition have formed primarily along α/β interfaces, with only a minor fraction of hydrides being along α/α grain boundaries.
- Though hydrides had a strong OR with the α phase into which they were growing, there was some apparent OR between the hydrides and β phase too.
- Majority of the hydrides were along those α/β interfaces which had a misorientation corresponding to Burger's OR. However, not all the α/β interface which are related by the Burger's OR are having the hydrides along them.
- Hydrides have grown on one of the low index planes of the β phase while their interface plane with the α phase appeared to be arbitrary.

Grain and/or phase boundaries are known to be some of the most potential sites for the heterogeneous nucleation of product phases [1, 17]. Hence the observation of the α/β interfaces to be the preferred sites for the hydride formation is not surprising. However, formation of the hydrides along α/β interfaces in preference to α/α boundaries (which are also present in significant proportion) needs to be explained. The main reason attributed for the effectiveness of the grain boundaries as potential nucleation sites is their relatively higher energy. However, in the present study, experimental evidence shows the formation of hydrides along the α/β interfaces which are related by Burger's OR. Such interfaces are expected to be low energy interfaces, due to relatively higher atomic matching across the interface [13, 109, 110]. Hence the governing factors for the selection of α/β interfaces as preferred hydride nucleation sites have to be more than mere boundary/interface energy.

In general, precipitation of a secondary phase in a two phase system depends on relative concentration, amount and solid solubilities of constituent phases in addition to nature and number of nucleation sites available for precipitation [17, 111]. In this context, spatial distribution of the hydrogen in the sample can have an important role in determining the preferred sites of hydride formation. The hydrogen charging temperature used in the present study was 300°C, which incidentally is also the operating temperature of the PHWR (pressurized heavy water reactor) reactors. At this temperature, the solid solubilities of hydrogen in β and α phases are considerably different, hydrogen being more soluble in the β phase [112, 113]. A hydrogen solubility ratio of 9 between $\beta - Zr(20\%Nb)$ and $\alpha - Zr$ was reported [114]. Such a large variation in hydrogen solubility in the constituent phases leads to considerable hydrogen partitioning between the two phases at the hydrogenation temperature. In other words, selective accumulation of the hydrogen in β phase takes place. Considering the nominal level of 300 ppm of hydrogen used in the present study, and taking the solubility of hydrogen in $\alpha - Zr$ as 60 ppm (at 300°C) [112, 114], it can be shown that only 17$\%$ of the total hydrogen will be in $\alpha - Zr$ at the hydrogenation temperature. In contrast, as high as 83$\%$ of total hydrogen will be in $\beta - Zr$ which constituted only 17$\%$ of the volume fraction of the microstructure used in the present study. When the sample is cooled, during which the hydride precipitation takes place, diffusion of hydrogen to the nearest potential nucleation site is expected to be the critical step [115]. Naturally, α/β interfaces happen to be the nearest interfaces for a majority of the hydrogen atoms due to higher concentration of the hydrogen in β grains. Further, diffusivity of the hydrogen in β phase is much higher than that in the α phase [116]. The potency of the α/β interfaces for aiding the nucleation of hydride phase is further enhanced by the fact that the β grains observed in the present study are primarily located at tri-junctions of the α grains. It is a well known fact that the tri-junctions are one of the strongest heterogeneous nucleation sites for solid state phase transformations, like precipitation [17, 111]. Since α phase does have some hydrogen dissolved in it at the temperature of hydrogenation, precipitation of hydrides along α/α grain boundaries is possible in a condition where there is no suitable α/β interface is present in the vicinity of the hydrogen atoms. This can explain the observation of a relatively small fraction of hydrides along α/α grain boundaries.

Present study had also shown that, though nucleation of the hydride takes place along the α/β interface, its growth happened only into the adjoining α grain. This can be attributed to stronger thermodynamic driving force arising out of the $\alpha \rightarrow ZrH_{1.5}$ transformation than the driving force available for $\beta \rightarrow ZrH_{1.5}$ transformation. This is a consequence of much higher affinity of hydrogen to $\alpha - Zr$ than to Nb present in β phase [112]. This implies, presence of OR between the β and δ-hydride, can't be due to $\beta \rightarrow ZrH_{1.5}$ transformation. The observed

δ/β OR can, however, be attributed to epitaxial growth of $ZrH_{1.5}$ on one of the low index planes of the β phase into the adjoining α phase. It is interesting to note that the observed $\beta(bcc)/\delta(fcc)$ OR of this study, is similar to the one reported in case of epitaxial growth of Fe (bcc) on Ag (fcc) substrate [117]. Such epitaxial growth of hydride phase on one of the low index planes of the β grains explains sharp and virtually strain free β/δ interfaces, see Fig. 5.2. This also explains why not all of the α/β interfaces have hydrides along them. It appears that only those interfaces are favorable which have one of the low index planes of the β constituting the interface. The observed OR between the interface δ-hydride and β was also a consequence of the fact that most of the α/β interfaces have Burger's OR and δ has stronger OR with the α phase.

5.5. Conclusions

In summary, present study brought out the important role played by the crystal orientation, which in turn determined the nature of interfaces, on the precipitation of hydrides making use of microtextural information obtained from EBSD. Following are the major observations

1. The study had provided the quantitative measure of strain partitioning during the formation of hydrides at the α/β interfaces. it was confirmed that the actual strain in the hydrides was rather small when they formed along the suitable α/β interfaces.

2. It was observed that hydride precipitation depends on the level of hydrogen partitioning at the hydrogenation temperature and availability of suitable β interfaces which are conducive for epitaxial growth of hydride phase in to the adjoining α phase.

CHAPTER 6

Deformation Heterogeneity in Zr : Understanding Through Discrete Dislocation Dynamics

6.1. Introduction

Plastic deformation in metallic materials is often heterogeneous [1, 118, 119]. The heterogeneity, in general, is correlated with crystallographic orientations and/or working temperatures. Temperature is known to affect slip-twin activation and in turn may influence deformation heterogeneity. Even in cubic aluminum [120], elevated temperature activation of non-octahedral slip was stipulated. For hexagonal Zirconium such activations are far more significant [39, 40, 121–123, 123, 124]. For elevated temperature deformations, further complications may arise through dynamic softening mechanisms. For example, even dynamic recovery and concurrent strain induced boundary migration were shown [125] to remarkably affect deformed microstructure developments. The effect of orientation on heterogeneous plastic deformation is also well documented. Kallend and Huang [126] had shown, in high purity copper, that X-ray peak broadening scales with Taylor factor. This was confirmed by Sam and Adams [127], and extended to low carbon steel by Rajmohan *et al.* [128]. More direct evidences from microtexture measurements were also provided by different research groups [129, 130]. It is believed that Taylor factor can provide a rough guide-line for stored energy of cold work. Orientations with high Taylor factor, in general, contain more stored energy.

Though Taylor factors of individual crystallites may offer a generalization [126–128] for the orientation dependence of stored energy, the practical picture is often more complex [118]. The deformed microstructures are expected to have mesoscale formation of near boundary gradient zones (NBGZ) [89] and various features of dislocation substructures [131]. Near neighbor incompatibilities in Taylor factors were shown [89] to influence the developments of NBGZ, while textural softening or change in Taylor factor offered explanations on the orientation and morphological angles of the microscopic shear bands.

Developments in deformed microstructures must originate from the dislocations and their dynamics. However, application of dislocation theory to the understanding of experimental observations has been relatively 'limited'. This is in spite of the large developments [61, 62, 65, 65, 67, 68, 71, 72, 132–140] in continuum based DD simulations over the past few decades. The evolving subject of DD simulations still has limitations on model assumptions and necessary computational resources. Ridha and Hutchinson's [141] study on deformed near cube orientation (100) $<$001$>$ is a notable example of the application of dislocation theory for the explanation of deformed microstructures. This work had shown that lower stored energy of near cube orientations was a consequence of non-interactions of orthogonal edge dislocations with Burgers vectors perpendicular to each other. Such examples are however, largely confined to cubic systems [65, 67, 135] with limited studies on hexagonal materials [142–144].

Hexagonal metallic materials have limited number of easy slip systems [3, 9, 39, 40, 44, 121, 123, 145, 146]. This is expected to make plastic deformation highly orientation sensitive [147]. Existence of secondary slip systems, and their temperature dependent activation, on the other hand, has the potential to reduce such orientation sensitivity. Predominantly single phase Zirconium, even in the absence of noticeable twinning, was reported [148] to show extreme heterogeneity in plastic deformation. This was shown under laboratory rolling or near PSC at room temperature. Near 'basal' oriented grains were observed to have minimal grain fragmentation and in-grain misorientation developments. They were also the orientations with negligible strain partitioning, as indicated by change in grain aspect ratio. The present study further enhances the scope of that investigation by considering: (i) possible temperature dependence and (ii) seeking explanation for the phenomenological observations through DD simulations.

6.2. Experimental & Simulation details

6.2.1. Material and Processing

Zircaloy 2, composition given in table 6.1, was used in the present study. Cast and forged Zircaloy 2 samples were subjected to 50% cold rolling. This was followed by annealing at $750°\mathrm{C}$ for 6h, to obtain a fully recrystallized microstructure. This was the starting material for 30% reduction in thickness in a laboratory rolling mill. Respective working temperatures of 25°, 200° and $400°\mathrm{C}$ (approximately 300, 500 and 700 K) were used. The samples were immediately quenched after warm rolling and no signatures of recrystallization were noted.

Table 6.1: Composition of the Zircaloy-2 used in the present study.

Element	Sn	Fe	Cr	Ni	O	H	N	Zr
Amount by weight	1.54%	0.15	0.12	0.2	1100 ppm	<5 ppm	30 ppm	Balance

6.2.2. DD Simulations

Dislocation structures

In creating the starting dislocation structure for the purpose of simulations, following experimental facts have been kept in mind.

- The deformation of Zr occurs primarily by dislocation activity on prismatic slip system ($\{10\bar{1}0\}\langle 2\bar{1}\bar{1}0\rangle$).
- At elevated deformation temperatures, pyramidal ($\{10\bar{1}1\}\langle 2\bar{1}\bar{1}3\rangle$) and basal ($\{0001\}\langle 2\bar{1}\bar{1}0\rangle$) slip systems also take part in dislocation activity [39, 40, 121, 123, 149].

In order to model deformation behavior in relevant temperature regimes (25° to $400°$C), dislocations on all three slip systems were created inside a simulation volume of approximately 10 X 10 X 10 μm^3. Though basal slip is expected to be insignificant in the temperature regime, basal dislocations were incorporated to study their effect, if any, on other mobile dislocations.

Finite segments of screw dislocations, of both $\overrightarrow{a}$ type and $\overrightarrow{c+a}$ type, were created in the simulation volume. The initial dislocation configuration(s) (see Fig. 6.1) had an approximate dislocation density of $10^{10} m/m^3$. The end points of dislocation segments (Fig. 6.1) were made immobile and hence these could act as potential Frank-Read sources. Both the location and length of these starting dislocation segments were randomly assigned. The initial density of $\overrightarrow{a}$ type dislocations was kept twice that of $\overrightarrow{c+a}$ type. Rationale behind this exercise was based on reported[150] higher densities of $\overrightarrow{a}$ type dislocations. Initial dislocation densities on all three planes (basal, prismatic and pyramidal planes) were, otherwise, kept similar. Periodic boundary conditions were used. Simulations with three random initial configurations were carried out. Fig. 6.1 shows these three configurations. Subsequently, sensitivity assessments (of DD simulation) were made with respect to all the three initial configurations.Considerable modifications were made to the DD simulation programme Paradis [132], for enabling simulations for hexagonal materials like Zr. These include, incorporating hexagonal specific slip systems, hexagonal specific mobility laws (explained in the next section). The incorporation of the slip systems was achieved by converting the usual hexagonal index systems to corresponding cartesian frame of reference. Table 6.2 illustrates various slip systems used in the present work and their actual cartesian values of Burger's vectors and slip planes.

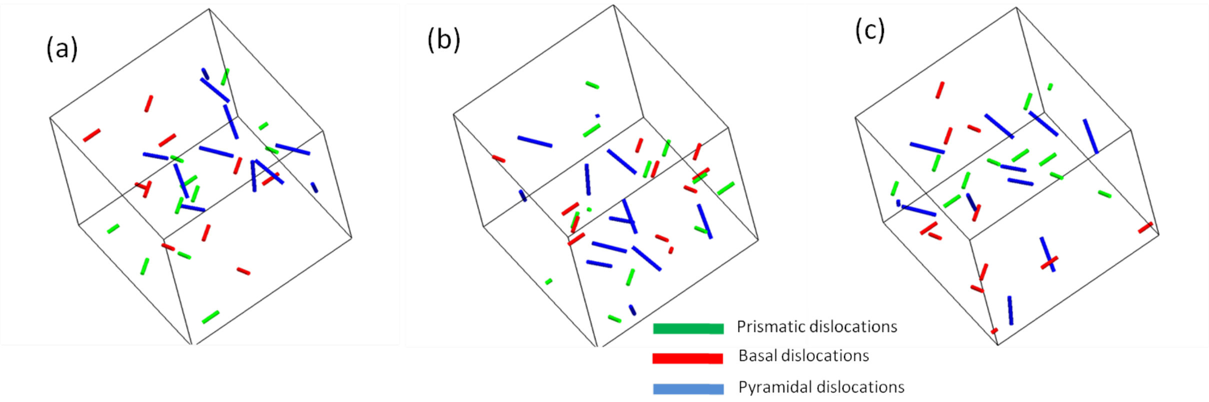

Figure 6.1: Three starting dislocation configurations (a), (b) and (c) used in the present study. Dislocations are colored according to their glide planes. Same color scheme is used throughout the manuscript.

Table 6.2: Various slip systems in their hexagonal and Cartesian notations, incorporated in the DD model of the present study.

	Hexagonal reference frame		Cartesian reference frame	
	Plane Normal $\overrightarrow{n}$	Burger's Vector $\overrightarrow{b}$	Plane Normal (Cartesian) $\overrightarrow{n}_{\mathbf{cart}}$	Burger's Vector (Cartesian) $\overrightarrow{b}_{\mathbf{cart}}$
S.No.	$[\mathbf{h\,k\,i\,l}]_{\mathbf{hex}}$	$[\mathbf{u\,v\,t\,w}]_{\mathbf{hex}}$	$[\mathbf{h\,k\,l}]_{\mathbf{Cartesian}}$	$[\mathbf{u\,v\,w}]_{\mathbf{Cartesian}}$
(1)	$[0\,0\,0\,1]$	$[1\,1\,\bar{2}\,0]$	$[-0.00\ -0.00\ +1.00]$	$[+1.615\ +2.797\ +0.000]$
(2)	$[0\,0\,0\,1]$	$[2\,\bar{1}\,\bar{1}\,0]$	$[-0.00\ -0.00\ +1.00]$	$[+3.230\ +0.000\ +0.000]$
(3)	$[0\,0\,0\,1]$	$[1\,\bar{2}\,1\,0]$	$[-0.00\ -0.00\ +1.00]$	$[+1.615\ -2.797\ +0.000]$
(4)	$[1\,0\,\bar{1}\,0]$	$[\bar{1}\,2\,\bar{1}\,0]$	$[+0.87\ +0.50\ +0.00]$	$[-1.615\ +2.797\ +0.000]$
(5)	$[1\,\bar{1}\,0\,0]$	$[1\,1\,\bar{2}\,0]$	$[+0.87\ -0.50\ +0.00]$	$[+1.615\ +2.797\ +0.000]$
(6)	$[0\,\bar{1}\,1\,0]$	$[2\,\bar{1}\,\bar{1}\,0]$	$[+0.00\ -1.00\ +0.00]$	$[+3.230\ +0.000\ +0.000]$
(7)	$[1\,0\,\bar{1}\,1]$	$[1\,1\,\bar{2}\,\bar{3}]$	$[+0.76\ +0.44\ +0.48]$	$[+0.859\ +1.487\ -2.736]$
(8)	$[0\,1\,\bar{1}\,1]$	$[\bar{1}\,\bar{1}\,2\,3]$	$[-0.00\ +0.88\ +0.48]$	$[-0.859\ -1.487\ +2.736]$
(9)	$[1\,\bar{1}\,0\,1]$	$[2\,\bar{1}\,\bar{1}\,\bar{3}]$	$[+0.76\ -0.44\ +0.48]$	$[+1.717\ +0.000\ -2.736]$

Mobility Law

In order to capture the dislocation evolution behavior in Zr, recourse was made to phenomenological description of the dislocation motion. This was necessary as no data is available for mobility of various dislocations in Zr.

The mobility law (6.1) was framed to account for the experimental observations [39, 40, 121, 123, 149] on slip activation.

$$\tau_i = A_i \exp\left(-\frac{T}{B_i}\right), \tag{6.1}$$

where τ_i is the critical resolved shear stress of the i^{th} slip system, where i refers to prismatic, pyramidal or basal as the case may be, and T is the absolute temperature. The parameters A_i, and B_i refer to the athermal component of Critical Resolved Shear Stress (CRSS) and the activation barrier for slip respectively, for the i^{th} slip system. Dislocation segments were allowed to move only if the local resolved shear stress on the segment exceeded the respective τ_i of the segment. Fig. 6.2 shows the values of these parameters and the respective plots of CRSS vs temperature for the three slip systems considered in the present study. The parameters for pyramidal and prismatic systems were taken from literature [39, 40, 121, 123]. No such data was available for basal slip. Since no significant basal slip in Zr was reported in the temperatures of interest to present study (*i.e.* from 25°C to 400°C), parameters for basal slip system were kept high enough to make basal slip virtually insignificant. In addition, dislocation climb is also not expected to be significant in this temperature domain, and hence dislocation nodal movement was restricted to be only along its slip plane. Based on the previous observations of the relatively higher mobility of the edge dislocations [116, 142] in comparison to screw components in *hcp* materials, mobility of edge components of dislocations was kept 2 orders of magnitude higher than screw components [142]. For a dislocation segment having a Burger's vector $\overrightarrow{\mathbf{b}}$ inclined at an angle θ to its line vector ($\overrightarrow{\xi}$), the mobility $(M))$ was interpolated smoothly from the computed mobility values of pure screw M_s to pure edge $M_e$segments as shown in Equation 6.2 [67].

$$M = \left(\frac{cos^2(\theta)}{M_s}\right) + \left(\frac{sin^2(\theta)}{M_e}\right)(\mathbf{I} - \xi \otimes \xi), \tag{6.2}$$

Once stress on a particular segment exceeds the CRSS, its velocity is determined by the mobility parameter (M_i) of the respective slip systems. These mobility parameters were determined by performing a series of simulations under uni-axial loading. Parameters resulting in reasonable yield stress values (200 MPa at 25°C) were used. Eq. 6.3 accounted for the drop in dislocation mobility, through thermal damping, at elevated temperatures.

$$M_i = \alpha_i^{Mob} \exp\left(-T \times \beta_i^{Mob}\right), \tag{6.3}$$

where M_i the dislocation mobility in the i^{th} type of slip system. α_i^{Mob} and β_i^{Mob} were fitted from

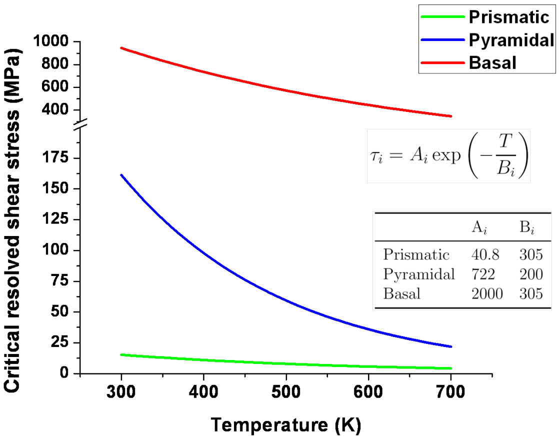

$$\tau_i = A_i \exp\left(-\frac{T}{B_i}\right)$$

	A_i	B_i
Prismatic	40.8	305
Pyramidal	722	200
Basal	2000	305

Figure 6.2: CRSS values as a function of temperature for different slip systems used in the present study. The values for basal slip were taken to be high enough to effectively make basal slip insignificant. The values for prismatic and pyramidal slip were taken from [39, 40, 121, 123]

Table 6.3: Moblity parameters for different slip systems, see Eq. 6.3

Slip system	α $(Pa^{-1}s^{-1})$	β
Basal ($\{0001\}\langle 2\bar{1}\bar{1}0\rangle$)	2.77×10^2	-0.3655×10^{-3}
Prismatic($\{10\bar{1}0\}\langle 2\bar{1}\bar{1}0\rangle$)	2.18×10^2	-0.3513×10^{-3}
Pyramidal($\{10\bar{1}1\}\langle 2\bar{1}\bar{1}3\rangle$)	0.50×10^2	-0.3500×10^{-3}

appropriate data [151] for prismatic slip. Such data were not available for basal and pyramidal slip. α_i^{Mob} and β_i^{Mob} parameters for basal and pyramidal slip (table 6.3) were chosen considering their lower mobilities with respect to prismatic dislocations. It may be noted that while the α_i^{mob} represents the athermal mobility of the dislocations in the lattice, β_i^{Mob} represents temperature effect on the mobility of the dislocations. Our trial simulations, as well as simulations conducted by others [152], showed that absolute values of mobility parameters had very little effect on the orientation and/or temperature sensitivity of simulation results. For the latter, CRSS appeared to have a stronger effect than the imposed mobility parameters.

6.3. Experimental Results

Fig. 6.3 shows temperature dependent microstructure developments. The starting structure consisted of near-equiaxed grains of greater than $3\mu m$ in size. Deformation brought relatively fine ($< 3\mu m$) fragmented grains. This refined the average grain size (Fig. 6.4(a)): from original 17 μm to 14, 10 and 8 after rolling at 300 K, 500 K and 700 K respectively. It is striking that the grain size refinement, and correspondingly the relative fragmentation, was more after the warm rolling. It needs to be noted, as also pointed out in ref. [148], the so-called non-fragmented ($> 3\mu m$) grains were near-basal oriented. The second important observation is from grain shape. As in Fig. 6.4(b), the non-fragmented grains remained largely equiaxed after room temperature deformation. The geometry of the plane strain compression [153] demands that the AR of an originally equiaxed grain to be changed to 1.3 after a 30% deformation. For the non-fragmented grains, experimental aspect ratio values were quite different from this ideal/expected values, see 'expected' values in Fig. 6.4(c). Interestingly, warm rolling (500 and 700 K PSC) caused more grain size refinement (Fig. 6.4(a) and (b)) and shift in grain aspect ratio: than rolling at room temperature (300 K).

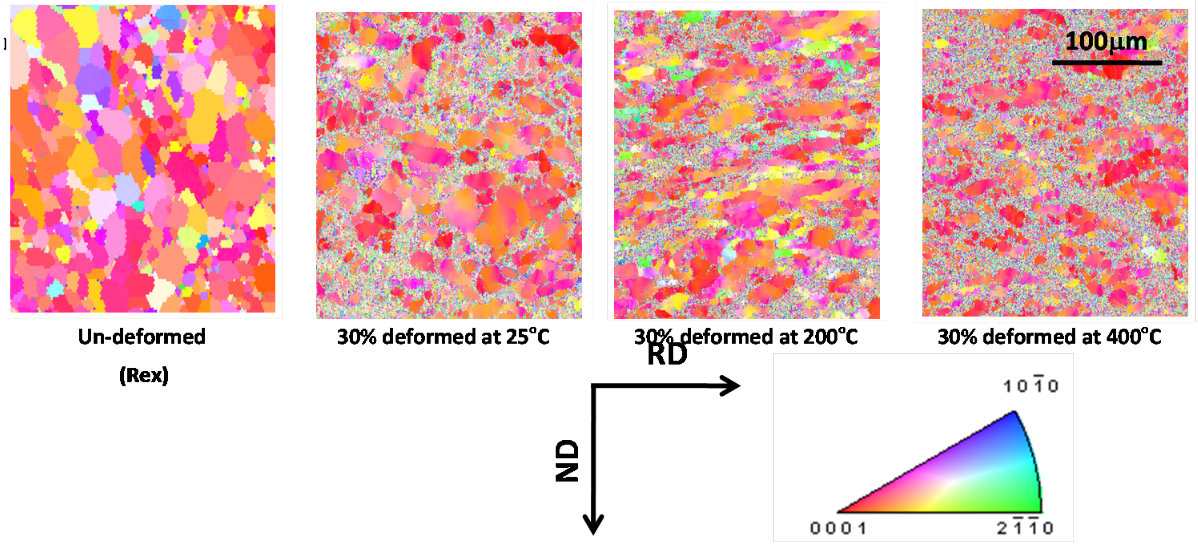

Figure 6.3: IPF maps of Zircaloy 2 at different working temperatures, demonstrating that some grains/orientations retained (*esp.* red colored grains representing basal orientated grains) their shape and size even after considerable deformation.

Heterogeneity in plastic deformation was also seen in TEM. This is shown for 10% cold rolled sample in Fig. 6.5 . Deformed microstructures were clearly distinguishable as regions containing extensive strain localizations (Fig. 6.5a) and with random dislocation arrays (Fig. 6.5b). The latter, referred in the literature [118] as Taylor lattice, had limited misorientations associated. Fig. 6.6 summarizes information on misorientation developments. In-grain misorientation developments were collated as GAM values. A relatively minor GAM development by room temperature rolling, while a substantial increase in GAM was achieved through warm rolling. This was true for the entire microstructure (Fig. 6.6a), and to a lesser extent for the grains above $3\mu m$ in size (Fig. 6.6b). In essence, all aspects of temperature dependent plastic deformation appeared to distinguish between room temperature and warm rolling. Deformation,

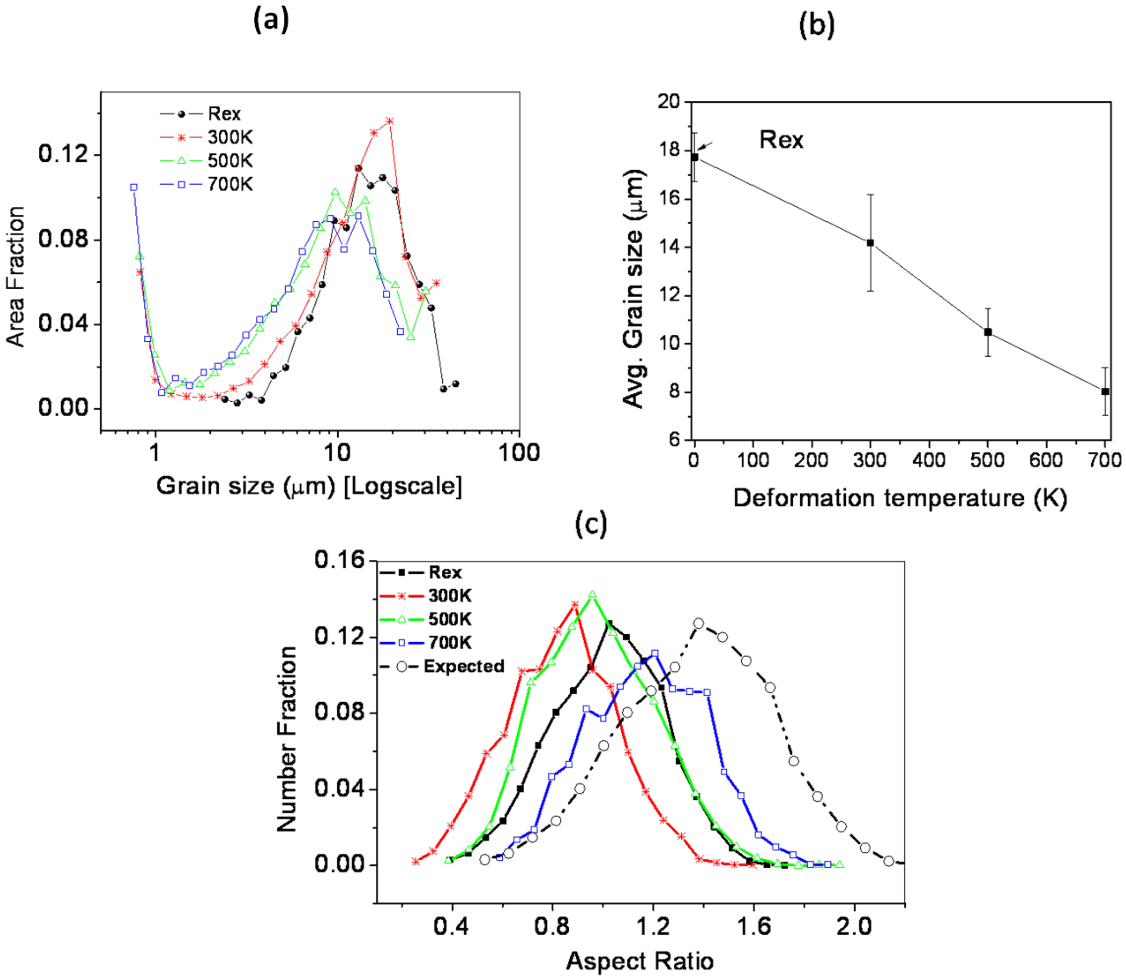

Figure 6.4: (a) Grain size distribution corresponding each working temperature and (c) The average grain sizes for the distribution shown in (a). (b) Grain aspect ratio distribution of the grains with size more than $3\mu m$ for each working temperature. The original aspect ratio distribution was modified, considering the imposed PSC of 30% reduction by rolling. This is included in (c) as 'expected' distribution. The 'expected' AR values considered length changes along RD and ND to be 1.3 and 0.7 times respectively from their original values.

represented in terms of grain size refinement, change in aspect ratio and in-grain misorientation developments, was more significant after warm rolling. This appears counter-intuitive.

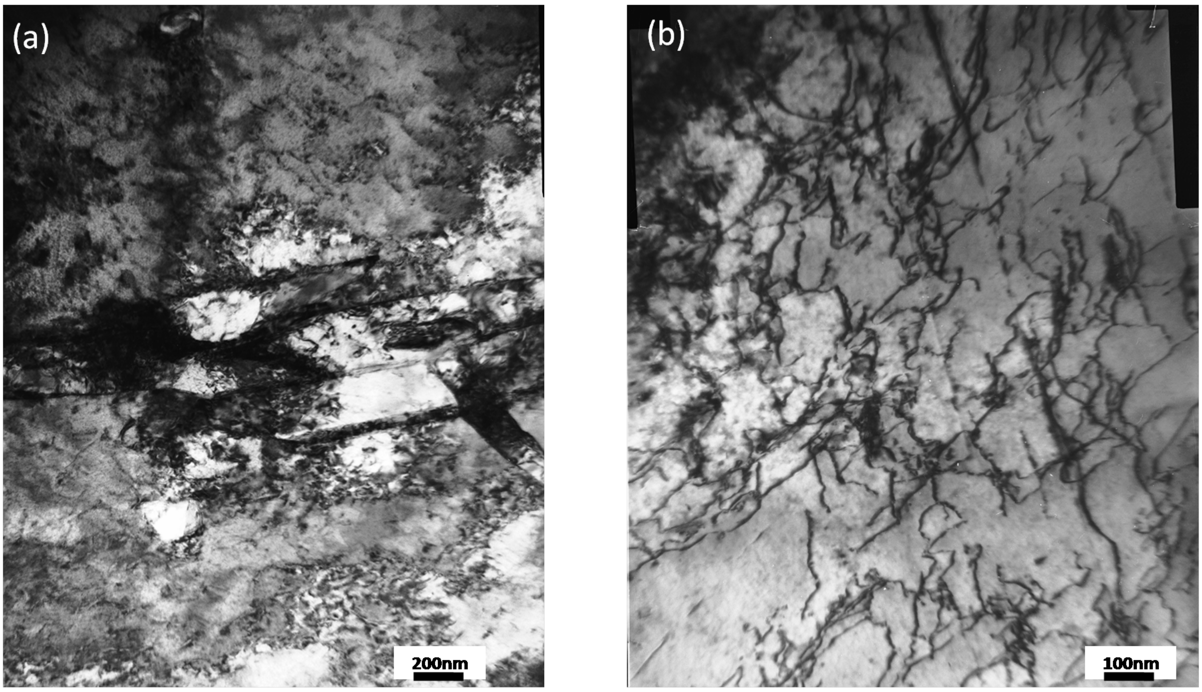

Figure 6.5: Bright field TEM micrograph showing the heterogeneous deformation in a zircaloy-2 sample subjected to 10% deformation. (a) Grain showing extensive strain localizations. (b) Grain with random dislocation array: the Taylor lattice [154].

Elevated temperature plastic deformation is expected to offer lesser signatures of plastic deformation. This can be attributed to possible dynamic recovery [1]. This study, thus, brings an interesting set of data on temperature dependent heterogeneous plastic deformation in Zirconium. The heterogeneity was in terms of fragmented and non-fragmented grains [148], and their different patterns of in-grain misorientation. Though the non-fragmented grains were found to be near-basal at all working temperatures, they had more GAM and changes in aspect ratio after warm rolling. It is clear that the so-called non-fragmented grains were more amenable to plastic deformation during warm (500 and 700 K) working.

6.4. Possible Explanation Through DD

At temperatures below 0.5 times to melting temperature, plastic deformation or slip is governed by dislocation dynamics [155, 156]. The observed temperature or orientation dependent plastic deformation is thus expected to have its origin in DD. In this section, results of the DD simulations are presented, with an emphasis on linking such results with microstructural ob-

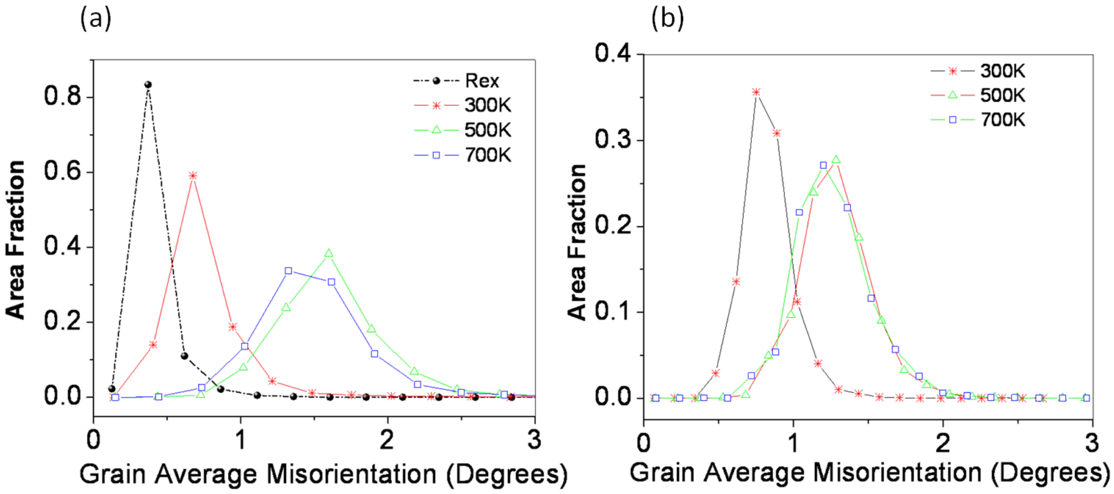

Figure 6.6: (a) GAM distribution of deformed Zircaloy 2 subjected to 30% deformation at different temperatures (b) GAM distribution of the non-deforming/non-fragmenting grains of (a). The grains greater than $3\mu m$ were considered as non-fragmenting. GAM distribution for original recrystallized sample is incorporated in (a) which indicates the measurement uncertainty.

servations made earlier (section 6.3). The aim of the present DD simulations was to elucidate the underlying mechanisms, and not to seek quantitative comparisons with experiments. DD is largely restricted to low plastic strains (due to computational constraints) and mostly single crystals. Even with such limitations, past DD studies brought out valuable insights into the effects of orientations [133], sample sizes [157], and cyclic loading [158]. However, most of these studies were carried out for cubic (fcc and bcc) materials [159–161]. The present study uses DD simulations to gain insights into the relatively less studied hcp-Zr system. Specifically, explanation(s) for the following experimental observations were sought:

1. Origin of orientation dependent fragmentation: the observation that non-fragmented grains were near-basal oriented.
2. Temperature dependence of grain fragmentation: 500 K and 700 K rolling led to more fragmentation (and signatures of plastic deformation) than room temperature rolling.

In order to explain the observed differences between the ‘basal’ oriented and ‘non-basal’ oriented grains, DD simulations were performed for the respective orientations. Prismatic orientation, due to its favorable Schmidt factor (under the loading conditions of the present study), has been chosen for the ‘non-basal’ orientation. Fig. 6.7 represents schematic of how the local crystal unit cell is oriented with respect to the sample reference frame for these two ideal orientations. A constant external stress resulting in plane strain deformation was applied to simulate the rolling experiments. The external stress was taken as,

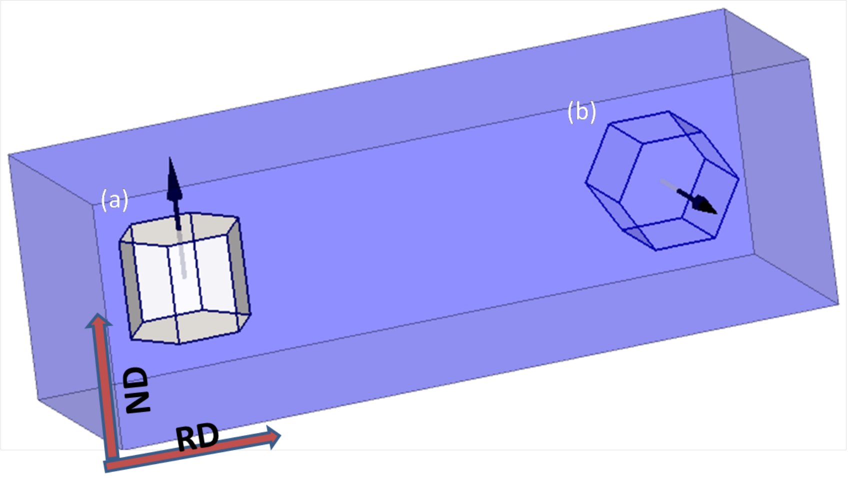

Figure 6.7: Schematic illustrating the (a) Basal and (b) Prismatic Orientations used for the DD simualtions.

$$\sigma_{\mathbf{global}} = \sigma \times \begin{bmatrix} 1 & 0 & 0 \\ 0 & 0 & 0 \\ 0 & 0 & -1 \end{bmatrix}, \tag{6.4}$$

where σ is a constant, set at $500 \times 10^6 Pa$, which is reasonably larger than the macroscopic yield stress of Zr. The effect of orientation was incorporated by rotating the global stress tensor, σ_{global}, to local crystal frame by the following tensor transformation,

$$\boldsymbol{\sigma}_{local} = [\mathbf{R}][\boldsymbol{\sigma}_{global}][\mathbf{R}^{-1}], \tag{6.5}$$

where σ_{local} is the local stress tensor and $\mathbf{R}$ is the orientation matrix of the crystal. The orientation matrices and corresponding 'Euler angle' notations for the two ideal orientations used in this study are tabulated in table 6.4.

Fig. 6.8 shows the results of the DD simulations for the 'basal' and 'prismatic' orientations at room temperature. Identical initial dislocation configuration (Fig. 6.1) was used for both orientations. It is clear that the 'basal oriented' simulation volume did not show appreciable dislocation activities (movement, multiplication *etc.*). In contrast, the 'prismatic oriented' simulation volume had significant modifications in dislocation configuration. This difference between the orientations is further quantified in Fig. 6.8c and d. The total plastic strain and dislocation density was one order of magnitude higher for 'prismatic orientation'. This is in agreement with experimental observations that basal grains were the non-fragmented ones. After room temperature rolling, they had insignificant changes in GAM and AR. In DD simulations, the

Table 6.4: Rotation matrices corresponding to different ideal orientations used in the DD simualations.

Orientation	$\mathbf{R}$	Euler Angle Notation ($\phi_1\,\phi\,\phi_2$)
Basal	$\begin{bmatrix} +1 & 0 & 0 \\ 0 & +0 & 0 \\ 0 & 0 & +1 \end{bmatrix}$	[0 0 0]
Prismatic	$\begin{bmatrix} +1 & 0 & 0 \\ 0 & 0 & +1 \\ 0 & -1 & 0 \end{bmatrix}$	[0 90 0]

‘basal orientation’ showed insignificant activity of the prismatic slip. This was further verified for various in-plane rotations and starting dislocation configurations. In contrast, plastic strain in ‘prismatic orientation’ came primarily from prismatic slip which is the primary slip system for this orientation. The pyramidal slip system was the primary slip system in ‘basal orientation’ due to favorable resolved shear stresses. However, their high CRSS at room temperature resulted in limited plastic strain.

Even without the DD simulations, the lower plastic strain for ‘basal orientation’ can be explained by comparing resolved shear stresses (for various slip systems) with corresponding CRSS values. Prismatic dislocations have low CRSS but experience low resolved shear stress. Pyramidal dislocations, on the other hand, experience high resolved shear stress, but also have very high CRSS values. As a result negligible plastic deformation is expected at room temperature near-basal oriented grains. However a CRSS based model does not account for dislocation-dislocation interactions and hence is not suited to explaining deformation behavior involving complex dislocation configurations.

Fig. 6.9 shows results from DD simulations for 700 K PSC for ‘basal’ and ‘prismatic’ orientations. Dislocation activities for ‘basal’ after 700 K was clearly higher than the room temperature deformation: see Fig. 6.8 versus Fig. 6.9. Higher dislocation activities were for dislocations on pyramidal planes ($\overrightarrow{c+a}$ type dislocations). This was the most remarkable difference between DD simulations performed at 300 (Fig. 6.8) and 700 K (Fig. 6.9). In the former, almost no movement of prismatic dislocations was observed for ‘basal orientation’.

The effects of orientation and temperature dependencies are further collated in Fig. 6.10. DD simulations showed increased dislocation densities ($d\rho$) with strain increment ($d\epsilon$). At a given temperature, $d\rho/d\epsilon$ was higher for prismatic orientation than basal. This points towards

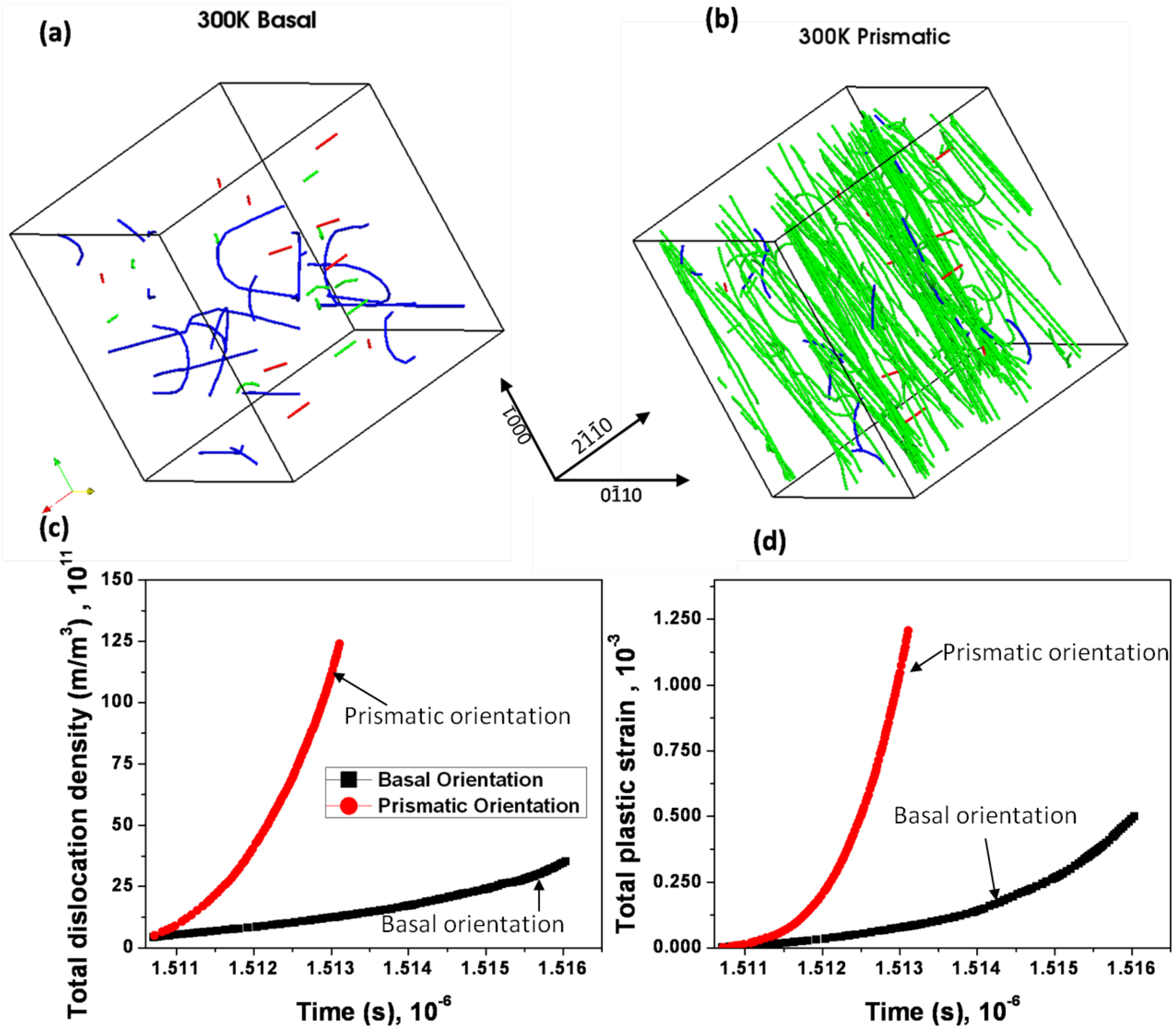

Figure 6.8: Dislocation structure evolution as computed by the DD simulations of deformation at room temperature in (a) basal and (b) prismatic oriented crystals. The dislocation structures correspond to similar simulation times. Dislocation segments are color coded according to Fig. 6.1. It is clear that basal oriented crystal showed relatively minor dislocation evolution while the prismatic oriented crystal witnessed considerable dislocation evolution and thus strain accumulation. (c) Evolution of total dislocation density and (d) plastic strain with time for 'basal' and 'prismatic' orientations.

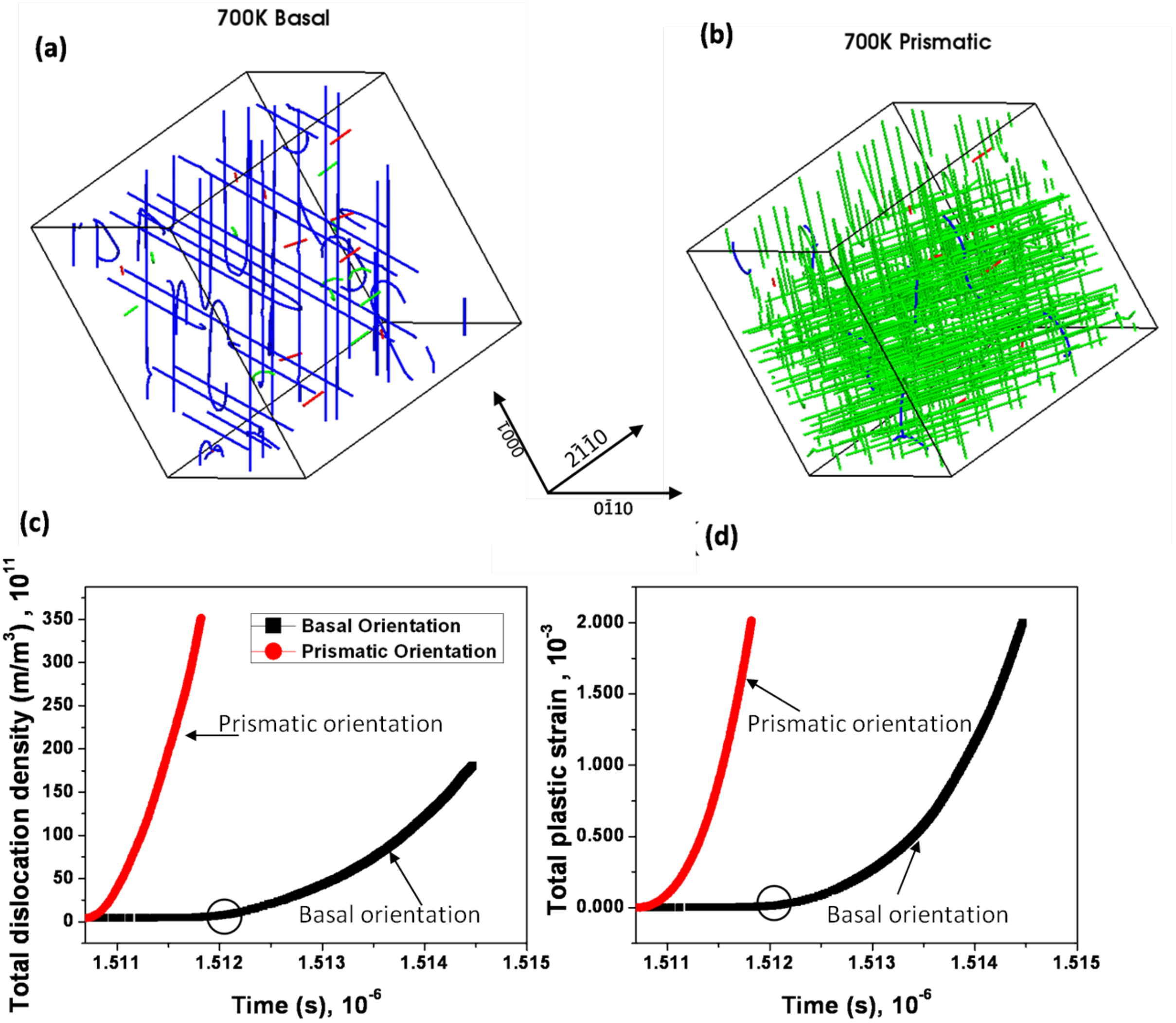

Figure 6.9: Dislocation structure evolution as computed by the DD simulations, in (a) basal, and (b) prismatic, oriented crystals at 700K (corresponding to $400°\mathrm{C}$). The dislocation structures snap shots correspond to similar simulation times. Similar color coding as that of the Fig.6.1 is used for the dislocation segments (c) Evolution of total dislocation density and (d) plastic strain with time for 'basal' and 'prismatic' orientations. Refer text for the explanation of the circled region.

lower tendency of junction formation in case of ‘basal orientation’. Immobilization of some dislocation segments in junctions, forces the remaining segments to bow out. A greater increase in dislocation density thus results from increased tendency of junction formation. In ‘prismatic orientation’ both prismatic and pyramidal slip systems had significantly high resolved shear stresses and several mobile segments on both planes. This increased the probability for dislocations on the two planes to intersect and form junctions. In contrast, in ‘basal orientation’ under room temperature PSC had limited activation of the pyramidal slip system. Thus there was almost no junction formation in ‘basal orientation’ under room temperature PSC, and correspondingly very low $d\rho/d\epsilon$ (Fig. 6.10).

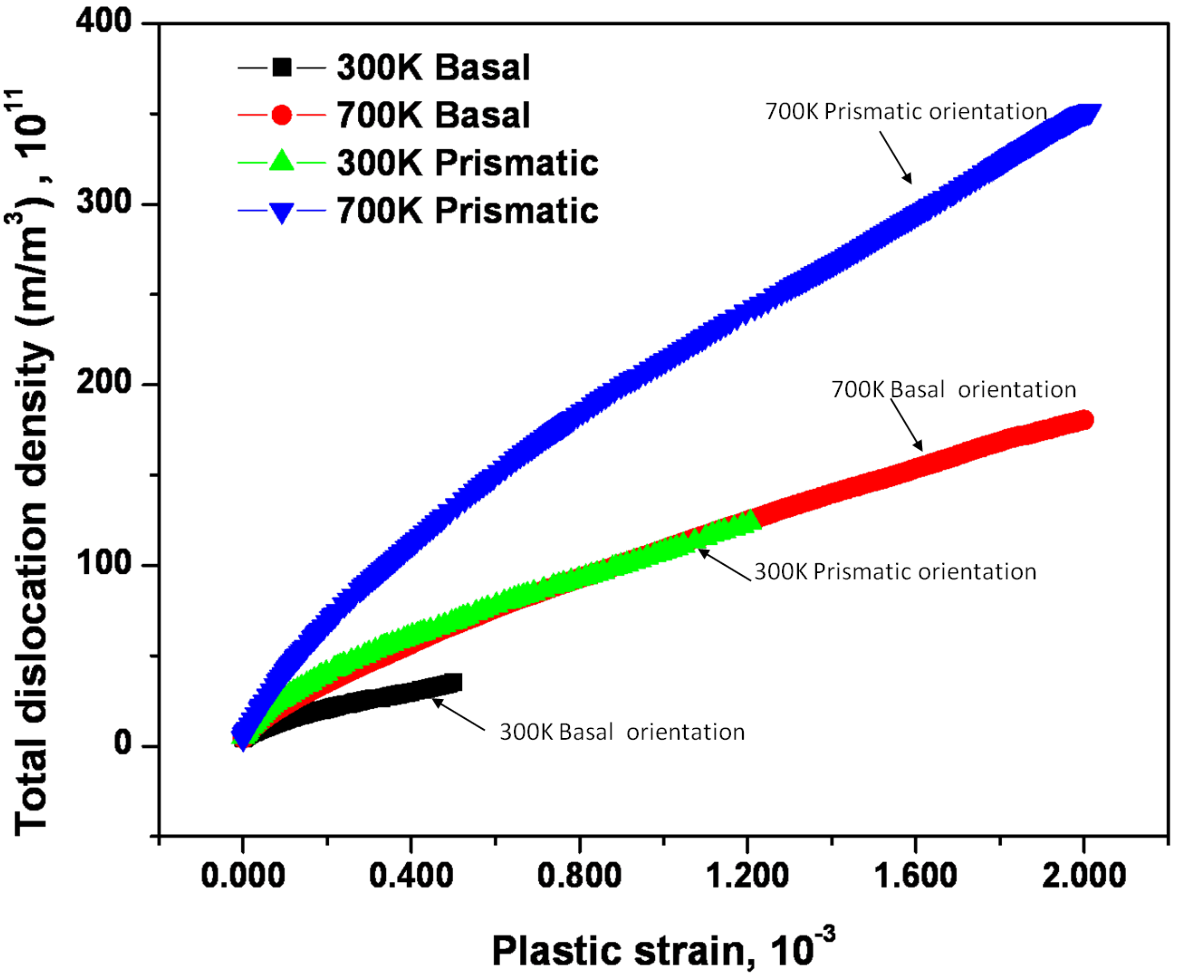

Figure 6.10: Computed evolution of dislocation density as a function of plastic strain for basal and prismatic orientations at different simulation temperatures.

DD simulations showed higher: (i) strain accumulation and (ii) $d\rho/d\epsilon$ in ‘basal orientation’ at 700 K compared to Room Temperature (RT). While (i) can be attributed to increased pyramidal slip activity (arising out of reduced CRSS) at 700 K, (ii) hints at the possible activation of other slip systems. DD simulations (700K PSC) on basal orientation brought out a novel observation of the activation of dislocations on “dormant” slip systems: slip systems having resolved shear stress lower than the respective CRSS. The activation of a dormant slip system (in this case prismatic) due to the higher activity of a primary slip system (in this case pyramidal) is shown in Fig. 6.11. The figure shows the resolved forces along the local burgers vector on each node of the prismatic dislocations. The initial state demonstrated negligibly small nodal resolved forces on all the prismatic dislocations for this ‘basal orientation’. Subsequent snapshots (Fig. 6.11, frames 2 to 5) depict the time evolution of dislocations under constant external applied stress. Since pyramidal dislocations had high resolved stresses and low CRSS at 700 K, their density increased considerably. Such density increases brought active pyramidal dislocations in close proximity of the inactive prismatic dislocations. This led to significant interaction forces on the dormant prismatic dislocations. Prismatic system being an inherently easy slip system (having low CRSS), resolved forces due to dislocation-dislocation interaction activated some of the dormant prismatic dislocations. This mechanism seems quite important for *hcp* crystals (Zr in particular) with limited number of easy slip systems. In a non-favorably oriented grain, such as basal, activation of dormant slip systems could provide a hitherto unexplored mode of plastic deformation. This is clearly reflected in Fig.s 6.9c and d. Respective increases in dislocation density and strain, beyond the point highlighted by a circle, are due to the activation of prismatic slip system due to interactions with the pyramidal dislocations. This can reduce the orientation sensitivity of deformation (Fig. 6.3,6.4,6.5, and 6.6) at 700 K. The proposed mechanism is in stark contrast to classical work hardening. In work hardening, dislocation interactions are expected to contribute towards strain hardening. Whereas the mechanism illustrated by DD simulations involved activation of dormant slip systems due to the stress field of a neighboring active dislocation.

Fig. 6.10 shows a comparison of results for ‘basal orientation’ at 700 K with those at 300 K. An obvious question is on the lack of similar activation of dormant dislocations at the lower working temperature. The CRSS of pyramidal dislocations is very high at 300 K. This resulted in significantly lower densities of pyramidal dislocations. Close interactions of the kind shown in Fig. 6.11 were rather improbable. For the indirectly activated slip systems to contribute towards appreciable plastic strain, sufficient density of primary slip system dislocations is necessary. The CRSS of the secondary slip systems also needs to be comparable to the interaction stresses of the dislocations. Present simulations show that these two conditions were satisfied

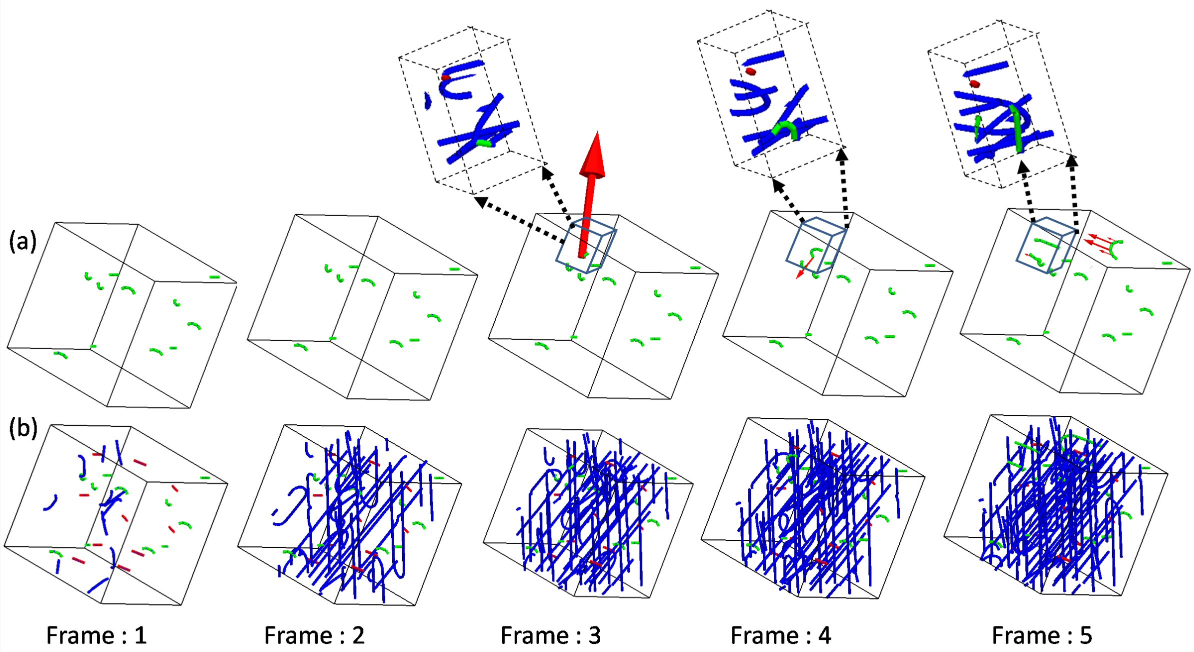

Figure 6.11: (a) Depiction of nodal forces along burgers vectors of prismatic dislocations in case of simulation of basal orientation at 700 K at various time steps. The red color arrows indicate the direction and magnitude of the resolved nodal force along local burgers vector. For the purpose of clarity, forces on prismatic dislocations only are shown. It can be observed that, the resolved nodal forces in the initial state are negligibly small rendering red arrows on them invisible (a reflection of orientation effect). However, as the pyramidal dislocations evolve, significant forces (due to interaction) are observed on certain prismatic dislocation. Once a critical force is generated frame (3), a prismatic source is observed to have got activated and starts to evolve. (b) Evolution of the overall dislocation structure at above time steps. For the sake of clarity, a zoomed in version of (a) from a different viewing angle, are shown (of the boxed region) of the region in which an inactive prismatic dislocation has been activated by the interacting pyramidal dislocations.

in case of ‘basal orientation’ at 700 K PSC, the end of plateau of Fig. 6.9c. This plateau corresponded to the build-up of “critical dislocation density” while the subsequent rapid increase occurred through interaction stresses exceeding CRSS value for prismatic dislocations. Since basal dislocations had very high CRSS values at both temperatures, they were not activated even at very high dislocation densities.

6.5. Conclusions

1. Experimental observations revealed orientation and temperature sensitive plastic deformation in hexagonal Zirconium. The starting microstructure had nearly equiaxed grains of $> 3\mu m$ size. Deformed microstructures contained below $3\mu m$ fragmented grains, and also larger grains generically termed as non-fragmented. The latter was predominantly ‘basal oriented’ for all working temperatures. Temperature dependent plastic deformation, in terms of grain size/shape refinement and in-grain misorientation developments, showed a remarkable difference between room temperature and warm (200 ° and $400°$C) rolling. Warm rolled microstructures contained significantly higher signatures of the plastic strain.

2. DD simulations of room temperature PSC successfully captured the deformation response of basal and prismatic orientations. Both dislocation density and plastic strain were significantly lower for basal orientations relative to prismatic orientation. However simulations for the elevated (700 K) temperature deformations showed higher strain accumulation in basal orientation (in comparison to corresponding room temperature deformation of basal) through increased pyramidal slip activity.

3. DD simulations also brought out a novel effect of dislocation-dislocation interactions. Dormant slip systems, slip systems where the applied stress was below CRSS, were activated due to interactions with active primary dislocations. This mechanism was shown to activate dormant dislocations in basal orientations, thus contributing to reduction in deformation heterogeneity during warm rolling.

CHAPTER 7

Deformation Twining in Zr : Role of Orientation and Composition

7.1. Introduction

Slip and twining are two principal modes of plastic deformation in metallic materials [3, 162]. It is well known that slip by dislocations contributes to the majority of observed deformation. Twinning on the other hand, results in significant changes in the crystal orientation and consequent crystallographic texture evolution [163–167]. Decades of research on plastic deformation had accumulated a rich body of knowledge on the deformation due to slip. This had helped development of accurate predictive models of textural evolution where slip is the dominant deformation mechanism as in the case of cubic materials [47, 63, 64, 168–170]. Hexagonal materials, on the other hand, due to limited number of easy slip systems, undergo considerable twinning [3, 39, 40, 121, 164, 171]. Twinning in these materials plays a crucial role in textural evolution and low temperature ductility. Our ability to develop predictive deformation models for *hcp* materials, thus critically depends on the ability for the prediction of twin nucleation and evolution during the deformation [167]. By far, the mechanism and criteria under which twins form and grow has been a subject on which the available knowledge is far from satisfactory. Several of the previous works on deformation modelling thus could not include the contribution from twinning [168, 172].

Zr being a *hcp* material is highly prone to deformation by twinning due to limited number of easy slip systems available [3, 39, 40, 121, 164, 171]. Further, alloy composition is expected to play a vital role on the relative activation of the available deformation modes. In this context, it becomes pertinent to develop understanding of the role of alloying elements on the deformation behavior of Zr in general and on twinning in particular. One of the key alloying elements in many commercial Zr-alloys, such as Zircaloy-2, Zircaloy-4, E635 and ZIRLO, is Tin (Sn). Thus Sn has been considered for the present study as a candidate element to bring out the role of alloying element on the twining behavior in Zr. Further, a highly textured microstucture was generated and samples were made along different directions to produce samples with widely different starting orientations. Such samples thus can bring out the effects of Sn as well as starting texture (orientation) on the twinning behavior. The study aimed to bring in some insights to answer long standing question of weather twin nucleation is actually governed by the stress state or strain state of the parent grain.

Due to the experimental difficulties of intercepting the nucleation event of twining, a majority of the studies have focused on indirect methods for finding out the nucleation criteria for twins. These include theoretical predictions using models based on various assumptions for twin nucleation. Comparison of model predictions with experimental results served as the validity of the model's assumptions on twin nucleation criteria. Even then inferences were never conclusive and a lot of ambiguity still remains. A majority of these models considered twin nucleation to be primarily stress driven [165, 166, 173–176]. As a complimentary to such indirect methods of understanding the twin nucleation, it is desirable to have an experimental understanding of the phenomenon as well. Presently there is no concrete experimental evidence of the governing criteria for the twin nucleation and the past studies relied chiefly on the assumptions/speculations regarding the same. Some studies indicate that twin nucleation is governed by the density and type of dislocation structure. For instance, there is considerable evidence to show that the twining dislocations are a result of non planar dissociation reactions from $\overrightarrow{a}$, $\overrightarrow{c+a}$ and $\overrightarrow{c}$ type dislocations [177–181]. Since dislocation structure and distribution is mainly influenced by the plastic strain in the grains, twinning must necessarily depend on the strain undergone by the potential parent grains as well. This raises the fundamental question of whether twining is stress controlled or strain controlled and/or what the relative role of stress and strain is in twining.

Present study aimed to answer this question through an extensive *in-situ* neutron diffraction/deformation investigation on Zr-Sn binary alloys. Using a systematic variation of the sample composition and deformation direction, we can activate different slip modes and monitor the sample behaviour in terms of twin formation and evolution using *in-situ* deformation and diffraction. Due to the *in-situ* nature of the experiments, we have simultaneous access to applied stress, strain along with intragranular strain states of the grain families. In addition, change in intensity of specific reflections, provides a mechanism to detect nucleation and subsequent evolution of the twinning. A comprehensive analysis of such data is presented in this chapter to gain insights into the controlling factors for the twining in the Zr. Although Zr has been considered for the study, the results are general enough to apply for any of the *hcp* material in general.

7.2. Experimental

Four model Zr-Sn binary alloys with nominal compositions of 0.15%, 0.23%, 0.33%, and 1.20% Sn (amounts are in weight percentage), were used in the present study (see Table 7.1, for detailed composition). Deliberately more compositions have been chosen towards lower Sn content, instead of using equal steps of Sn variation. The reasons for the same shall be explained in the later sections. All alloys were prepared using single batch of Zr sponge to minimize variation in trace elements. In the light of the expected role of the interstitial elements on the twinning behaviour, total interstitial content variation was kept to a narrow range in these four alloys (see table 7.1 for the actual composition). The ingots were prepared by quadruple electron beam melting. The cast structure of the ingots was broken by hot extrusion at $800°\mathrm{C}$. Blocks of $35mm \times 22mm \times 15mm$ were cut from the extruded material and β heat treated at $1050°\mathrm{C}$ for 20 minutes followed by water quenching. The purpose of the heat treatment was to reduce any potential micro segregation of Sn and generate a similar starting microstructure with no preferred crystallographic texture. After β quenching, the blocks were stress relieved at $500°\mathrm{C}$ for 24 hours followed by $1°\mathrm{C}$/min cooling. Prior to hot rolling, the blocks were homogenized at $550°\mathrm{C}$ for 40min and subsequently rolled at $550°\mathrm{C}$ to a reduction of 65% followed by annealing treatment at $550°\mathrm{C}$ for 24 hours. The purpose of this thermomechanical process was to generate a fully recrystallized microstructure and a typical crystallographic texture with the majority of basal poles aligned along ND with some spread along TD. The purpose of creating this microstructure was to enable compression tests with the majority of the $\langle c \rangle$ axis either aligned perpendicular (compression along RD) or nearly parallel (compression along ND) to the loading direction during the *in-situ* neutron diffraction studies.

Compression samples along three principal directions (RD, TD, and ND) have been extracted from the aforementioned TMP processed samples. These were cylindrical samples of 12mm in length and 8mm in diameter in case of deformation tests along RD and TD. Due to thickness limitation of the rolled samples, sample dimensions for the tests along the ND were restricted to 8mm in length and 6mm in diameter.

Table 7.1: Composition of the Zr-Sn binary alloys used in the present study.

Alloy Designation		Elements				
		Sn (wt%)	O (ppm)	C (ppm)	N (ppm)	Zr
Alloy 1	0.15 % Sn	0.15	530	80	48	Balance
Alloy 2	0.23 % Sn	0.23	880	80	45	Balance
Alloy 3	0.33 % Sn	0.33	830	30	49	Balance
Alloy 4	1.20 % Sn	1.20	930	120	34	Balance

7.2.1. In-situ Loading and Neutron Diffraction Experiments

The time of flight neutron diffraction beam line ENGIN-X, at ISIS, Rutherford Appleton laboratory, UK, was used for the *in-situ* compression loading and diffraction experiments of the present study. The schematic of the experimental set up (Fig. 7.1), shows that the location of the detectors allows the capturing of diffraction data along two principle directions of the sample, *e.g.*, along the rolling direction (longitudinal detector) and normal direction (transverse detector). The diffraction peaks carry information regarding the lattice strain evolutions, and deformation mechanisms through the changes in their peak positions (for intragranular elastic lattice strains), intensity (for twinning) and FWHM. For instance, onset of twinning can be detected by the sudden change in the lattice strain evolutions of the grain family undergoing twinning (as shall be demonstrated in the following section). Similarly, significant changes in the FWHM of the diffraction spectra indicate high slip assisted plastic deformation activity from the grain families corresponding to the respective diffraction peaks.

In-situ compression loading experiments were carried out using a 100 kN Instron compression rig. The samples were compressed along the chosen direction and the data points in the elastic regime (up to 50MPa below the macroscopic yield point) were captured in constant stress state. This is followed by a continuous strain controlled loading up to 0.18 true strain. In order to make effective use of beam time, the data points in the plastic regime were captured at two different strain rates: a slower rate of $7 \times 10^{-6}/s$ until 0.025 strain followed by $2.8 \times 10^{-5}/s$ until 0.18 strain. The frequency of measurement points was increased around the yield point by the deliberate selection of low strain rate, as the onset of plasticity is a key area of interest in understanding deformation mechanisms. In order to obtain a reasonably good signal to noise ratio of the diffraction peaks, acquisition time for the diffraction spectra at each of the measurement points was kept to around 5 min. Due to the very slow strain rate, the sample temperature was constant throughout the loading experiment. Further, the energy range of the neutron spectrum at ISIS is rather low to cause any radiation damage to the sample during the *in-situ* experiments. Thus the effects seen in the present study do not have any contribution from the radiation damage related phenomena.

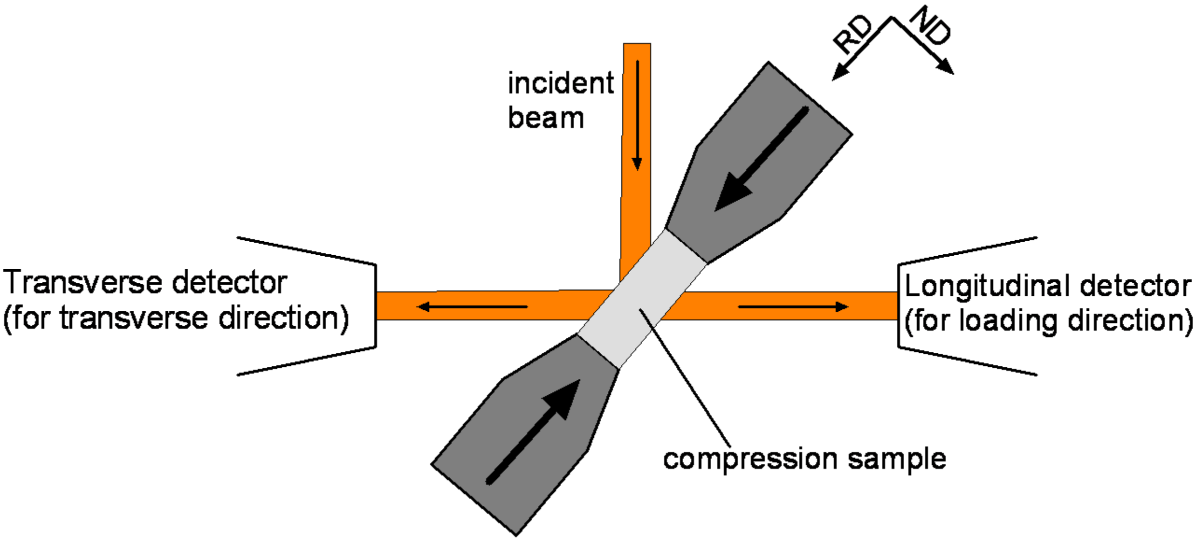

Figure 7.1: Schematic illustrating (a) *in-situ* neutron diffraction experimental set up. (b) and (c) show the orientation of the crystallographic planes sensed by the two neutron detectors that are mounted on either side of the incident beam. Essentially, crystallographic planes of the sample, because of diffraction, act like mirrors to the incident neutron beam and deflect the incident beam on to the detectors. Depending on the location of the detectors, the response of either plane can be captured in the longitudinal (b) and transverse (c) direction in respect to the loading direction. RD and ND in (a) indicate the orientation of the sample's "Rolling" and "Normal" directions, as used in the present study in case of deformation along the RD.

7.3. Results

Fig. 7.2 depicts the typical microstructure and texture of the recrystallized material (here Zr-1.2%Sn) prior to *in-situ* loading and diffraction experiments. No significant microstructural differences were observed in the four alloys considered for the present work. As it can be observed from the grain orientation map (inverse pole figure colour code), the starting microstructure is completely recrystallized with an average grain size of $4.5\mu m$ (based on EBSD measurements). Grain size analysis of the other three alloys gave $5.5\mu m$ for Zr-0.15%Sn, $4.5\mu m$ for Zr-0.23%Sn and $5\mu m$ for Zr-0.33%Sn. TEM micrographs (Fig. 7.2.b) also show grains with low dislocation density and well defined high angle grain boundaries, typical of recrystallized material. As illustrated in Fig. 7.2c, the starting texture is predominantly basal poles aligned towards ND of the sample, with a ±30° spread along TD. Further, there is also a slight tendency of the

$< 11\bar{2}0 >$ poles being preferentially aligned towards RD.

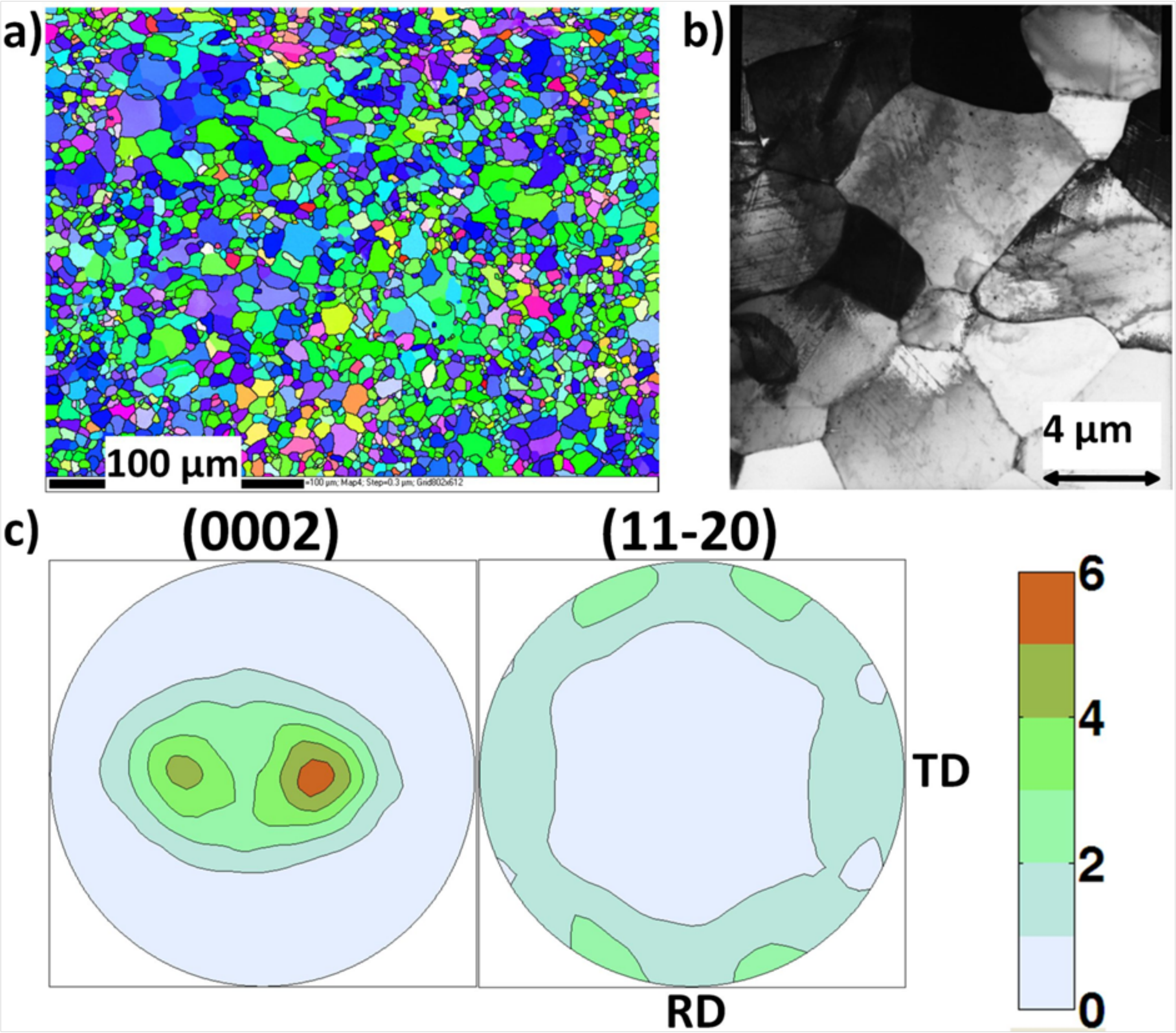

Figure 7.2: Typical starting microstructure, (a) EBSD and (b) TEM, and (c) texture of the samples subjected to *in-situ* loading in neutron diffraction studies. In the present case the results were recorded on the Zr-1.2% Sn alloy. It may be noted that the starting microstructure of the other alloys was rather similar to this and hence avoided for the sake of brevity.

7.3.1. Flow Behaviour as a Function of Composition and Deformation Direction at Room Temperature

Fig. 7.3 depicts flow behaviour of the Zr-Sn alloy samples as a function of Sn content and deformation direction. These curves are from the data collected during in-situ deformation and diffraction experiments. Following key observations can be made from the figure.

1. There was a systematic increase in the flow stress with increase in Sn in case of deformation along all directions (RD, TD and ND). This confirmed the expected solid solution

strengthening effect of Sn. However, the increase in flow stress appeared to be non linear with Sn content. The flow data, table 7.2, suggested that strengthening effect of Sn got saturated for higher Sn alloys. This can be ascertained from the fact that relative increase in the yield stress (σ_y) of alloys for a given change in Sn ($\Delta(\%Sn)$) was more at lower Sn values. This was the reason for choosing a more number of alloy compositions at lower Sn levels in this study, as the effect of Sn is more prominent in lower range of Sn content.

2. The flow stress for a given Sn content, increased in the order of deformation along RD, TD and ND, signifying strong effect of texture on the deformation, see Fig 7.3 and Table 7.2.

3. The flow curves in case of deformation along RD, exhibited a comparatively low strain hardening (referred hereafter as 'flat response') regime during the initial stage of plastic deformation. Further, such a flat response became more pronounced with increasing Sn content of the alloy, see Fig. 7.3a. A zoomed in version of this regime is included in the figure to bring out this effect more clearly. This observation indicated that, although the onset of plasticity was delayed by the increased Sn (*i.e.*, increase in yield point with Sn), once plasticity sets in, there was increased extent of strain burst with increased Sn, in RD deformation.

4. There was a conspicuous absence of such a flat response regime in case of compression tests along ND and to some extent along TD.

5. Flow curves in case of RD show a systematic trend of increased strain hardening as a function of both Sn and plastic strain (at larger strains). TD and ND deformation, however, did not show such trend.

Table 7.2: Macroscopic yield points for Zr-Sn alloys as determined in the present study.

Alloy	Yeild stress (MPa)		
	RD	TD	ND
0.15 % Sn	260	270	400
0.23 % Sn	281	300	420
0.33 % Sn	303	350	450
1.20 % Sn	352	360	500

In summary, role of Sn on the flow behaviour was seen to be highly dependent on deformation direction.

7.3.2. Evolution of Intragranular Elastic Strains as a Function of Composition and Deformation Direction

Fig. 7.4 presents the evolution of the intragranular elastic strains for three principal families of grains, viz to 0002, $10\bar{1}0$ and $10\bar{1}1$. The data represents relative change in the elastic strains from the unloaded (or initial) state of the sample and corresponds to compressive strain along the loading direction. As expected, all the curves show initial linear response corresponding to elastic deformation at low stress levels. The onset of plasticity was marked by deviation from such linearity and can be seen to be clearly a function of alloy Sn content. An observation of particular interest for the present study was the behaviour of 0002 reflection, for RD, TD and ND deformations. As can be seen, RD and TD deformations showed, a regime of increased elastic strain at constant applied stress, followed by an abrupt relaxation of significant amount of strain. This is a clear signature of twining. Thus intragranular strain evolutions of 0002 reflection confirmed significant twin activity for loading along RD and TD. Similarly based on the behaviour of 0002 reflection for ND loading tests, one can infer that there was no detectable twinning. The unloading of elastic strains exhibited by the grain families $10\bar{1}0$ and $10\bar{1}1$ indicate the micro plasticity and consequent relaxation in elastic strains in theses grain families. Here also one can notice increased unloading effect with increased Sn content. Fig. 7.5 shows a more detailed picture of intragranular strain evolutions in case of RD deformed samples for all of the compositions used in the present study. Following inferences can be drawn from this figure.

1. The $10\bar{1}0$ grain family showed the highest degree of unloading (*i.e.* reduction in elastic strain despite a further increase of applied stress) around the onset of plastic yield and twinning, which is a signature of extensive plasticity in this grain family. It is also noticeable that the initial degree of unloading increases with increasing Sn content.

2. The $10\bar{1}1$ grain family did not display a sharp unload at the early stage of plastic yield but with increasing level of plasticity, this grain family takes up less and less additional elastic strain despite a further increase of applied stress. With increasing Sn content the $10\bar{1}1$ and $10\bar{1}0$ elastic strain responses become less distinguishable.

3. The 0002 grain family exhibits significant build up of the lattice strain before a sudden

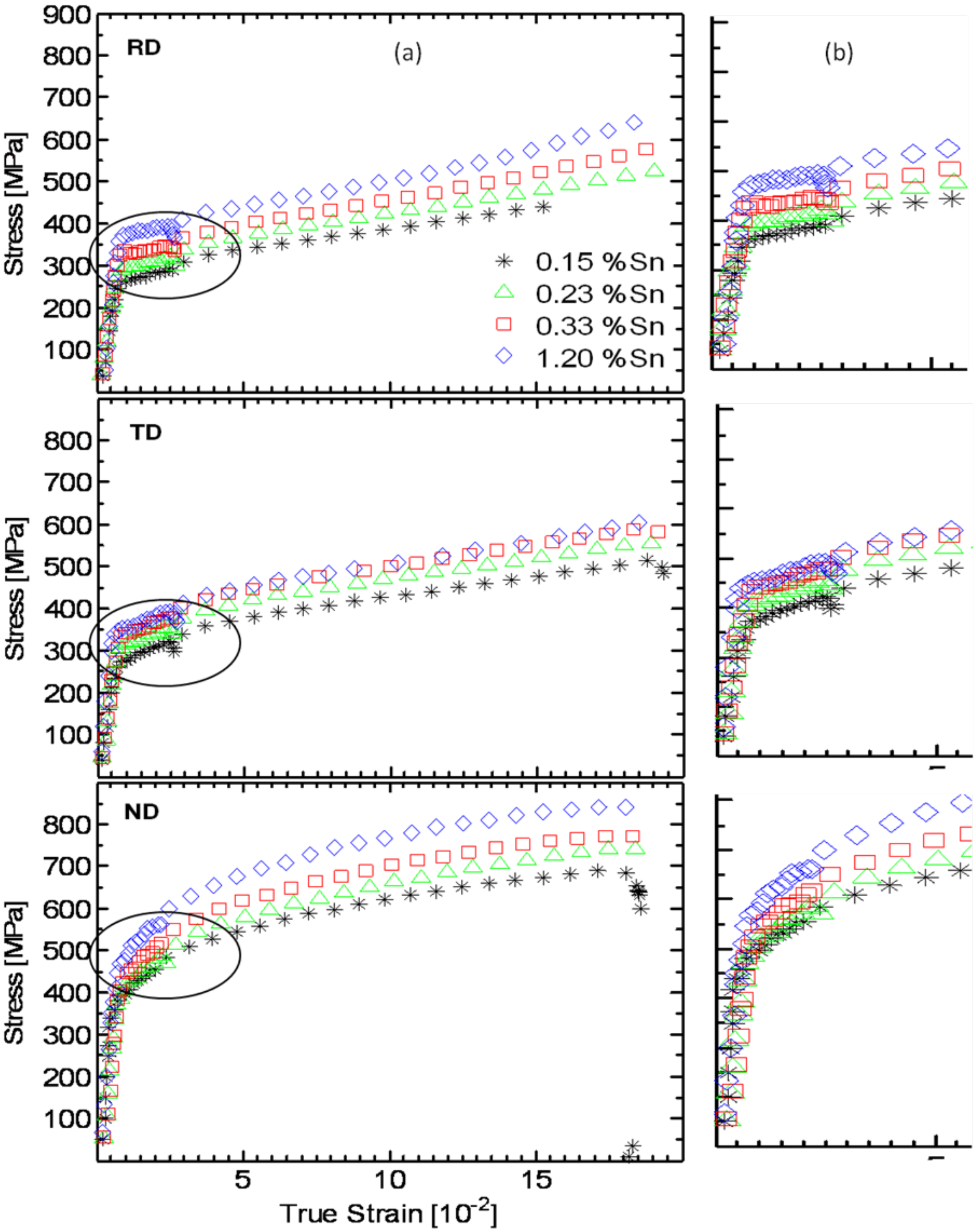

Figure 7.3: (a) Flow curves of the Zr-Sn alloys subjected to compression experiments along three different directions, i.e., RD, TD, and ND. (b) Zoomed in version of the circled parts of (a), *i.e.*, low plastic strain regime.

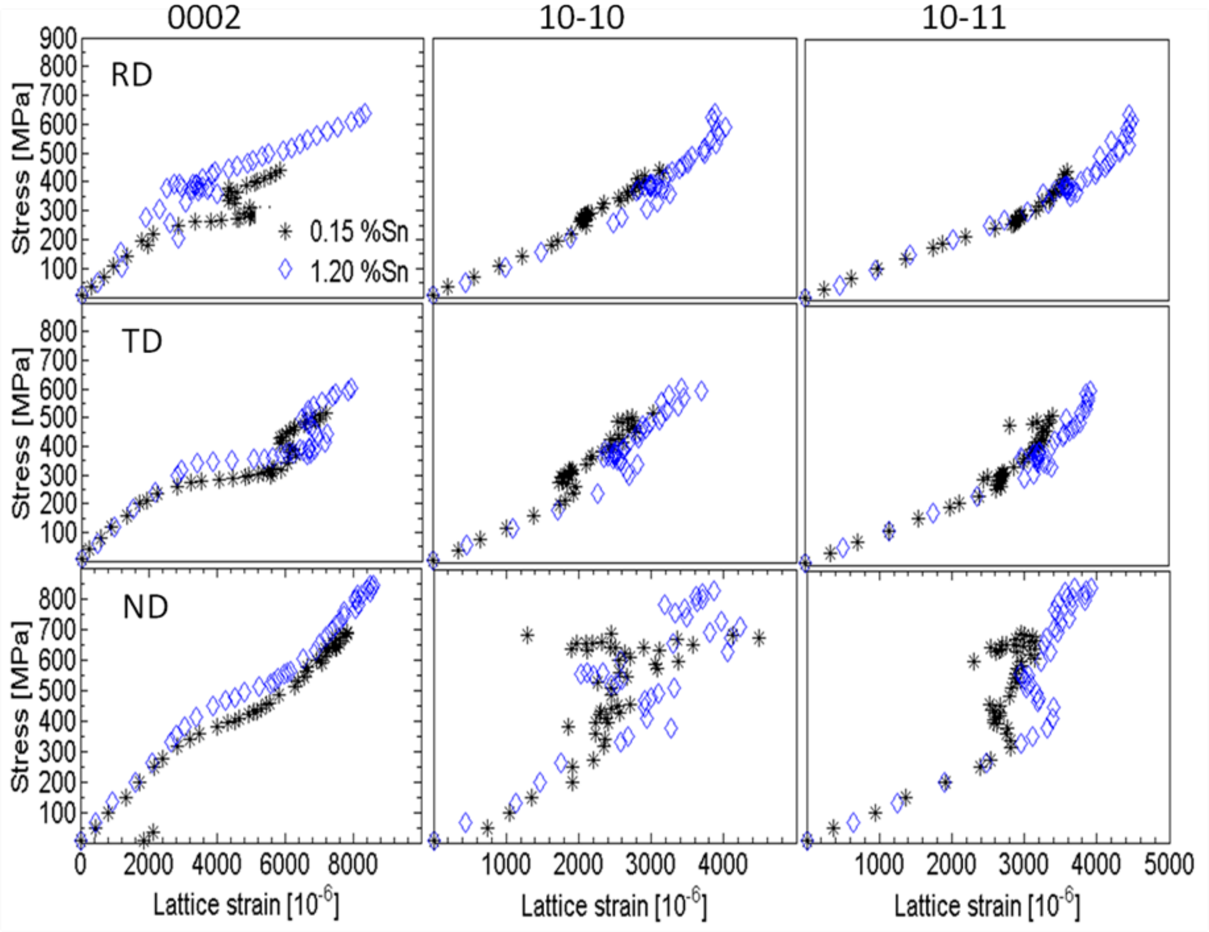

Figure 7.4: Evolution of compressive intragranular strains of grain families corresponding to 0002, $10\bar{1}0$ and $10\bar{1}1$ reflections for Zr-0.15%Sn and Zr-1.2%Sn during deformation along RD, TD and ND. For the purpose of clarity only two alloys (representing extremes of composition) are shown in the figure. The behaviour of the excluded alloys lied in between these two alloys. The data is computed from the peak shift of the respective reflections as recorded by the longitudinal detector. Thus the strains correspond to those along the loading direction of the sample.

unload followed by a continued increase in build up of lattice strain. As discussed in the next section, this unloading can be related to twinning type characterized by the orientation relationship $10\bar{1}2 < 10\bar{1}1 >$ commonly known as "tensile twinning". This twinning mode rotates the $\langle c \rangle$ axis by about 85° from a tensile (here transverse loading direction, tensile stress is the result of Poisson effect) towards a compression direction (here loading direction). Therefore, after the onset of twinning, the 0002 grain family detected along RD is made up of both pre existing 0002 grains and the reoriented 0002 twinned volumes. The observed unloading is a result of relatively lower elastic strain of the twinned volumes (as twinning is essentially a stress relaxation mechanism).

4. The stress at which the onset of twinning was observed, now after referred to as critical stress for twin nucleation, (indicated with a horizontal line in the Fig. 7.5 was found to increase with increasing Sn content.

7.3.3. Nucleation and Evolution of Twinning

In *hcp* materials like Zr, most common twin mode is the 85° tensile twin under the uni-axial compressive deformation. Under the measurement conditions used in the present study, see section 7.2, formation and evolution of such twins shall result in appreciable change in measured intensity of 0002 reflection from one detector to another. This is because of the 85° rotation involved in the formation of this kind of twins. Thus we employ change in the integrated intensity of 0002 reflection as a function of applied stress and strain (during *in-situ* experiments) to determine the critical stress and strains needed for the onset of twinning and monitor evolution of the twinning during the deformation. Fig. 7.6 collates data of change in integrated intensity of 0002 reflection as seen by longitudinal detector (*i.e.*, along deformation direction) for all RD, TD and ND deformations. Following inferences can be drawn from the figure.

1. Extent of twinning (as measured by change in integrated intensity) was highest for deformation along RD, followed by deformation along TD. ND deformation, however, did not show any detectable change in intensity indicating no twinning occurred in this case.

2. In case of deformation along RD, there was a clear and strong effect of Sn. Higher Sn corresponded to higher extent of twinning. In contrast, the extent of twinning for TD deformation was practically independent of Sn content. While the lowest Sn alloy had

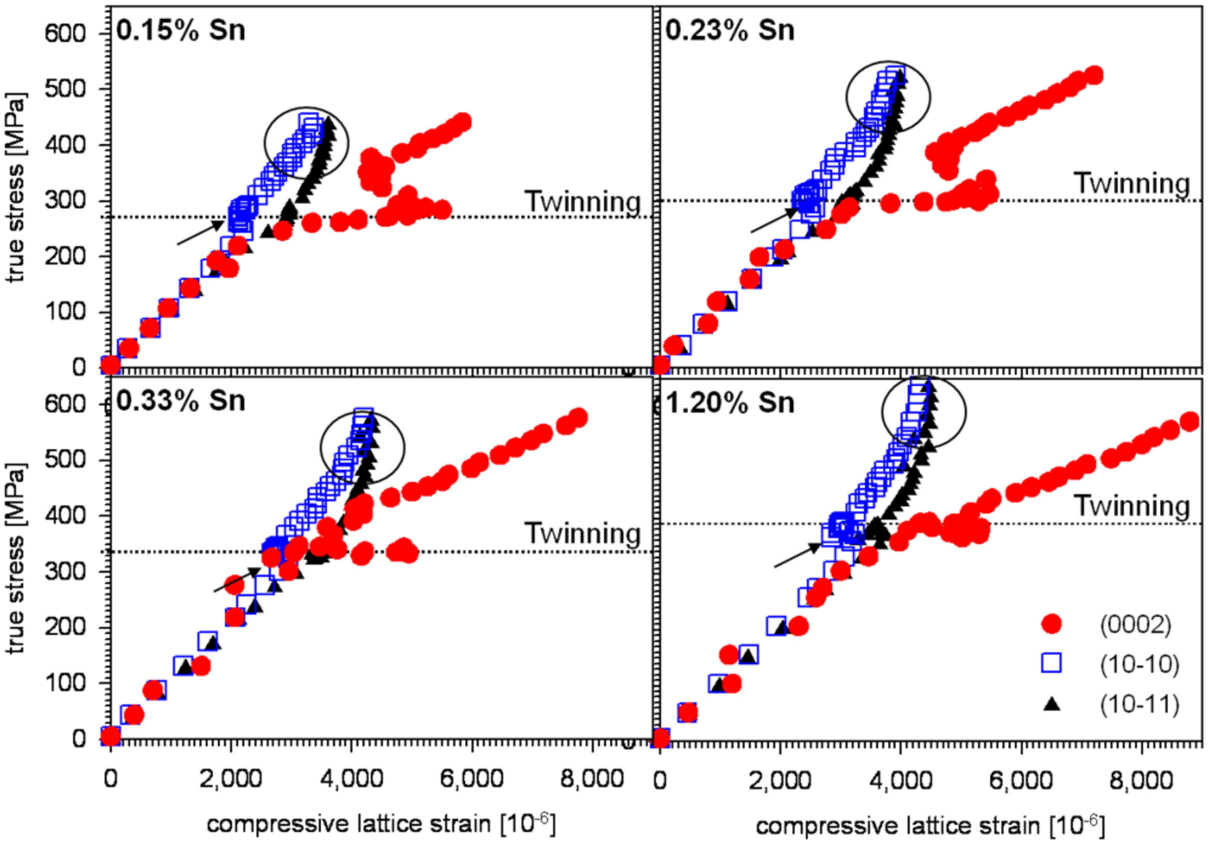

Figure 7.5: Evolution of elastic lattice strains, along the loading direction for RD deformation samples, for the three families of orientations (0002, $10\bar{1}0$ **and** $10\bar{1}1$) **during *in-situ* compressive loading and neutron diffraction experiment for all the four Zr-Sn alloys used in the present study. The horizontal dotted lines in the plots represent the macroscopic applied stress at which onset of twinning was observed. Circled regions highlight the fact that with increasing Sn content, the differences between the** $10\bar{1}0$ **and** $10\bar{1}1$ **responses (*i.e.*, separation of the respective curves) decreases. Increased extent of unloading of the** $10\bar{1}0$ **family of grains with increasing Sn content can also be observed (marked with the arrows).**

experienced a change of 1500% in 0002 intensity (nominal values) for a macroscopic true strain of 0.15, sample with 1.2%Sn had seen 3200% change in the 0002 intensity for the same strain for deformation along RD. In case of deformation along TD, however, these two samples had seen a similar change of only 300% in the intensity of 0002 reflection, signifying near independence of extent of twinning on the Sn content for deformation along TD. It may be emphasized that although extent of twinning in TD is lower than RD, it was nevertheless quite significant in TD unlike ND.

3. The critical strain needed for the onset of twinning in both RD and TD deformations was fairly independent of the Sn content. On the other hand, critical stress required for the same was seen to scale with the alloy's Sn content in both RD and TD deformation.

The *in-situ* loading/diffraction experiments have also thrown light on the actual intragranular strains (and conversely stress state) of the parent grains which underwent twinning, Fig 7.7. This was achieved by monitoring the peak shifts of the 0002 reflection using transverse detector. For the sake of clarity, only the results of two extreme compositions for RD and TD deformations were included in the plots. The onset of twinning had been marked on the plots using arrows. As can be seen, the relative difference in the intragranular strains of the twining grains of alloys with different Sn contents is similar for both RD and TD deformations. This suggests that the relative difference in stress state of the grains undergoing twinning in case of high Sn content alloy was fairly similar in both RD and TD with respect to their corresponding low Sn alloys. However, Fig 7.6, shows that alloy with high Sn had far higher twinning volume fraction when deformed along RD than in case when it was compressed along TD. This observation thus implies that although stress state was similar, RD and TD deformation gave rise to wide differences in extent of twining in high Sn alloy. This suggests that stress alone is insufficient to determine the twining behaviour.

Although change in integrated intensity of 0002 reflection did point towards the onset and evolution of twins during evolution, such an observation was still an indirect observation. A direct and conclusive evidence for the twin formation and type of twins would be microstructural characterization by EBSD and TEM. In order to corroborate the *in-situ* loading and diffraction experiments, a detailed microstructural characterization using EBSD was undertaken on the deformed samples.

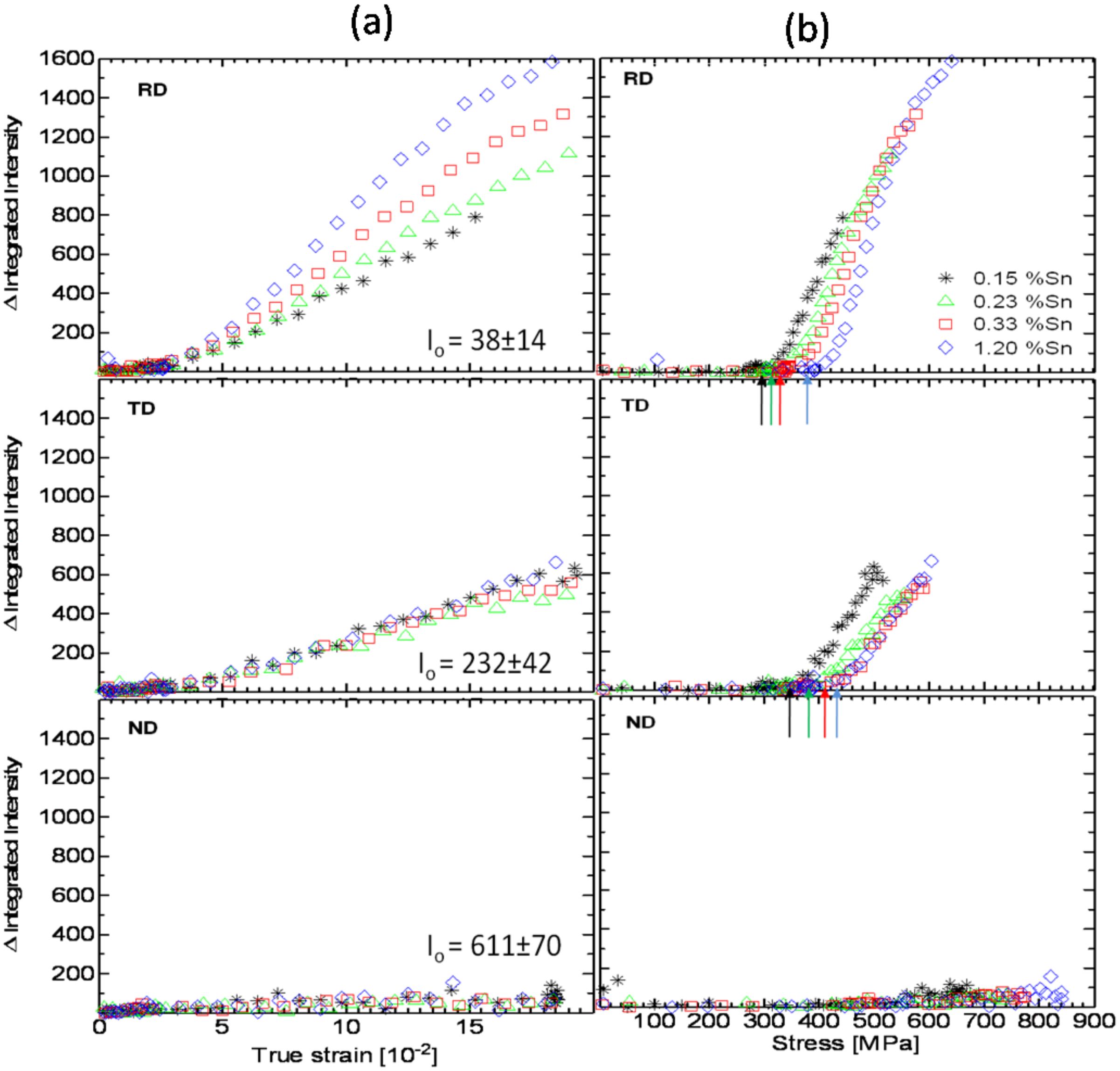

Figure 7.6: Change in integrated intensity of 0002 **reflection for all four alloys as a function of applied (a) strain and (b) stress.** I_o **values included in the plots represent the mean initial intensify of the unloaded (initial state) samples.**

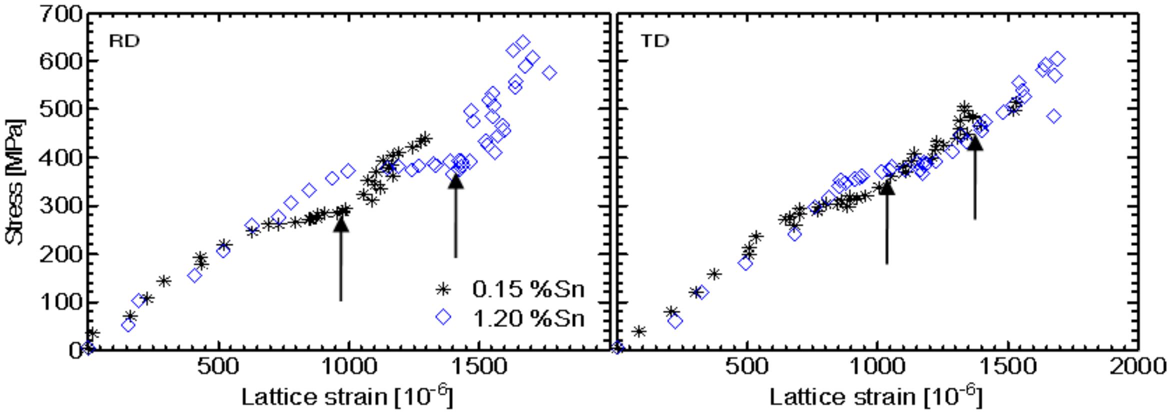

Figure 7.7: Intragranular lattice strain evolution of 0002 family of grains recorded from transverse detector. The inflections in the curves represent the onset of twining and thus the strain state and corresponding stress state at the time of twin nucleation of the parent grains of twins.

7.3.4. Microstructural Characterization of the Deformed Structures

Fig. 7.8 shows the microstructure of the four compositions used in the present study after 10% compressive plastic strain along RD. These deformed microstructures showed that twins were indeed of 85° tensile type, as expected. Further, these microstructures were in full agreement with the *in-situ* loading and diffraction results presented in Fig 7.6, in terms of twin volume fraction. These maps confirmed that volume fraction of twining increased with Sn content, for the RD deformation. Another important observation from these micrographs was the fact that increase in volume fraction of twins in case of higher Sn alloys was due to larger number of twins than due to bigger twins. TEM examination was also carried out for the characterization of the twins, but on samples deformed to a plastic strain of 2-3%, with an objective of understanding the nucleation stage of twins. This strain, as can be seen in the Fig. 7.6, is just sufficient to nucleate the twins in different alloys. As shown in the Fig 7.9, twins of approximately 200nm width were formed at this level of deformation. More interestingly, it was observed that, the grains in which twins could be observed have shown comparatively high dislocation density, indicating significant plasticity by slip.

7.4. Discussion

Three key points emerged from the present study. They are

1. While the extent of twinning strongly depended on Sn content of the alloy in case of compression along RD, the same was virtually independent of Sn content in case of TD

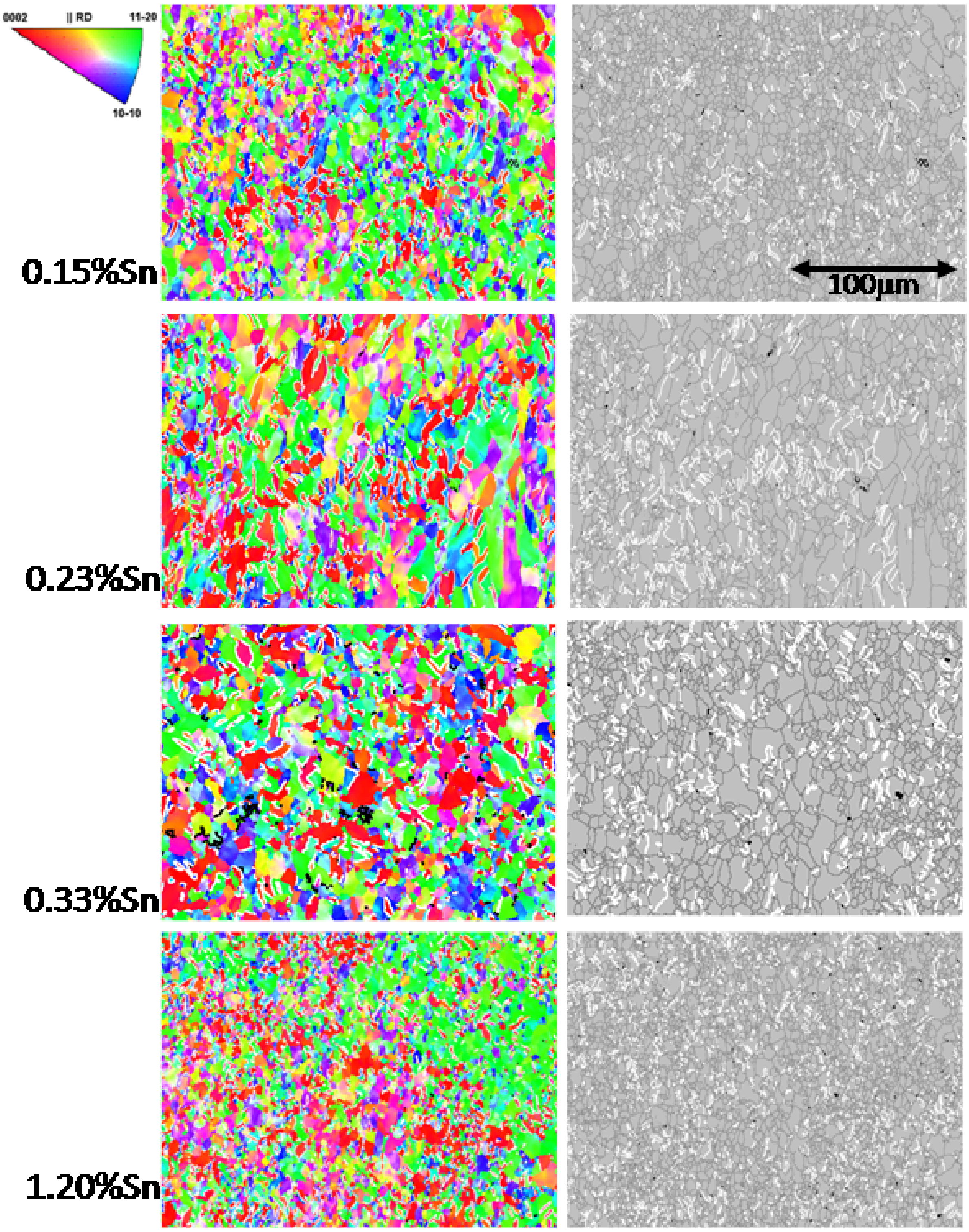

Figure 7.8: IPF color coded EBSD maps showing the twinning behaviour as a function of Sn content for RD deformed samples. These microstructures were recorded from samples subjected to a compressive strain of 10%. The gray scale maps show the twin boundaries (with misorientation corresponding to 85° tensile twins) demarcated with white lines for better visualization of twins.

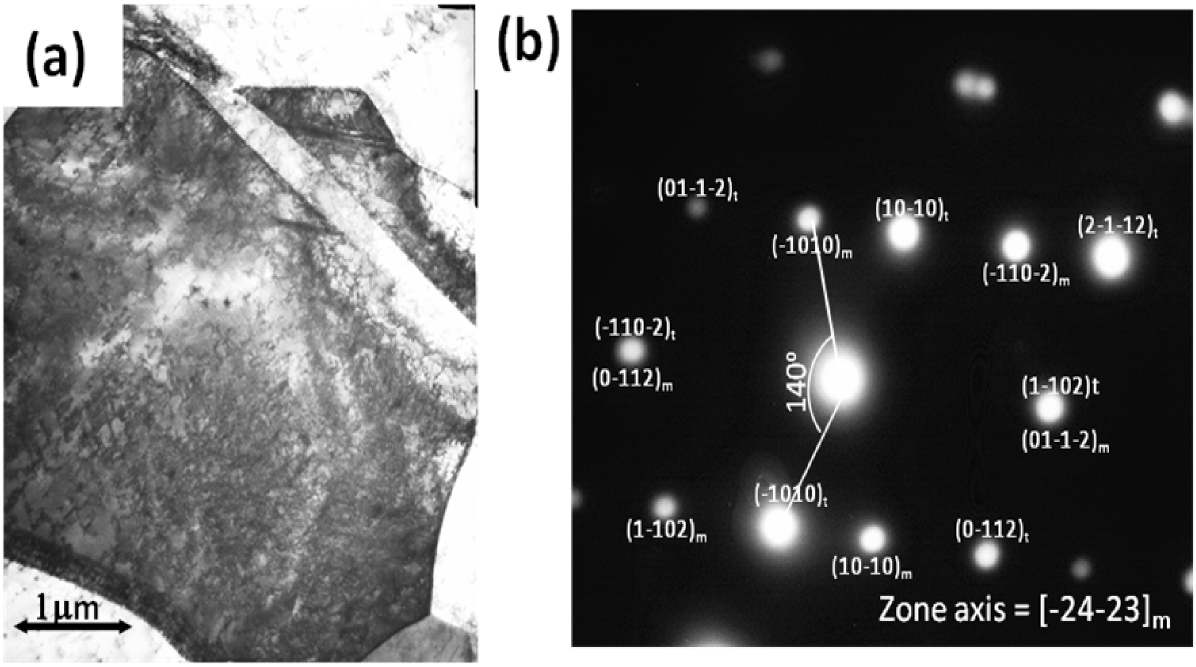

Figure 7.9: TEM analysis with (a) bright field micrograph showing the formation of a twin in the early stage of deformation. The image is from a sample subjected to only 3% compressive deformation, and (b) composite diffraction pattern from the twin and matrix region recorded along $[\bar{2}4\bar{2}3]$ **zone axis of the matrix grain. Misorientation between the matrix and twin is** $140°@[\bar{2}4\bar{2}3]$ **which is symmetrically equivalent to** $85°@[2\bar{1}\bar{1}0]$ **tensile twins.**

deformation.

2. The critical macroscopic strain for the onset of twining was found to be fairly independent of Sn content and deformation direction in both RD and TD. On the other hand, stress required for the onset of twining was observed to be strongly influenced by Sn in both directions of deformation.

3. Increase in Sn content had resulted in increased flat regime of the flow curve in case of RD compression samples. Such effect was distinctly absent in case of compression along ND and TD.

While (1) and (2) are directly concerned with the twining behaviour in the present system, (3) does not, *prima facie*, seem to be directly related with (1) and (2). However, it will be shown that there exists a strong correlation of (1) and (2) with (3). Before showing this correlation it is worthwhile to discuss a bit more on (1). The observed lack of dependence of extent of twinning on Sn for deformation along TD (in stark contrast to deformation along RD, where Sn was seen to influence the extent of twinning to a remarkable degree) might of course arise even if the overall extent of twining is far too low to be detected by the diffraction. In such a situation subtle changes brought by the Sn might be masked by the poor statistics arising out of low twin volume fractions. However, the effect observed here is real and indeed there is no role of Sn in TD deformation as far as extent of twining is considered. Following are the reasons for this assertion.

- Both initial intensity and change in the same for 0002 reflection for the TD deformation were significant, rendering confidence in statistics of the diffraction data, see Fig 7.6.
- The volume of the sample probed by *in-situ* neutron diffraction was close to $96mm^3$, containing close to 2 million crystals (assuming a mean size of $10\mu m$ of grains). Thus issues of under sampling are not expected to arise.
- Microstructural observations also supported the diffraction results and showed relative lack of Sn effect on the twin volume fraction for TD deformation.
- Even the macroscopic flow behaviour had signatures of lack of Sn effect on the twining. As can be seen in Fig. 7.3, RD deformation had shown increased strain hardening (slope of the curves) with Sn at larger strains. This can be attributed to hardening arising out of twinning at larger strains. On the other hand, flow curves determined using compression along TD, did not show any change in the strain hardening at larger strains as a function of Sn content. This signifies that the extent of twinning was rather similar in all Sn bearing alloys for this deformation direction.

Thus we infer that role of Sn in terms of extent of twinning was indeed less significant in TD deformation when compared to RD compression. The anomalous ‘flat response’ in the stress-strain behaviour of the alloys (observation (3)) was earlier attributed to the possible presence of the residual stresses in the undeformed samples. Wide differences in the thermal expansion coefficients along the $\langle a \rangle$ and $\langle c \rangle$ axis of the unit cell of the *hcp* crystal was the rationale behind such an argument. Present study clearly brought out that ‘flat response’ increased with Sn content and thus the argument of residual stresses in the alloy can’t be used in the present case. On the contrary, present results exemplify a specific slip mode getting more affected due to Sn than the others. The initial texture of the samples subjected to compression along RD was such that a majority of the grains had favorable orientation for the prismatic slip, *i.e.*,$\langle a \rangle$ type slip on prismatic planes. Previous works have shown that the $\langle a \rangle$ type dislocations in *hcp* Zr undergo dissociation into partials creating a stacking fault. Addition of Sn to Zr is known to dramatically decrease the stacking fault energy of the system. Fig. 7.10, depicts the experimental information obtained from Ref [182] on the change in SFE as a function of the Sn content in Zr. It is amply clear that addition of Sn results in significant drop in SFE of Zr. Further it is also apparent that drop is more prominent at lower Sn additions and saturates for higher Sn contents. This explains the observed non linear effect of Sn on the change in flow stress, see Fig. 7.3. The drop in SFE should, in principle, increase the stacking fault width and thus inhibit non-planar slip (cross slip). Thus increased Sn content, apart from increasing the initial barrier for dislocation motion, is likely to increase the planarity of the slip. This has the effect of decreasing the potential strain hardening, thus explaining the observed flat response regime in case of RD compression tests. The absence of such a marked flat response in case of ND compression tests further substantiates above argument. In case of the ND compression, a majority of the grains have orientation not conducive for the prismatic $\langle a \rangle$ slip, but are amenable for the relatively harder pyramidal $\langle c + a \rangle$ slip. This explains the observed higher flow stress for ND compression tests. Since the $\langle c + a \rangle$ dislocations have a non planar core structure, they are expected to only show higher yield stress with higher Sn content but are not supposed to get influenced by the change in SFE due to the addition of Sn. Thus we did not see any flat response in ND compression tests. Thus the experimental evidence of the present study suggests $\langle a \rangle$ type slip getting more affected and becoming increasingly planar with increased Sn content and leading to high strain accumulation at relatively lower stress values. This can have an important bearing on the twinning behaviour of the samples as a function of Sn content.

As far as twinning is concerned, present results show that RD compression had highest extent of twinning followed by TD and virtually absent in case of ND compression. The fact that 85° tensile twin requires tensile stress along $\langle c \rangle$ axis can explain this observation, as the initial texture of the material renders such stress state to exist more in case of RD than in TD for a majority of grains. However, the remarkable point to be noted here is this. In case of RD deformed samples, both low Sn and high Sn alloy had similar starting texture but had wide differences in their extent of twining. Fig. 7.7 shows that higher Sn alloy had higher operating stress (macroscopic) at the time of twin onset. One might attribute the higher twinning volume fraction in case of high Sn alloy to this high stress. If this argument were true, TD deformed samples must also show differences in their twining extent as a function of Sn content. As Fig. 7.6 amply illustrated, extent of twining was fairly independent of Sn content for TD deformation. It may be recalled that the ‘difference in the stress’ state of the low and high Sn

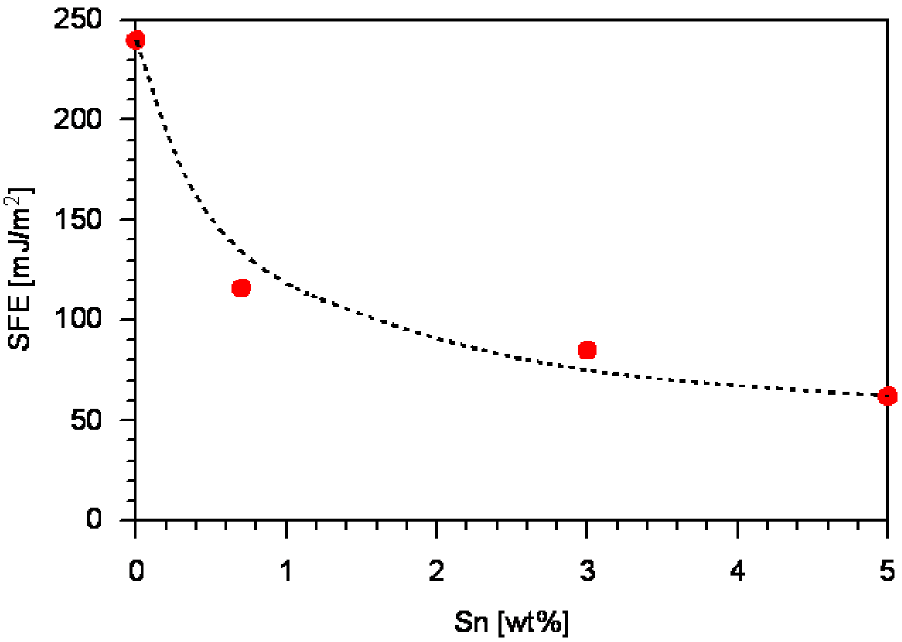

Figure 7.10: Change in stacking fault energy of Zr with Sn. Plotted using the data from [182]

alloys at the onset of twining was indeed same for RD and TD deformation, Fig 7.7. In fact, the absolute value of the stress was higher in case of TD samples. Thus stress state alone can't explain the observed strong effect of Sn on twinning in RD and absolute lack of it in TD case.

To probe if the alloys with different Sn contents in RD and TD, had any other differences that might help us explain the observed behaviour, we resort to analysis of peak broadening. Peak broadening during the plastic deformation is an indication of the dislocations density/activity in the grains contributing to the peak and thus serve as finger prints of the plastic flow activity [183, 184]. Since the macroscopic stress-strain behaviour, by way of changing flat response, has given indications of wide differences in $\langle a \rangle$ slip between the alloys with different Sn contents, $11\bar{2}0$ reflection was chosen for the analysis, as this reflection gets most influenced by the $\langle a \rangle$ type dislocations. The results are illustrated in Fig. 7.11. It is clear that in case of RD deformation, there was clear distinction between lowest and highest Sn alloy. No such distinction could be made in case of TD deformation. This result corroborates well with the observed flat regime in RD and lack of it in TD. The FWHM evolution of $11\bar{2}0$ confirms the higher activity and build up of the $\langle a \rangle$ type dislocation before onset of twinning in case of sample with higher Sn for RD deformation. Thus, though the macroscopic strain observed before the onset of the twinning was seen to be same for all samples with different Sn contents, microscopically, the orientations which had undergone twining, must have had very high strains and consequently dislocations, built up before the onset of twining, particularly the higher Sn content samples in case of RD. Further, the fact that only a set of favorable orientations can take part in initial deformation signifies that the actual strain by the twining orientations is much more than the what was observed macroscopically. In addition, relatively higher dislocation density observed in the parent grains of the twins at the nucleation stage also supports this conjecture (see Fig. 7.9.a). Thus a possible sequence of events could be : (a) activation of prismatic $\langle a \rangle$ slip in the favorably oriented grains and the build up of sufficient density of $\langle a \rangle$ dislocations and their consequent interaction with the twining dislocations (b) once the threshold stress was available, nucleation and growth of the twins. Thus for the higher Sn samples that were deformed along the RD, the increased planarity of the slip caused by the increased Sn content must have resulted in higher build up of dislocation density (through activation of existing frank read sources [17, 155]) before the critical stress for twin nucleation had reached. This must cause higher number of twins to nucleate and consequently get reflected as increased extent of twining with Sn content. TD deformation on the other hand, must have significant contribution from the pyramidal slip as well and thus the change in the contribution from the prismatic $\langle a \rangle$ slip with Sn, becomes insignificant. This got reflected in undetectable differences in the samples with different Sn contents of their FWHM before the twinning.

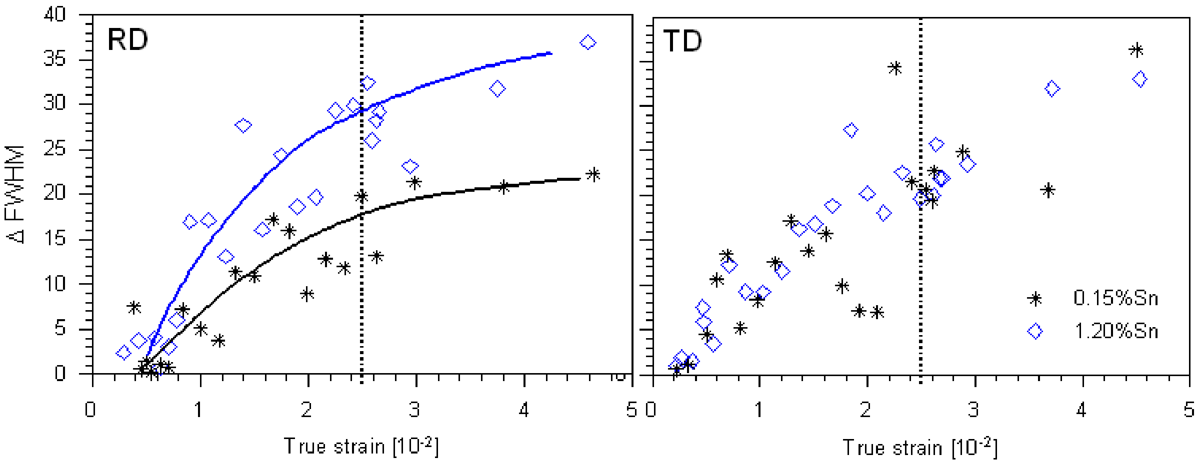

Figure 7.11: Change in the FWHM for 11$\bar{2}$0 reflection as recorded by the longitudinal detector during the *in-situ* neutron diffraction experiments. The vertical lines in the figure represent the strains at which onset of twining was detected. It is clear that in case of RD deformation high Sn alloy had much higher stored energy (correlated by high FWHM) compared to the low Sn alloy. TD deformation on the other hand does not show such distinction between low Sn and high Sn alloy.

Thus we may draw a conclusion that the available dislocation density (or pre existing strain) at the time of the available critical stress determines the density of the twin nuclei and consequent twin evolution. In case of RD deformation, higher Sn alloy had higher plastic strain in the potential twinning grains, making more nucleation sites available. These contributed to observed higher extent of twining (through larger number of twins rather than smaller number of bigger twins) in case of high Sn alloy for RD deformation. On the other hand, TD deformation did not show appreciable differences in the high and low Sn containing alloys in terms of their dislocation densities of the potential twining grains, making both of them behave similarly in terms of twinning extent, even though high Sn alloy was stronger and had higher stress available for twin formation. Thus results indicate that the extent of twinning is nucleation controlled than growth controlled. In summary present study clearly brings out that although stress state is important for the formation of twins, twining behaviour is (in terms of extent) is governed by the pre strain (dislocation density, particularly $\langle a \rangle$ type) in the potential twining grains. Thus the deformation models incorporating twining should consider the local plastic strain in addition to the stress state for inducing twining.

7.5. Conclusions

Present investigation using *in-situ* neutron diffraction cum deformation on Zr-Sn binary alloys had tried to bring out the role of Sn on deformation mechanisms in general and and on twinning in particular. Following are the major conclusions that could be drawn

1. The role of Sn on the deformation mechanisms (twinning in particular) was seen to be deformation direction (or orientation) dependent. It was observed that deformation along RD was characterized by huge influence of Sn on the extent of twinning while the deformation along TD was found to be least sensitive to amount of Sn of the alloy for the extent of twinning.

2. In general (for both RD and TD deformations) it was observed that the critical stress required for the twining increased with the Sn content while the critical macroscopic strain for the onset of twinning was rather insensitive to the amount of Sn of the alloy.

3. Using the combined evidence of EBSD, TEM and neutron diffraction it was inferred that there needs to be some critical plastic strain for the initiation of twinning. Thus it is suggested that the modeling efforts aimed at capturing the twining behavior must necessarily account for the local strain in addition to local stress state of the grains undergoing the twinning.

CHAPTER 8

Effect of Crystal Orientation on Homogeneous Nucleation of Dislocations in Zr

8.1. Introduction

Having seen the effects of crystallographic orientation on the plastic deformation behavior of the *hcp* Zr (in other words on the behavior of dislocations) in the previous chapter, it is natural to look into more fundamental issue of “if such effects exist at much more fundamental level of homogeneous nucleation of dislocations”. While the motion of the dislocations was well understood to be chiefly governed by the available resolved shear stress via Schimd’s law [155, 185, 186], the very formation of such dislocations has however, been not so well understood. Some pioneering studies on this issue have been reported in the recent past in case of *fcc* systems which gave rise to some interesting insights into the nucleation phenomenon of the dislocations [185, 186]. However, these were limited to cubic crystal symmetry [135, 187, 188] and the situation in case of *hcp* is expected to be very different from these because of the following considerations.

1. Because of lower symmetry of the *hcp* crystal compared to its *fcc* counterpart, the role of the orientation (or deformation direction) is expected to be more prominent [3, 9].
2. Unlike in *fcc* crystals where, unique slip systems (of $\{111\}<110>$ [1, 155]) are found experimentally, there exists several alternate slip systems in *hcp* crystals (*e.g.* basal, prismatic and pyramidal [39, 40, 121, 123]).

Thus in the present part of the thesis it was aimed to investigate the fundamental dislocation nucleation event in case of *hcp* Zr and its dependence on the loading direction as a function of deformation temperature and directionality of loading (*i.e.* tensile vs compressive deformation). Essentially same simulation approach as that of the [185] had been followed in this work as well. However, simulation of *hcp* crystals differs from that of their *fcc* counterparts particularly in terms of crystal generation and analysis of the dislocation networks that get generated during the simulation. These have been explained in the next section followed by the results and discussion.

8.2. Simulation Setup and Methodology

8.2.1. Generation of *hcp* Crystal Orientations

In order to capture the homogeneous nucleation of the dislocations, we need to have a defect free ideal crystal. Further, to study the effect of crystal orientation (alternately, loading direction) we need to generate the model crystals in different crystallographic orientations. In case of materials with cubic symmetry (*e.g. bcc* and *fcc*) creating model crystals in arbitrary orientations is a trivial task. However, the same is not the case in case of *hcp* crystals. This arises from the fact that we need to generate a crystal of appropriate dimensions along the three orthogonal directions of the simulation box to maintain periodicity (for simulating the infinite crystal) which requires that the each dimension of the box be an integral multiple of the lattice vector in that direction. For *hcp* materials like Zr which have non-rational c/a ratio, this condition can't be satisfied. In order to circumvent this problem, we relax the condition of strict orthogonality of the three basis vectors, and instead chose three such vectors which are perpendicular to each other within a tolerance of 1°. Even then not all orientations can be practically handled due to extremely large lattice vectors and correspondingly large simulation boxes for many of the orientations (especially for those orientations in which c axis of the *hcp* unit cell makes a non zero angle with all of the unit vectors of the simulation box. Attention must also be paid to overall shape of the simulation box. For avoiding the artifacts in the simulation results, simulation box should be as far as possible equal in dimensions along all three principle directions. Thus only few set of orientations can satisfy these conditions. In order to chose an appropriate dimension of the simulation box that is small enough to facilitate faster computation but large enough to eliminate size effects on the results, a series of trial simulations with different simulation boxes (accordingly different number of atoms or system sizes) have been performed. These had shown that a minimum 150 Å is needed to get converged values of stress needed for dislocation nucleation in this system. Accordingly all the orientations have been generated keeping the box dimension to be smallest 'integral multiple of the lattice vector' beyond 150 Å along that direction of the box. For each orientation, the uni-axial deformation has been simulated along three directions. Fig. 8.1 shows these directions in the crystallographic reference frame.

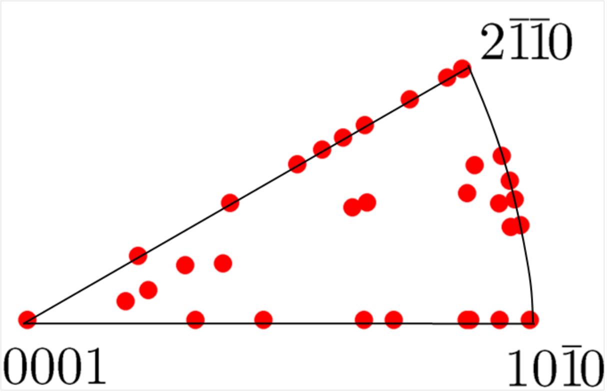

Figure 8.1: Representation of crystallographic directions along which uni-axial tensile and compressive deformations have been simulated to bring out the effect of orientation.

8.2.2. Simulation Details

A parallel molecular dynamics code (LAMMPS) is used to deform the single crystal atomistic models [73]. EAM potentials [189] presented in [190] were used for the inter atomic potentials. Thes potentials have been succesfully used in the past for the modeling of dislocation core structures in the Zr[151, 191]. First, the configuration is equilibrated using MD in the isobaric-isothermal (Normal Pressure and Temperature (NPT)) ensemble at a pressure of 0 bar and a temperature of either 10 or 300K for 10 ps [192]. This step has the effect of relaxing any internal strains/stresses (arising due to use of non-ideal lattice parameters) and also due to relaxation of orthogonality of the basis vectors used for the generation of the crystal (see section 8.2.1). Next, the configuration is deformed in uni-axial tension/compression at a constant strain rate of $10^9\ s^{-1}$ with a stress-free condition for the other two boundaries. The system stress is calculated using the virial definition without the kinetic portion [193], i.e.,

$$\boldsymbol{\sigma}_{\alpha\beta} = \frac{1}{V}\sum_{i}^{N^*}\sum_{j\neq i}^{N} f_\alpha^{ij} r_\beta^{ij}, \tag{8.1}$$

where f_α^{ij} is the force vector between atoms i and j in the direction α, r_β^{ij} is the distance vector in direction β, N is the number of neighbor atoms for atom i, N^* is the total number of atoms in the simulation cell, and V is the simulation cell volume. The volume averaged stress tensor $\sigma_{\alpha\beta}$ is the same as the global stress used in previous works. Similar to the previous works in this field, the stress required for dislocation nucleation is defined as the maximum uni-axial stress reached during the simulation.

Simulations were preformed for both tensile and compressive deformations to bring out the tension/compression asymmetry. A typical simulation involved, generation of crystal with given orientation and dimensions ensuring periodicity along all three directions followed by energy minimization. This step ensures relaxing the atomic positions to the optimum positions for further equilibration and consequent thermal equilibration. The minimized atomic configuration is then subject to equilibration at the desired temperature followed by actual deformation simulation along the chosen direction $(X, Y or Z)$. In order to save computation time, a given orientation is equilibrated for a given time and the same equilibrated configuration was saved and used for all of the deformations along the three principal directions. During the deformation step both the atomic configurations and the system's properties such as volume, energy *etc.* are periodically dumped and monitored for the capturing of the dislocation nucleation event. Nucleation was identified initially by monitoring the sudden drop in the applied stress during the simulation. This stress, *i.e.* the maximum stress of a given simulation was taken as the critical stress for nucleation of the dislocations for that particular deformation direction.

8.2.3. Analysis of Atomic Configurations for Identification of Dislocations

In addition to capturing the critical stresses and strains for the nucleation of the dislocations, it is also important to characterize the basic properties of the dislocations such as their Burger's vector, slip plane *etc.* For this purpose algorithm proposed by Stukowski *et al.* was employed [194–196]. Following were the steps followed for the analysis of the atomic configurations resulting from a typical MD simulation.

1. Identification and isolation of the atomic clusters (defect clusters) not belonging to model *hcp* configuration. This was done by using the Common Neighbor Analysis (CNA) analysis available in the LAMMPS software.

2. Selection of those defect clusters which satisfy certain criteria of having a minimum number of atoms beyond a threshold value and be sufficiently away from the simulation box boundaries (to avoid artifacts to due to clusters present at boundaries). This had eliminated tiny clusters of defect atoms which arose due to thermal noise and retained only the potential dislocation loops for the further analysis.

3. Determination of the slip plane of the dislocation loops

   (a) Identified the bounding box of the all of the defect atoms of a given cluster.
   (b) Found out the rotation $\mathbf{R}$ needed to be applied on to the defect cluster to make the volume of its bounding box minimum. The standard optimization algorithms available in the field of mathematics which can minimize any arbitrary objective function were employed for this purpose. Here the objective function was the volume of the bounding box for a given rotation applied to it.
   (c) The plane normal $\overrightarrow{n^{local}}$ of the largest face of the resulting bounding box was assgined to be the slip plane of the dislocation loop concerned.
   (d) This was followed by rotating back the plane normal $\overrightarrow{n^{local}}$ by the inverse of the rotation $\mathbf{R}^{-1}$ to get the actual plane normal in the global frame of reference $\overrightarrow{n^{global}}$.
   (e) Further the cartesian vector so obtained (n^{global}) was converted into the equivalent crystallographic frame $n^{Crystallographic}$ by applying the transformation

$$\overrightarrow{n^{Crystallographic}} = \overrightarrow{n^{global}} \times \mathbf{R}^{crystal}, \tag{8.2}$$

   in which the $\mathbf{R}^{crystal}$ is the orientation matrix expressing the orientation of the simulated crystal.

4. Determining the Burger's vector $\overrightarrow{\mathbf{b}}$. [1]
   (a) Isolated part of the crystal volume containing the defect cluster to be analyzed along with some finite thickness of the '*good atoms*' for the analysis.
   (b) Constructed a plane perpendicular to the dislocation loop's plane.
   (c) Made a complete circuit (*Burger's circuit*) of atoms lying in the plane using atomic positions from the ideal (undeformed) crystal. The size of the circuit should be sufficiently large to encompass the dislocation loop to be characterized, but small enough to be as close to the boundary of the loop being investigated as possible. Ensure one of the arms of the loop actually passes through the defect cluster when translated to the defect crystal to be analyzed.

---

[1] This is a simplification of a more sophisticated algorithm of the Stuoski *et al.* The original algorithm had been modified in the present work to enable extraction of Burger's vector even in the absence of the so called '*good atoms*' at the center of the dislocation loop. Hence the algorithm is explained in very brief and the details can be found at [194–196]

(d) Start with an arbitrary atom with position vector $\overrightarrow{P_i^{ideal}}$ in the selected *Burger's circuit* and proceed to next atom $\overrightarrow{P_j^{ideal}}$ to find the atomic translation vector $\overrightarrow{t_{i\to j}^{ideal}} = \overrightarrow{P_j^{ideal}} - \overrightarrow{P_i^{ideal}}$ connecting the two in the ideal crystal.

(e) Apply the same translation vector on to the selected atom of the defect crystal. In the case of presence of a dislocation, the translation $\overrightarrow{t_{i\to j}^{ideal}}$ applied shall not result in the position of the next atom but instead results in position offset by an error $\epsilon_i = \overrightarrow{P_j^{defect}} - (\overrightarrow{P_i^{defect}} + \overrightarrow{t_{i\to j}^{ideal}})$

(f) The Burger's of the dislocation loop is then the summation of all of the errors when the initial position is reached.

$$\overrightarrow{\mathbf{b}} = \sum_{i=1}^{n} \epsilon_i \tag{8.3}$$

8.3. Results and Discussion

Fig. 8.2 shows typical stress-strain response during tensile deformation along three different crystallographic directions. The differences among the three curves clearly brought out the role of the crystallographic orientation on the stress strain behavior of the Zr in general, and the critical stress for the nucleation of the dislocations in particular. Apart from the differences in the maximum stress reached (which corresponds to the critical stress for homogeneous nucleation, the curves also differed in the manner in which the stress dropped from the peak stress. On the other hand the critical strain at which the dislocation nucleation event was observed was found to be not too sensitive to the deformation direction (in other words the crystal orientation). Fig. 8.3 depicts the time evolution of the dislocations during the simulation.

Fig. 8.4 summarizes the results of the simulations for the dependence of the critical stress on the deformation direction. Following are key results that points emerged from the study.

- There is a considerable asymmetry in the extent of stress required for the homogeneous nucleation of the dislocations in compression and tension. The critical stress required for the nucleation of dislocations was in general was more in case of compressive deformation. Such a behavior is expected because of the fundamental nature of the atomic interactions. The nature of the atomic interactions is such that the potential energy change in the system is much more rapid (steep) when two interacting atoms are brought closer than their equilibrium distance (in other words compressed towards each other) than when

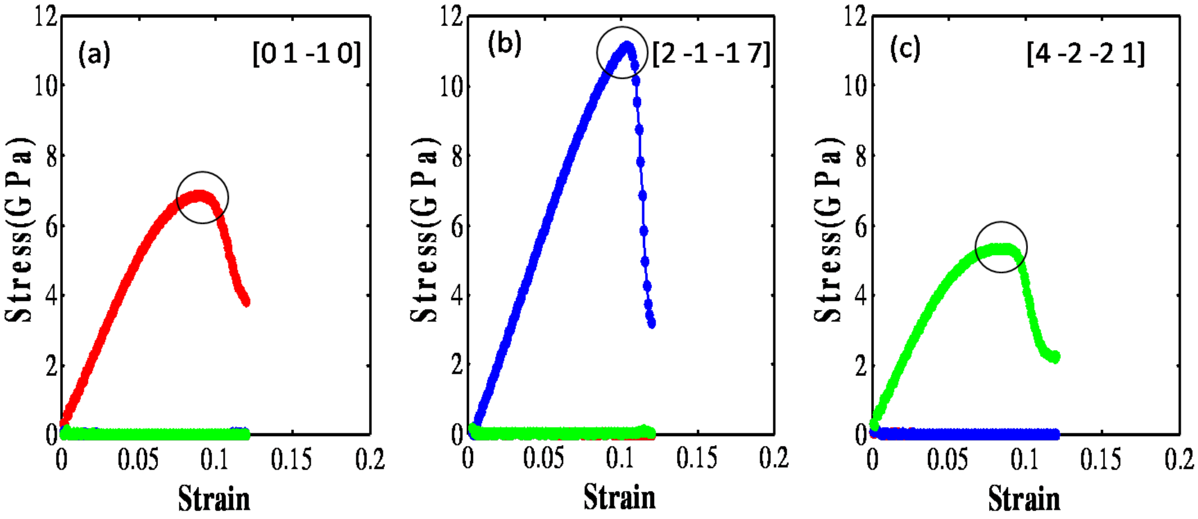

Figure 8.2: The simulated stress-strain response of the single crystal Zr deformed along three different crystallographic directions (a)$[01\bar{1}0]$, (b) $[2\bar{1}\bar{1}7]$ and (c) $[4\bar{2}\bar{2}1]$. The circled regions correspond the critical stress for the dislocation nucleation. The results correspond to temperature of 300K.

they are pulled apart. This asymmetry arises due to the nature of the nuclear-nuclear repulsion being stronger than the nuclear-electronic attraction forces at shorter inter atomic distances. Thus the present simulations do show the expected compression/tension asymmetry in the critical stress for dislocation nucleation.

- The critical stress for nucleation was also found to be decreasing with increasing deformation temperature. Such an effect can be attributed to the higher concentration of the defects generated due to random thermal oscillations of atoms aiding to the applied stress in the nucleation of the dislocations.

- The simulations reveal that the $[2\bar{1}\bar{1}0]$ direction happens to be the strongest direction for compressive deformation while the direction $[0001]$ offered highest resistance for the nucleation of dislocation during tensile deformation. Again this is a consequence of the above mentioned fact. $[2\bar{1}\bar{1}0]$ being a close packed direction of the *hcp* crystal does offer high resistance in compression to let the defects nucleate and grow into dislocations. Similarly, the nucleation of the dislocations, becomes difficult due to lack of sufficient resolved stress on the primary slip systems (*i.e.* prismatic planes of the *hcp*) when loading direction is $[0001]$ during the tensile loading making this one of the hardest directions for the nucleation of the dislocations.

- The detailed analysis of the slip planes of the dislocation loops (using the methodology

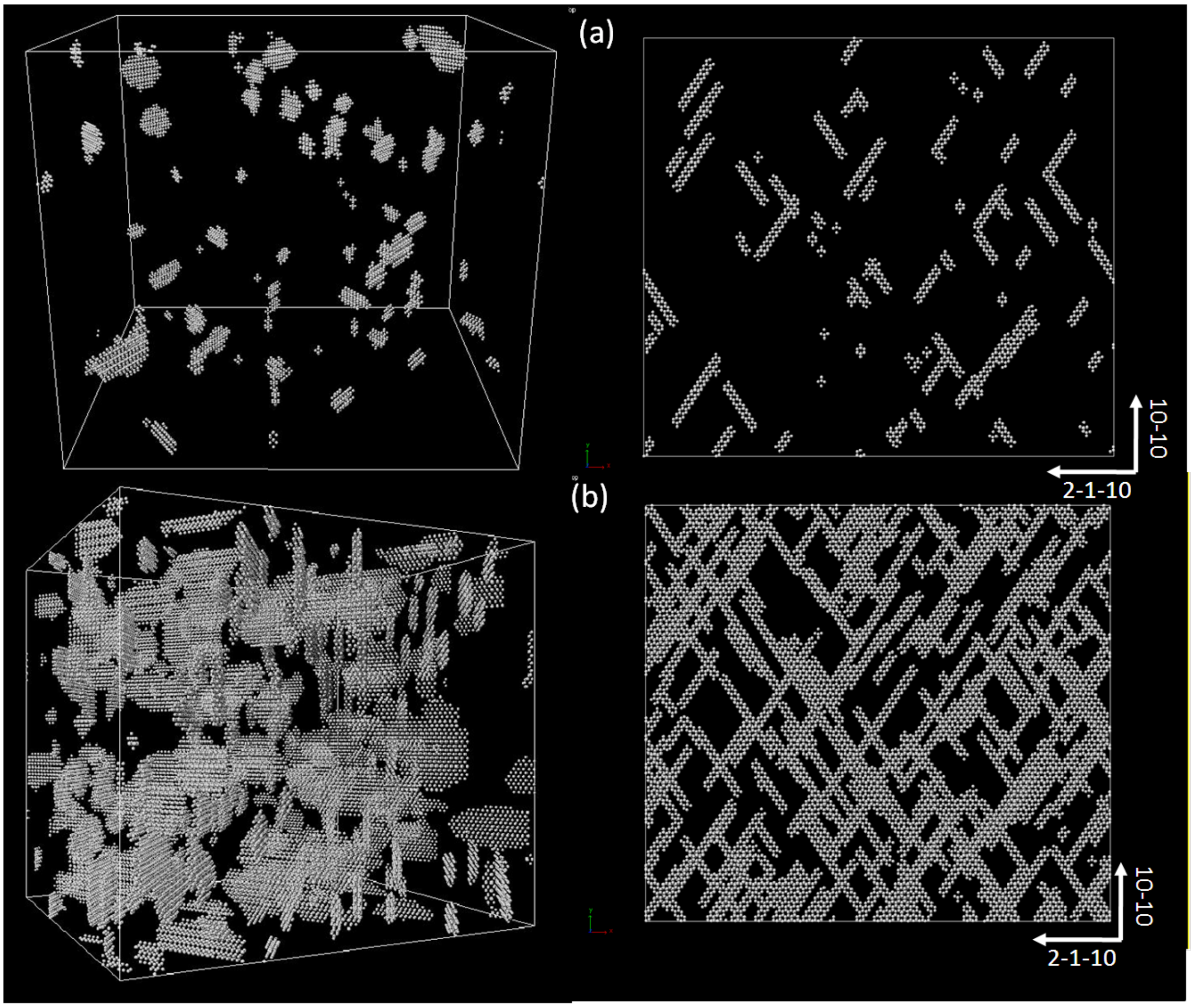

Figure 8.3: Dislocation nucleation as captured by the MD simulation of tensile deformation along $[01\bar{1}0]$ direction of the Zr crystal. (a) Snap shot at the beginning of the nucleation event (corresponding to the peak stress of the Fig.8.2 (a). (b) Snap shot at at an advanced stage of simulation, corresponding to larger strains, showing growing dislocation loops. For the purpose of visualization all the '*good atoms*' *i.e.*, those atoms which have their neighborhood corresponding the *hcp* configuration, are omitted from the image. Two views (isotropic and XY projection) of the same snap shots are presented side by side for gaining insights into the crystallographic aspects of the planes of the dislocation loops. It can be seen that all of them lie on the prismatic planes $< 10\bar{1}0 >$ for this case.

Table 8.1: Number of dislocations found for a particular slip plane for deformation at 10 K

Basal Type of dislocations	606
Prismatic Type of dislocation	819
Pyramidal type of dislocations	869

Table 8.2: Number of dislocations found for a particular slip plane for deformation at 300 K

Basal Type of dislocations	326
Prismatic Type of dislocation	1164
Pyramidal type of dislocations	1239

described in the section 8.2.3) from the simulation snapshots for all of the individual simulation runs is summarized in the tables 8.1 and 8.2. These are the summarized results from a different snap shots of MD simulation runs corresponding to different loading directions. This analysis suggested that the population of the dislocation loops, in general was higher in prismatic planes. The experimental evidence presented by other studies also indicate higher concentration of the dislocations $\overrightarrow{a}$ which are usually expected to move on the prismatic planes in case of Zr. Thus the results of the present study are in agreement with the available experimental information.

- In addition to energetically favorable $\overrightarrow{a}$ type dislocation loops, nucleation of $\overrightarrow{c}$ type of dislocations was also observed. It may be noted that there exists considerable TEM evidence for existence of such dislocations. Thus the present simulations, did predict the formation of the energetically non favorable Burger's vectors in this system in accordance with the experimental evidence. Fig. 8.5 shows the distribution of Burger's vector magnitude, for a particular simulation run showing the presence of the dislocations with non $\overrightarrow{a}$ type Burger's vectors. Presence of the $\overrightarrow{c+a}$ type dislocations, however, was not detected. Thus it appears, based on the present simulations, that homogeneous nucleation of $\overrightarrow{c+a}$ is not easy. But the fact that significant amount of $\overrightarrow{c+a}$ type dislocations are seen in practice suggests that these could be due to the interaction of the $\overrightarrow{a}$ and $\overrightarrow{c}$ type dislocations or form heterogeneously under conditions which could not be simulated in the present set of simulations.

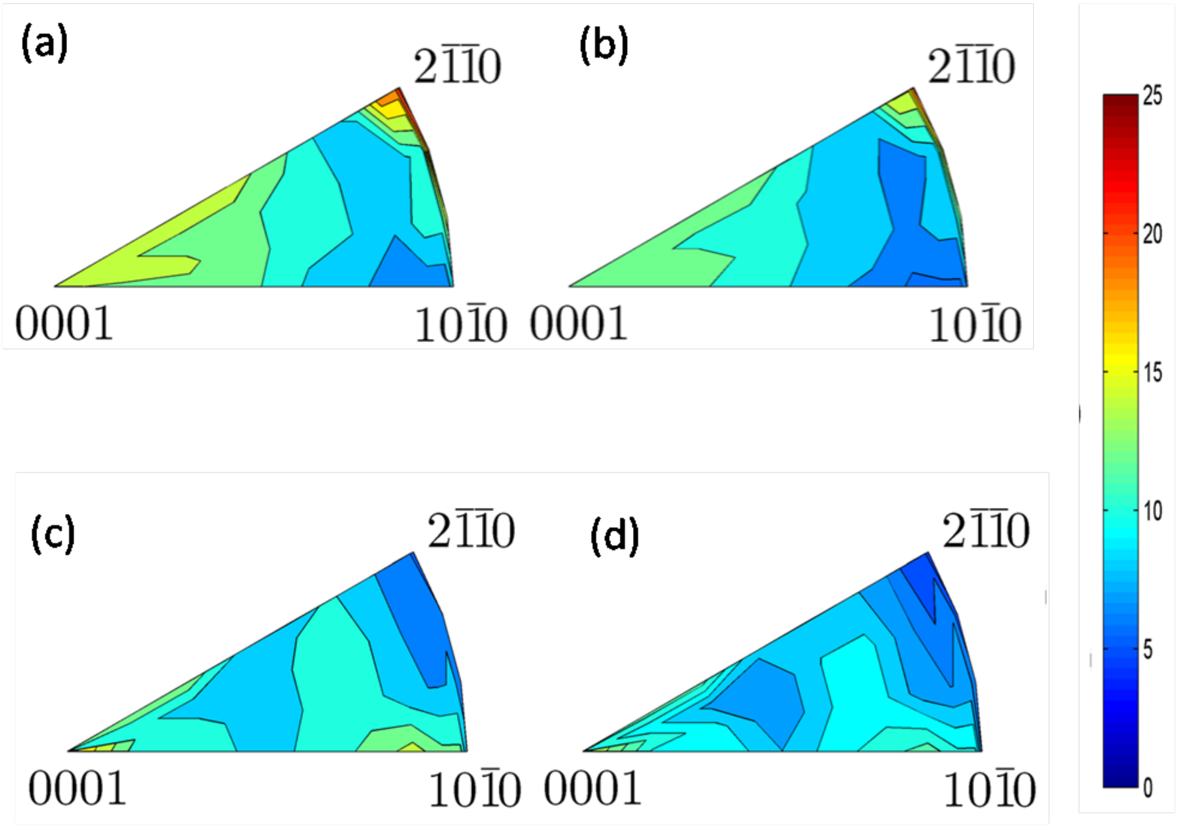

Figure 8.4: Pictorial representation of the critical stress for homogeneous nucleation of the dislocations in Zr as a function of deformation direction, temperature in compression and tension. (a) Compression at 10 K, (b) Compression at 300 K, (c) Tension at 10 K, (d) Tension at 300 K.

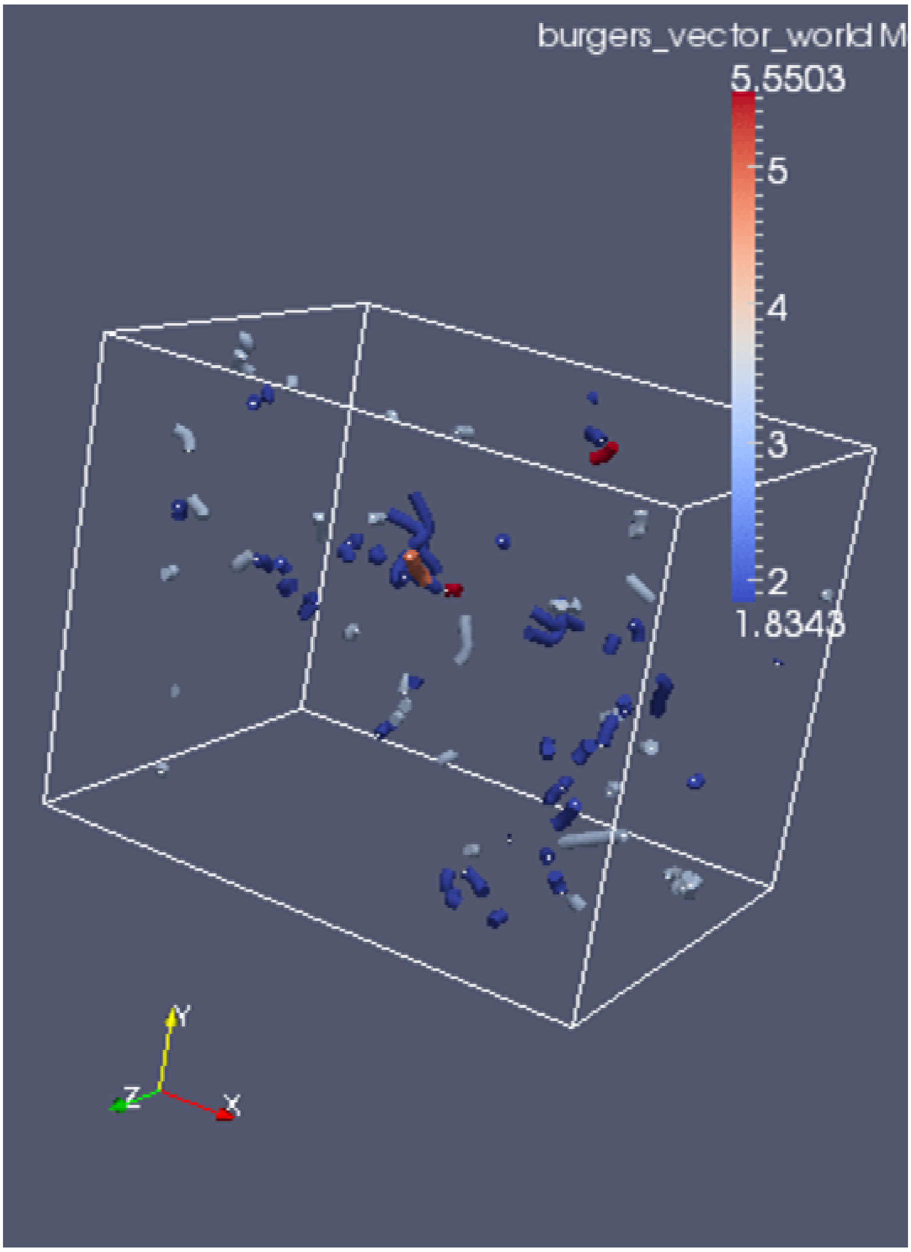

Figure 8.5: Snap shot showing the dislocation networks that got nucleated along with their Burger's vectors (as per color coding shown).

8.4. Conclusions

Present study made an attempt to quantify the role of crystal orientation on the critical stress needed for the nucleation of dislocations in the *hcp* crystal taking Zr as the model material. Following important observations have come out of the study

1. Simulations have indicated significant asymmetry in the stress required for the nucleation of dislocations in the tension and compression
2. Simulations have predicted nucleation of $\vec{a}$ type dislocations on the prismatic planes to be more favorable than the competing $\vec{a}$ type dislocations on basal planes.
3. Under certain crystallographic orientations, formation of $\vec{c}$ type dislocations had also been noticed.
4. Present simulations, however, did not show the formation of $\overrightarrow{c+a}$ dislocations.

CHAPTER 9

Summary

The thesis was conceptualized to further the existing understanding in the microstructural developments of Zr based alloys, with a focus on employing the local orientation information for deciphering the microstructural evolutions and to asses its role in (a) phase transformation and (b) deformation in case of *hcp* Zr alloys. Towards this end a range of experimental and modeling methods were employed. Some interesting finding and contributions that have come out of the present thesis are summarized as below.

9.1. $\beta \rightarrow \alpha$ Phase Transformation

This is perhaps the most common phase transformation through which literally every Zr based component goes through its fabrication cycle and hence was made part of the present thesis. Following are the main contributions of the present work.

- An automated method for reconstruction of the high temperature β phase based on the measured microtexture (*i.e* local orientation) data of the product phase (α) was developed. The algorithm is based on the novel misorientation based weightage factor for arriving at optimized solution for the parent grain.

- Using the algorithm, it had also been demonstrated that exact identification and hence quantification of the variant selection during the $\beta \rightarrow \alpha$ phase transformation is possible.

- The applicability of the algorithm for the reconstruction of high temperature phase had been demonstrated in case of several different modes of $\beta \rightarrow \alpha$ transformations including Widmnstatten and martensitic transformations.

9.2. Hydride Formation ($\alpha \rightarrow \delta$ Transformation)

Due to its deleterious effects on the properties of the Zr alloys, this transformation had been studied extensively in the past using TEM. However, present study focused on the role of local orientations and interfaces on the formation of hydrides using EBSD. For this purpose Zr-2.5%Nb alloy, which is the pressure tube material for the CANDU type of nuclear reactors, was chosen as the material. The objective being to asses the role of the presence of β phase on the $\alpha \rightarrow \delta$ transformation. Following are the main conclusions.

- The study had provided the quantitative measure of strain partitioning during the formation of hydrides at the α/β interfaces. it was confirmed that the actual strain in the hydrides was rather small when they formed along the suitable α/β interfaces.
- It was observed that hydride precipitation depends on the level of hydrogen partitioning at the hydrogenation temperature and availability of suitable β interfaces which are conducive for epitaxial growth of hydride phase in to the adjoining α phase.
- By analysing several tens of hydrides, following orientation relationship had been established between the α β and δ phases.

$$
\begin{gathered}
\{0001\}_\alpha \parallel \{111\}_\delta \\
< 2\bar{1}\bar{1}0 >_\alpha \parallel < 110 >_\delta . \\
\{011\}_\beta \parallel \{111\}_\delta \\
< 100 >_\beta \parallel < 110 >_\delta
\end{gathered}
$$

9.3. Deformation Heterogeneity in Zr: Role of Orientation and Temperature

Probably ‘heterogeneity in plastic deformation’ is one of the most well accepted but least understood phenomenon in case of crystalline materials in general and more so in case of lower symmetry materials like *hcp* Zr. In the present thesis, the heterogeneity in deformation had been studied with respect to two important variable *viz*, local crystal orientation and temperature. For this purpose single phase Zr based alloy (Zircaloy-2) was subjected to plane-strain compression at different temperatures and was analyzed by detailed EBSD for identifying orientation sensitive deformation behavior. In order to rationalize the experimental observations, a

DD simulation approach had been adopted and following important findings have come out of the investigation.

- Experimental observations highlighted the orientation and temperature sensitive plastic deformation in *hcp* zirconium. The starting microstructure had nearly equiaxed grains of $> 3\mu m$ size. Deformed microstructures contained below $3\mu m$ fragmented grains, and also larger grains generically termed as non-fragmented. The latter was predominantly 'basal oriented' for all working temperatures. Temperature dependent plastic deformation, in terms of grain size/shape refinement and in-grain misorientation developments, showed a remarkable difference between room temperature and warm (200 ° and $400°$C) rolling. Warm rolled microstructures contained significantly higher signatures of the plastic strain.
- DD simulations of room temperature PSC successfully captured the deformation response of basal and prismatic orientations. Both dislocation density and plastic strain were significantly lower for basal orientations relative to prismatic orientation. However simulations for the elevated (700 K) temperature deformations showed higher strain accumulation in basal orientation (in comparison to corresponding room temperature deformation of basal) through increased pyramidal slip activity.
- DD simulations also brought out a novel effect of dislocation-dislocation interactions. Dormant slip systems, slip systems where the applied stress was below CRSS, were activated due to interactions with active primary dislocations. This mechanism was shown to activate dormant dislocations in basal orientations, thus contributing to reduction in deformation heterogeneity during warm rolling.

9.4. Criteria for Deformation Twinning

Studies on deformation mechanisms in *hcp* materials are far from complete with out dealing with the twinning. One of the fundamental questions that remained elusive for understanding was : Is twin nucleation strain controlled or stress controlled?. Present thesis tried to provide an answer to this long standing question by performing a series of controlled *in-situ* deformation experiments under neutron diffraction apparatus to look for signatures of twinning and corresponding stress and strain state of the samples. For this a purpose Zr-Sn binary alloys with systematic variation in their Sn content were used in different crystallographic texture conditions for the deformation studies. In addition, detailed postmortem analysis by EBSD and TEM was carried out to gain insights into the data provided by the neutron diffraction experiments. Following are the major conclusions.

- The role of Sn on the deformation mechanisms (twinning in particular) was seen to be deformation direction dependent, in other words texture dependent. It was observed that deformation along RD was characterized by huge influence of Sn on the extent of twinning while the deformation along TD was found to be least sensitive to amount of Sn of the alloy for the extent of twinning.
- In general (for both RD and TD deformations) it was observed that the critical stress required for the twining increased with the Sn content while the critical macroscopic strain for the onset of twinning was rather insensitive to the amount of Sn of the alloy.
- Using the combined evidence of EBSD, TEM and neutron diffraction it was inferred that there needs to be some critical plastic strain for the initiation of twinning. Thus it is suggested that the modeling efforts aimed at capturing the twining behavior must necessarily account for the local strain in addition to local stress state of the grains undergoing the twinning.

9.5. Homogeneous Nucleation of Dislocations : Role of Crystal Orientation

The thesis had extended the study on the role of orientation to atomic scale by exploring the variation brought in by the crystallographic orientation on the critical stress required for the nucleation of the dislocations: the fundamental defects responsible for the deformation behavior. This is first such study in case of *hcp* materials and had brought out following interesting observations.

- Simulations have indicated significant asymmetry in the stress required for the nucleation of dislocations in the tension and compression.
- Simulations have predicted nucleation of $\vec{a}$ type dislocations on the prismatic planes to be more favorable than the competing $\vec{a}$ type dislocations on basal planes.

- Under certain crystallographic orientations, formation of $\overrightarrow{c}$ type dislocations had also been noticed.

- Present simulations, however, did not show the formation of $\overrightarrow{c+a}$ dislocations. Thus the experimental observation of these dislocations could be due to the interaction of the existing $\overrightarrow{a}$ and $\overrightarrow{c}$ type dislocations or conditions other than those imposed in the present simulations are responsible for their formation.

9.6. Scope for Further Research

Present thesis essentially used crystallographic orientation information for understanding the phase transformation and deformation behavior. While some answers have been provided to certain fundamental questions on these aspects present work had also opened up new questions/possibilities for further work as summarized below.

- High temperature microstructure reconstruction algorithm can be extended to handle the retained second phase (parent phase) which can then be used in the case of dual phase microstructures.

- The quantification of variant section under different conditions of applied stress, deformation *etc* will be of great interest to pursue.

- In the case of deformation behavior, DD model can be extended to include cross slip to make more realistic predictions.

- Application of crystal plasticity based FEM models for the modeling intragranular strain behavior observed during the *in-situ* deformation and neutron diffraction studies will be a great way of furthering our understanding on the deformation mechanism and their relative role in these *hcp* materials.

- It will be of great interest to develop the understanding on the combined role of phase transformation and deformation. In particular hot deformation processes such as hot extrusion involve this kind of scenario and developing models for prediction of texture and microstructure evolution should be a useful future work.

APPENDIX I

Worked Example of Reconstruction by New Algorithm

Here is the worked example of the crux of the ‘Reconstruction Algorithm’ developed as a part of the present thesis. For the purpose of clarity, only the most important parts of the algorithm are presented here. It may be noted that the actual automated code that was developed as part of this work handles several more operations than what are listed here. These include file handling operations, input and output operations, Euler angle to rotation matrix conversions and vice versa, methods to compare different solutions to find the common solutions *etc*. As these are operations which only act as auxiliary operations and reasonably straight forward, they are excluded from the description. Focus is on giving sufficient details for the reader so that they can grasp the core idea of the new algorithm with a working example and use it for their own code in case they wish. The values used here represent actual values based on the Burger’s OR and hence can be used for cross checking any code. It is emphasized here that the orientation data given here are not mere schematic numbers but represent the actual $\beta \rightarrow \alpha$ transformation.

Let the transformation involved be $\beta \rightarrow \alpha$ as observed in Zr. Let us assume that we have the orientation information of the product grains in terms of average euler angles (in Bunge notation) of each grain available from a typical EBSD scan. Such data is shown in Table I.1 and corresponding microstructure is schematically represented in Fig. I.1.

We first illustrate how to find the parent orientation for one product grain. The same procedure can be applied to each of the measured product grains in a loop for achieving the automation.

Following are the steps for solving one grain. Let us concentrate on G_1 for this purpose. Rest of the description shall be around this product grain only.

1. **Construct the triplets ($G_i^{i,i+1,i+2}$):** Table I.2 lists all the possible triplets of the neighbors for the grain G_1 with the condition that each grain of the triplet be neighbor to each other.

Table I.1: Orientation and neighbor grain ID data of product grains as measured by EBSD. All the angles are in degrees and represent Bunge Euler Angles of orientation.

Grain ID G_i	Orientation $[\phi_1\,\phi\,\phi_2]$			Neighbor List $(G_{i+1}\dots G_{i+n})$
G_1	[1.00	45.00	4.63]	G_2, G_5, G_3, G_4
G_2	[44.90	90.00	24.94]	G_4,G_1, G_5
G_3	[135.03	90.00	24.94]	G_5,G_1,G_4
G_4	[270.28	45.00	4.60]	G_2,G_1,G_3
G_5	[30.00	80.00	24.00]	G_2, G_1,G_3
G_6	[0.00	47.0	55.0]	G_1, G_4

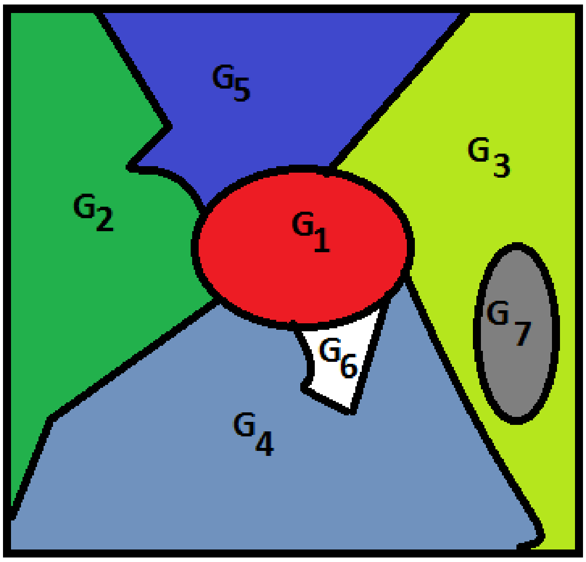

Figure I.1: Schematic microstructure used for the illustration of the 'Misorientation based reconstruction' algorithm. Each product (α) grain is colored uniquely.

2. **Find all β orientations for each triplet (B^{β}_{li}):** Using equation 4.1 find out all of the parent variants (6 each for each grain of the triplet making a total of 18 β variants for each triplet) that can give rise to the measured orientations of the triplet under question. The value of the Burger's operator ($T_l^{\alpha\rightarrow\beta}$) is [215 90 45] in Bunge Euler angle notation. Table I.3 lists all of the variants for all the triplets formed by G_1. Note that these angles represent equivalent symmetric orientations of the orientation computed by Eq. 4.1 and fall in fundamental zone of the parent phase symmetry. Only then we can make numerical comparison of different variants of β belonging to different grains of each triplet to identify common parent variants, if any. In order to facilitate the reader the common β variants from each triplet have been highlighted in Table I.3.

Table I.2: Triplets list for G_1.

$G_i^{i,i+1,i+2}$	Triplets
$G_1^{1,5,2}$	$[G_1\ G_5\ G_2]$
$G_1^{1,5,3}$	$[G_1\ G_5\ G_3]$
$G_1^{1,3,4}$	$[G_1\ G_3\ G_4]$
$G_1^{1,4,2}$	$[G_1\ G_4\ G_2]$
$G_1^{1,4,6}$	$[G_1\ G_4\ G_6]$

3. **Extract potential solutions (S_k) from successful triplets:** Table I.4 lists the potential solutions as observed from the Table I.2. Note that potential solution is the mean of β variants of all the three grains of a given triplet.

4. **Find out the mean orientations ($S_{k,l}^m$) and misorientations ($\Delta S_{k,l}^m$) among the potential solutions and corresponding weighing factors ($W_{k,l}^m$):** Table I.5 lists all of the computed values of ($S_{k,l}^m$), ($\Delta S_{k,l}^m$) and ($W_{k,l}^m$). Note that the user defined parameter δ_{max} was taken to be 3° for these estimations.

5. **Estimate optimized solution using weighatge factors:** Apply Eq. 4.5 for the values listed in table I.5 to get the following optimized solution for G_1.

$$S_{final} = [0.29\ 0.28\ 0.00]$$

These steps shall be repeated for each and every product grain. Exceptions also need to be accounted for. These include those grains for which less than two neighbors exist, for *e.g.* G_7 in Fig. I.1. This can happen in case of grains which are totally embedded inside other grains. In such cases, the solution of the outer grain can be assigned to the embedded grains.

Table I.3: Estimated β variants for each of the triplets of G_1 using Eq. 4.1. The β solutions that match are shown highlighted in grey. Successful triplets having common β variant in all three constituent grains are shown in green and other in red.

Triplets	$B_i^{1...6}$ $[\phi_1\,\phi\,\phi_2]$	$B_{i+1}^{1...6}$ $[\phi_1\,\phi\,\phi_2]$	$B_{i+2}^{1...6}$ $[\phi_1\,\phi\,\phi_2]$
$G_1^{1,5,2}$	[230.50 57.00 12.47]	[185.57 61.70 35.17]	[198.29 52.27 39.30]
	[297.25 47.63 26.15]	[344.41 82.48 6.39]	[0.12 0.00 0.00]
	[97.76 83.19 0.39]	[125.49 61.44 33.63]	[18.36 52.26 39.19]
	[293.06 41.16 22.06]	[344.11 75.19 0.00]	[269.46 82.90 7.15]
	[0.77 0.00 0.00]	[8.38 38.65 30.87]	[26.09 48.37 27.14]
	[219.79 52.05 18.68]	[67.52 49.61 31.96]	[77.65 57.28 40.08]
$G_1^{1,5,3}$	[230.50 57.00 12.47]	[185.57 61.70 35.17]	[288.42 52.27 39.30]
	[297.25 47.63 26.15]	[344.41 82.48 6.39]	[0.00 0.00 0.00]
	[97.76 83.19 0.39]	[125.49 61.44 33.63]	[108.49 52.26 39.19]
	[293.06 41.16 22.06]	[344.11 75.19 0.00]	[0.41 82.90 7.15]
	[0.77 0.00 0.00]	[8.38 38.65 30.87]	[116.22 48.37 27.14]
	[219.79 52.05 18.68]	[67.52 49.61 31.96]	[167.78 57.28 40.08]
$G_1^{1,3,4}$	[230.50 57.00 12.47]	[288.42 52.27 39.30]	[139.76 56.99 12.49]
	[297.25 47.63 26.15]	[0.00 0.00 0.00]	[206.45 47.61 26.14]
	[97.76 83.19 0.39]	[108.49 52.26 39.19]	[6.93 83.21 0.39]
	[293.06 41.16 22.06]	[0.41 82.90 7.15]	[202.33 41.15 22.05]
	[0.77 0.00 0.00]	[116.22 48.37 27.14]	[0.02 0.00 0.00]
	[219.79 52.05 18.68]	[167.78 57.28 40.08]	[129.10 52.04 18.70]
$G_1^{1,4,2}$	[230.50 57.00 12.47]	[139.76 56.99 12.49]	[198.29 52.27 39.30]
	[297.25 47.63 26.15]	[206.45 47.61 26.14]	[0.12 0.00 0.00]
	[97.76 83.19 0.39]	[6.93 83.21 0.39]	[18.36 52.26 39.19]
	[293.06 41.16 22.06]	[202.33 41.15 22.05]	[269.46 82.90 7.15]
	[0.77 0.00 0.00]	[0.02 0.00 0.00]	[26.09 48.37 27.14]
	[219.79 52.05 18.68]	[129.10 52.04 18.70]	[77.65 57.28 40.08]
$G_1^{1,4,6}$	[230.50 57.00 12.47]	[139.76 56.99 12.49]	[0.00 3.00 0.00]
	[297.25 47.63 26.15]	[206.45 47.61 26.14]	[220.81 49.90 15.85]
	[97.76 83.19 0.39]	[6.93 83.21 0.39]	[295.32 42.65 18.09]
	[293.06 41.16 22.06]	[202.33 41.15 22.05]	[208.54 45.71 24.20]
	[0.77 0.00 0.00]	[0.02 0.00 0.00]	[292.27 35.82 13.34]
	[219.79 52.05 18.68]	[129.10 52.04 18.70]	[172.95 87.44 7.41]

Table I.4: List of potential solutions (S_k) for grain G_1.

S_k	$[\phi_1\ \phi\ \phi_2]$		
S_1	[0.27	0.00	0.00]
S_2	[0.37	0.00	0.00]
S_3	[0.25	1.00	0.00]

Table I.5: Potential mean solutions ($S^m_{k,l}$) and their weightage factors ($W^m_{k,l}$) for grain G_1.

$S^m_{k,l}$	$[\phi_1\ \phi\ \phi_2]$			$\Delta S^m_{k,l}$	$W^m_{k,l}$
$S^m_{1,2}$	[0.32	0.00	0.00]	0.1	0.42
$S^m_{1,3}$	[0.26	0.00	0.00]	1.002	0.29
$S^m_{2,3}$	[0.30	0.50	0.00]	1.007	0.29

Bibliography

[1] B. Verlinden, J. Driver, I. Samajdar, and R. R. Doherty, *Thermo Mechanical Processing of Metallic Materials*. Elsevier Ltd, 1st ed., 2007.

[2] B. Cox, "Some thoughts on the mechanisms of in-reactor corrosion of Zirconium alloys," *J. Nucl. Mater.*, vol. 336, no. 2-3, pp. 331–368, 2005.

[3] E. Tenckhoff, "Review of Deformation Mechanisms, Texture, and Mechanical Anisotropy in Zirconium and Zirconium Base Alloys," *J. ASTM Int.*, vol. 2, no. 4, p. 12945, 2005.

[4] A. T. Motta, A. Yilmazbayhan, M. J. G. da Silva, R. J. Comstock, G. S. Was, J. T. Busby, E. Gartner, Q. Peng, Y. H. Jeong, and J. Y. Park, "Zirconium alloys for supercritical water reactor applications: Challenges and possibilities," *J. Nucl. Mater.*, vol. 371, pp. 61–75, 2007.

[5] D. Rodgers, C. Coleman, M. Griffiths, G. Bickel, J. Theaker, I. Muir, Bahurmuz, S. S. Lawrence, M. R. Levi, and M. Resta Levi, "In-reactor performance of pressure tubes in CANDU reactors," *J. Nucl. Mater.*, vol. 383, no. 1-2, pp. 2–7, 2007.

[6] R. A. Holt, "In-reactor deformation of cold worked Zr-2.5 Nb pressure tubes," *J. Nucl. Mater.*, vol. 372, no. 2-3, pp. 182–214, 2008.

[7] M. Griffiths, "A review of microstructure evolution in zirconium alloys during irradiation," *J. Nucl. Mater.*, vol. 159, pp. 190–218, 1988.

[8] R. Holt and S. Aldridge, "Effect of extrusion variables on crystallographic texture of Zr-2.5 wt% Nb," *J. Nucl. Mater.*, 1985.

[9] K. L. Murty and I. Charit, "Texture development and anisotropic deformation of zircaloys," *Prog. Nucl. Energy*, vol. 48, no. 4, pp. 325–359, 2006.

[10] S. Banerjee and P. Mukhopadhyay, *Phase Transformations - Examples from Titanium and Zirconium Alloys*, vol. 12 of *Pergamon Materials Series*. Pergamon, 2007.

[11] R. Krishnan and M. K. Asundi, "Zirconium alloys in nuclear technology," *Proceedigs Indian Acadamy Sci. (Engg. Sci.)*, vol. 4, pp. 41–56, 1981.

[12] K. V. Mani Krishna, S. K. Sahoo, I. Samajdar, S. Neogy, R. Tewari, D. Srivastava, G. K. Dey, G. H. Das, N. Saibaba, and S. Banarjee, “Microstructural and textural developments during Zircaloy-4 fuel tube fabrication,” *J. Nucl. Mater.*, vol. 383, no. 1-2, pp. 78–85, 2008.

[13] D. Srivastava, G. K. Dey, and S. Banerjee, “Evolution of microstructure during fabrication of Zr-2.5% Wt Nb alloy pressure tubes,” *Metall. Mater. Trans. A*, no. 10, pp. 2707–2718.

[14] K. M. Kumar, I. Samajdar, N. Venkatramani, G. K. Dey, R. Tewari, D. Srivastava, and S. Banerjee, “Explaining absence of texture development in cold rolled two-phase Zr-2.5 wt% Nb alloy,” *Acta Mater.*, vol. 51, no. 3, pp. 625–640, 2003.

[15] S. K. Sahoo, *Heterogeneous Deformation in Zirconium Based Alloys*. PhD thesis, IIT Bombay, 2009.

[16] M. K. Kumar, *Cold Deformation Texture and Microstructure in Zirconium Alloys*. PhD thesis, IIT Bombay, 2005.

[17] D. A. Porter and K. E. Sterling, *Phase Transformation in Metals and Alloys*. Nelson Thornes, 2001.

[18] N. Gey, E. Gautier, M. Humbert, A. Cerqueira, J. L. Bechade, and P. Archambault, “Study of the α/β phase transformation of Zy-4 in presence of applied stresses at heating: analysis of the inherited microstructures and textures,” *J. Nucl. Mater.*, vol. 302, no. 2-3, pp. 175–184, 2002.

[19] N. Gey, M. Humbert, E. Gautier, and J. Béchade, “Study of the $\beta \to \alpha$ variant selection for a zircaloy-4 rod heated to the β transus in presence or not of an axial tensile stress,” *J. Nucl. Mater.*, vol. 328, no. 2-3, pp. 137–145, 2004.

[20] M. M. G. Glavicic, P. A. P. Kobryn, T. R. T. Bieler, and S. L. S. Semiatin, “An automated method to determine the orientation of the high-temperature beta phase from measured EBSD data for the low-temperature alpha-phase in Ti-6Al-4V,” *Mater. Sci. Engg.*, vol. 351, no. 1-2, pp. 258–264, 2003.

[21] N. Gey and M. Humbert, “Characterization of the variant selection occurring during the $\alpha \to \beta \to \alpha$ phase transformations of a cold rolled titanium sheet,” *Acta Mater.*, vol. 50, no. 2, pp. 277–287, 2002.

[22] L. Germain, N. Gey, R. Mercier, P. Blaineau, and M. Humbert, “An advanced approach to reconstructing parent orientation maps in the case of approximate orientation relations: Application to steels,” *Acta Mater.*, vol. 60, no. 11, pp. 4551–4562, 2012.

[23] M. Humbert, N. Gey, B. Gardiola, and C. Esling, “Restitution of high temperature parent textures of bcc and hcp polycrystals by a non-linear positivity method,” *Acta Mater.*, vol. 49, no. 3, pp. 445–451, 2001.

[24] L. Germain, N. Gey, and M. Humbert, “Reliability of reconstructed beta-orientation maps in titanium alloys.,” *Ultramicroscopy*, vol. 107, no. 12, pp. 1129–35, 2007.

[25] M. Humbert, N. Gey, C. Patapy, E. Joussein, M. Huger, R. Guinebretière, T. Chotard, and A. Hazotte, "Identification and orientation determination of parent cubic domains from electron backscattered diffraction maps of monoclinic pure zirconia," *Scr. Mater.*, vol. 63, no. 4, pp. 411–414, 2010.

[26] C. Cayron, B. Artaud, and L. Briottet, "Reconstruction of parent grains from EBSD data," *Mater. Charact.*, vol. 57, no. 4-5, pp. 386–401, 2006.

[27] C. Cayron, "Groupoid of orientational variants.," *Acta Crystallogr. A.*, vol. 62, pp. 21–40, 2006.

[28] D. O. Northwood and U. Kosasih, "Hydrides and delayed hydrogen cracking in zirconium and its alloys," *Int. Met. Rev.*, vol. 28, pp. 92–121, 1983.

[29] K. V. Mani Krishna, A. Sain, I. Samajdar, G. K. Dey, D. Srivastava, S. Neogy, R. Tewari, and S. Banerjee, "Resistance to hydride formation in Zirconium: An emerging possibility," *Acta Mater.*, vol. 54, no. 18, pp. 4665–4675, 2006.

[30] C. E. Ells, "Hydride precipitates in zirconium alloys (A review)," *J. Nucl. Mater.*, vol. 28, no. 2, pp. 129–151, 1968.

[31] C. E. Ells, "The stress orientation of hydride in Zirconium alloys," *J. Nucl. Mater.*, vol. 35, no. 3, pp. 306–315, 1970.

[32] C. J. Simpson and C. E. Ells, "Delayed hydrogen embrittlement in Zr-2.5 wt % Nb," *J. Nucl. Mater.*, vol. 52, no. 2, pp. 289–295, 1974.

[33] I. S. Batra, R. N. Singh, P. Sengupta, B. C. Maji, K. Madangopal, K. V. Mani Krishna, R. Tewari, and G. K. Dey, "Mitigation of hydride embrittlement of zirconium by yttrium," *J. Nucl. Mater.*, vol. 389, no. 3, pp. 500–503, 2009.

[34] R. N. Singh, R. Lala Mikin, G. K. Dey, D. N. Sah, I. S. Batra, and P. Stå hle, "Influence of temperature on threshold stress for reorientation of hydrides and residual stress variation across thickness of Zr-2.5Nb alloy pressure tube," *J. Nucl. Mater.*, vol. 359, no. 3, pp. 208–219, 2006.

[35] R. N. Singh, R. Kishore, S. S. Singh, T. K. Sinha, and B. P. Kashyap, "Stress-reorientation of hydrides and hydride embrittlement of Zr-2.5 wt% Nb pressure tube alloy," *J. Nucl. Mater.*, vol. 325, no. 1, pp. 26–33, 2004.

[36] S. Neogy, D. Srivastava, R. Tewari, R. Singh, G. Dey, and S. Banerjee, "Microstructural study of hydride formation in Zr-1Nb alloy," *J. Nucl. Mater.*, vol. 322, no. 2-3, pp. 195–203, 2003.

[37] D. G. Westlake, "The habit planes of zirconium hydride in zirconium and zircaloy," *J. Nucl. Mater.*, vol. 26, no. 2, pp. 208–216, 1968.

[38] D. G. Westlake, "Author's reply: The habit planes of zirconium hydride in zirconium and zircaloy," *J. Nucl. Mater.*, vol. 33, no. 2, pp. 245–246, 1969.

[39] A. Akhtar, "Basal slip in zirconium," *Acta Met.*, vol. 21, pp. 1–11, 1973.

[40] A. Akhtar, “Compression of zirconium single crystals parallel to the c-axis,” *J. Nucl. Mater.*, vol. 47, pp. 79–86, 1973.

[41] O. Woo, G. Carpenter, and S. MacEwen, “Dislocations in zirconium alloys,” *J. Nucl. Mater.*, vol. 87, no. 1, pp. 70–80, 1979.

[42] J. E. Bailey, “Electron microscope studies of dislocations in deformed zirconium,” *J. Nucl. Mater.*, vol. 7, no. 3, pp. 300–310, 1962.

[43] L. Xiao, H. Gu, and Z. Kuang, “Cyclic deformation behavior of zircaloy-4 at different temperatures,” *Acta Metall.*, vol. 8, no. 3, pp. 219–225, 1995.

[44] L. Xiao and H. Gu, “Dislocation structures in zirconium and zircaloy-4 fatigued at different temperatures,” *Metall. Mater. Trans. A Phys. Metall. Mater. Sci.*, vol. 28, no. 4, pp. 1021–1033, 1997.

[45] L. Xiao, Y. Umakoshi, and J. Sun, “Biaxial low cycle fatigue properties and dislocation substructures of zircaloy-4 under in-phase and out-of-phase loading,” *Mater. Sci. Eng. A*, vol. 292, no. 1, pp. 40–48, 2000.

[46] L. Xiao, Y. Umakoshi, and J. Sun, “Cyclic deformation behaviour and microstructures of hydrided Zircaloy-4 under biaxial loading,” *Metall. Mater. Trans. A Phys. Metall. Mater. Sci.*, vol. 32, no. 11, pp. 2841–2850, 2001.

[47] F. Roters, P. Eisenlohr, L. Hantcherli, D. D. D. Tjahjanto, T. R. R. Bieler, and D. Raabe, “Overview of constitutive laws, kinematics, homogenization and multiscale methods in crystal plasticity finite-element modeling: Theory, experiments, applications,” *Acta Mater.*, vol. 58, no. 4, pp. 1152–1211, 2010.

[48] C. G. Van de Walle, “First-principles calculations for defects and impurities: Applications to III-nitrides,” *J. Appl. Phys.*, vol. 95, no. 8, p. 3851, 2004.

[49] H. M. Zbib, M. Rhee, and J. P. Hirth, “On plastic deformation and the dynamics of 3D dislocations,” *Int. J. Mech. Sci.*, vol. 40, no. 2-3, pp. 113–127, 1998.

[50] D. Xu, R. Yang, J. Li, J. Chang, H. Wang, D. Li, and S. Yip, “Atomistic simulation of the influence of pressure on dislocation nucleation in bcc Mo,” *Comput. Mater. Sci.*, vol. 36, no. 1-2, pp. 60–64, 2006.

[51] K. W. Schwarz, “Simulation of dislocations on the mesoscopic scale. I. Methods and examples,” *J. Appl. Phys.*, vol. 85, no. 1, p. 108, 1999.

[52] C. L. Kelchner, S. J. Plimpton, and J. C. Hamilton, “Dislocation nucleation and defect structure during surface indentation,” *Phys. Rev. B - Condens. Matter Mater. Phys.*, vol. 58, no. 17, pp. 11085–11088, 1998.

[53] M. Horstemeyer, M. Baskes, and S. Plimpton, “Computational nanoscale plasticity simulations using embedded atom potentials,” *Theor. Appl. Fract. Mech.*, vol. 37, no. 1-3, pp. 49–98, 2001.

[54] S. Cheng, J. Spencer, and W. Milligan, “Strength and tension/compression asymmetry in nanostructured and ultrafine-grain metals,” *Acta Mater.*, vol. 51, no. 15, pp. 4505–4518, 2003.

[55] B. Devincre, T. Hoc, L. Kubin, and B. D. T. Hoc, "Dislocation mean free paths and strain hardening of crystals," *Science*, vol. 320, no. 5884, pp. 1745–1748, 2008.

[56] H. M. Zbib, T. Diaz De La Rubia, M. Rhee, and J. P. Hirth, "3D dislocation dynamics: stress-strain behavior and hardening mechanisms in fcc and bcc metals," *J. Nucl. Mater.*, vol. 276, no. 1-3, pp. 154–165, 2000.

[57] M. Tang, L. Kubin, and G. Canova, "Dislocation mobility and the mechanical response of b.c.c. single crystals: A mesoscopic approach," *Acta Mater.*, vol. 46, no. 9, pp. 3221–3235, 1998.

[58] N. Ghoniem, S. Tong, J. Huang, B. Singh, and M. Wen, "Mechanisms of dislocation-defect interactions in irradiated metals investigated by computer simulations," *J. Nucl. Mater.*, vol. 307-311, no. 2, pp. 843–851, 2002.

[59] T. A. Khraishi and I. Demir, "On Cauchy singular integrals and stress intensity factors for 2D mode I cracks in an infinite solid," *Mech. Res. Commun.*, vol. 30, no. 4, pp. 353–364, 2003.

[60] H. M. Zbib and T. A. Khraishi, *A Tribute to F.R.N. Nabarro*, vol. 14 of *Dislocations in Solids*. Elsevier, 2008.

[61] S. Groh, S. Olarnrithinun, W. Curtin, A. Needleman, V. Deshpande, and E. V. der Giessen, "Fatigue crack growth from a cracked elastic particle into a ductile matrix," *Philos. Mag.*, vol. 88, no. 30-32, pp. 3565–3583, 2008.

[62] W. Curtin, V. Deshpande, A. Needleman, E. Van der Giessen, and M. Wallin, "Hybrid discrete dislocation models for fatigue crack growth," *Int. J. Fatigue*, vol. 32, no. 9, pp. 1511–1520, 2010.

[63] F. Roters, P. Eisenlohr, T. R. Bieler, and D. Raabe, *Crystal Plasticity Finite Element Methods: In Materials Science and Engineering*. 2010.

[64] D. Raabe, Z. Zhao, S. J. Park, and F. Roters, "Theory of orientation gradients in plastically strained crystals," *Acta. Mater.*, vol. 50, no. 2, pp. 421–440, 2002.

[65] M. C. Fivel, "Discrete dislocation dynamics: an important recent break-through in the modelling of dislocation collective behaviour," *Comptes Rendus Phys.*, vol. 9, no. 3-4, pp. 427–436, 2008.

[66] M. Fivel, *Multiscale Modeling of Heterogenous Materials*. London, UK: ISTE, 2008.

[67] V. V. Bulatov and W. Cai, *Computer Simulations of Dislocations*. Oxford University Press, 2006.

[68] W. Cai, A. Arsenlis, C. Weinberger, and V. V. Bulatov, "A non-singular continuum theory of dislocations," *J. Mech. Phys. Solids*, vol. 54, no. 3, pp. 561–587, 2006.

[69] W. Cai and V. V. Bulatov, "Mobility laws in dislocation dynamics simulations," *Mater. Sci. Eng. A*, vol. 387-389, no. 1-2 SPEC. ISS., pp. 277–281, 2004.

[70] S. M. A. Khan, H. M. Zbib, and D. A. Hughes, "Stress patterns of deformation induced planar dislocation boundaries," in *Mater. Res. Soc. Symp. Proc.*, vol. 683, pp. 56–61, 2001.

[71] M. Fivel, M. Verdier, and G. Canova, “3D simulation of a nanoindentation test at a mesoscopic scale,” *Mater. Sci. Eng. A*, vol. 234-236, pp. 923–926, 1997.

[72] M. C. Fivel, C. F. Robertson, G. R. Canova, and L. Boulanger, “Three-dimensional modeling of indent-induced plastic zone at a mesoscale,” *Acta Mater.*, vol. 46, no. 17, pp. 6183–6194, 1998.

[73] S. Plimpton, “Fast Parallel Algorithms for Short - Range Molecular Dynamics,” *J. Comp. Phy.*, vol. 117, no. June 1994, pp. 1–42, 1995.

[74] M. P. Allen, “Introduction to Molecular Dynamics Simulation,” *Comp. Soft Matter*, vol. 23, 2004.

[75] “Open Genie: A software for neutron diffraction analysis, http://www.isis.stfc.ac.uk.”

[76] R. Tewari, D. Srivastava, G. Dey, J. Chakravarty, and S. Banerjee, “Microstructural evolution in Zirconium based alloys,” *J. Nucl. Mater.*, vol. 383, no. 1-2, pp. 153–171, 2008.

[77] H. K. D. H. Bhadeshia, E. Keehan, L. Karlsson, H. O. Andr, and H. Andrén, “Coalesced Bainite,” *Indian Inst. Met.*, vol. 59, pp. 689–694, 2006.

[78] S. Kundu and H. Bhadeshia, “Transformation texture in deformed stainless steel,” *Scr. Mater.*, vol. 55, no. 9, pp. 779–781, 2006.

[79] S. Kundu and H. Bhadeshia, “Crystallographic texture and intervening transformations,” *Scr. Mater.*, vol. 57, no. 9, pp. 869–872, 2007.

[80] I. Lischewski and G. Gottstein, “Nucleation and variant selection during the $\alpha \rightarrow \gamma \rightarrow \alpha$ phase transformation in microalloyed steel,” *Acta Mater.*, vol. 59, no. 4, pp. 1530–1541, 2011.

[81] M. Glavicic, P. Kobryn, and S. Semiatin, “Validation of an automated EBSD method to deduce the β - phase texture in Ti-6Al-4V with a colony-α microstructure,” *Mater. Sci. Eng. A*, 2004.

[82] A. Sankaran, E. Bouzy, M. Humbert, and A. Hazotte, “Variant selection during nucleation and growth of γ-massive phase in TiAl-based intermetallic alloys,” *Acta Mater.*, vol. 57, no. 4, pp. 1230–1242, 2009.

[83] I. Lischewski, D. M. Kirch, A. Ziemons, and G. Gottstein, “Investigation of the α-γ-α Phase Transformation in Steel: High-Temperature In Situ EBSD Measurements,” *Texture, Stress. Microstruct.*, vol. 2008, pp. 1–7, 2008.

[84] J. Romero, M. Preuss, and J. Quinta da Fonseca, “Capturing the texture changes in a zirconium alloy during the allotropic phase transformation,” *Scr. Mater.*, vol. 61, no. 4, pp. 399–402, 2009.

[85] C. Cayron, “ARPGE: A computer program to automatically reconstruct the parent grains from electron backscatter diffraction data.,” *J. Appl. Crystallogr.*, vol. 40, no. Pt 6, pp. 1183–1188, 2007.

[86] C. Cayron, “Importance of the $\alpha \rightarrow \beta$ transformation in the variant selection mechanisms of thermomechanically processed titanium alloys,” *Scr. Mater.*, vol. 59, no. 5, pp. 570–573, 2008.

[87] T. Karthikeyan, S. Saroja, and M. Vijayalakshmi, “Evaluation of misorientation angle-axis set between variants during transformation of bcc to hcp phase obeying Burgers orientation relation,” *Scr. Mater.*, vol. 55, no. 9, pp. 771–774, 2006.

[88] V. Randle and O. Engler, *Introduction to Texture Analysis Microtexture and Orietation Mapping*. Taylor and Francis Limited, 2003.

[89] S. Mishra, P. Pant, K. Narasimhan, A. Rollett, and I. Samajdar, “On the widths of orientation gradient zones adjacent to grain boundaries,” *Scr. Mater.*, vol. 61, no. 3, pp. 273–276, 2009.

[90] I. Lonardelli, N. Gey, H.-R. R. H. Wenk, M. Humbert, S. C. Vogel, and L. Lutterotti, “In situ observation of texture evolution during $\alpha \rightarrow \beta$ and $\beta \rightarrow \alpha$ phase transformations in titanium alloys investigated by neutron diffraction,” *Acta Mater.*, vol. 55, no. 17, pp. 5718–5727, 2007.

[91] M. Humbert and N. Gey, “Elasticity-based model of the variant selection observed in the $\beta \rightarrow \alpha$ phase transformation of a Zircalloy-4 sample,” *Acta Mater.*, vol. 51, no. 16, pp. 4783–4790, 2003.

[92] J. K. Mackenzie and M. J. Thomson, “Some statistics associated with the random disorientation of cubes,” *Biometrika*, 1957.

[93] J. Mackenzie and J. K. Meckenzie, “The distribution of rotation axes in a random aggregate of of cubic crystals,” *Acta Metall.*, vol. 12, pp. 223–225, 1964.

[94] M. P. Puls, “Assessment of aging of Zr-2.5Nb pressure tubes in CANDU reactors,” *Nucl. Eng. Des.*, vol. 171, pp. 137–148, 1997.

[95] P. Vizcaíno, A. D. A. Banchik, J. P. J. Abriata, and P. VizcaiÌno, “Hydrogen in Zircaloy-4: Effects of the neutron irradiation on the hydride formation,” *J. Mater. Sci.*, vol. 42, no. 16, pp. 6633–6637, 2007.

[96] H. Chu, S. Wu, K. Chien, and R. Kuo, “Effect of radial hydrides on the axial and hoop mechanical properties of Zircaloy-4 cladding,” *J. Nucl. Mater.*, vol. 362, no. 1, pp. 93–103, 2007.

[97] H. C. Chu, S. Wu, and R. Kuo, “Hydride reorientation in Zircaloy-4 cladding,” *J. Nucl. Mater.*, vol. 373, no. 1-3, pp. 319–327, 2008.

[98] Y. Shinohara, H. Abe, T. Iwai, N. Sekimura, T. Kido, H. Yamamoto, and T. Taguchi, “In Situ TEM Observation of Growth Process of Zirconium Hydride in Zircaloy-4 during Hydrogen Ion Implantation,” *J. Nucl. Sci. Technol.*, vol. 46, no. 6, pp. 564–571, 2009.

[99] Sakai, Tadamiti, Kakuma, Tsutom, Nagai, and Nobuyuki, “Resistometric study of the precipitation of hydrides in unalloyed and alloyed zirconium,” *Trans Jap Inst Met*, vol. 14, no. 3, pp. 194–198, 1973.

[100] K. Une, K. Nogita, S. Ishimoto, and K. Ogata, “Crystallography of Zirconium Hydrides in Recrystallized Zircaloy-2 Fuel Cladding by Electron Backscatter Diffraction,” *J. Nucl. Sci. Technol.*, vol. 41, no. 7, pp. 731–740, 2004.

[101] K. Une and S. Ishimoto, “Crystallographic measurement of the β to α phase transformation and δ-hydride precipitation in a laser-welded Zircaloy-2 tube by electron backscattering diffraction,” *J. Nucl. Mater.*, vol. 389, no. 3, pp. 436–442, 2009.

[102] N. A. P. K. Kumar, J. A. Szpunar, and Z. He, “Preferential precipitation of hydrides in textured zircaloy-4 sheets,” *J. Nucl. Mater.*, vol. 403, no. 1-3, pp. 101–107, 2010.

[103] J. S. Bradbrook, G. W. Lorimer, and N. Ridley, “The precipitation of zirconium hydride in zirconium and zircaloy-2,” *J. Nucl. Mater.*, vol. 42, no. 2, pp. 142–160, 1972.

[104] V. Perovic and G. C. Weatherly, “The nucleation of hydrides in a Zr-2.5 wt%Nb alloy,” *J. Nucl. Mater.*, vol. 126, no. 2, pp. 160–169, 1984.

[105] V. Perovic, G. C. Weatherly, S. R. MacEwen, and M. Leger, “The influence of prior deformation on hydride precipitation in zircaloy,” *Acta Metall. Mater.*, vol. 40, no. 2, pp. 363–372, 1992.

[106] V. Perovic, G. C. Weatherly, and C. J. Simpson, “Hydride precipitation in α/β zirconium alloys,” *Acta Metall.*, vol. 31, no. 9, pp. 1381–1391, 1983.

[107] V. Perovic, G. C. Weatherly, and C. J. Simpson, “The role of elastic strains in the formation of stacks of hydride precipitates in zirconium alloys,” *Scr. Metall.*, vol. 16, no. 4, pp. 409–412, 1982.

[108] P. Stå hle, R. N. Singh, L. Banks-Sills, P. Stahle, M. Ristinmaa, and S. Banerjee, “δ-hydride habit plane determination in α-zirconium at 298 K by strain energy minimization technique,” *Defect Diffus. Forum*, vol. 279, pp. 105–110, 2008.

[109] V. D. Hiwarkar, S. K. Sahoo, K. V. Mani Krishna, I. Samajdar, G. K. Dey, D. Srivastav, R. Tewari, S. Banarjee, and R. D. Doherty, “Coarsening of second phase in a two-phase Zr-2.5Nb: On the role of phase boundaries,” *Acta Mater.*, vol. 57, no. 19, pp. 5812–5821, 2009.

[110] D. Srivastava, K. Madangopal, S. Banerjee, and S. Ranganathan, “Self accomodation morphology of martensite variants in Zr2.5wt%Nb alloy,” *Acta Metall. Mater.*, vol. 41, no. 12, pp. 3445–3454, 1993.

[111] R. Doherty, D. A. Hughes, F. Humphreys, J. J. Jonas, D. J. Jensen, M. Kassner, W. King, T. McNelley, H. McQueen, and A. Rollett, “Current issues in recrystallization: a review,” *Mater. Sci. Eng. A*, vol. 238, no. 2, pp. 219–274, 1997.

[112] D. Khatamian and V. C. Ling, “Hydrogen solubility limits in alpha and beta zirconium,” *J. Alloy. Compd.*, vol. 253-254, pp. 162–166, 1997.

[113] B. C. Skinner and R. Dutton, *Hydrogen diffusivity in alpha-beta zirconium alloys and its role in delayed hydride cracking*. The Minerals, Metals and Materials Society, 1990.

[114] D. Khatamian, “Solubility and partitioning of hydrogen in metastable Zr-based alloys used in the nuclear industry,” *J. Alloy. Compd.*, vol. 293-295, pp. 893–899, 1999.

[115] R. Tang and X. Yang, “Dissolution and precipitation behaviors of hydrides in N18, Zry-4 and M5 alloys,” *Int. J. Hydrogen Energy*, vol. 34, no. 17, pp. 7269–7274, 2009.

[116] A. Aladjem, “Zirconium-hydrogen,” *Diffus. Defect Data Pt.B Solid State Phenom.*, vol. 49-50, pp. 281–329, 1996.

[117] Yoshihiko, Gotoh, M. Uwaha, and I. Arai, “Interpretation of the epitaxial orientation relationship at bcc (110) / fcc (111) interfaces,” *Appl. Surf. Sci.*, vol. 33, pp. 443–449, 1998.

[118] B. Bay, N. Hansen, D. Hughes, and D. Kuhlmann-Wilsdorf, “Evolution of fcc deformation structures in polyslip,” *Acta Metall.*, vol. 40, pp. 205–219, 1992.

[119] I. Samajdar, P. Ratchev, B. Verlinden, and E. Aernoudt, “Hot working of AA1050-relating the microstructural and textural developments,” *Acta Mater.*, vol. 49, pp. 1759–1769, 2001.

[120] C. Maurice and J. J. Driver, “High temperature plane strain compression of cube oriented aluminium crystals,” *Acta Metall. Mater.*, vol. 41, no. 6, pp. 1653–1664, 1993.

[121] A. Akhtar, “Prismatic slip in zirconium single crystals at elevated temperatures,” *Met. Trans. A*, vol. 6, pp. 1217–1221, 1975.

[122] L. Capolungo, I. J. Beyerlein, and Z. Qwang, “The role of elastic anisotropy on plasticity in hcp metals: A three-dimensional dislocation dynamics study,” *Model. Simul. Mater. Sci. Eng.*, vol. 18, no. 8, 2010.

[123] I. J. Beyerlein and C. N. Tome, “A dislocation-based constitutive law for pure Zr including temperature effects,” *Int. J. Plast.*, vol. 24, no. 5, pp. 867–895, 2008.

[124] G. G. Yapici, C. N. Tomé, I. J. Beyerlein, I. Karaman, S. C. Vogel, and C. Liu, “Plastic flow anisotropy of pure zirconium after severe plastic deformation at room temperature,” *Acta Mater.*, vol. 57, no. 16, pp. 4855–4865, 2009.

[125] S. Raveendra, H. Paranjape, S. Mishra, H. Weiland, R. Doherty, and I. Samajdar, “Relative Stability of Deformed Cube in Warm and Hot Deformed AA6022: Possible Role of Strain-Induced Boundary Migration,” *Metall. Mater. Trans. A*, vol. 40, no. 9, pp. 2220–2230, 2009.

[126] J. S. Kallend and Y. C. Huang, “Determination of the orientation dependence of the stored energy of cold work,” pp. 783–786, Netherlands Soc for Materials Science, 1984.

[127] D. D. Sam and B. L. Adams, “Orientation and strain dependence of stored energy of cold work in axisymmetric copper,” *Metall. Trans. A*, vol. 17, no. 3, pp. 513–517, 1986.

[128] N. Rajmohan, Y. Hayakawa, J. A. Szpunar, and J. H. Root, “Neutron diffraction method for stored energy measurement in interstitial free steel,” *Acta Mater.*, vol. 45, no. 6, pp. 2485–2494, 1997.

[129] I. Samajdar and R. D. Doherty, “Role of S[(123)<634 >] orientations in the preferred nucleation of cube grains in recrystallization of FCC metals,” *Scr. Metall. Mater.*, vol. 32, no. 6, pp. 845–850, 1995.

[130] D. Juul Jensen, “Growth rates and misorientation relationships between growing nuclei/grains and the surrounding deformed matrix during recrystallization,” *Acta Metall. Mater.*, vol. 43, no. 11, pp. 4117–4129, 1995.

[131] J. Gil Sevillano, I. Ocaña Arizcorreta, and L. P. Kubin, “Intrinsic size effects in plasticity by dislocation glide,” *Mater. Sci. Eng. A*, vol. 309-310, pp. 393–405, 2001.

[132] A. Arsenlis, W. Cai, M. Tang, M. Rhee, T. Oppelstrup, G. Hommes, T. G. Pierce, and V. V. Bulatov, “Enabling strain hardening simulations with dislocation dynamics,” *Model. Simul. Mater. Sci. Eng.*, vol. 15, pp. 553–595, 2007.

[133] V. V. Bulatov, L. L. Hsiung, M. Tang, A. Arsenlis, M. C. Bartelt, W. Cai, J. N. Florando, M. Hiratani, M. Rhee, G. Hommes, T. G. Pierce, and T. D. de la Rubia, “Dislocation multi-junctions and strain hardening.,” *Nature*, vol. 440, no. 7088, pp. 1174–8, 2006.

[134] S. P. Fitzgerald, S. Aubry, S. L. Dudarev, and W. Cai, “Dislocation dynamics simulation of Frank-Read sources in anisotropic α-Fe,” *Model. Simul. Mater. Sci. Eng.*, vol. 20, no. 4, 2012.

[135] Y. Liu, E. Van der Giessen, and A. Needleman, “An analysis of dislocation nucleation near a free surface,” *Int. J. Solids Struct.*, vol. 44, no. 6, pp. 1719–1732, 2007.

[136] L. Kubin and Y. Estrin, “Evolution of dislocation densities and the critical conditions for the Portevin-Le Chatelier effect,” *Acta Metall. Mater.*, 1990.

[137] R. Madec, B. Devincre, and L. P. Kubin, “On the nature of attractive dislocation crossed states,” *Comput. Mater. Sci.*, vol. 23, no. 1-4, pp. 219–224, 2002.

[138] L. P. Kubin, and C. Fressengeas, and G. Ananthakrishna, “Chapter 57 Collective behaviour of dislocations in plasticity,” *Dislocations in Solids*, vol. 11, no. C, pp. 101–192, 2002.

[139] L. Kubin, B. Devincre, and T. Hoc, “Modeling dislocation storage rates and mean free paths in face-centered cubic crystals,” *Acta Mater.*, vol. 56, no. 20, pp. 6040–6049, 2008.

[140] R. Madec, B. Devincre, and L. P. Kubin, “From dislocation junctions to forest hardening,” *Phys. Rev. Lett.*, vol. 89, no. 25, 2002.

[141] A. Ridha and W. Hutchinson, “Recrystallisation mechanisms and the origin of cube texture in copper,” *Acta Metall.*, 1982.

[142] G. Monnet, B. Devincre, and L. P. Kubin, “Dislocation study of prismatic slip systems and their interactions in hexagonal close packed metals: Application to zirconium,” *Acta Mater.*, vol. 52, no. 14, pp. 4317–4328, 2004.

[143] C. C. Wu, S. Aubry, P. W. Chung, and A. Arsenlis, “Dislocation dynamics simulations of junctions in hexagonal close-packed crystals,” in *Mater. Res. Soc. Symp. Proc.*, vol. 1424, pp. 67–72, 2012.

[144] L. Capolungo, “Dislocation junction formation and strength in magnesium,” *Acta Mater.*, vol. 59, no. 8, pp. 2909–2917, 2011.

[145] S. Cai, M. Daymond, R. Holt, M. Gharghouri, and E. Oliver, “Evolution of interphase and intergranular stresses in Zr-2.5Nb during room temperature deformation,” *Mater. Sci. Eng. A*, vol. 501, no. 1-2, pp. 166–181, 2009.

[146] T. M. Poletika, S. L. Girsova, S. V. Kolosov, and G. N. Narimanova, "Plastic flow localization in h.c.p. Zr alloys on macro- and microscale levels," *Mater. Sci. Eng. A*, vol. 483-484, pp. 91–94, 2008.

[147] C. Efstathiou, H. Sehitoglu, and J. Lambros, "Multiscale strain measurements of plastically deforming polycrystalline titanium: Role of deformation heterogeneities," *Int. J. Plast.*, vol. 26, no. 1, pp. 93–106, 2010.

[148] S. K. Sahoo, V. D. Hiwarkar, I. Samajdar, G. K. Dey, D. Srivastav, R. Tiwari, and S. Banerjee, "Heterogeneous deformation in single-phase Zircaloy 2," *Scr. Mater.*, vol. 56, no. 11, pp. 963–966, 2007.

[149] A. Ma, F. Roters, and D. Raabe, "A dislocation density based constitutive model for crystal plasticity FEM including geometrically necessary dislocations," 2006.

[150] I. C. Dragomir, T. Ungar, and T. Ungár, "Contrast factors of dislocations in the hexagonal crystal system," *J. Appl. Crystallogr.*, vol. 35, no. 5, pp. 556–564, 2002.

[151] H. Khater and D. Bacon, "Dislocation core structure and dynamics in two atomic models of α-zirconium," *Acta Mater.*, vol. 58, no. 8, pp. 2978–2987, 2010.

[152] C. C. Wu, P. W. Chung, S. Aubry, L. B. Munday, and A. Arsenlis, "The strength of binary junctions in hexagonal close-packed crystals," *Acta Mater.*, vol. 61, no. 9, pp. 3422–3431, 2013.

[153] I. Samajdar and R. D. Doherty, "Cube recrystallization texture in warm deformed aluminum: understanding and prediction," *Acta Mater.*, vol. 46, no. 9, pp. 3145–3158, 1998.

[154] N. Hansen and D. Kuhlmann-Wilsdorf, "Low energy dislocation structures due to unidirectional deformation at low temperatures," *Mater. Sci. Eng.*, vol. 81, pp. 141–161, 1986.

[155] J. P. Hirth and J. Lothe, *Theory of Dislocations*. John Wiley and Sons, Inc., 1982.

[156] V. V. Bulatov and F. F. A. L. K. B. D. S. Yip, "Connecting atomistic and mesoscale simulations of crystal plasticity," *Nature*, vol. 391, pp. 669–672, 1998.

[157] P. Pant, K. Schwarz, and S. P. Baker, "Dislocation interactions in thin FCC metal films," *Acta Mater.*, vol. 51, no. 11, pp. 3243–3258, 2003.

[158] C. Depres, M. Fivel, and L. Tabourot, "A dislocation-based model for low-amplitude fatigue behaviour of face-centred cubic single crystals," *Scr. Mater.*, vol. 58, no. 12, pp. 1086–1089, 2008.

[159] A. Arsenlis, M. Rhee, G. Hommes, R. Cook, and J. Marian, "A dislocation dynamics study of the transition from homogeneous to heterogeneous deformation in irradiated body-centered cubic iron," *Acta Mater.*, vol. 60, no. 9, pp. 3748–3757, 2012.

[160] A. Alankar, D. Field, and H. Zbib, "Explicit incorporation of cross-slip in a dislocation density-based crystal plasticity model," *Phil. Mag.*, vol. 92, no. 24, pp. 3084–3100, 2012.

[161] A. Alankar, I. N. Mastorakos, D. P. Field, and H. M. Zbib, "Determination of dislocation interaction strengths using discrete dislocation dynamics of curved dislocations," *J. Eng. Mater. Technol. Trans. ASME*, vol. 134, no. 2, 2012.

[162] P. Polukhin, S. Gorelik, and V. Vorontsov, *Physical principles of plastic deformation.* Moscow: Mir Publ,Moscow, USSR, 1983.

[163] J. W. Christian, *The Theory of Transformations in Metals and Alloys (Part I + II), 3rd Edition*. Newnes, 2002.

[164] J. Christian and S. Mahajan, "Deformation twinning," *Prog. Mater. Sci.*, 1995.

[165] H. Abdolvand, M. R. Daymond, and C. Mareau, "Incorporation of twinning into a crystal plasticity finite element model: Evolution of lattice strains and texture in Zircaloy-2," *Int. J. Plast.*, vol. 27, no. 11, pp. 1721–1738, 2011.

[166] H. Abdolvand and M. R. Daymond, "Internal strain and texture development during twinning: Comparing neutron diffraction measurements with crystal plasticity finite-element approaches," *Acta Mater.*, vol. 60, no. 5, pp. 2240–2248, 2012.

[167] D. G. L. Prakash, R. Ding, R. J. Moat, I. Jones, P. J. Withers, J. Q. D. Fonseca, and M. Preuss, "Deformation twinning in Ti-6Al-4V during low strain rate deformation to moderate strains at room temperature," *Mater. Sci. Eng. A*, vol. 527, no. 21-22, pp. 5734–5744, 2010.

[168] A. Ma, F. Roters, and D. Raabe, "On the consideration of interactions between dislocations and grain boundaries in crystal plasticity finite element modeling - Theory, experiments, and simulations," *Acta Mater.*, vol. 54, no. 8, pp. 2181–2194, 2006.

[169] P. Van Houtte, A. K. Kanjarla, A. Van Bael, M. Seefeldt, L. Delannay, P. V. Houtte, and A. V. Bael, "Multiscale modelling of the plastic anisotropy and deformation texture of polycrystalline materials," *Eur. J. Mech. - A/Solids*, vol. 25, no. 4, pp. 634–648, 2006.

[170] S. Leclercq, G. Rousselier, and G. Cailletaud, "A generic method for modeling the behavior of anisotropic metallic materials: Application to recrystallized Zirconium alloys," *Mech. Mater.*, vol. 39, no. 5, pp. 458–472, 2007.

[171] J. J. Fundenbergert, M. Philippe, F. Wangner, and C. Esling, "Modelling and prediction of mechanical properties for materials with hexagonal symmetry (Zinc , Titanium and Zirconium alloys)," *Acta Mater.*, vol. 45, no. 10, pp. 4041–4055, 1997.

[172] D. Li, H. Garmestani, and S. Ahzi, "Processing path optimization to achieve desired texture in polycrystalline materials," *Acta Mater.*, vol. 55, no. 2, pp. 647–654, 2007.

[173] R. Y. Zhang, M. R. Daymond, and R. A. Holt, "A finite element model of deformation twinning in zirconium," *Mater. Sci. Eng. A*, vol. 473, no. 1-2, pp. 139–146, 2008.

[174] M. Shiekhelsouk, V. Favier, K. Inal, and M. Cherkaoui, "Modelling the behaviour of polycrystalline austenitic steel with twinning-induced plasticity effect," *Int. J. Plast.*, vol. 25, no. 1, pp. 105–133, 2009.

[175] I. J. Beyerlein and C. N. Tome, "A probabilistic twin nucleation model for HCP polycrystalline metals," *Proc. R. Soc. A Math. Phys. Eng. Sci.*, vol. 466, no. 2121, pp. 2517–2544, 2010.

[176] G. Proust, C. N. Tomé, and G. C. Kaschner, "Modeling texture, twinning and hardening evolution during deformation of hexagonal materials," *Acta Mater.*, vol. 55, no. 6, pp. 2137–2148, 2007.

[177] S. Mendelson, "Zonal dislocations and dislocation reactions with twins in hcp metals," *Scr. Metall.*, vol. 4, pp. 5–8, 1970.

[178] S. Mendelson, "Zonal Dislocations and Twin Lamellae in h.c.p. Metals," *Mater. Sci. Eng.*, vol. 4, pp. 231–242, 1969.

[179] J. Wang, J. P. Hirth, and C. N. Tomé, "$(10\bar{1}2)$ Twinning nucleation mechanisms in hexagonal-close-packed crystals," *Acta Mater.*, vol. 57, no. 18, pp. 5521–5530, 2009.

[180] J. Wang, R. G. Hoagland, J. P. Hirth, L. Capolungo, I. J. Beyerlein, and C. N. Tomé, "Nucleation of a $(10\bar{1}2)$ twin in hexagonal close-packed crystals," *Scr. Mater.*, vol. 61, no. 9, pp. 903–906, 2009.

[181] J. Wang, I. J. Beyerlein, J. P. Hirth, C. N. Tome, and C. Tomé, "Twinning dislocations on $\{10\bar{1}1\}$ and $\{10\bar{1}3\}$ planes in hexagonal close-packed crystals," *Acta Mater.*, vol. 59, no. 10, pp. 3990–4001, 2011.

[182] D. H. Sastry, M. J. Luton, and J. J. Jonas, "Stacking fault energy and its influence on high-temperature plastic flow in Zr-Sn alloys," *Philos. Mag.*, vol. 30, no. 1, pp. 115–127, 2006.

[183] I. Groma, "X-ray line broadening due to an inhomogeneous dislocation distribution," *Phys. Rev. B*, vol. 57, no. 13, pp. 7535–7542, 1998.

[184] I. Groma and F. Székely, "Analysis of the asymptotic properties of X-ray line broadening caused by dislocations," *J. Appl. Crystallogr.*, 2000.

[185] M. Tschopp and D. McDowell, "Influence of single crystal orientation on homogeneous dislocation nucleation under uniaxial loading," *J. Mech. Phys. Solids*, vol. 56, no. 5, pp. 1806–1830, 2008.

[186] M. a. Tschopp, D. E. Spearot, and D. L. McDowell, "Atomistic simulations of homogeneous dislocation nucleation in single crystal copper," *Model. Simul. Mater. Sci. Eng.*, vol. 15, no. 7, pp. 693–709, 2007.

[187] H. Van Swygenhoven, P. Derlet, and A. Frø seth, "Nucleation and propagation of dislocations in nanocrystalline fcc metals," *Acta Mater.*, vol. 54, no. 7, pp. 1975–1983, 2006.

[188] J. Wang, J. Li, S. Yip, S. Phillpot, and D. Wolf, "Mechanical instabilities of homogeneous crystals," *Phys. Rev. B*, vol. 52, no. 17, pp. 12627–12635, 1995.

[189] M. S. Daw, S. M. Foiles, and M. I. Baskes, "The embedded-atom method: a review of theory and applications," 1993.

[190] M. I. Mendelev and G. J. Ackland, "Development of an interatomic potential for the simulation of phase transformations in Zirconium," *Philos. Mag. Lett.*, vol. 87, no. 5, pp. 349–359, 2007.

[191] R. Voskoboinikov, Y. Osetsky, and D. Bacon, “Core structure, dislocation energy and Peierls stress for edge dislocations with (0001) and slip planes in α-Zr,” *Mater. Sci. Eng. A*, vol. 400-401, no. 2005, pp. 45–48, 2005.

[192] P. H. Hünenberger, “Thermostat Algorithms for Molecular Dynamics Simulations,” *Adv. Polym. Sci.*, vol. 173, pp. 105–149, 2005.

[193] M. Zhou, “A new look at the atomic level virial stress: on continuum-molecular system equivalence,” *Proc. R. Soc. A Math. Phys. Eng. Sci.*, vol. 459, no. 2037, pp. 2347–2392, 2003.

[194] A. Stukowski and K. Albe, “Extracting dislocations and non-dislocation crystal defects from atomistic simulation data,” *Modell. Simu. Mater. Sci. Engg.*, vol. 18, p. 25016, 2010.

[195] A. Stukowski, J. Markmann, J. Weissmüller, and K. Albe, “Atomistic origin of microstrain broadening in diffraction data of nanocrystalline solids,” *Acta Mater.*, vol. 57, no. 5, pp. 1648–1654, 2009.

[196] A. Stukowski, “Structure identification methods for atomistic simulations of crystalline materials,” *Model. Simul. Mater. Sci. Eng.*, vol. 20, p. 045021, 2012.